THE MODELLING OF HYDROGEN IN AMORPHOUS AND GLASSY SEMICONDUCTORS

By

Michael Kay

B.Sc.(Hons) in Physics, University of Lancaster, 1993

M.Sc. in Physics of Amorphous Electronic Materials, University of Dundee, 1994

A THESIS SUBMITTED IN PARTIAL FULFILLMENT OF
THE REQUIREMENTS FOR THE DEGREE OF
DOCTOR OF PHILOSOPHY

in

THE CONDENSED MATTER PHYSICS RESEARCH GROUP
DEPARTMENT OF PHYSICS AND ASTRONOMY

THE UNIVERSITY OF LEICESTER

Submitted December 1998

ProQuest LLC
789 East Eisenhower Parkway
P.O. Box 1346
Ann Arbor, MI 48106-1346

Abstract

The behaviour of hydrogen in crystalline and amorphous semiconductors has been simulated using the positive muon as a microscopic probe. Measurements have been made on a wide range of materials: polycrystalline and amorphous silicon, both doped and intrinsic; polycrystalline and amorphous germanium; crystalline GaAs and GaP; and selenium-based glassy chalcogenides. Using the techniques of μSR (Muon Spin Resonance/ Rotation/ Relaxation/ Repolarisation), the evolution of the spin polarisation of the muon is monitored. In semiconductors and insulators, the muon is bonded to an electron to form muonium ($\mathrm{Mu} = \mu^+ \mathrm{e}^-$) and it is this species that behaves as an analogue of isolated atomic hydrogen. The muon spin polarisation is greatly influenced by the local environment, and its study has yielded information on the sites occupied by the muon/muonium, via determinations of diamagnetic fractions and hyperfine parameters. The technique of muon spin repolarisation has been used for the first time in conjunction with recently derived theoretical expressions to extract this information. Preliminary measurements using the technique of muon spin resonance on a newly developed facility at the Rutherford Appleton Laboratories have also been made.

Contents

List of Tables

List of Figures

List of Acronyms and Symbols

Acronym/Symbol	
AB	Anti-bonding site
BC	Bond-Centre site
CVD	Chemical Vapour Deposition
ESR	Electron Spin Resonance
LF	Longitudinal Field
Mu	Muonium
Mu_T^0	Neutral muonium at the isotropic[1]site
Mu_{BC}^0	Neutral muonium at the bond-centre[2]site
Mu^D	Diamagnetic muonium
PECVD	Plasma Enhanced Chemical Vapour Deposition
RDF	Radial Distribution Function
T	Tetrahedral interstitial site
TF	Transverse Field
TF20	Transverse Field at 20 Gauss
μSR	Muon spin rotation/ repolarisation/ relaxation/ resonance
VAX	Virtual Access eXtension
ZF	Zero field

[1]This notation was originally used for tetrahedral cages only, but in this thesis it has been adopted for all isotropic sites.

[2]This notation was originally used for bond-centre sites only, but in this thesis it has on occasions been adopted as the symbol for all anisotropic sites including the radical state.

Acknowledgements

Over the period of my pre-doctoral study at Leicester, I have been assisted and guided by a great many people. Many thanks goes to all these people. Of all these people, most worthy of gratitude is my supervisor Professor E.A. Davis. During the period he introduced me to a field which I had previously neither experience nor understanding of. Further special thanks goes to Professor S.F.J. Cox, Professor Eugenie Mytilineou and Dr Kim Chow, all of whom have contributed to both the research contained within this thesis and to furthering my education. We have shared many happy and memorable moments whilst conducting experiments, and a happy student makes an eager student.

Further acknowledgements must be expressed to the staff at the ISIS facility of the Rutherford Appleton Laboratories, especially to Dr Steve Cottrell and Dr Chris Scott without whom not even a murmur of a single muon would surely have been heard.

In Leicester, I wish to express my utmost gratitude to Mr. Stuart Thornton, who in a barrage of other work always managed to seize a few moments and repair apparatus, without which many of my samples would never have been made. Further thanks goes to Dr Jaeho Choi who guided me through Leicester's sputtering system, and who, with generous assistance from his wife, introduced me to the culinary delights of Korean food. Many a happy moment was shared in conversation with Dr Martin Durell, Mr Richard Bayliss and Miss Marie Bassford, so thanks to them also, as well as all members of the Leicester CMP group, students, academic staff and laboratory technicians.

Finally, I would like to thank those pillars of support amongst my other friends and family. Thanks to all my family of Melbourne Hall Evangelical Free Church, especially Rev. and Mrs Paul Bassett, Dr and Mrs Reuben Danladi and to Miss Margaret Rice, who have encouraged me in all things spiritual and academic. Sincere thanks to my family; my Mum, Dad, twin brother Dylan and Nana. To my beautiful wife, Eriko, without whom I would surely have gone hungry and homeless, and also to Mum and Dad Tomizawa ご助力頂きましたことを心より感謝申し上げます。

Chapter 1

Introduction

1.1 Hydrogen in crystalline and amorphous semiconductors

In recent years the role of hydrogen in the growth of semiconductors, its ability to attach itself to unsatisfied orbitals leading to the passivation of dangling bonds and dopants, and the phenomenon of induced metastability have become increasingly important as topics of research. The presence of hydrogen can be accidental as well as deliberate; in either case an understanding of its effects is important from both an applied and fundamental viewpoint. Hydrogen is intentionally introduced typically during the deposition and fabrication of semiconductor devices; whereas during wet/dry chemical etching, crystal growth or deposition of device overlayers, hydrogen can be unintentionally introduced into the material.

Though research into hydrogen in semiconductors did not intensify till the 1980s, hydrogen's ability to alter the electronic properties in crystalline semiconductors was studied some decades earlier in the early 1950s[1]. The diffusion of hydrogen in elemental semiconductors was studied by Van Wieringen and Warmoltz[2]; they determined the diffusion coefficient and solubility of hydrogen gas in both silicon and germanium, concluding that it was likely to diffuse via interstitial sites. Of importance, was the conclusion by Sakurai and Hagstrom[3] that a hydrogen atom can be attached to the dangling orbital of a surface silicon atom, thereby forming a Si–H covalent bond, which is now known to be stronger than a Si–Si bond and leads to a relaxation of the lattice.

This was best seen in samples at 573 K, which appeared to be the optimum temperature for hydrogen saturation of the surface, where the rate of hydrogen desorption balanced the rate of hydrogen adsorption. Nonetheless, it was proved that, irrespective of the temperature of the substrate, hydrogenation can help in the reconstruction of surface atoms. By the mid-1970s, the role of hydrogen in amorphous semiconductors had become an increasingly important aspect of semiconductor research. Previously, efforts to chemically dope evaporated and sputtered a-Ge and a-Si had been unsuccessful, but it was found that by the incorporation of hydrogen into the materials, thereby passivating defect states, donor and acceptor states due to phosphous and boron could be made effective[4]. Similarly, the unavoidable introduction of hydrogen in the production of a-Ge and a-Si by the glow discharge decomposition of germane and silane, again allowed the doping of these materials[5].

Of relevance to the application of amorphous semiconductors in devices was an early belief that hydrogen was involved in the radiative process of a-Si and therefore the luminescence of the material[6]. This led to an increased research into hydrogen in amorphous semiconductors, even though soon after it became clear that hydrogen in fact neutralised dangling bonds which typically behave as non-radiative recombination centres[7]. Further to this, a more subtle effect of hydrogen incorporation in crystalline materials was later seen. With the boron doping of single-crystal silicon, shallow acceptor levels are created, the acceptor (B) is surrounded by four Si bonds, only three of which can actually be satisfied, and therefore a bond with an unpaired electron exists (i.e. a hole). What was found was that, upon the introduction of hydrogen, thereby supplying an electron for bonding, the resistivity of the material increased, indicating the passivation of the substitutional acceptors. With the growing importance of microelectronics, an understanding of the effects of hydrogen on such a micro-scale in the resulting devices is of increasing necessity.

1.1.1 Hydrogen passivation of defect centres

Owing to its importance in semiconductor device applications, silicon is probably the must studied and therefore the best understood of all the semiconductors. The application of hydrogen in passivating defects in silicon is also well documented, especially in single-crystal silicon. Therefore in this discussion of defects, c-Si and a-Si(:H) will be of primary concern. Possibly the most important defect in any crystalline material is its surface. Therefore as well as the analysis of the 'bulk' defects, research into 'surface science' has grown in importance; besides, understanding gained from the study of the surface may be relevant to bulk properties such as interfaces and grain boundaries. Defects in semiconductors can be classified as point, line, planar or volume defects. Point defects include those that occupy or share a single lattice site, typically substitutional impurities, vacancies and self- or impurity-interstitials. A combination of defects can result in line, plane and volume defects. Dislocations are a type of line defect and arise from plastic deformation; grain boundaries can be considered to be arrays of dislocations. There is interest in the passivation of all these defect types.

As mentioned previously, Sakurai and Hagstrom[3] concluded that a hydrogen atom can become attached to the dangling orbital of each surface silicon atom, leading to a relaxation of the lattice by allowing the lattice perturbed at the surface to "reconstruct" itself. In electronic grade crystalline silicon, there tend to be very few bulk defect states; hence there is a strict periodicity of the lattice and long-range order. Conversely, in amorphous silicon, bonds can be distorted and stretched, and many bonds are broken resulting in dangling bonds. As well as there being no long-range order or lattice periodicity, a-Si contains a high concentration of these bulk defects (about $10^{20}\,\mathrm{cm}^3$), which form midgap states that act as non-radiative recombination centres, making the material essentially non-photoconducting. By hydrogenation passivation of the dangling bonds, the gap state concentration can be reduced to about $10^{15}\,\mathrm{cm}^3$ and as a consequence hydrogenated amorphous silicon (a-Si:H) has been of greater interest for device fabrication.

Of further relevance to the fabrication of devices is the hydrogenation passivation

of p-n junctions[8] for which it has been found that exposure to atomic hydrogen results in a substantial decrease in leakage current. It was assumed that, at the surface, widening of the bandgap, due to hydrogenation, created potential barriers that 'reflect' electrons/holes away from the surface. Unfortunately, as devices decrease in size, there appears to be little understanding of hydrogen on the microscopic scale, essential for further device development.

A grain boundary, the interface between two adjacent crystals, is typically a site rich in dangling bonds. As a consequence, the Fermi level is held near midgap. Just as in a-Si:H where hydrogenation has allowed movement of the Fermi level, passivating grain boundary dangling bonds unpins the Fermi level[9], thereby allowing the valence and conduction bands to flatten at these boundaries. If a p-n junction is intersected by a grain boundary, then the short-circuit current and the open-circuit voltage is reduced when carriers recombine at the dangling bonds. This is particularly relevant in photo-voltaic devices, where efficiency can be increased from about 8% to about 11% by hydrogenation[9].

Other regions of a material were there is a large concentration of defect states are dislocations. A dislocation is a type of line imperfection along which slip propagates through a material, typically crystalline, though the localisation can be simply at a point or along a line, or maybe over an area. The resulting interruptions in the lattice result in dangling bonds and therefore midgap pinning of the Fermi level. One method in which dislocations can occur is by the growth of a material onto a substrate where the two lattice constants differ. A severe stress across the boundary can occur, which is partly relieved by a dislocation.

Ion-implantation creates a large number of defects, generating dangling bonds that form centres for non-radiative recombination. As well as competing with radiative transitions, these centres also reduce the carrier lifetime. Upon hydrogenation, hydrogen passivates the dangling bonds, hence neutralising these centres, and the luminescence process then increases in efficiency, important in devices, such as light-emitting diodes. Of relevance to microelectronics is that hydrogen diffusion through silicon is reduced

by the hydrogen becoming trapped at dislocations and implantation-induced defects[10]. With this trapping of hydrogen, metastable effects are reduced.

1.1.2 Hydrogen-induced defects

So far, only the positive aspects of hydrogenation have been discussed; unfortunately there are also negative aspects of the incorporation of hydrogen into a material, typically hydrogen-induced defects. When hydrogen diffuses into single-crystal silicon, extended defects and electrically active defects occur[11]. The possibility that these defects are related to radiation or plasma damage is negligible, since they are created even when a remote hydrogen plasma is used during hydrogenation. For example, with hydrogen (or deuterium) gas flowing through a microwave cavity, the sample is exposed only to the downstream products from the plasma, i.e. free radicals and molecular species; therefore ballistic effects are reduced. Johnson *et al* [11] exposed n-type silicon to monatomic hydrogen, which introduced a very high concentration of hydrogen (about 10^{20} atoms/cm^3) immediately adjacent to the surface, though the H concentration rapidly decreased (to about 10^{18} atoms/cm^3) with distance into the bulk. Defects described as *hydrogen-stabilised platelets* or *microcracks* appeared within 0.1μm of the exposed surface, which correlated with the region of high hydrogen concentration. These platelets are planar defects, not associated with stacking faults but microcracks in which the separation between adjacent planes of silicon atoms is increased because of small displacements of the Si atoms from their lattice sites.

As well as the formation of platelets, electronic deep levels can be induced in the band gap as a consequence of hydrogenation. Like platelets, they are considered to be formed independently of ballistic species from the plasma or radiation damage because they can be introduced with a remote hydrogen plasma. These electronically active gap states have been detected by photoluminescence spectroscopy, by which H-induced radiative transitions were observed (see Figure 1.1).

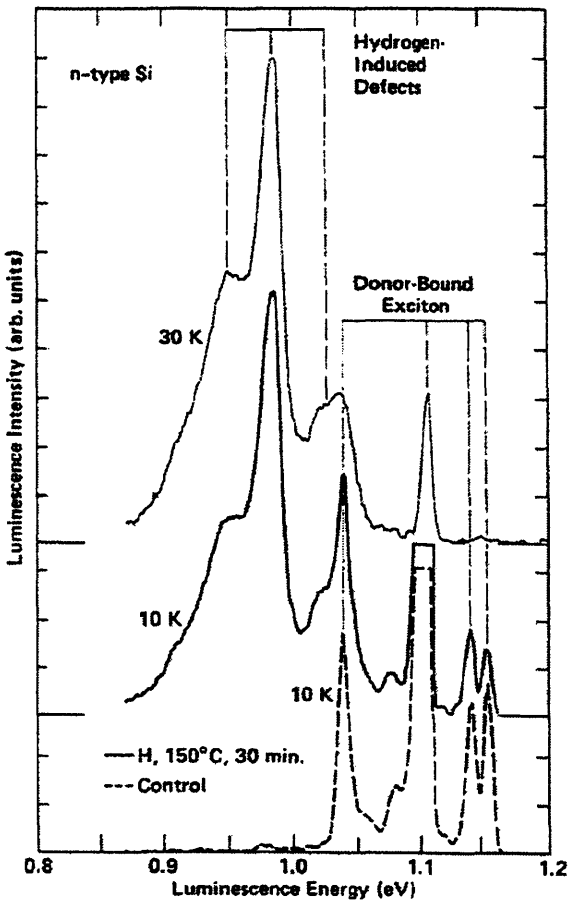

Figure 1.1: Luminescence spectra for n-type silicon before and after hydrogenation (from [11]).

1.1.3 Hydrogen diffusion and metastability

As already discussed, hydrogen's primary benefit is in the passivation of dangling bonds; unfortunately though, a hydrogen concentration larger than is actually necessary for this purpose, can sometimes be present; for example electronic grade a-Si:H prepared by glow-discharge decomposition contains about 10 at% - far more than required. Even though it forms a strong bond to silicon, hydrogen in a-Si:H is not particularly stable; in fact if heated above 300-400°C, H_2 gas will be evolved. This evolution of hydrogen requires hydrogen diffusion. Hydrogen diffusion has been linked with induced metastabilities, probably the best known being the Staebler-Wronski effect[12] where illumination causes the creation of dangling bonds; others include heating of the sample and charge injection.

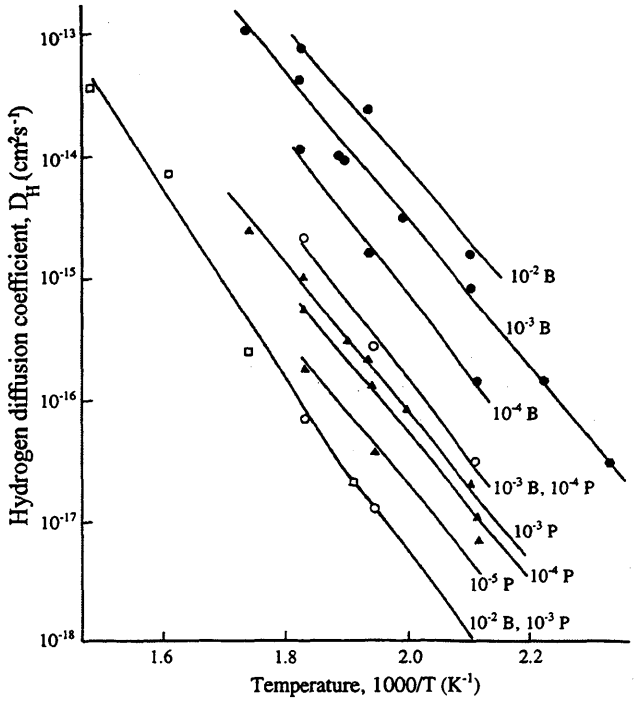

Figure 1.2: Temperature dependence of the hydrogen diffusion coefficient in a-Si:H, at different doping levels (from [15], [16]).

The diffusion coefficient, D_H is thermally activated and can be expressed as:-

$$D_H = D_{H_0} \exp\left(\frac{-E_D}{kT}\right) \tag{1.1}$$

where E_D is the activation energy. It seems that all the hydrogen diffuses with a single diffusion coefficient, which is rather surprising when considering the inhomogeneous hydrogen distribution. This suggests that much of the hydrogen is in similar bonding sites[13]. Shinar *et al*[14] showed that hydrogen diffusion is time dependent, according to

$$D_H = D_0 t^{\beta-1} \tag{1.2}$$

where $\beta \sim 0.8$ at 250°C. An increase in D_H occurs when the material is doped [15],[16], see Figure 1.2. Similarly when non-optimal growth conditions are used and large voids or columnar growth morphology occur then D_H again increases. Hydrogen recombines into H_2 which easily diffuses through the voids[17]. In general, the release of hydrogen from the bonds into mobile interstitial sites is assumed to be responsible for hydrogen diffusion. A possible reaction to describe the diffusion is :

$$\text{Si–H} \rightleftharpoons \text{Si–} + \text{H}_i \tag{1.3}$$

where the Si–H bond is broken creating a dangling bond and interstitial hydrogen (H_i). For there to be the breaking of Si–H bonds, there must also be the formation of Si–H bonds. Again for a-Si:H, there can be a large distribution of Si–Si bond angles and bond lengths; therefore, as the bond becomes distorted by a nearby hydrogen atom, whose binding energy is greater than that of silicon to silicon, then the bond breaks leaving a Si–H bond and a neighbouring dangling bond[18]. In the above reaction, the dangling bond is an electronic defect generating midgap states. Due to its charge, the defect state reduces the energy required to release the hydrogen by an amount $E_D - E_F$, where E_D is the energy of the gap state and E_F is the Fermi energy. The increase of the diffusion coefficient by doping can therefore be explained as an electronic effect, modifying the electronic structure.

1.2 Non-crystalline semiconductors

Research into non-crystalline semiconductors appears to have begun on glasses. In the 1950s, studies of chalcogenide glasses[19] found that they behaved like intrinsic semiconductors; by adding dopants their electrical conductivity could not be increased. At the time, drift mobility measurements were being made on vitreous selenium[20] and amorphous germanium[21]. Ovshinsky's discovery that chalcogenide glasses have switching and memory effects[22] brought increased activity to research into non-crystalline materials. Soon, the device application of these materials was envisaged; with optical memory effects, imaging and photodoping all having great potential. Application of the materials in photothermal and photovoltaic devices was made possible by the discovery that amorphous silicon can be doped both n and p-type.

Crystalline materials exhibit a great deal of order in which the atoms are arranged in a pattern that repeats periodically over three dimensions to an infinite extent. On the other hand, non-crystalline materials exhibit varying degrees of randomness and disorder, to an extent far greater than an imperfect crystal, which may contain point or line defects, such as vacancies or dislocations. The differing types of disorder are generalised as topological, spin, substitutional or vibrational disorder, as shown in Figure. 1.3.

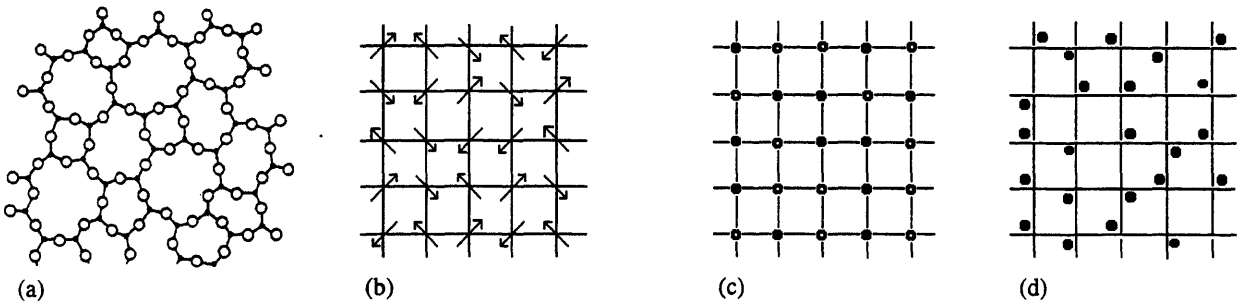

Figure 1.3: Types of disorder: (a) topological disorder (no long-range order), (b) spin disorder (on regular lattice), (c) substitutional disorder (on regular lattice), (d) vibrational disorder (about the equilibrium positions of a regular lattice).

Briefly, topological disorder occurs when there is no translational periodicity (Figure 1.3(a)) and spin or magnetic disorder occurs when the perfect crystal lattice remains but each atomic site possesses a spin or magnetic moment which is oriented randomly (Figure 1.3(b)). Materials which contain randomly oriented spin are referred to as *spin glasses*, but should not be confused with genuine glasses. Substitutional disorder occurs when an atom of a second material is substituted, on one of the lattice sites, for an atom of the material common to the lattice (Figure 1.3(c)). Vibrational disorder occurs when the random motion of atoms about their equilibrium positions destroys the perfect periodicity that occurs in crystals at 0 K (Figure 1.3(d)).

Non-crystalline semiconductors can be subdivided into two types, *glassy* and *amorphous*. Glassy materials will be defined as those materials which can be quenched from the super-cooled melt and typically exhibit a glass transition and an abrupt change in derivative thermodynamic properties e.g. heat capacity or thermal expansivity. The glass transition temperature has been recorded in some chalcogenides and reflects the ability to prepare them from a semiconductor melt by rapid quenching to temperatures below the glass transition temperature. Although glassy materials by their nature are amorphous, the classification of an amorphous semiconductor will be limited to non-crystalline materials that are normally prepared on cooled substrates as thin films by an atomic deposition procedure, such as sputtering, chemical vapour deposition, ion bombardment or even electroplating. More specifically though, a material is defined to be

amorphous if its diffraction pattern consists of diffuse rings (or halos) instead of sharply defined Bragg rings or spots, which are characteristic of single crystal or polycrystalline materials (Figure 1.4).

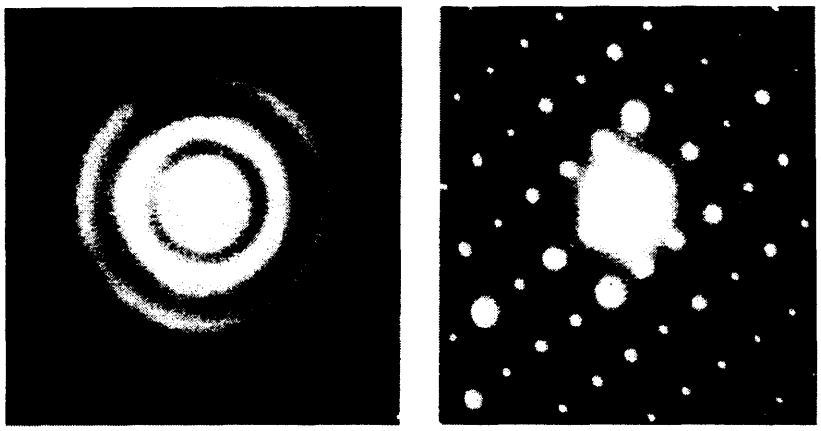

Figure 1.4: Transmission electron diffraction patterns of thin films of As_2Se_3 in amorphous (left) and crystalline phases (right) (from [25]).

1.2.1 The preparation of amorphous materials

In the production of amorphous materials, a wide variety of differing deposition techniques are available. The three techniques used in preparing samples studied in this work will be discussed. Of these, perhaps the most widely used is *thermal evaporation*, even though it is really only suitable for the deposition of thin-film samples. Conceptually, it is perhaps the simplest and easiest to understand. A source compound, for example, Si or Ge, is vapourised and the material deposited onto a substrate. A schematic diagram of the apparatus is shown in Figure 1.5(a). To reduce the presence of impurities within the sample, the evaporation chamber is evacuated. A large direct current passes between the electrodes and through the 'boat', which acts as a heated resistive element. If the evaporating material has a high melting point, an electron gun can be placed in the chamber to bombard the material with high energy vapourising electrons. Though the evapoaration method is relatively simple and effective, in that a wide variety of materials can be deposited, it does have disadvantages. If deposition occurs at room temperature, the surface mobility of the deposited atoms may be small, resulting in large concentra-

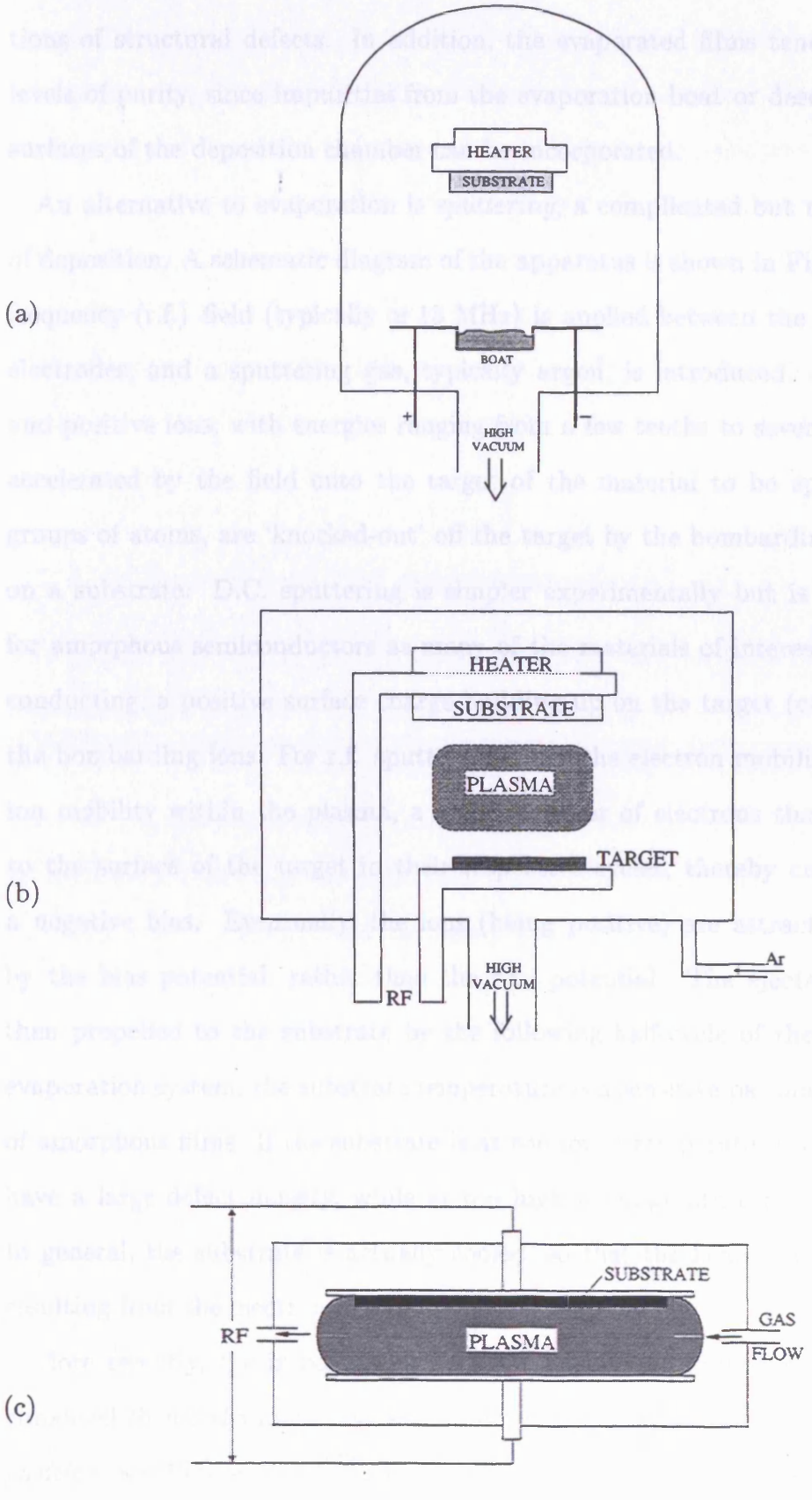

Figure 1.5: Schematic illustration of (a) a thermal evaporation chamber, (b) a r.f sputtering chamber and (c) a capacitive glow-discharge chamber.

tions of structural defects. In addition, the evaporated films tend to have rather low levels of purity, since impurities from the evaporation boat or desorbed gases from the surfaces of the deposition chamber can be incorporated.

An alternative to evaporation is *sputtering*, a complicated but more flexible method of deposition. A schematic diagram of the apparatus is shown in Figure 1.5(b). A radio-frequency (r.f.) field (typically $\simeq$ 13 MHz) is applied between the substrate and target electrodes, and a sputtering gas, typically argon, is introduced. A plasma is created and positive ions, with energies ranging from a few tenths to several electron volts, are accelerated by the field onto the target of the material to be sputtered. Atoms, or groups of atoms, are 'knocked-out' off the target by the bombarding ions and collected on a substrate. D.C. sputtering is simpler experimentally but is not generally useful for amorphous semiconductors as many of the materials of interest are not sufficiently conducting, a positive surface charge building up on the target (cathode) which repels the bombarding ions. For r.f. sputtering, since the electron mobility is higher than the ion mobility within the plasma, a larger number of electrons than ions are attracted to the surface of the target in their respective cycles, thereby creating a build-up of a negative bias. Eventually, the ions (being positive) are attracted from the plasma by the bias potential, rather than the r.f. potential. The ejected target material is then propelled to the substrate by the following half-cycle of the r.f. field. Like the evaporation system, the substrate temperature is a sensitive parameter in the deposition of amorphous films. If the substrate is at too low a temperature, the resultant film can have a large defect density, while at too high a temperature the film may crystallise. In general, the substrate is actually cooled, so that the heating effect of the r.f. field, resulting from the electron bombardment, is minimised.

More recently, the importance of a third deposition method has increased; plasma-enhanced chemical vapour deposition, more commonly known as *glow-discharge decomposition*, see Figure 1.5(c)[23], is now the method predominantly used for the deposition of high quality, low-defect-density, electronic-grade materials. Like sputtering, this method is dependent upon the production of a plasma by a r.f. field in a low-pressure gas

(usually argon), but it is a chemical deposition process, rather than a physical process, dependent upon the decomposition of chamber gas (e.g. silane for the deposition of silicon films) resulting in the deposition of a solid film on the substrate placed directly in the plasma. Inductive and capacitive couplings are both used, but the capacitive method is used more commonly since it can be scaled up, so as to allow deposition of large surface areas, ideal for manufacturing devices. Being a chemical process, the variable parameters are more numerous than the aforementioned physical processes. These include gas pressure/temperature and flow rate, substrate temperature, and the r.f. power applied to the plasma.

1.2.2 Glasses and the glass transition

Two events may occur when a liquid melt is cooled, either crystallisation or glass-formation. The formation of a glass by cooling requires the prevention of the nucleation and growth processes responsible for crystallisation. Crystallisation of the liquid may occur at the material's melting point, T_m; if not then the liquid becomes *supercooled* at temperatures below T_m and eventually a *glass* is formed. This change in the melt can be monitored by observing the temperature dependence of melt-volume (see Figure 1.6). In principle, it should be possible to cool any liquid to form a glass, provided a suitably

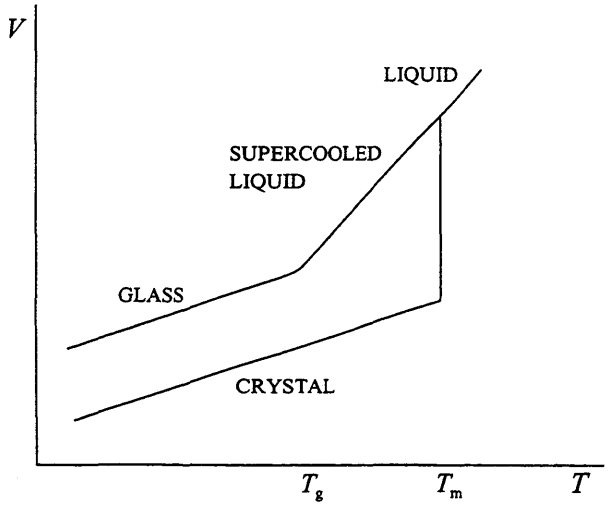

Figure 1.6: Schematic illustration of the temperature dependence of the volume as a supercooled liquid is cooled through the glass-transition temperature, T_g. Also shown is the first-order phase transition that accompanies crystallisation from the melt.

large cooling rate can be achieved. The most rapid quench rate can be achieved by a technique known as the 'splat cooling technique', where quench rates can reach up to 10^7 deg/s. This can be compared to 1–10 deg/s for air quenching in the production of chalcogenide glasses. The difference in structures for the glassy and crystalline forms of a hypothetical oxide, A_2O_3, is shown in Figure 1.7. At T_m, a discontinuity of the

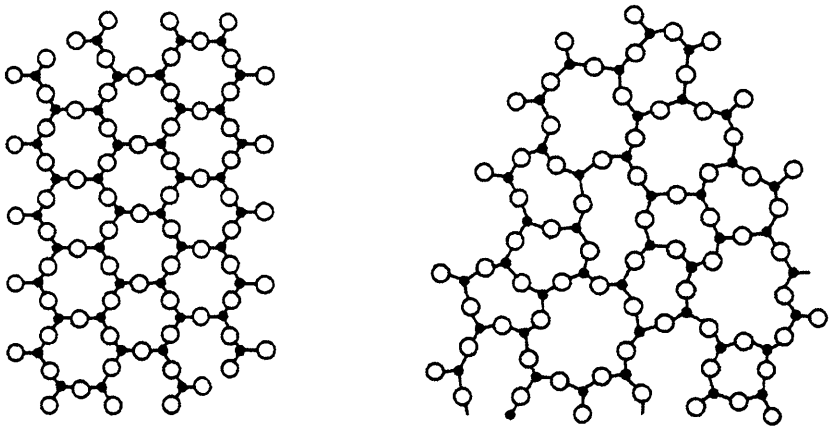

Figure 1.7: Schematic two-dimensional illustration of (a) a hypothetical crystalline compound A_2O_3, and (b) the Zachariasen model for the glassy form of the same compound.

gradient, $\frac{\partial V}{\partial T}$, (where $\frac{\partial^2 V}{\partial^2 T} \rightarrow \infty$) characterises crystal formation; whereas a more gradual change of gradient characterises glass formation. The region were this change of $\frac{\partial V}{\partial T}$ occurs is called the "glass transition temperature", T_g, and is sometimes difficult to pinpoint exactly. A problem is that T_g is dependent on the thermal history of the glass, and therefore varies with different cooling rates; hence it is unrealistic to expect the T_g to behave as a defined parameter of the particular material type. With the slow variation of $\frac{\partial V}{\partial T}$ at T_g, a discontinuity of derivative variables such as the heat capacity $C_p = (\frac{\partial H}{\partial T})_p$ and the thermal expansion coefficient $\alpha_T = \frac{\partial lnV}{\partial T}$ occurs. Indeed, measurement of the temperature dependences of these differentials, C_p and α_T, are considered more reliable for identifying T_g than similar measurements for the thermodynamic variables volume V, entropy S and enthalpy H.

In a non-crystalline semiconductor the covalent bonding to nearest neighbours is determined by the chemical nature of the atoms. Bond-angles and bond-lengths vary not just from material to material but also with the local environment within the same ma-

terial. The nature of the atoms in covalently bonded glasses and amorphous materials is that all covalent bonds be satisfied, thereby obeying Mott's '8–N' rule, where N is the number of valence electrons; the coordination number N_c is therefore given by (8–N). For example, selenium in group VI of the periodic table has $N_c = 2$.

It has been suggested[24] that there exists a connection between glass-forming ability and the average coordination number. It is argued that when the number of mechanical constraints (related to N_c) acting on each atom, arising from interatomic forces acting on it, is equal to the number of degrees of freedom available N_d, then the glass-forming tendency is maximised. It follows that when a system has a number of constraints greater than N_d it is 'overconstrained' and cannot easily form a glass, although amorphous structures can result if the material is rapidly cooled. For a system in 3-d space, the number of degrees of freedom is taken to be $N_d = 3$. A further differentiation between glasses and amorphous materials is the flexibility of covalent bond angles, which is largest in two-fold coordinated group VI elements *e.g.* Se, and smallest for tetrahedrally coordinated group IV elements *e.g.* Si. Consider the case of silicon. If a covalent random network is attempted without the presence of group VI elements, amorphous silicon results, which is no longer a glass and very over-constrained. It seems that there is a greater glass-forming tendency when the short-range order imposed by bond stretching and bending forces is just large enough to exhaust the local degrees of freedom. With an increasing average covalent coordination number the internal strain increases, and for a reducing coordination number the entropy increases because the materials become insufficiently crosslinked .

1.2.3 Defects

Both amorphous semiconductors and chalcogenide glasses can have significant defect densities. The midgap density of states can be large enough to 'pin' the Fermi level near the midgap. A common defect-type in chalcogenide glasses is the chain-end dangling bond 'D^0', where the superscript refers to the states' neutral charge. Figure 1.8(a) shows a defect state with one electron occupancy, at a certain energy in the gap. If a

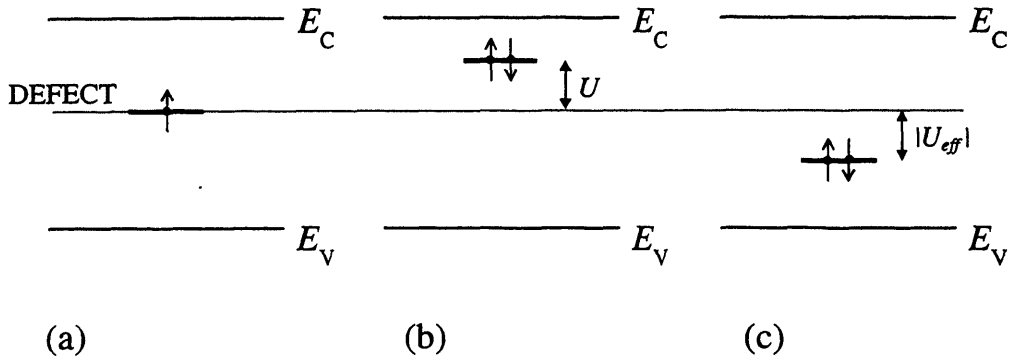

Figure 1.8: Schematic illustration of positive and negative correlation energies.

second electron is added to this defect site, then there is a double occupancy, and the Coulomb interaction between the two electrons leads to an increase in the energy of the state, known as the correlation energy 'U', Figure 1.8(b). This situation is known as 'positive U'. If this double-occupied state interacts with the lattice, to such a degree that the lattice is relaxed, then the energy of the defect state is lowered by an amount larger than U, the initial gain in energy. In Figure 1.8(c), the resultant energy level of the double-occupied defect state is **below** the energy of the single occupied state by an amount U_{eff}, the effective correlation energy, often referred to as 'negative U_{eff}'. It is possible that the second electron may have transferred from another region of the lattice. In chalcogenide glasses, because of their chain-like structures, chain-end dangling bonds are common, and typically electron transfer can occur between two neutral dangling bond D^0 states, resulting in the creation of two **charged** defects D^+ and D^-. This reaction can be represented thus :

$$2D^0 \rightarrow D^+ + D^- + \text{energy} \tag{1.4}$$

The defect occupation is denoted as D^+ (empty), D^0 (single occupancy) and D^- (double occupancy). Because of the lower effective correlation energy, energy is gained and the reaction is said to be exothermic. This can be represented on a configuration-coordinate (CC) diagram as in Figure 1.9, where comparisons of the state energies are made for the two neutral D^0 states and the charged D^+ and D^- states. Although the position on the horizontal axis is called a configuration coordinate q, it is not an ordinary Cartesian coordinate. Rather, it is a symbolic representation in one dimension of the entire set of

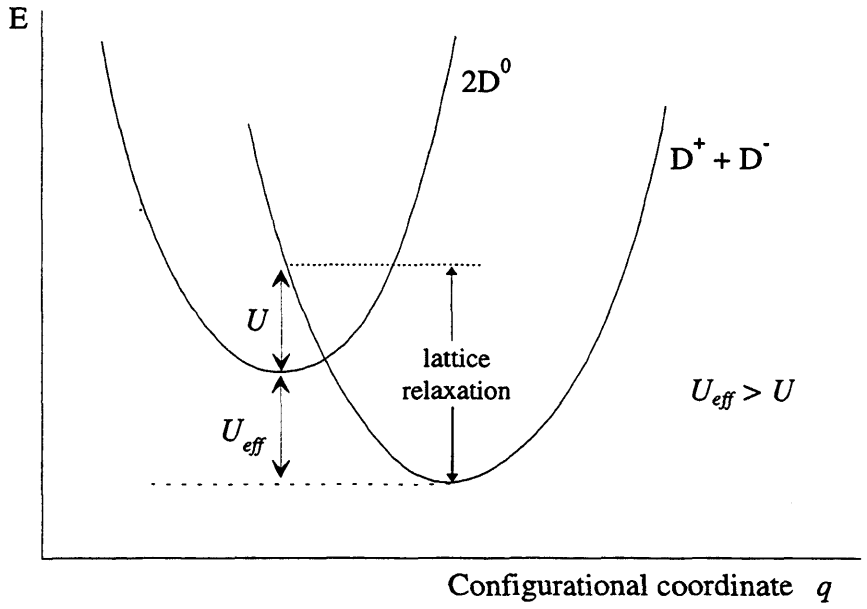

Figure 1.9: Configuration-coordinate diagram for the formation of a D^+–D^- pair. The transfer of an electron between two D^0 centres to give a D^+–D^- pair, at the same configuration, costs energy U. The D^+–D^- centres then relax to a different configuration, and the overall energy is reduced by the effective correlation energy U_{eff}, where $U_{eff} > U$.

real three-dimensional coordinates that specify the positions of the defect itself and all the nearby atoms with which it interacts. A value of q therefore represents a complete configuration for those atoms, and a change in q implies a possibly complicated set of changes in the positions of the atoms.

Of importance is the ability of the lattice to reconfigure, or relax. Chalcogenide glasses are regarded as flexible materials and can therefore 'relax' leading to the negative-U situation. On the other hand, the networks of tetrahedral materials, such as Si and Ge, are rigid and therefore lattice relaxation is difficult; hence the situation of positive-U remains.

Bibliography

[1] E. Mellwo, Zeitschrift für Physik, **138**, (1954), 478.

[2] A. Van Wieringen and N. Warmoltz, Physica, **22**, (1956), 849.

[3] T. Sakurai and H. D. Hagstrum, J. Vac. Sci. and Technol. **13**, (1976), 807.

[4] W. Paul, A. J. Lewis, G. A. N. Connell and T. D. Moustakas, Solid-State Commun. **20**, (1976), 969.

[5] W. E. Spear and P. G. LeComber, Solid-State Commun. **17**, (1975), 1193.

[6] J. I. Pankove and D. E. Carlson, Appl. Phys. Lett. **31**, (1977), 450.

[7] J. I. Pankove, Appl. Phys. Lett. **32**, (1978), 812.

[8] J.I. Pankove, M. A. Lampert and M. L. Tarng, Appl. Phys. Lett **32**, (1978), 439.

[9] B.W. Faughnan, Semiconductors and Semimetals **34**, (1991), 35. Reference therein.

[10] C.W. Magee and C. P. Wu, Semiconductors and Semimetals **34**, (1991), 35. Reference therein.

[11] N.M. Johnson, F. A. Ponce, R. A. Street and R. J. Nemanich, Phys. Rev. B. **35**, (1987), 4166.

[12] D. L. Staebler and C. R. Wronski, Appl. Phys. Lett. **31**, (1977), 292.

[13] R. A. Street, Physica B **170**, (1991), 69.

[14] J. Shinar, R. Shinar, S. Mitra and J.Y. Kim, Phys. Rev. Lett **62**, (1989), 2001.

[15] R.A. Street, C.C. Tsai, J. Kakalios and W.B. Jackson, Philos. Mag. **B 56**, (1987), 305.

[16] D.E. Carlson and C.W. Magee, Appl. Phys. Lett. **33**, (1978), 81.

[17] W. Beyer, Physica B **170**, (1991), 105.

[18] R. A. Street, C. C. Tsai, J. Kakalios and W. B. Jackson, Philos. Mag. B **56**, (1987), 305.

[19] B. T. Kolomiets, Proc. Intl. Conf. on Semiconductor Physics, Prague 1960, (Czechoslovak Academy of Sciences, 1961), Phys. Stat. Solidi **7**, (1964), 359, 713, p.884.

[20] W. E. Spear, Proc. Phys. Soc. (London), **870**, (1957), 1139.

[21] J. Tauc, R. Grigorovici and A. Vancu, Phys. Stat. Solidi **15**, (1966), 627.

[22] S. R. Ovshinsky, Phys. Rev. Lett. **21**, (1968), 1450.

[23] W. E. Phillips, Adv. Phys. **26**, (1977), 811.

[24] J. C. Phillips, J. Non-Cryst. Sol. **34**, (1979), 153.

[25] N.F. Mott and E.A. Davis, Electronic Processes in Non-Crystalline Materials, 1st edn. (OUP: 1971).

Chapter 2

Muons and Muonium

A wide range of elementary particles are at the disposal of scientists to obtain detailed information on structures, surfaces and dynamics. Electrons are extensively used in the electron microscope for the probing of surfaces at the nano-scale, presenting an increase of magnification of several orders of magnitude over optical microscopes, and capable of resolution on the atomic scale. For many years, electron, neutron and X-ray diffraction have been established techniques for the analysis of a material's structure. Over recent years, the positive muon has become more of an accepted 'probe' particle. With experiments being conducted at large accelerator laboratories, using what have become known as μSR techniques, structural and dynamical information has been gained, at the atomic level, on a wide and diverse range of semiconductors, insulators and magnetic materials.

2.1 Muons

2.1.1 What are muons?

As already mentioned, the muon is an elementary particle - an unstable member of the lepton family - having a lifetime of 2.2 μs. Aside of its short lifetime, it can be regarded as similar to a heavy electron, for the case of the negative muon, or a heavy positron for the case of the positive muon. Some of the muon's properties are shown in Table 2.1. At present all muon facilities rely upon the production of pions as the parents of the muons. This production occurs when a low-Z target material, typically carbon or beryllium, is

Property	Values
Mass (m_μ)	206.77 x m_e
	0.112 x m_p
Charge	$+e$, $-e$
Spin (I)	$\frac{1}{2}\hbar$
Magnetic moment (μ_μ)	3.183 x μ_p
g factor (g_μ)	2.002
Lifetime (τ_μ)	2.197 μs
Gyromagnetic ratio (γ_μ)	2π x 13.55 kHz G^{-1}
	8.5165 x 10^4 s^{-1} G^{-1}

Table 2.1: Properties of the muon (μ^+, μ^-).

exposed to a sufficently high-energy proton beam, and therefore a proton accelerator is required to promote such high energies. The production process of the parent pions (π^+, π^0 or π^-) are as follows :

$$\begin{aligned} p+p &\rightarrow p+n+\pi^+ \\ p+p &\rightarrow p+p+\pi^0 \end{aligned} \qquad (2.1)$$

$$\begin{aligned} p+n &\rightarrow p+n+\pi^0 \\ p+n &\rightarrow p+p+\pi^- \\ p+n &\rightarrow n+n+\pi^+ \end{aligned}$$

The charged pion mass is 140 MeV, in contrast to the electron mass of 0.5 MeV and the proton mass of 938 MeV. The pion is short-lived, having a lifetime of only 26 ns, and it decays via the following reaction :-

$$\begin{aligned} \pi^+ &\rightarrow \mu^+ + \nu_\mu \\ \pi^- &\rightarrow \mu^- + \overline{\nu}_\mu \end{aligned} \qquad (2.2)$$

In the rest frame of the pion, the decay is spatially isotropic, with the muon and neutrino being emitted collinearly in opposite directions (see Figure 2.1). As can be seen, the parent pion, π^+ has a spin of zero; the conservation of angular momentum therefore requires that μ^+ and ν_μ be together also in a state of zero spin angular momentum. As a consequence of neutrinos being restricted to a left-hand helicity (spin antiparallel to the momentum), conservation of angular momentum requires that the helicity of the muon must also be left-handed. Thus the μ^+ spin is antiparallel to its momentum, and in any particular direction the muon must be fully longitudinally polarised. In the case of π^- decay, both the $\overline{\nu}_\mu$ and the μ^- are emitted with positive helicity, i.e. the spin is parallel to the momentum. There are two ways in which spin polarised muon beams can be produced; the first involves exploitation of pions decaying in flight, and for the second one makes use of the low-energy pions which are at rest before decay. Concentrating on the latter of the two methods, the pions will already have stopped in the target near to its surface; on the other hand, negative pions, upon stopping in the target, are rapidly captured around target nuclei and no decay into muons and neutrinos occurs. Positive muons remain between target nuclei and decay according to Equation 2.2. A flaw here is that the pions must actually stop at, or close to, the surface of the target; hence this method is called *surface* muon generation, from which high intensity fully polarised positive muons can be produced. Unlike neutrinos, muons are charged particles and can

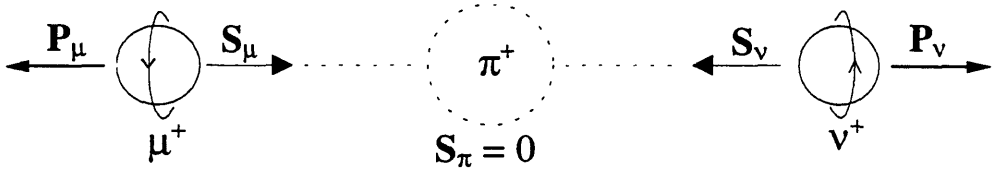

Figure 2.1: Illustration of the decay of the π^+ into a μ^+ and a ν_μ in the rest frame of the pion.

be deflected in magnetic fields. In a typical muon beam, quadrupole magnets are used to generate the magnetic fields necessary to focus the beam, and bending-magnets are used to select a particular momentum for the transmitted muons by varying the deflection of

muons with different momenta. The magnetic force generated can be expressed as:

$$\text{Force} = Bev \tag{2.3}$$

where B is the magnetic field, e is the charge and v the muon velocity. Under this force, the particle executes a circular path, of radius R, such that

$$Bev = \frac{mv^2}{R} \tag{2.4}$$

From this it can be seen that, since the deflection $(\frac{1}{R})$ is proportional to $\frac{Be}{mv}$, the larger the momentum, the smaller the deflection. For pulsed beams of muons, contaminants, usually positrons, exist in the beam. Since the positrons travel near light-speed, similar methods, using a crossed magnetic field/ electric field separator, can be employed to tailor the beam.

2.1.2 Muon decay

Upon implantation into the sample, the evolution of the muon polarisation can be monitored because, the muon emits a positron preferentially in the direction of the muon spin at the moment of muon decay (Figure 2.2). The muon decays according to the following

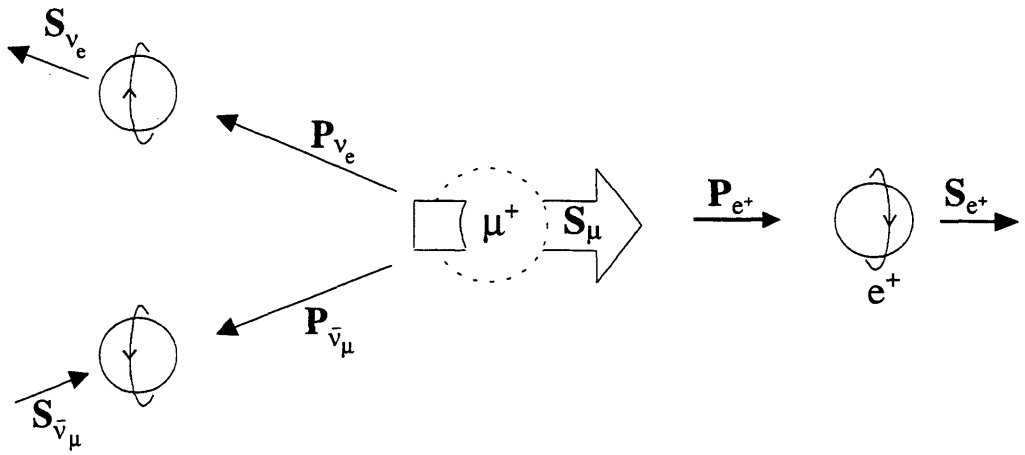

Figure 2.2: Illustration of the decay of the μ^+ in the rest frame of the muon.

reaction

$$\begin{aligned} \mu^+ &\rightarrow e^+ + \nu_e + \overline{\nu}_\mu \\ \mu^- &\rightarrow e^- + \overline{\nu}_e + \nu_\mu \end{aligned} \tag{2.5}$$

This decay is spatially anisotropic, where the angular distribution of the positrons peaks in the direction of the muon spin at the moment of disintegration. The probability that the positron is emitted at an angle θ to the instantaneous spin direction can be expressed as: -

$$p(\theta) = 1 + a\cos\theta \tag{2.6}$$

which can then be represented on a polar diagram (Figure 2.3). It is important to remem-

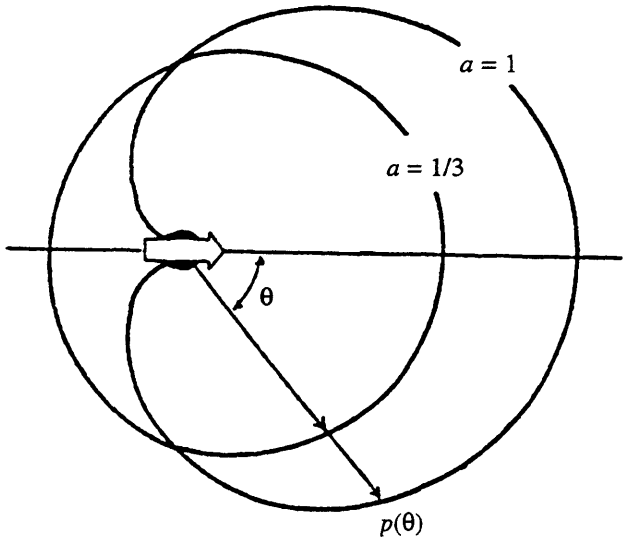

Figure 2.3: Angular distribution of positrons for asymmetry parameters 1 and $\frac{1}{3}$.

ber that Figure 2.3 is a two-dimensional representation of a three-dimensional surface, in which the $a = 1$ surface is apple-shaped. The asymmetry parameter, a, characterises the asymmetry of the distribution, and its value is dependent upon the momentum of the emitted positron. It has a maximum value of 1 for only a small number of the highest energy positrons, and is actually negative for low-energy positrons. Averaging over the complete distribution of positron momenta, a is found to be equal to $\frac{1}{3}$.

2.1.3 Muon implantation and internal fields

When implanted into the materials, the positive muons behave similar to low-mass protons; though the charge and spin are common to both, the muon is about $\frac{1}{9}$th the mass

of the proton. These similarities between the proton and the muon are important in the formation of muonium (see Section 2.2.1), since muonium is exploited as a hydrogen analogue using the μSR techniques (see Section 3.2). The muon can respond to the local magnetic and electronic environments within the sample, and thereby act as an atomic-scale probe. Since muons localise at specific sites in lattices or molecules, their μSR spectra (see Section 3.2.1) can be used to characterise these local magnetic and hyperfine fields. The muon does not always behave as a passive impurity. Generally, as a result of its being a charged particle, it can disturb and influence the localised environment in which it resides. In a regular lattice, the muon can reside in an interstitial site, where the local environment can respond to the introduction of this new 'neighbour', much in the same way that a regular lattice can be distorted by the incorporation of a point defect, where angles and bond lengths can be changed (Figure 2.4). It is the

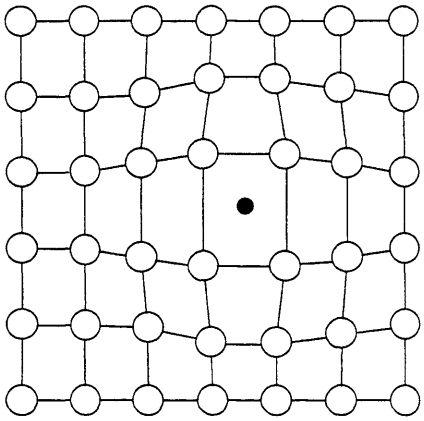

Figure 2.4: Interstitial muon site in a lattice.

interaction of the muon with its immediate environment that is of major importance; in particular, the measurement of its response to localised magnetic fields has been the focal point of μSR experiment design. It is therefore important that there is an understanding of the influence of magnetic fields upon the muon, μ^+. As a spin-$\frac{1}{2}$ particle, in an applied magnetic field the muon has two possible spin orientations, casually referred to as *spin-up* and *spin-down*. The spin-up state is defined as the state where the spin is parallel to the magnetic field, and likewise the spin-down is the state where the spin is antiparallel to the field. At low field, the two states are of approximately equal energy, but as the magnitude of the field is increased, an energy level splitting occurs

(Figure 2.5). This energy difference is called the *Zeeman energy* and varies linearly with

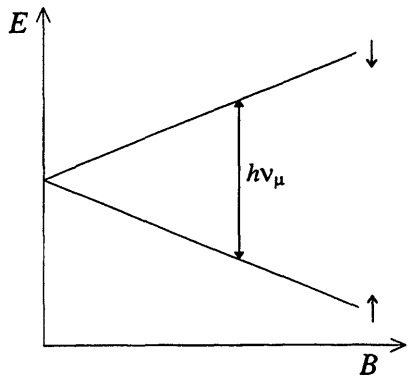

Figure 2.5: Energy level splitting for the spin-$\frac{1}{2}$ muon.

the magnetic field, B. Like most energies, the Zeeman energy is expressed in units of frequency, ν_μ, called the *Larmor frequency*, and since $\omega_\mu = 2\pi\nu_\mu$,

$$E_\downarrow - E_\uparrow = \Delta E = h\nu_\mu = \hbar\omega_\mu = \hbar\gamma_\mu B. \tag{2.7}$$

The Larmor frequency of the muon ν_μ should not be confused with the neutrino ν_μ discussed earlier in Section 2.1.2. In future usage of the symbol ν_μ in this thesis should be considered to be muon's Larmor frequency. From the linear dependence of the energy on field, a constant of proportionality exists, referred to as the muon *gyromagnetic ratio* where :

$$\gamma = 2\pi \,\mathrm{x}\, 13.55\,\mathrm{kHz/gauss}. \tag{2.8}$$

As well as an external applied field, internal localised fields additionally exist within the material, whose sources include atomic and nuclear moments. Each muon site can therefore be under the influence of several different magnetic fields, both external and internal, all of which add vectorially to produce a resultant single field at any of the individual muon sites. It is important to understand that the analysis of the muon behaviour can be unique to a particular site-type, such is the sensitivity of the muon to local environments. In addition, when muons do 'sit' in equivalent sites in the lattice, and thereby experience identical fields, the muons will precess in phase, and maintain their initial polarisation. The distribution of local magnetic fields, between different sites, will lead to muon precessions at different frequencies, leading to dephasing of the muons and

a loss of polarisation. In Figure 2.6, the case of muon spin rotation is shown, in which the precession of the μ^+ polarisation vector $\boldsymbol{P}(t)$ can be seen, where ν is the polar angle, ϕ is the azimuthal angle of $\boldsymbol{H}$, $\boldsymbol{P}(0)$ is in the z direction. Under some circumstances, a

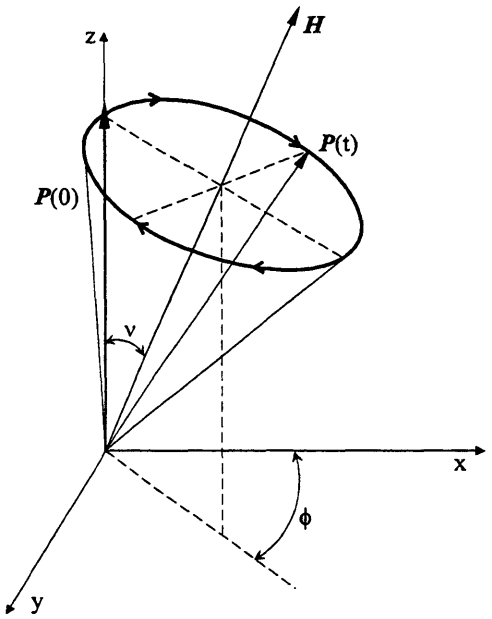

Figure 2.6: Muon precession of the μ^+ polarisation vector $\boldsymbol{P}(t)$ for an arbitrary angle of orientation of the applied field $\boldsymbol{H}$ with respect to $\boldsymbol{P}(0)$.

muon, upon implantation, does not occupy a spin-eigenstate. Such an example would be when the sample is subject to a *transverse field*, i.e. the external magnetic field is applied perpendicular to the initial beam polarisation. From Figure 2.6, when $\nu = 90^o$ the field $\boldsymbol{H}$ would be along the x-axis and the polarisation vector $\boldsymbol{P}(t)$ would precess in the y-z plane. In such a condition, the muons are neither in the spin-up state nor spin-down state with respect to the field, but exist in more of a superposition of both up and down states. In general though, throughout a lattice there will be a montage of *spin-up* and *spin-down* near neighbours, which results in a wide distribution of localised fields, that is to say that two different muons may 'sit' in similar interstitial sites, yet still experience quite different magnetic fields. This wide distribution of magnetic fields leads to the broadening of energy levels at any particular external field, B, and a spread of the density of states at each energy. When an electron, with an unpaired spin, overlaps the muon site, then the muon experiences an additional field known as the *hyperfine field.*

Analysis of the muon-electron hyperfine interaction can be exploited to yield information of the local environment in which the muon resides.

2.1.4 Muon polarisation and relaxation

As mentioned eariler, the initial muon beam is approximately 100% polarised, this is to say all of the muons have their spins aligned in the same direction, either spin-up or spin-down. Upon implantation into the sample, the initially energetic muon can pick up an electron, whereby the muon-electron magnetic interaction, the hyperfine interaction, is introduced. As a spin-$\frac{1}{2}$ particle, the electron can also exist in either the *spin-up* or *spin-down* configurations. Under these circumstances, if the muon is initially spin-up, say, then it can either interact with a spin-up or spin-down electron. If a large group of muons are implanted into the sample, then there will be a reduction in the number of spin-up muons, since those interacting with spin-down electrons will be 'trapped' in the spin-down state. This reduction in the percentage of spin-up muons, is referred to as a *loss of polarisation.* Where the number of spin-up muons is $n_\uparrow$ and the number of spin-down muons is $n_\downarrow$, then *polarisation* is defined as the proportional difference of the implanted muons, so that :

$$P = \frac{(n_\uparrow - n_\downarrow)}{(n_\uparrow + n_\downarrow)}. \tag{2.9}$$

In the μSR experiments, the polarisation is measured via the asymmetry in the muon decay. The acronym, μSR stands for either muon spin-*repolarisation, relaxation, resonance* or *rotation.* This covers the variety of observations possible, for example longitudinal relaxation, where the muon polarisation decays, over the muon lifetime, to approximately zero whilst under the influence of an external field parallel to the initial beam polarisation. Many of the observation techniques are dependent on the analysis of resulting depolarisation or a relaxation of the μ^+ assembly. The term *depolarisation* harbours varieties of spin dynamics, including spin interactions where the phase coherence of the spin assembly could theoretically later be recovered. On the other hand, *relaxation* refers to interactions which result in a permanent loss of polarisation. An example of such a relaxation would be *spin-lattice relaxation*, where the bare μ^+ spin interacts with the

local magnetic field distribution, such that the high initial polarisation, often approaching 100%, is lost after thermal equilibrium is attained, resulting in a distribution of spin-up/spin-down states :

$$\frac{n_\downarrow}{n_\uparrow} = e^{\frac{-h\nu_\mu}{k_B T}}. \tag{2.10}$$

The time-dependent decay of the polarisation can be expressed in terms of two parts, a constant part, P_0, and a relaxing part $P_1(t)$. When the field experienced by the muon ν_μ is much greater than the local field ν_L in a large external field, $P_1(t)$ can be expressed as an exponentially decaying relaxation function, such that:

$$P_z(t) = P_0(t)P_1(t) = P_0(t)e^{-\lambda t} \tag{2.11}$$

where λ is the relaxation rate and is usually expressed in the units of μs^{-1}. It is worth noting though that often, the relaxation rate is expressed in terms of T_1, where:

$$\lambda_{LF} = \frac{1}{T_1} \tag{2.12}$$

and $1/T_1$ is a measure of the loss of spin-alignment with the magnetic field. All μSR facilities have both lower and upper limits to their sensitivity, i.e. their ability to detect very slow or very fast relaxations. For example, in materials with no atomic moments, only nuclear moments, there can be no spin-lattice relaxation, owing to a lack of electronic spins, which results in extremely low relaxation rates, rates which can seldom be accurately measured. At the other extreme, in some materials such as GaAs, the relaxation rate is so high that a *missing fraction* occurs, i.e. a fraction of the polarisation measured at $t = 0$ is missing, so that the 'real' polarisation is actually higher.

Before relaxation can occur, a quantum of energy $h\nu_\mu$ must be supplied for a spin-up to spin-down transition to occur, or must be absorbed for the spin-down to spin-up transition (Figure 2.5). Therefore, for a situation of low temperature and high fields, spin-lattice relaxation is highly improbable. If there is a fluctuation of the local field though, for example, by the spin-flip transitions of the host spins, then this provides the necessary magnon reservoir, and allows the necessary thermalisation transitions.

In addition to experiments conducted with longitudinal fields, many are conducted with transverse fields, which gives rise to different relaxation rates. Recall that when

the muons occupy similar sites, experiencing identical magnetic fields, they precess in phase, resulting in an undamped precession signal (Figure 2.7). It is important to note

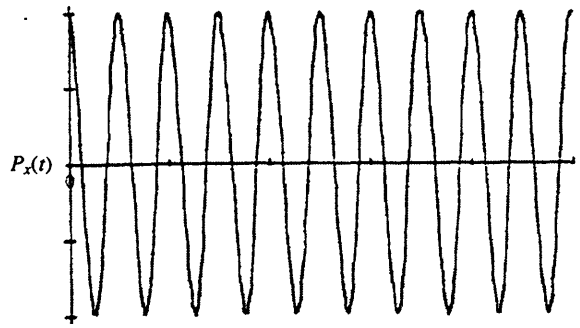

Figure 2.7: Pure undamped transverse precession signal, corrected for muon lifetime.

that the raw μSR spectrum has been corrected by removing the exponential decay due to the μ^+ lifetime, leaving only $P_x(t)$, where the count rate of the positrons in a detector can be expressed as

$$N(t) = N_0\, e^{\frac{-t}{\tau_\mu}} + B_g \tag{2.13}$$

where the first term represents the muon lifetime, and the second term represents any background count from stray particles. Fortunately, at the ISIS facility, B_g can be ignored since it is 10^5 smaller than N_0. Though, when there is a distribution of fields experienced, the muons precess out of phase. With this precession, dephasing, a damping of the asymmetry signal (Figure 2.8), occurs. Just as for the longitudinal relaxation,

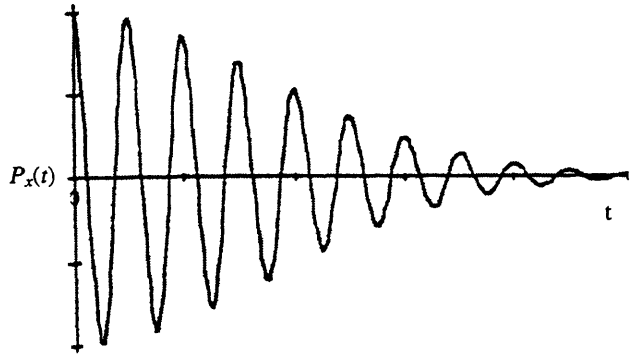

Figure 2.8: Pure gaussian damped transverse-field precession signal, corrected for muon lifetime.

where the relaxation function was expressed as $P_1(t)$, for a transverse field there can

also be a relaxation function $P_2(t)$, the subscript being in agreement with expression $\frac{1}{T_2}$ where

$$\lambda_{TF} = \frac{1}{T_2} \tag{2.14}$$

and $1/T_2$ is a measure of the dephasing of the muon precessions. This function $P_2(t)$ is usually Gaussian, though sometimes it can be Lorentzian, and is commonly referred to as the *transverse-field relaxation function.*

2.2 Muonium

2.2.1 What is muonium?

So far consideration has only been given to the bare muon. In this section, the hydrogen analogue *muonium* will be discussed, where it resides and its implications for potential sites of atomic hydrogen. In Section 2.1.3, the similarities between the muon and the proton were discussed. It might therefore be expected that, upon implantation, the muon would behave like a proton and pick up an electron, and thus form a hydrogen-like atom. This is in fact what happens, though the muon must first be thermalised, during which process it slows down and loses much of its initial kinetic energy. This 'atom' has become known as muonium, written as 'Mu', where

$$\mathrm{Mu} = \mu^+\mathrm{e}^-. \tag{2.15}$$

At this point it is perhaps useful to detail the available symbols for muonium :

Mu = neutral paramagnetic atomic muonium ($\mu^+\mathrm{e}^-$)

Mu^+ = positively charged diamagnetic atomic muonium (μ^+), electron lost

Mu^- = negatively charged diamagnetic atomic muonium ($\mu^+\mathrm{e}^-\mathrm{e}^-$), electron gained

μ^+ = positively charged pre-thermalised free muon

Some of muonium's properties are shown in Table 2.2[1]. It is the analysis of muonium, especially its hyperfine interaction, that can indicate at what site the muon prefers to reside. In the situation where the electron wavefunction overlaps the muon, the electron spin (S) and the muon spin (I) become coupled by the Fermi contact hyperfine

Property	Values
Rest mass (m_{Mu})	0.113 x m_H
	207.8 x m_e
Reduced mass (m_{Mu})	0.9956 x m_H^r
	0.9952 x m_e
Bohr radius $(a_0)_{Mu}$	1.0044 x $(a_0)_{Mu}$
	0.5315 Å
Gyromagnetic ratio (γ_{Mu})	8.8 x 10^6 s^{-1} G^{-1} (triplet)
	2π x 1.4 MHz/G
Binding energy (vacuum state)	13.6 eV (equal to hydrogen)

Table 2.2: Properties of muonium (Mu).

interaction[2], where:

$$\begin{aligned} \mathcal{H}_{hf} &= \frac{8}{3}\pi g_\mu \mu_B^\mu g_e \mu_B^e \boldsymbol{S}.\boldsymbol{I}\delta(r) \\ &= A\boldsymbol{S}.\boldsymbol{I} \end{aligned} \tag{2.16}$$

resulting in a term called the *hyperfine constant*, A. For the simplest situation where the hyperfine coupling between the muon and the electron is isotropic, the coupling can be described in terms of a single hyperfine coupling constant:

$$\begin{aligned} A &= \hbar\omega_0 \\ &= \frac{\frac{8}{3}\pi g_\mu \mu_B^\mu g_e \mu_B^e}{a_0^3} \end{aligned} \tag{2.17}$$

where μ_B^μ and μ_B^e are the muon and electron Bohr magnetons, and g_μ and g_e are the muon and electron g factors, respectively. The constant, A (usually expressed in units of frequency), is a measure of the electron density at the muon site, and the experimentally measured value of the vacuum-state hyperfine constant is $A_{Mu} = 4463\,\mathrm{MHz}$[1]. Outside of this situation, delocalisation of the spin density onto the neighbouring atoms introduces a hyperfine coupling between the muon and the nucleus, called the *superhyperfine*

interaction. Where the spin density is completely delocalised and therefore there is no overlap of the electron density onto the muon site, then $A = 0\,\text{MHz}$.

As was discussed for the bare muon (Section 2.1.3), an understanding of the influence of the magnetic field upon muonium is important. Since both the muon and the electron are spin-$\frac{1}{2}$ particles, with spin-up and spin-down possibilities, then four spin-states are available. Neglecting the situation at zero-field and at very high fields, where level 'crossing' can occur, each spin-orientation has a separate energy level, where each level has a different field dependence. In Figure 2.9 is shown the *Breit-Rabi diagram*, the

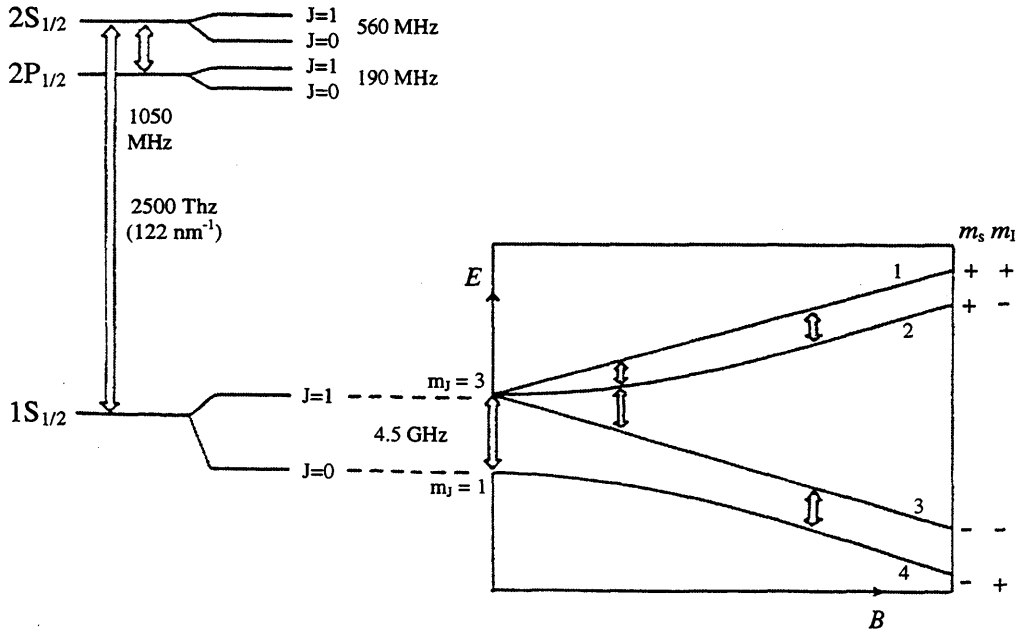

Figure 2.9: The hyperfine energy-level (Breit-Rabi) diagram for isotropic (1s level) muonium.

energy level dependence in an applied field, for the differing spin states. Where the spin states are indicated, the electron spin (m_S) is represented on the left, the muon spin (m_I) is represented on the right hand side, such that '+, -' represents m_S = '+' state and m_I = '-' the muon state. The '+' symbol is said to represent the 'spin-up' $m_S = m_I = \frac{1}{2}$, and the '–' symbol represents the 'spin-down' $m_S = m_I = -\frac{1}{2}$. When $m_F = 1$, the three energy levels are commonly referred to as the *triplet spin states*, and for $m_F = 0$, the energy level is referred to as the *singlet spin state.* At zero field, the singlet and triplets are separated by an energy splitting equal to the hyperfine constant,

A. In theory this constant could be measured directly, from the singlet-to-triplet state muon oscillation, but the resulting high frequency signal (e.g. $A_{Si} = 2012\,\mathrm{MHz}$.) means that a very good timing resolution of the positron counters and the associated electronics is essential. Unfortunately, most 'conventional' μSR spectrometers have a band-pass of only about 500MHz.

It is important to note that Figure 2.9 represents only an *isotropic* hyperfine interaction $A\boldsymbol{I}.\boldsymbol{S}$ between the muon and the electron. For anisotropic states, where muonium resides in a bond-centred position for example, which has axial symmetry, the hyperfine energy-levels are shown in Figure 2.10. It should be stressed that this figure is for the [111]

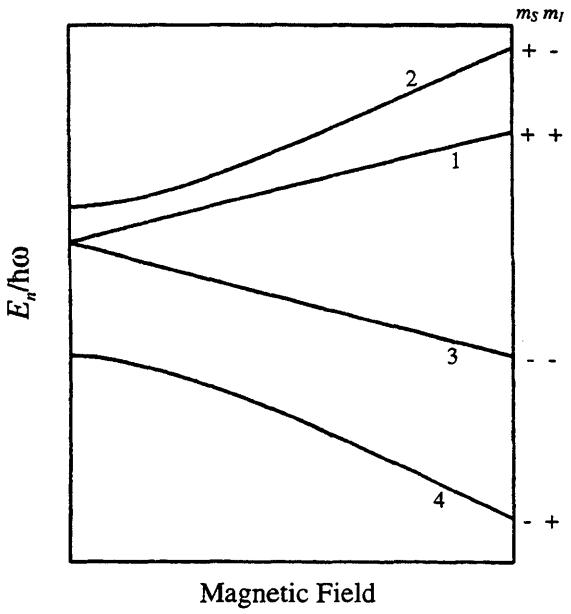

Figure 2.10: The hyperfine energy-level diagram for anisotropic muonium Mu_{BC}, for the case $\theta = 0$ (where the [111] symmetry axis is parallel to the applied field).

symmetry axis parallel to the applied field, and since the energy eigenvalues for Mu_{BC} are orientation dependent then, if the [111] axis were at a different orientation to the field, for example perpendicular to it, a different diagram would apply (see, for example, Figure 3.15 in the next chapter).

At high enough fields, i.e. when the external field is larger than the hyperfine field, such that $B \gg B_0$, where B_0 is the hyperfine field, dependent on the hyperfine constant

as

$$B_0 = \frac{2\pi A}{\gamma_e + \gamma_\mu} \tag{2.18}$$

where $\gamma_e + \gamma_\mu \approx 2.8$, the muon and electron spins become effectively decoupled. As the spins become decoupled, the muon spin can return to its initial alignment, thereby increasing the polarisation of the muon ensemble. This is the principle behind *muon spin repolarisation* - a technique used extensively in this work and to be described more fully in the next chapter. The field at which the spins of the muon and the electron are decoupled varies with the sample material, depending on the value of the hyperfine constant. For example, the hyperfine constants of isotropic muonium in Si, Ge and diamond, namely, $A_{Si} = 2012\,\text{MHz}$, $A_{Ge} = 2361\,\text{MHz}$ and $A_{diamond} = 3700\,\text{MHz}$ (where the lower the constant, the larger the delocalisation of the electron wavefunction onto neighbouring atoms) lead to decoupling fields of 4515, 5299 and 8303 gauss.

Depending on the local environment, i.e. the muonium site-type, the hyperfine interaction may not necessarily be isotropic. In such case, the Hamiltonian operator is written as :

$$\mathcal{H}_{hf} = \boldsymbol{S.A.I} \tag{2.19}$$

where $\boldsymbol{A}$ is now a tensor. The anisotropic hyperfine constant can be now described in terms of two parameters: $A_{||}$ known as A-parallel (parallel to the external applied magnetic field), and $A_\perp$ known as A-perpendicular (perpendicular to the external applied magnetic field). For the condition when the hyperfine coupling is anisotropic, but axially symmetric, the tensor can be written as :

$$\mathcal{H}_{hf} = \boldsymbol{S} \begin{pmatrix} A_\perp & 0 & 0 \\ 0 & A_\perp & 0 \\ 0 & 0 & A_{||} \end{pmatrix} \boldsymbol{I} \tag{2.20}$$

This can be expressed as :

$$\mathcal{H}_{hf} = A_{||} S_z I_z + A_\perp (S_x I_x + S_y I_y) \tag{2.21}$$

$$= A_\perp \boldsymbol{S.I} + (A_{||} - A_\perp) S_z I_z \tag{2.22}$$

where z defines the axis of symmetry, for example the <111> directions in crystalline silicon. Equation 2.22 can in turn be expressed in terms of isotropic and anisotropic components :

$$A_{||}S_zI_z + A_{\perp}(S_xI_x + S_yI_y) = A_{iso}\boldsymbol{S.I} + B\Big(2S_zI_z - (S_xI_x + S_yI_y)\Big) \tag{2.23}$$

$$\text{where } A_{iso} = \frac{1}{3}(A_{||} + 2A_{\perp}) \tag{2.24}$$

$$\text{and } B = \frac{1}{3}(A_{||} - A_{\perp}) \tag{2.25}$$

The ratio $\frac{A_{iso}}{A_{Mu}}$ is often referred to as the *spin-density* on the muon. For a muonium state that is isotropic, $A_{||} = A_{\perp} = A_{iso}$. As for the simple case of an isotropic muonium site, where the single hyperfine coupling constant varies with the material, the various hyperfine parameters can also vary between materials. These parameters are now accurately known for a wide number of materials[3] (Table 2.3).

Sample	$A_{\perp}$ (MHz)	$A_{||}$ (MHz)	A (MHz)
Si	16.819	92.59	2066.3
Ge	27.269	131.037	2359.5
GaP	219	79.48	2914
GaAs	217.8	87.74	2883.6

Table 2.3: Hyperfine parameters for isotropic Mu (A) and anisotropic muonium Mu* ($A_{||}$, $A_{\perp}$) in diamond and zincblende semiconductors.

2.2.2 Level crossing resonance

A further method of characterising muonium in semiconductors is known as *muon level-crossing resonance* and *cross-relaxation* and is typically given the acronym of μLCR or CR, respectively. Experimentally, the arrangements differ little to that of the standard LF-μSR configuration, with the muon spin again antiparallel to the applied longitudinal field. Such a configuration is shown later in Section 3.2.1.

One of the success stories of μLCR, is its ability to help identify differing charged diamagnetic states. An absence of a hyperfine interaction means that the diamagnetic states are not easily identified by traditional μSR methods. Quadrupole interactions can, however, provide a useful 'signature' by such level crossing resonance. The technique is dependent on the tuning of the muon Zeeman energy, by a longitudinal magnetic field, so as to match the combined Zeeman and quadrupole energy on surrounding nuclei. When matched to another energy level separation in the system, cross relaxation can occur between the muon and the adjacent nucleus via flip-flop transitions, and a resonant muon depolarisation may then be observed. Such polarisation transfer is displayed as resonant dips in the muon polarisation, as is shown in Figure 2.11 for GaAs, and attributed to the Mu_T^- centre. These resonances provide a measure of the nuclear or superhyperfine

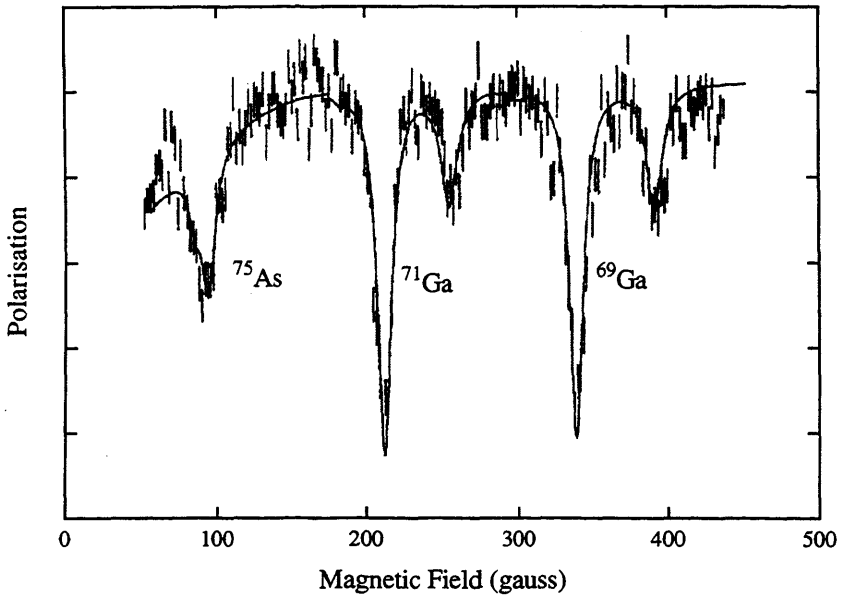

Figure 2.11: Level crossing resonance spectrum for diamagnetic muonium in n-type c-GaAs, characterising the quadrupole interactions of Ga and As nuclei neighbouring the muon site (from [4]).

interactions; the electric quadrupole interaction dictates the position of the resonance, and the magnetic dipole-dipole interaction determines its amplitude.

2.2.3 Where does it 'live'?

As already discussed, in tetrahedral semiconductors two types of centre have been identified for muonium, one isotropic and the other anisotropic. In fact, the existence of these two distinct sites can be identified in Fourier transform μSR spectra[5] (see Figure 2.12). Though the existence of isotropic muonium has been known for many years, it is only relatively recently that the site of anisotropic muonium has been identified[6].

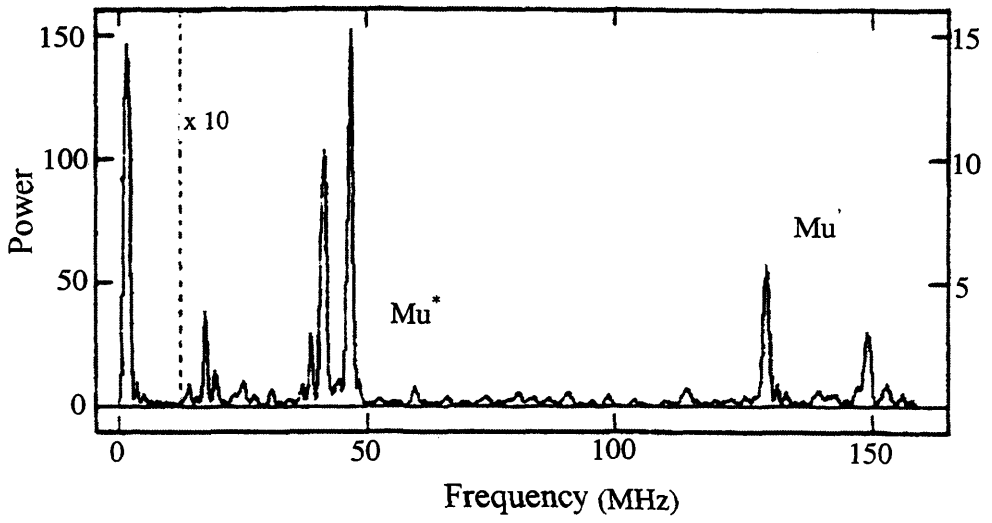

Figure 2.12: Fourier transform μSR spectrum for silicon, where Mu' represents tetrahedral muonium, and Mu* represents bond-centre muonium.

For each site-type, several names and labels have, for historical reasons, been used. Isotropic muonium is often referred to as *normal muonium*, but since the identification of its site, it is more commonly referred to as *tetrahedral muonium*; the symbol Mu is often used but more recently Mu_T has become widespread and this notation will be used throughout this thesis. Anisotropic muonium historically has been known as *anomalous muonium*, primarily since its site-type was unknown for many years, and carried the symbol Mu* (Mu-star); but again, more recently use of the name *bond-centred muonium* and the notation Mu_{BC} has become widespread. In Figure 2.13, the various available sites are shown for a tetrahedrally coordinated lattice. Tetrahedral muonium corresponds to interstitial muonium, located at, or near to, the cage centre. In μSR experiments, the muonium can be identified as isotropic when it either remains in an isotropic position, or it is time-averaged isotropic. In an amorphous material, for example, isotropic cage-

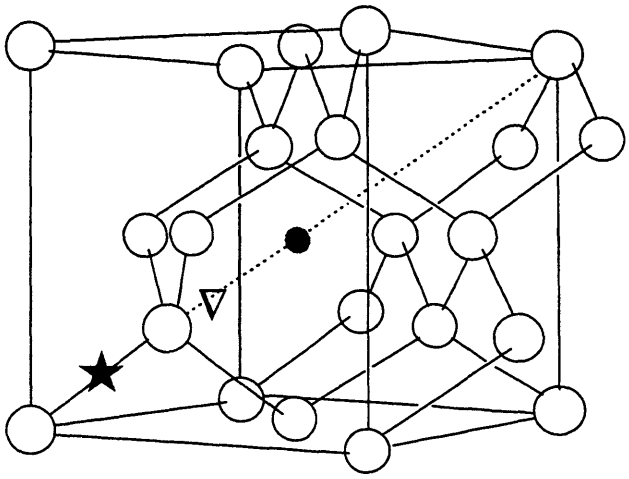

Figure 2.13: Interstitial muonium sites in a zinc-blende structure. The paramagnetic tetrahedral (•) and bond-centre (⋆) sites are shown, as well as the anti-bonding (∇) site.

centre sites are few, but if the muonium diffuses rapidly within the cage, or even between differing cage sites, it can, over the lifetime of the muon, appear to be isotropic. For bond-centred muonium, it is now known that the muon resides at the centre of a covalent bond. Since the bond-centre's isotropic term, A_{iso}, is extremely small, it can be deduced that the electron density at the muon site is likewise extremely small. In Figure 2.14, the bond-centre site is illustrated for the case of crystalline silicon. For the muonium to reside in this site, an elongation of the Si–Si bond, by as much as 40%, must occur. Pre-stretched bonds, such as are postulated to occur in amorphous Si, should lead to a lower formation energy and greater stability of this site [7]. If not pre-stretched, elongation of the bond leads to a lattice distortion; typically called a lattice relaxation, illustrated in Figure 2.14. Furthermore, for the bond-centre model, the unpaired electron is believed to occupy an orbital whose wave-function is antisymmetric about the muon site, and is therefore non-bonding on the muon, and as such can account for the low isotropic hyperfine coupling of such a centre. Such an orbital is derived from the Si–Si antibonding orbital, and can account for the muon site's low electron density, as there is a node in the amplitude of the electron wavefunction[6] at the bond centre, at which the muon 'sits'. An additional situation can occur, where the muon lies along the bond but is displaced from the bond-centre position[8], which can lead to an enhanced contact interaction between the muon and the electron. Such a situation occurs for III-V

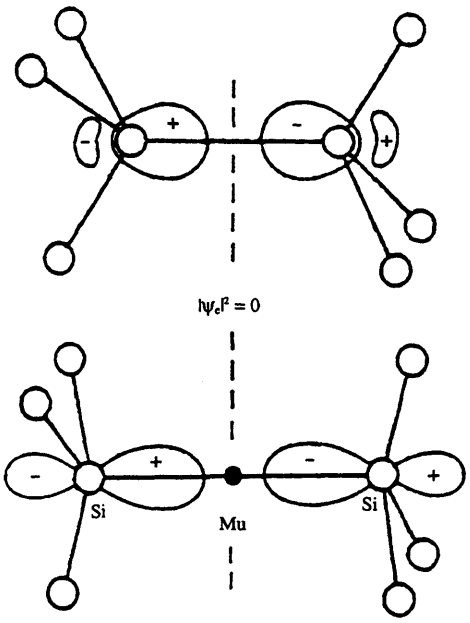

Figure 2.14: The incorporation of muonium into a bond-centred site. The associated electron resides in a non-bonding orbital, and the Si–Si atom separation is increased (from [7]).

semiconductors, e.g. gallium arsenide, where the lattice is similar to that of diamond but has alternate atoms of different species. The resulting loss of symmetry leads to an inability of the muon to reside precisely at the bond centre, and as a consequence, $|A_{||}|$ is larger than $|A_{\perp}|$, the opposite to that which occurs for elemental semicondutors. In silicon, the bond-centred site is known to be energetically favoured over the Mu_T site, and the most stable. For germanium though, it is thought that both Mu_T and the Mu_{BC} states are roughly energetically equivalent, and only a small barrier exists for muonium conversion between each state[9].

At this point, it is important to mention that the formation of muonium, as well as its varying site-types, is medium dependent, and does not occur in all materials. As an example, muonium is not formed in simple metals, which initially seems strange due to the abundance of conduction electrons. The solution lies in that the positive muon attracts a large number of conduction electrons, creating an electron cloud around the muon site. The nearest neighbour electrons are therefore attracted to the muon, but are also mutually repelled by the other electrons; the next-nearest neighbour electrons are

thus screened from the positive muon charge by the nearest neighbour electrons. From the charge screening and subsequent reduction in the Coulomb potential, a bound state with any single electron becomes impossible. As such, the implanted muon remains bare and diamagnetic.

2.2.4 Diamagnetic states and ionisation

As already mentioned, the asymmetry signal can be divided into the *muonium fraction*, the *missing fraction* and the *diamagnetic fraction*. Where muons are seen to precess at the Larmor frequency appropriate to the applied field, they must reside in a state that is locally diamagnetic; this proportion of the asymmetry signal is referred to as the *diamagnetic fraction*, and carries the symbol f_d or f_{μ^+}. A diamagnetic state is said to occur when there is no unpaired electron in the vicinity of the muon, and hence no hyperfine interaction occurs. Examples of such states can be the 'dangling bonds' of semiconductors, ionised paramagnetic sites, such as Mu_T^- (an electron gained) and Mu_{BC}^+ (an electron lost), or states that are paired with other impurities or dopants. Unfortunately, the individual diamagnetic species cannot be identified directly from μSR spectra. However, the overall diamagnetic fraction can be found from the maximum asymmetry values, at $t = 0\,\mu$s, of transverse-field measurements (see Chapter 3).

Bibliography

[1] D.E. Casperson, T.W. Crane, A.B. Denison, P.O. Egan, V.W. Hughes, F.G. Mariam, H. Orth, H.W. Reist, P.A. Souder, R.D. Stambaugh, P.A. Thompson and G. zu Putlitz, Phys. Rev. Lett. **38**, (1977), 956-9.

[2] V.W. Hughes and T. Kinoshita, Muon Physics vol. 1. ed. V.W. Hughes and C.S. Wu (New York: Academic) (1977).

[3] B.D Patterson, Rev. Mod. Phys. **60**, (1988), 69 (and references therein).

[4] K.H. Chow *et al*, Phys. Rev. **B 51**, (1995), 14762.

[5] J.H Brewer, K.M. Crewe, F.N Gygax, R.F. Johnson, B.D. Patterson, K.W. Blazey, T.L. Estle and S.L. Rudaz, Phys. Rev **B 32**, (1985), 530.

[6] S.F.J. Cox and M.C.R. Symons, Chem. Phys. Lett. **126**, (1986), 516.

[7] C.J. Van de Walle and N.H. Nickel, Phys. Rev. **B 51**, (1995), 2636.

[8] R.L. Jones, Physica B, **170**, (1991), 181.

[9] S.K. Estreicher, Mat. Sci. & Eng. R-Reports **74**, (1995), 319.

Chapter 3

Experimental Techniques

3.1 ISIS and beamline facilities

The μSR data included within this thesis was collected at the ISIS pulsed muon source, at the Rutherford Appleton Laboratories, in Oxfordshire, England. The ISIS Facility provides beams of muons and neutrons that enable the probing of condensed matter structure and dynamics on a microscopic scale. Such is the influence of the μSR research at the laboratories, that several different beamlines exist, and there is a continuing programme of beamline upgrade and development. At present though, the muon spectroscopy facility has six muon ports available, the EC facility of MuSR and EMU, and the development facility DEVA (primarily used for RF-μSR and ultra-slow muon experiments), and a further three ports on the Japanese RIKEN-RAL muon facility.

3.1.1 ISIS Muon production and transport

The plan of the Experimental Hall at the ISIS Facility is shown in Figure 3.1[1]. The ISIS Facility is a 'pulsed source', where pions are produced by high energy protons hitting a graphite target, protons and neutrons being 'knocked' out of the target atoms simultaneously. The pions decay to produce the all-important muons, see Equation 2.1. In contrast to ISIS, other facilities, such as the Tri-University Meson Facility (TRIUMF) in Canada, produce a continuous beam. At ISIS, the proton beam is obtained from several stages, the first of which is the production of H^- ions, by the ionising of hydrogen

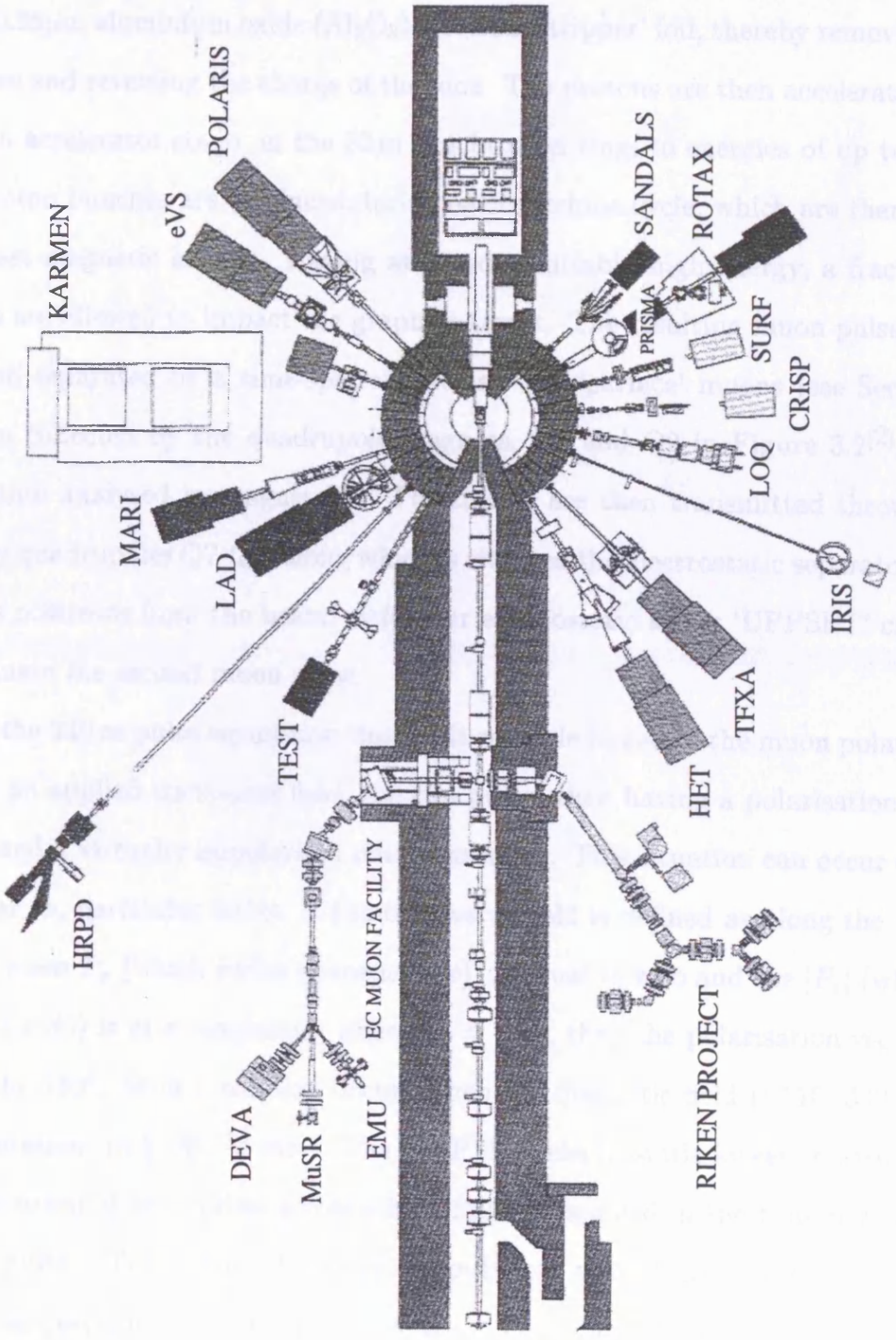

Figure 3.1: The instruments of the Experimental Hall, at the ISIS Synchrotron Facility.

gas. These ions are then fed through three linear accelerator stages to attain energies of 70 MeV, and then 'stripped' to produce the proton beam by passing the H^- ions through a thin 0.25μm aluminium oxide (Al_2O_3) electron 'stripper' foil, thereby removing the two electrons and reversing the charge of the ions. The protons are then accelerated through a fourth accelerator stage, in the 52 m synchrotron ring, to energies of up to 800 MeV. Two proton bunches are produced during each machine cycle, which are then extracted using fast magnetic kickers. Having attained a suitably high energy, a fraction of the protons are allowed to impact the graphite target. The resulting muon pulses are 70 ns wide and separated by a time-span of 340 ns. The 'surface' muons (see Section 2.1.1) are then collected by the quadrupole magnets, Q1 and Q2 in Figure 3.2[2], and then momentum analysed in magnet B1. The muons are then transmitted through a drift space by quadrupoles Q7-Q8, along which is situated the electrostatic separator A, which removes positrons from the beam. A further electrostatic kicker 'UPPSET' can be used to eliminate the second muon pulse.

Over the 340 ns pulse separation time, it is possible to rotate the muon polarisation by 180^o by an applied transverse field, the two pulses then having a polarisation difference of 180^o and a virtually unpolarised muon ensemble. This situation can occur only at, or very near to, particular fields. If the transverse field is defined as along the x-axis (see fig 2.6), when P_x (which varies as $\cos(\omega t + \phi)$) is equal to zero and the $|P_z|$ (which varies as $\sin(\omega t + \phi)$) is at a maximum, where $\omega_\mu = \gamma_\mu B$, then the polarisation vector $\mathbf{P}$(t) is rotated by 180^o. Such a rotation occurs when the magnetic field is 110, 330, 550 gauss etc. (equivalent to $\frac{\pi}{2}$, $\frac{3\pi}{2}$, $\frac{5\pi}{2}$ etc.). The 'UPPSET' electrostatic kicker consists of closely spaced horizontal electrodes, across which 15 kV is applied in the time period between the two pulses. The muons of the second pulse are then 'kicked' from the path of the first pulse, resulting in maintenance of the polarisation of the beam. These 'kicked' muons are not discarded, but an additional electrostatic kicker, incorporating a central electrode and two outer electrodes, is now used to divide and distribute these two muon pulses to the three experimental beamlines, MuSR, EMU and DEVA. A high voltage is applied to the centre electrode, resulting in the deflection of the first muon pulse, half

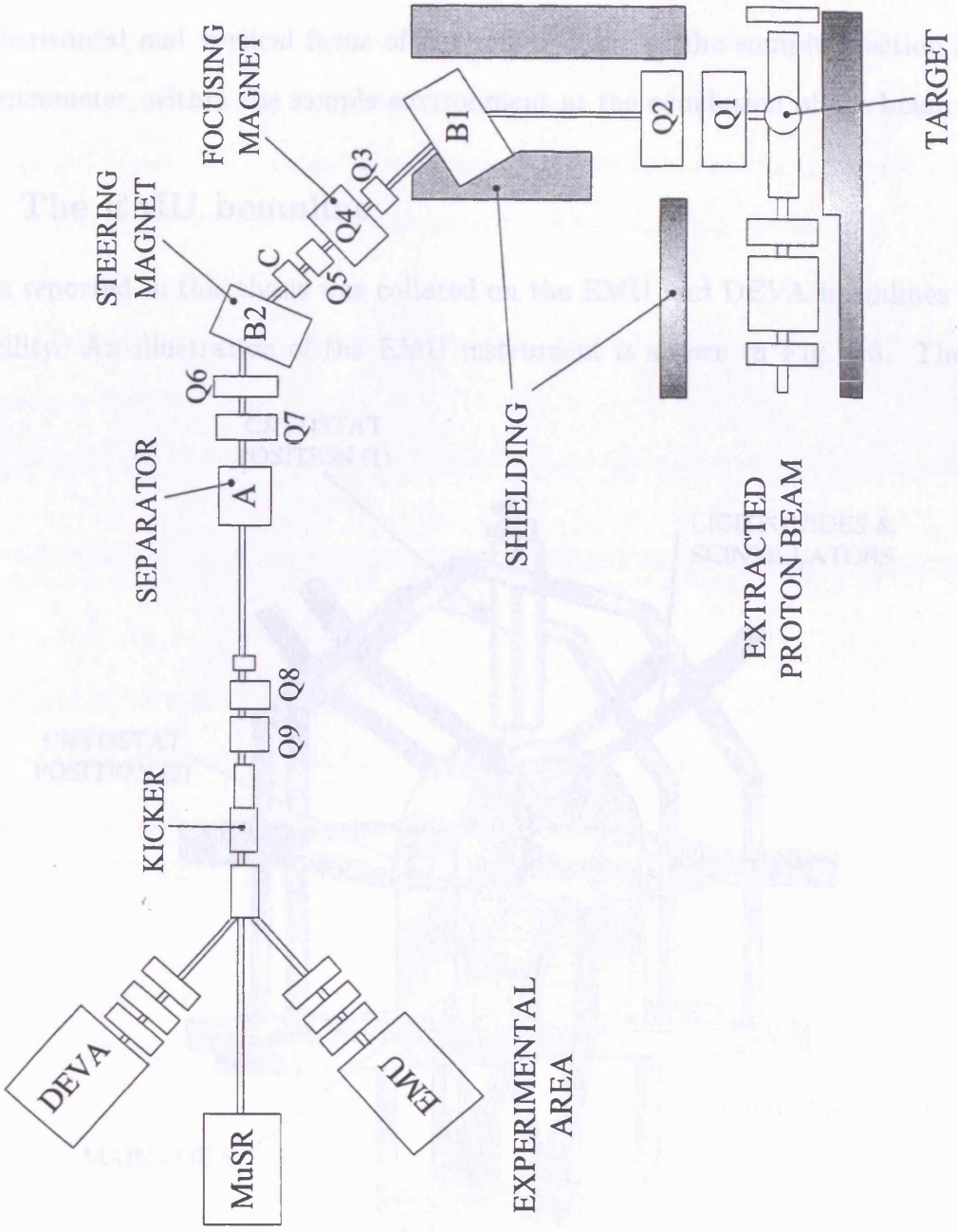

Figure 3.2: Layout of the ISIS pulsed muon beam, detailing the beamline before the experimental facilities of EMU, MuSR and DEVA.

of which is 'fed' to the EMU beamline, and the other half to the DEVA development beamline. Shortly before the arrival of the second muon pulse, the applied electrode voltage is removed, thereby allowing the muon ensemble to continue undeflected to the MuSR beamline. Shortly before the end of each beamline is a quadrupole doublet, which gives a horizontal and vertical focus of the muon beam at the sample position in the μSR spectrometer, within the sample environment at the conclusion of the beam line.

3.1.2 The EMU beamline

The data reported in this thesis was collated on the EMU and DEVA beamlines of the ISIS Facility. An illustration of the EMU instrument is shown in Fig. 3.3. The μSR

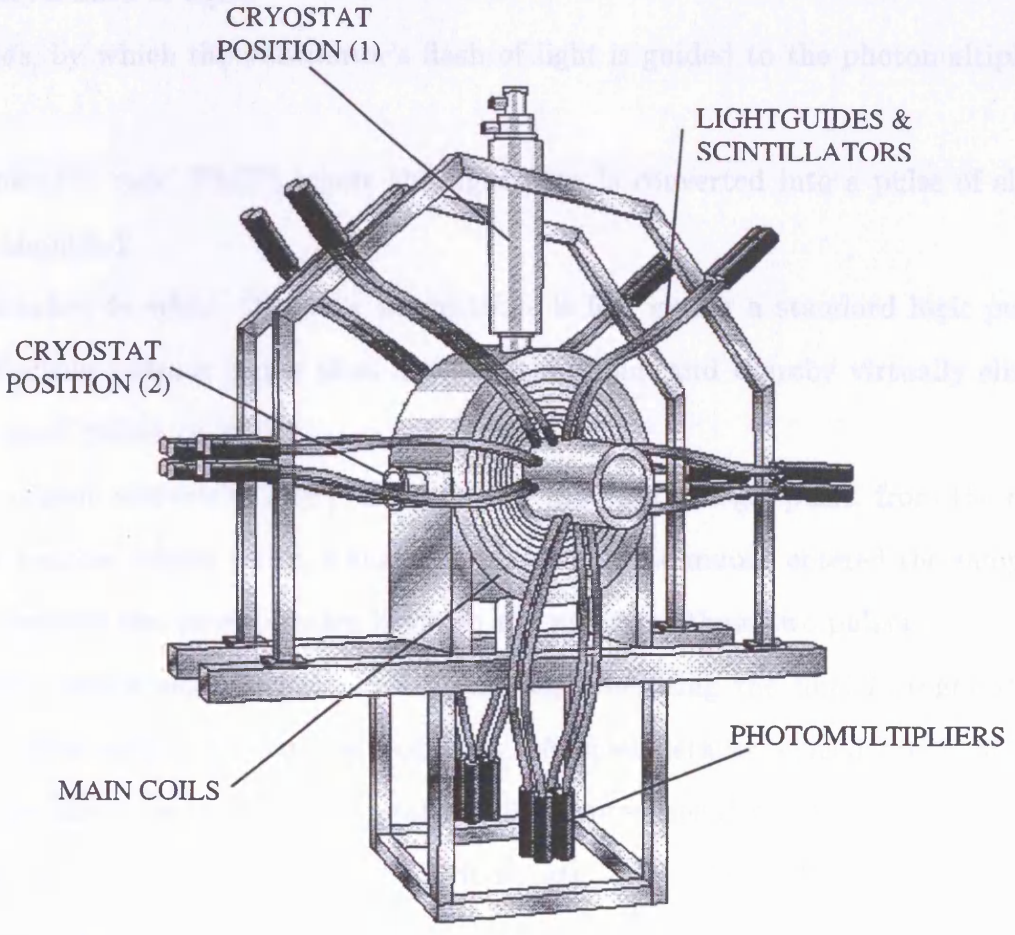

Figure 3.3: Schematic illustration of the EMU spectrometer at the ISIS facility (from [3]).

spectrometer is comprised of three elements,

i) The positron detectors

ii) Sample environment equipment

iii) Coils to provide applied magnetic field.

Since ISIS is a pulsed muon source, hundreds of muons can be stopped in the sample for any single pulse. The positron detectors must therefore be able to detect very high count rates over the average muon lifetime of 2.2μs. To address this high count rate, too large for detectors under normal conditions, the detectors have been subdivided into small 'segments', each with its own detector equipment. A basic **detector** is comprised of a :-

a) *Plastic scintillator*, through which the positron, from the decay of the muon, passes and generates a flash of light.

b) *Lightguide*, by which the scintillator's flash of light is guided to the photomultiplier tube.

c) *Photomultiplier tube* (PMT), where the light flash is converted into a pulse of electrons, and amplified.

d) *Discriminator*, to which the pulse of electrons is fed, giving a standard logic pulse when the electron pulse is larger than a preset threshold, and thereby virtually eliminating the small pulses of 'noise'.

e) *Time-to-digital converter* (TDC), this has two inputs, the logic pulse, from the discriminator, and the trigger pulse, which identifies when the muons entered the sample; the TDC measures the time duration between the arrival of these two pulses.

f) *Computers*, which analyse these measurements, generating the final histograms of *count rate* versus *arrival time* of the positrons. A more detailed consideration of the ISIS computer facilities will be made later in this chapter (see Section 3.3.1).

For all the experiments discussed in this dissertation, the *time-differential* μSR technique was used, where the arrival time of the muon in the sample, t_μ, and its subsequent decay time, t_τ, are recorded. The time histogram is then constructed for the intervals defined by $\Delta t = (t_\tau - t_\mu)$. For the EMU beamline, there are 32 detectors, thereby reducing the count rate in each detector, and with this, reducing the *dead time*. Owing

to the limitations of the time resolution of the detector count rate, when the time interval between the arrival of two successive positrons is negligible, the detectors can only resolve the presence of a single positron event. Hence, after such a double-event, there is a 'dead time', i.e. no events are recorded, and a reduced count rate will occur. With these 32 detectors, come 32 histograms, the data from which is 'fed' into the computers, and specialised software, called UDA, is used to analyse the data. These detectors are separated into two circular arrays, those 'forward' of the sample position, and those 'backward' of the sample position, with each group consisting of 16 separate detectors, clearly shown in Figure 3.3, their geometry being optimised for longitudinal field and zero-field measurements. On EMU, there are currently two methods of grouping the positron histograms; firstly, the 'simple' grouping, whereby the histograms are merely added together; and secondly, the 'forward-backward' grouping, where the asymmetry is calculated from :

$$A(t) = a_0 G(t) = \frac{N_F - \alpha N_B}{N_F + \alpha N_B} \tag{3.1}$$

where a_0 is the initial asymmetry, $G(t)$ is the relaxing term, describing the decay of the polarisation, N_F is the positron counts of the 'forward' detectors, N_B is the positron counts of the 'backward' detectors, and α is an experimental correction term, taking into account the exact position of the sample with respect to the detectors. The α can usually be determined by a transverse-field measurement, where α is the amount of movement necessary so that the muon liftime-corrected $A(t)$ asymmetry curve can oscillate about the time axis. Recall from Equation 2.13, that the number of positron counts is also dependent on the muon lifetime. The advantage of the 'forward-backward' grouping method, is that the muon lifetime-dependent term, $e^{\frac{-t}{\tau_\mu}}$, is eliminated from the final asymmetry value, resulting in the "raw asymmetry"; once the α value has been included, $A(t)$ is known as the "corrected" asymmetry, and it is this form which is the most commonly used in μSR analysis.

On the DEVA beamline, only 2 detectors are present, one 'forward' and one 'backward'. Therefore, to avoid dead-time problems, the number of muons allowed to enter the sample is reduced, typically by reducing the width of the beam-slits, found between the sample

equipment and the final 'kicker' of the beamline. As a consequence, until the number of detectors is significantly increased, the count-rate of DEVA will remain low, and therefore the duration of experiments will be long.

Of importance in μSR experiments is the ability to vary the applied field, the orientation in which it is applied, and also the temperature at which the sample rests. In Figure 3.3, the *main coils* are shown which provide the longitudinal magnetic fields. These water-cooled copper Helmholtz coils can supply magnetic fields of up to 4500 gauss (450 mT), which although adequate, is smaller than other facilities, such as TRIUMF, which can generate longitudinal fields (LF) of the order of Tesla, rather than milli-Tesla. Although EMU was primarily designed for longitudinal measurements, limited transverse-field measurements are still possible since the small calibration coils, designed for TF measurements at 20 gauss, can supply up to 100 gauss (10 mT). The difference in LF and TF geometries is discussed in Section 3.2.1. A third type of measurement is also possible on the EMU beamline, that of *Zero-Field* (ZF), through the installation of zero-field coils which can compensate for fields of up to 0.03 gauss (3 μT). To provide variability of the sample temperature, the sample environment equipment of EMU has been designed to include a cold-finger sample holder, an evacuation sample chamber, heating electrodes and one of three cryostats. The evacuation of the chamber is important so that very low sample temperatures are attainable, and so that, once reached, the sample may be maintained at a constant temperature, with very little variation from the preset. Generally, a closed-cycle refrigerator is used, in which a temperature range of 12 - 340 K is attained, with the heaters being used to stabilise the sample temperature, as well as to heat the sample from low temperatures to above room temperature. Two other cryostats are also available for very low temperatures; an Oxford Instruments cryostat can reach temperatures down to 2 K, and a Sorption cryostat can go down to 350 mK. With the availability of a furnace, temperatures in the range of 300 K to 1000 K are also attainable.

3.2 μSR techniques

3.2.1 Longitudinal and transverse-field geometries

As their names suggest, a longitudinal field configuration exists when the magnetic field is applied parallel to the muon beam, and a transverse field occurs when the magnetic field is applied perpendicular to the muon beamline. For each of the configurations different detector geometries are, in principle, necessary. Schematic illustrations of the zero/longitudinal field (ZF/LF) and transverse field (TF) configurations are shown in Figure 3.4. For the LF-configuration, the detector arrangment is perpendicular to the initial polarisation, and to the applied magnetic field. With the TF-configuration, the magnetic field is applied perpendicular to the initial direction of muon polarisation, whereby the the muon precesses in a plane perpendicular to the field. For the latter, the ideal detector arrangement would be where the detectors are positioned symmetrically about the field direction. On the EMU beamline though, a different configuration has been designed, which has been optimised to perform longitudinal field experiments. As can be seen from Figure 3.3, the lightguides and scintillators appear to be positioned for the LF configuration only. However, the lightguides are actually bent, so that the scintillators cover an area both above, below, to the left and to the right side of the sample environment, as well as in front of and behind it. Such a design introduces a TF-configuration to one which is predominantly LF, and therefore TF measurements are still possible on the EMU and DEVA beamlines.

When transverse or zero/longitudinal fields are applied to the sample, quite different asymmetry curves are produced. Such curves are shown for both TF and LF applied fields in Figure 3.5. From such curves, the 'relative fractions' can be calculated. For the transverse-field experiments, analysis of the maximum amplitude of the oscillating signal yields the diamagnetic fraction, since only diamagnetic muons are expected to precess at low frequencies. It is important to understand the difference in the precession frequencies, in order to understand why transverse field experiments yield the diamagnetic fraction, while longitudinal field experiments yield the total polarisation. Since the precession

(a)

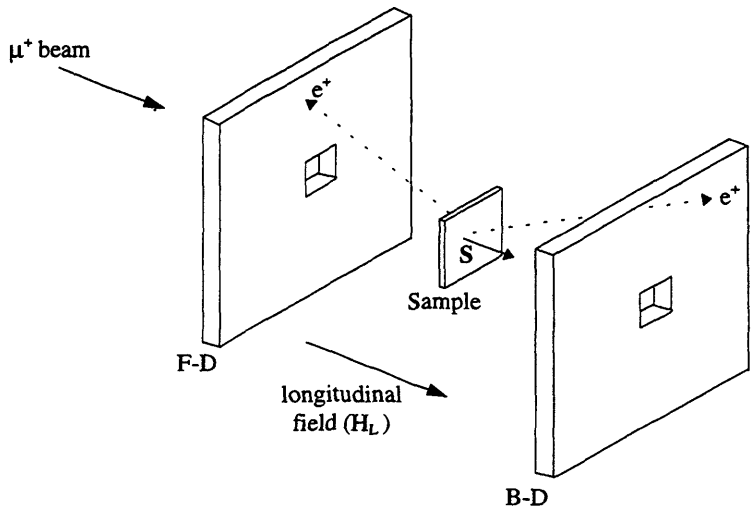

(b)

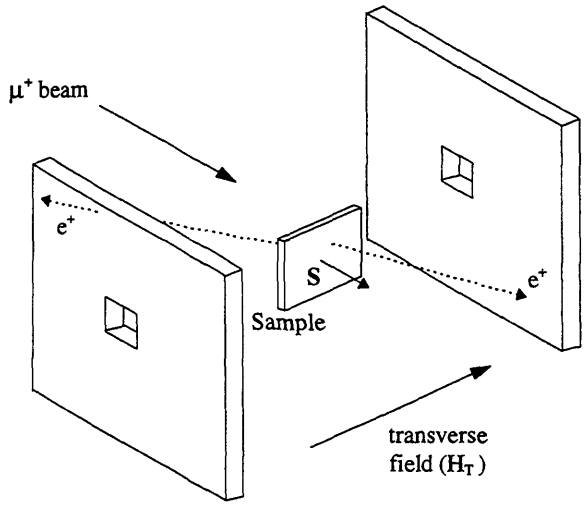

Figure 3.4: Schematic illustration of the differing configurations for μSR measurements. Figure (a) shows the zero and longitudinal geometries, and Figure (b) shows the transverse-field configuration.

(a)

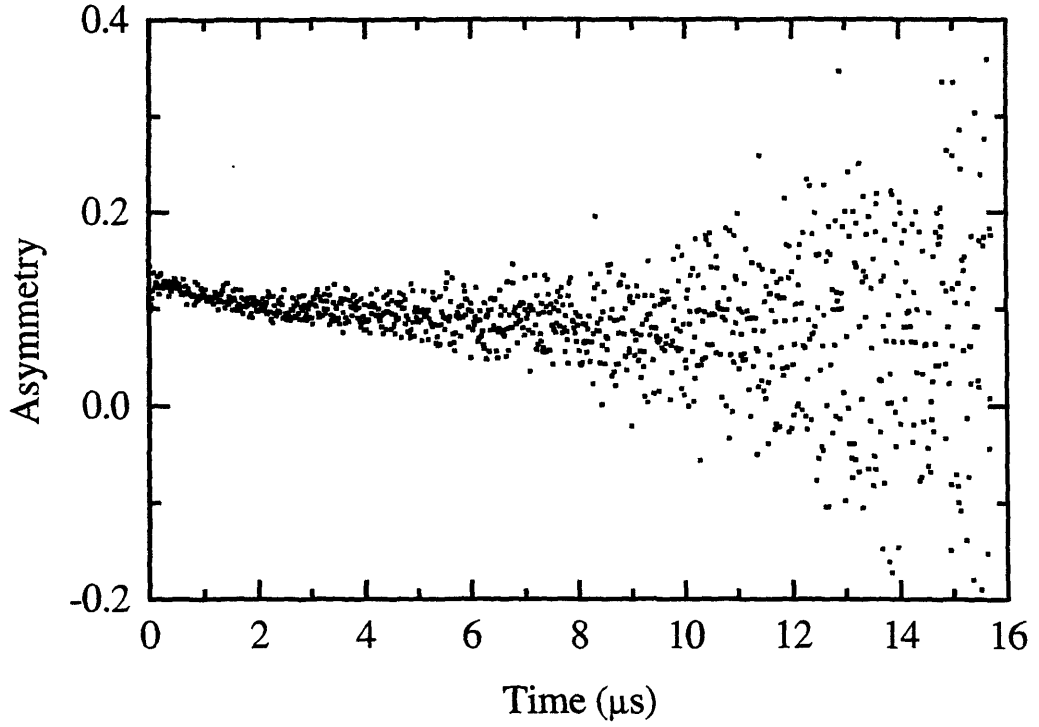

(b)

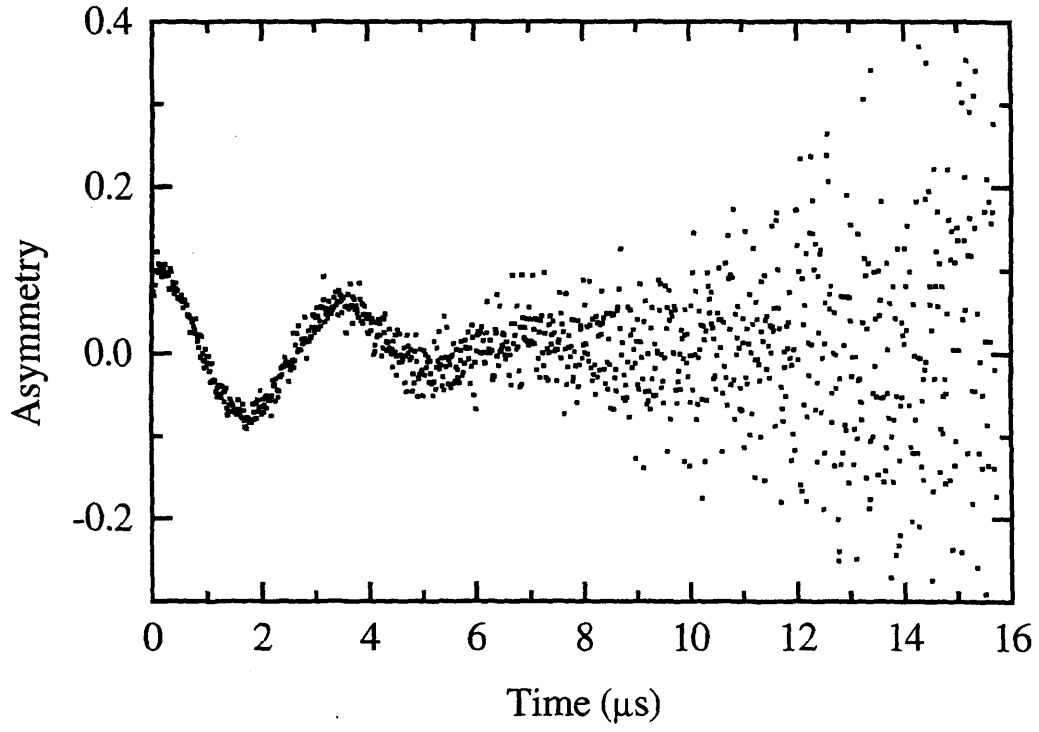

Figure 3.5: Curves showing the raw data for a-Si:H at 15K, for 20 gauss, in (a) longitudinal configuration, and (b) transverse configuration.

frequency, ω, is equal to γB, we have, for an external applied transverse field of 20 gauss:

Diamagnetic site precession

$$\begin{aligned} \gamma_{\mu+} &= 2\pi \text{ x } 13.55 \text{ kHz/gauss} \\ \omega_{\mu+} &\approx 1.7 \text{ MHz.} \end{aligned} \tag{3.2}$$

Paramagnetic muonium precession

$$\begin{aligned} \gamma_{\text{Mu}} &= 2\pi \text{ x } 1.4 \text{ MHz/gauss} \\ \omega_{\text{Mu}} &\approx 170 \text{ MHz.} \end{aligned} \tag{3.3}$$

From this it can be seen that the precession of the muonium is approximately 100 times larger than that of the bare muon. As such, the diamagnetic precession signal can be detected but, except at very low fields, the paramagnetic precession frequencies are usually too high to be detected at the ISIS Facility. It should be stressed though that at very low fields, i.e. < 10 gauss, muonium precession can be seen in some materials.

For the case where the applied field is parallel or antiparallel to the muon beam, precession will not occur. The diamagnetic signal will therefore remain constant. At the same time, the paramagnetic muonium signal can be expressed in terms of a 'constant' term and an oscillating term[4].

$$\begin{aligned} P_z(t) &= \frac{1+2x^2}{2(1+x^2)} + \frac{1}{2(1+x^2)}\cos(\omega_{24}t) \\ P_x(t) &= 0 \\ P_y(t) &= 0 \end{aligned} \tag{3.4}$$

where $x = \frac{(\gamma_e+\gamma_\mu)B}{2\pi A_\mu}$ and $\omega_{24} = 2\pi A_\mu\sqrt{1+x^2}$. In a situation reminiscent of that for the transverse field, this paramagnetic oscillating term is usually at a very high frequency. Unfortunately, ISIS cannot detect large frequencies; such a limitation is due to the the finite muon pulse width (70 ns), where the bandpass for the facility is the fourier transform of the muon pulse shape.

Therefore, to conclude, from our TF20 curves, the diamagnetic fraction can be calculated by measuring the maximum amplitude of the signal precessing at the muon

Larmor frequency. Sometimes at low enough fields, a second precession signal can be seen superimposed on the dominant signal; this is the muonium precession oscillating at a frequency approximately 100 times larger than the muon frequency. On a longitudinal curve, the sinusoidal precession signal is no longer seen, and a relaxing asymmetry curve results. Contained within this signal, is both the constant diamagnetic and the pseudo-constant paramagnetic signals. By subtraction of the diamagnetic fraction, assuming a 'missing' fraction of 0 %, the total paramagnetic fraction is then found. Unfortunately, this method cannot discriminate directly between the varying paramagnetic states and species, just as the transverse field measurements cannot distinguish between the varying diamagnetic states. However, theoretical fittings, measurements of relaxation rates and temperature and field dependences, can all be used to determine the specific state types.

3.2.2 The DEVA beamline

The DEVA beamline differs from the well-established MuSR and EMU beamlines, in that it is a development facility, for which the majority of equipment is brought in to the facility by the beamline users. DEVA is used for both Radio-Frequency μSR (RF-μSR) experiments, and Ultra-Slow Muon μSR. Of consideration in this thesis is the use of the DEVA beamline as an RF-μSR facility. A diagram of the apparatus used to generate the high power RF-field is shown in Figure 3.6.

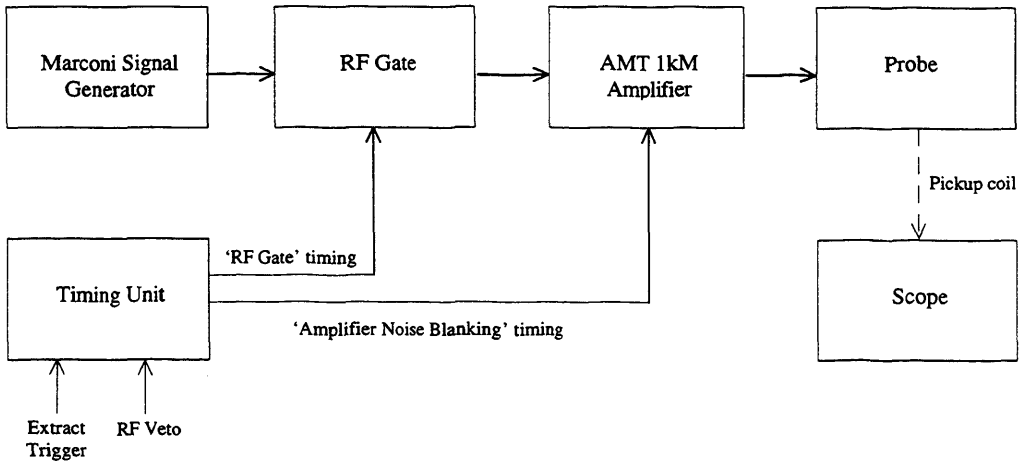

Figure 3.6: Block diagram of the RF-apparatus used on the DEVA facility. (From [5]).

The time-differential radio-frequency muon spin resonance (TD-RFμSR) spectrometer will now be considered. Such an addition at the ISIS Facility is ideal, principally because the RF-μSR technique avoids the limitations with which LF/TF-μSR is burdoned at the ISIS Facility. On the EMU and MuSR beamlines, the magnetic fields are limited to maximum values of 4500 gauss and 2000 gauss respectively. Unfortunately, for some materials such as GaAs, high-field measurements are very important, since it is at high fields where special features, such as a 'cusp' in the repolarisation curve, can appear. Under the same external circumstances as a standard LF/TF-μSR experiment, the application of an RF-field allows the muon scientist to probe muon spin transitions that would otherwise only be visible at much higher fields, sometimes of the order of 10^4 gauss. Since ISIS uses a pulsed muon source, and the RF pulses can be made very short, excessive heating of the sample is prevented. As for LF/TF-μSR experiments, of primary interest is the study of diamagnetic and paramagnetic states. Likewise, the variable parameter is often the external applied magnetic field. For this situation, a 'standard' resonance frequency must be set. On DEVA, the frequency of the applied RF-field used is 19.6 MHz, at which a magnetic field scan is performed. The inverse of this situation is also possible, whereby for a fixed applied magnetic field a frequency scan of the polarisation is made, such a scan can be seen in Figure 3.7. This technique

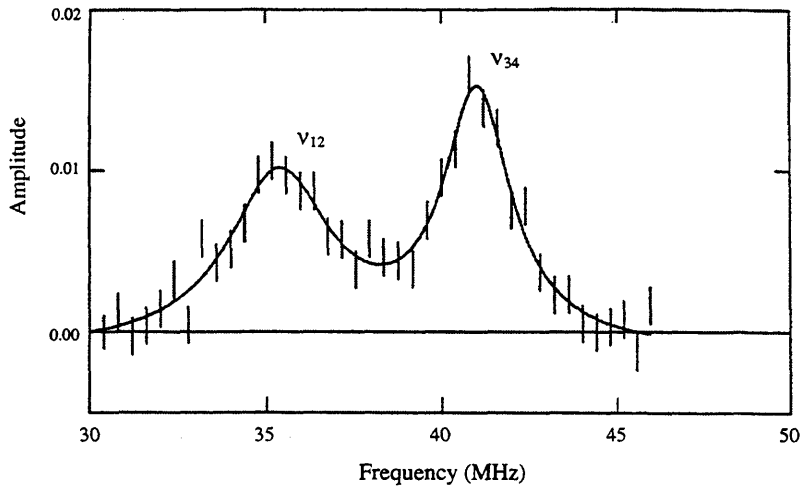

Figure 3.7: The rf-resonance peaks for a Mu_{BC} site, for 10^{15} cm^{-3} n-type silicon at 14 K, and a fixed field of 105 G. The term ν_{xy} refers to the transition type between states x and y (from [6]).

is, however, not yet possible on the existing DEVA facility.

When a 'field scan' is made, it is economical in beamtime to know where the resonance peaks of the diamagnetic or paramagnetic states are expected. For a frequency of 19.6 MHz, diamagnetic states are expected to produce signals at about 1400 - 1500 gauss, and the paramagnetic states (for isotropic muonium) to occur at about 7 - 21 gauss.

This field difference occurs as a consequence of the resonance condition, $\gamma B = 2\pi\nu$ (see Equation 2.7); at the ISIS facility, the resonance frequency is fixed, thereby ν is fixed, and the field at which resonance occurs is given by $\frac{2\pi\nu}{\gamma}$. For the bare (diamagnetic) muon, $\gamma \approx 0.0136\,\mathrm{MHz/G}$; however, for muonium at low fields the effective $\gamma \approx \frac{\gamma_e}{2}$, and thus the muonium γ is about 1.4 MHz/G. As to the origin of this approximation of $\gamma \approx \frac{\gamma_e}{2}$, it is necessary to consider the eigenvalues in Table 3.1. In the figure, the level number

Level	Eigenvalues
1	$\nu_1 = \varepsilon_1/h = \frac{1}{4}A_\mu + \frac{1}{2}(\gamma_e - \gamma_\mu)B$
2	$\nu_2 = \varepsilon_2/h = -\frac{1}{4}A_\mu + \frac{1}{2}\sqrt{A_\mu^2 + (\gamma_e + \gamma_\mu)^2 B^2}$
3	$\nu_3 = \varepsilon_3/h = \frac{1}{4}A_\mu - \frac{1}{2}(\gamma_e - \gamma_\mu)B$
4	$\nu_4 = \varepsilon_4/h = -\frac{1}{4}A_\mu - \frac{1}{2}\sqrt{A_\mu^2 + (\gamma_e + \gamma_\mu)^2 B^2}$

Table 3.1: The eigenvalues of muonium with an isotropic hyperfine parameter.

corresponds with the energy number of Figure 2.9. There are four principal transition frequencies to consider, namely ν_{12}, ν_{23}, ν_{14} and ν_{34}. Assuming that the magnetic field, B, is small, such that $A_\mu \gg (\gamma_e + \gamma_\mu)B$, and thus $A_\mu^2 \gg (\gamma_e + \gamma_\mu)^2 B^2$, it can be seen that for the ν_{12} and ν_{23} frequencies, the A_μ terms cancel out. This leaves the frequency field dependent, being now approximately equal to $\frac{1}{2}(\gamma_e - \gamma_\mu)B$, though, since $\gamma_e \gg \gamma_\mu$, γ_μ can be ignored. Hence, the effective γ is equivalent to $\frac{\gamma_e}{2}$. For the other transition frequencies of ν_{14} and ν_{34}, the A_μ terms do not cancel out, and therefore, since $A_\mu \gg (\gamma_e + \gamma_\mu)B$, the transition frequencies are effectively equal to A_μ. They are therefore approximately constant at low fields, and by their field independence, cannot contribute to a field-scan of RF-μSR.

With the fixed condition of γ_{Mu} being some 100 times larger than $\gamma_{\mu+}$, the resonance field of the diamagnetic site will about 100 times larger than the field for the paramagnetic site. It is at these fields where the muon is expected to resonate between its two spin states, 'up' and 'down' (sometimes referred to as '+' and '−' respectively), the resonant field supplying the required energy to "flip" the muons. These spin transitions can be seen in the muonium Breit-Rabi diagram of Figure 2.9, with the muon spin flipping in the low-field regime. In an RF-field, the muons continuously flip between each of the transition states. As mentioned in Chapter 2, such spin-flip transitions lead to a rapid depolarisation of the muon so, although the initial asymmetry (a_0) is common to both the RF_{ON} and the RF_{OFF} situations, with an applied RF-field the relaxation rate will increase. In Figure 3.8, the different asymmetry curves are shown for the RF_{ON} and the RF_{OFF} configurations. For RF-μSR, the total number of positron counts, N, between

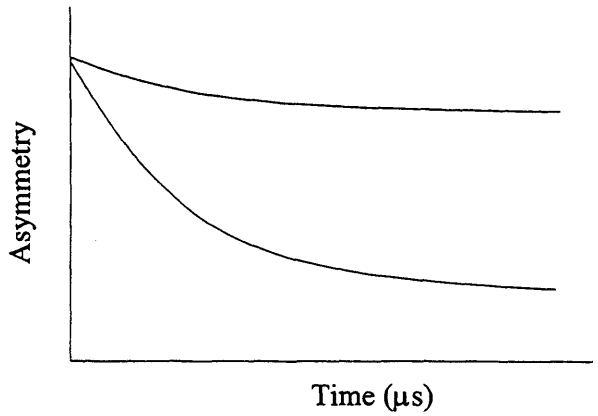

Figure 3.8: The asymmetry curves for the slow-relaxing RF_{OFF} and the fast-relaxing RF_{ON} configurations.

times *t1* and *t2* is then calculated for both the RF_{OFF} and RF_{ON} situation, to find N_{OFF} and N_{ON} respectively. This integration is shown in Figure 3.9. The final value of the integrated asymmetry, A_{RF}, is calculated in a manner similar to the TF/LF case, where the difference of the positron counts at the 'forward' and 'backward' detectors is normalised to eliminate the effects of the muon lifetime. In the RF case, the integrated asymmetry is calculated thus :

$$A_{RF} = \left(\frac{N_{ON} - N_{OFF}}{N_{ON} + N_{OFF}}\right)_F - \left(\frac{N_{ON} - N_{OFF}}{N_{ON} + N_{OFF}}\right)_B \tag{3.5}$$

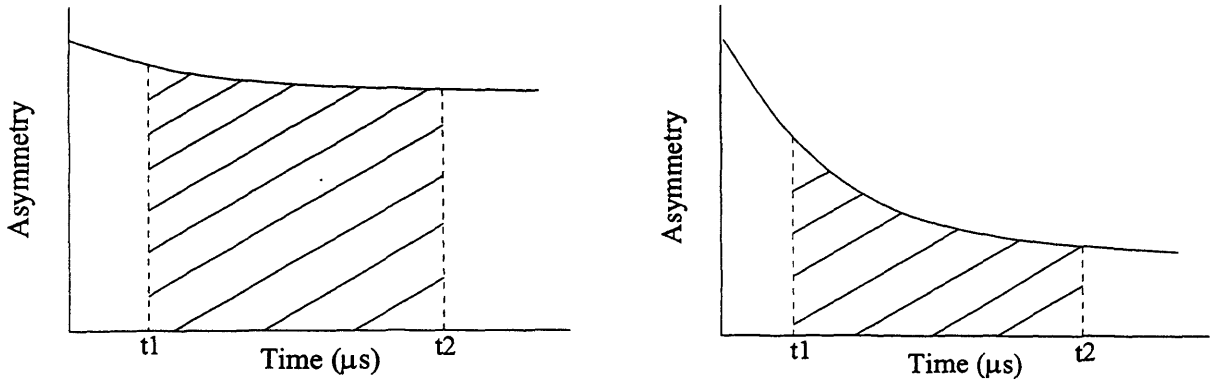

Figure 3.9: The time-integration of the asymmetries, between times t1 and t2, for the slow-relaxing RF_{OFF} (left) and the fast-relaxing RF_{ON} (right) configurations.

where $(N_{ON} + N_{OFF})_F$ is the normalisation factor, and the 'F' subscript refers to the 'Forward' detectors, and the 'B' subscript refers to the 'Backward' detectors. In Figures. 3.10 and 3.11, the resultant integrated asymmetry curves are observed, taken for p-type c-Si[6]. A single peak is observed for the diamagnetic site, but for the paramagnetic site, narrower resonance peaks, corresponding to the ν_{12} and ν_{23} state transitions, and an intense narrow (central) peak corresponding to the superposition of the ν_{12} and ν_{23} transitions can be seen. Such a superposition of transitions, occurring at the low magnetic field where $\nu_{12} = \nu_{23}$, accounts for the larger amplitude of the resonance peak, and the field at which this peak occurs.

On DEVA, the sample environment can reduce the sample temperature to as low as 25K. Typically, as with LF/TF-μSR, the asymmetry dependence is measured for a wide range of sample temperatures. The sample is cooled using the cold-finger method, and the RF-field applied via a rectangular coil consisting of 8 coils. To avoid potential problems with electrical breakdowns, the RF coil was built onto a ceramic (Shapel) blade that is bolted on to the metal cold finger. The rectangular coil was again constructed as part of a 50Ω resonance circuit.

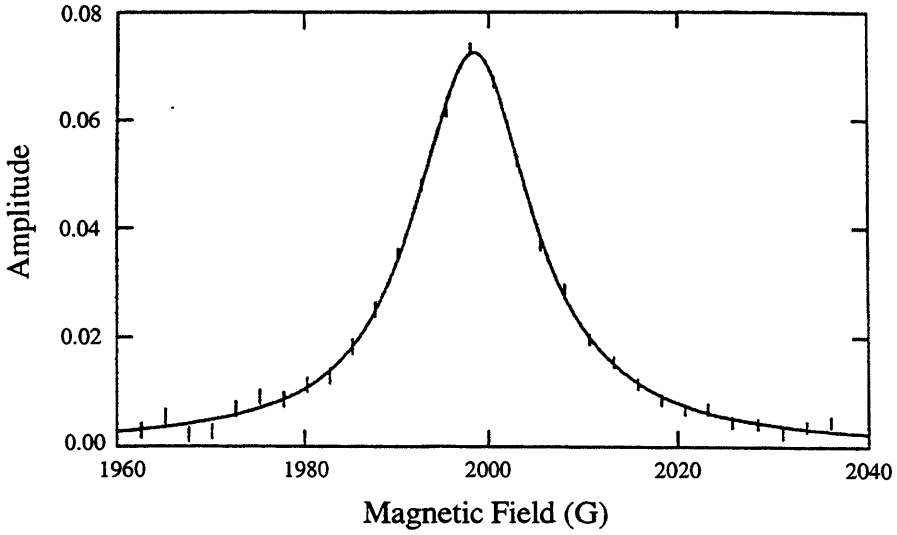

Figure 3.10: The rf-resonance peak for a diamagnetic site, for $10^{11}\,\mathrm{cm}^{-3}$ p-type silicon at 310 K, with an oscillator frequency of 27.1 MHz (From [6]).

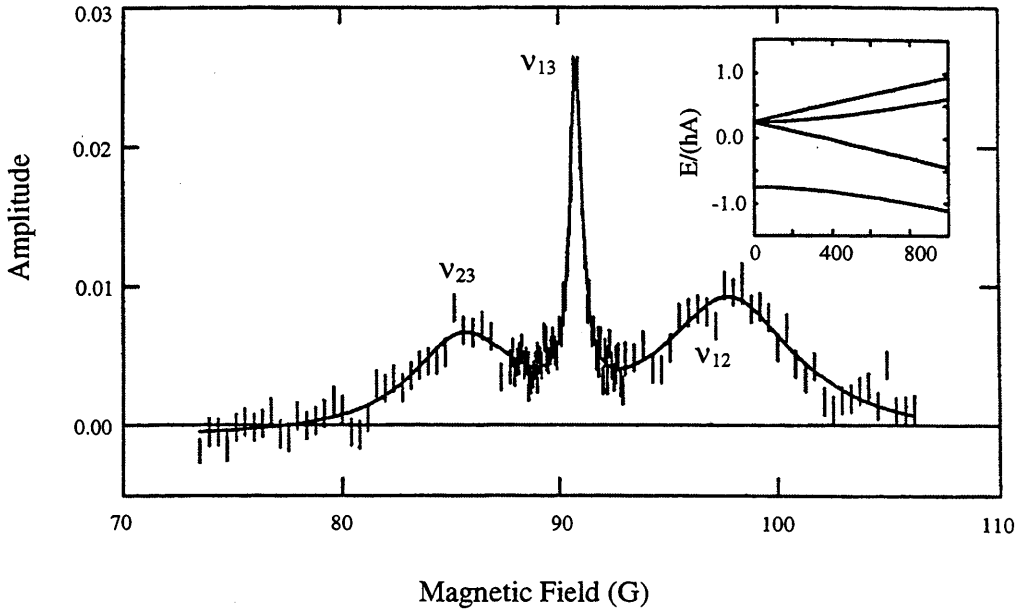

Figure 3.11: The rf-resonance peak for a paramagnetic Mu_T site, for $10^{13}\,\mathrm{cm}^{-3}$ p-type silicon at 10 K with an oscillator frequency of 127 MHz (From [6]).

3.3 μSR data analysis

3.3.1 ISIS Computer support and UDA analysis

For the computing and analysis of μSR spectra, ISIS is home to an extensive computer network, principally of VAX stations and PCs, and specialised hardware and software for the collection, analysis and 'fitting' of experimental data. A schematic illustration of the computer network and VAXcluster is shown in Figure 3.12. Of great benefit to the muon users is that control of an ISIS instrument, e.g. EMU or MuSR, can be performed on the relevant 'Front End Minicomputer' (FEM) connected to the node of the VAXcluster. Control of the sample environment, i.e. temperature and applied field, collection of data, and preliminary data analysis can all be controlled remotely via the relevant software on the X-Windows of the FEM.

The running of EMU can be divided into four main stages :-

i) 'RUN' details

ii) Sample environment

iii) ICP - instrument control program

iv) Data manipulation and display

After the preparation and mounting of the sample, the 'RUN' details must be decided. The experiments upon a sample-type are divided into 'runs', where the run is designated a specific 'run-number'. Whenever the sample or its environment are changed, a new run-number is assigned, which is essential for storage, identification and analysis of the spectrometer histograms. Examples of other run details are the defined time channels i.e. which detector is used to monitor the experiment and which detectors are used to collect and store the data.

Next, the sample environment must be defined. This is a collection of the parameters that may vary from run to run. Some of the parameters relate directly to the sample, and others to the beam itself. Sample parameters include the temperature at which data is to be collected, the magnitude of the applied magnetic field, the direction of the applied field, and the orientation of the sample itself, the latter being of particular importance

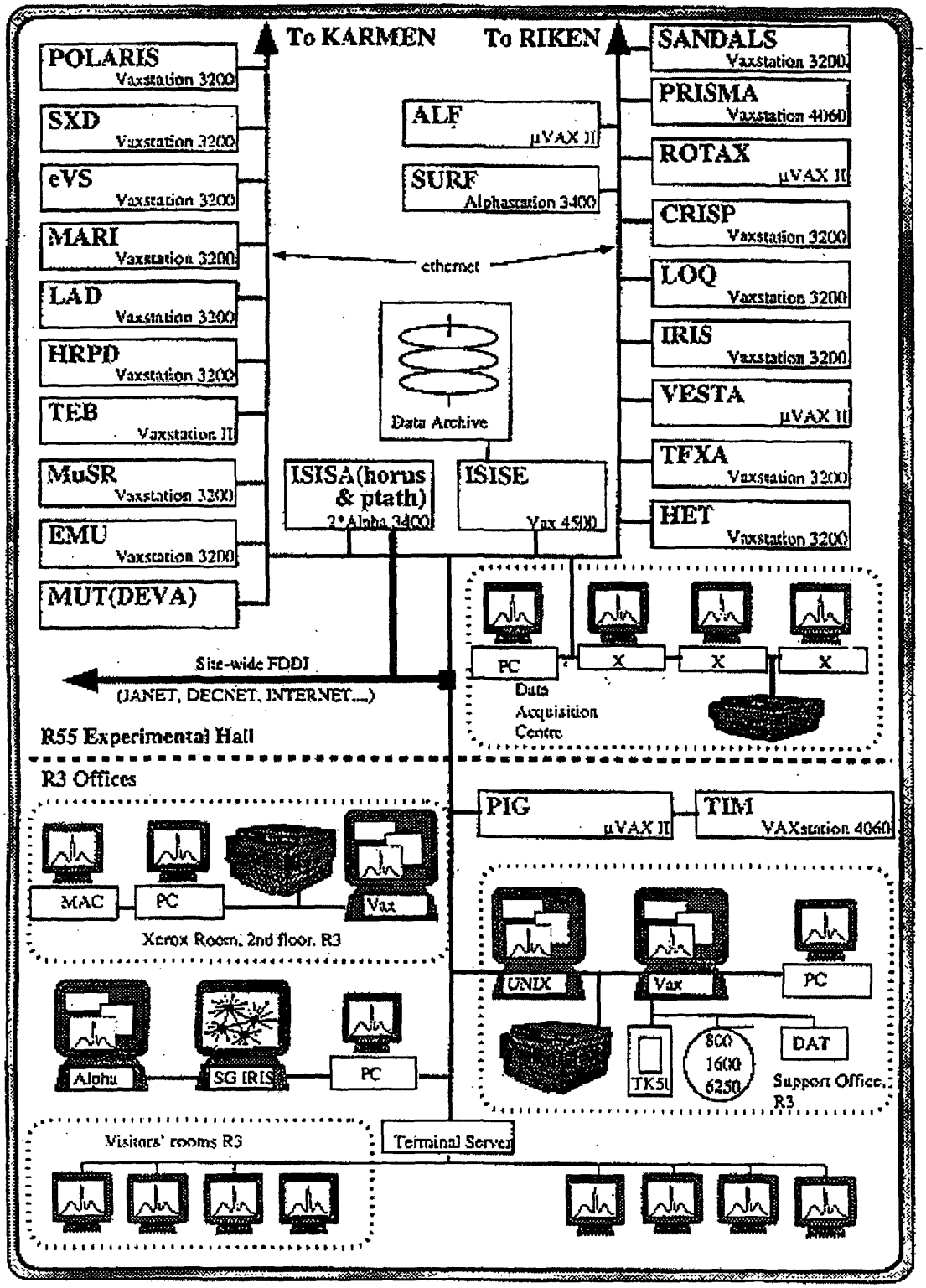

Figure 3.12: Schematic illustration of the computer network and VAXcluster of the ISIS Facility.

for crystalline samples. Beam parameters include the 'slit width', which controls the size of the beam-spot on the sample, and also the incident muon count rate.

As already mentioned, the μSR instruments can be controlled remotely via the computers supplied at ISIS. The front end of this control is the 'Instrument Control Program', which is used to start, stop and control the run, using information in the set-up phase. It is via this program that the applied fields and temperature of the sample can be controlled. However, the changeover from low-field to high-field power supplies and the switching off of the liquid helium compressor when returning to sample room temperature, all need to be performed manually.

After the completion of the RUN, the data can be manipulated and displayed in a graphical form on the VAX X-windows. A data analysis package, known as UDA, is available on the computer network, for the analysis, fitting and printing of each run. The fitting procedures vary depending upon the field orientation. For TF analysis, several theoretical functions are predefined in UDA, the two most commonly used being the Lorentzian and Gaussian. Their forms are given below.

Function Name	**Definition**
Lorentzian	$a_0 \cos(\omega t + \phi) \exp(-\lambda t)$
Gaussian	$a_0 \cos(\omega t + \phi) \exp(-(\lambda t)^2)$

Here ϕ is the phase difference, and λ the polarisation relaxation rate. For LF analysis, the predefined theoretical functions are :

Function Name	**Definition**
Lorentzian	$a_0 \exp(-\lambda t)$
Gaussian	$a_0 \exp(-(\lambda t)^2)$

Unlike the transverse-field fitting, the LF asymmetry function is split into two separate components, a) a fast-relaxing component, and b) a slow-relaxing component. Therefore, assuming that a 'Lorentzian' function is used, the fitted asymmetry function can be expressed as

$$A(t) = a_0 G(t) = a_0^f e^{-\lambda_f t} + a_0^s e^{-\lambda_s t} \tag{3.6}$$

where the superscripts represent (f)ast and (s)low components. It is the addition of a_0^f and a_0^s which gives a_0, the total asymmetry at time $t=0$. To obtain the value of the polarisation at $t=0$, the total asymmetry must be normalised. This is done by dividing a_0 by the corresponding value for silver :

$$P_0 = \frac{a_0}{a_{0_{Ag}}} \tag{3.7}$$

Since silver (Ag) is a metal, no muonium is formed. As a result there is no loss of polarisation when compared to the initial beam and the polarisation is therefore considered to be 100 % polarised, i.e. $P_0 = 1$. As such, all other materials are compared with silver's total polarisation, thereby allowing calculation of the polarisation fraction, for both field and temperature dependences.

3.3.2 Repolarisation curves

In order to obtain information on sites occupied by the muons, the hyperfine constant and the relative fractions of the diamagnetic and paramagnetic states must be found. To gain such details theoretical fits of the longitudinal muon polarisation experimental results have been necessary. Later in this thesis, theoretical fits are made to experimentally gained repolarisation curves. Several different theoretical approximations have been used to fit differing regimes of the repolarisation curves, i.e. plots of the normalised asymmetry (polarisation) versus magnetic field. In Section 2.2.1, the muon spin 'repolarisation' technique was only briefly discussed. In this section, the technique will be considered in more detail than previous, paying particular attention to the theoretical analysis of *repolarisation curves.*

The experimental set-up is the same as the standard LF-μSR and the parameter of primary interest is the initial amplitude at $t=0$ of the LF-μSR signal, as a function of magnetic field. In these experiments, few data are collected relevant to the dynamics of the muonium states, and therefore is seldom used as a probe into such dynamic pathways. As the name suggests, repolarisation experiments depend on the returning of the polarisation to $P_z(t) = 1$ at high enough magnetic fields. To extract the relative fractions and parameters from the curves, there is also a dependence on the variation

of the behaviour of the different sites in magnetic fields. For example, consider an isotropic muonium state such as Mu_T. Its polarisation parameter of $P_z(t)$ is expressed by Equation 3.4. At ISIS, the oscillating component is usually unresolvable, due to the limited timing resolution of the apparatus, and so this component is averaged to zero, and therefore $P_z(t)$ can be expressed by the field dependence of the first term in Equation 3.4. By comparison, the $P_z(t)$ for Mu_{BC} centre exhibits far more complicated behaviour, due to its highly anisotropic interaction. As a consequence, a simple expression such as Equation 3.4 cannot be obtained, although low- and high-field approximations have been generated which will be discussed later in this section.

Theoretical repolarisation curves for Mu_T and Mu_{BC}, with parameters relevant for Si, are shown in Figure 3.13. A_{iso} is the hyperfine constant of the isotropic component, and

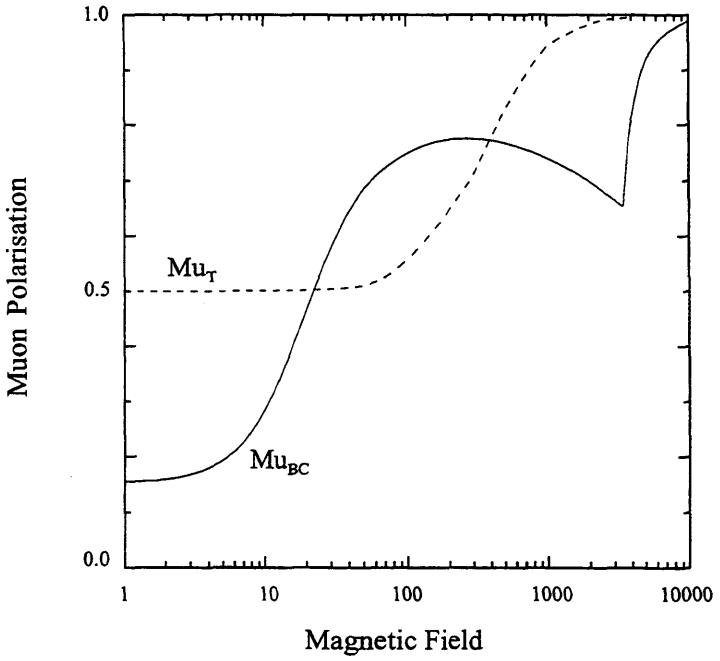

Figure 3.13: Theoretical repolarisation curves for the Mu_T site, where $A = 1000\,\text{MHz}$, and the Mu_{BC} site, of pcr-Si, where $A_{iso} = 67.3\,\text{MHz}$ and $B = 25.3\,\text{MHz}$ (adapted from [8]).

B is a measure of the degree of anisotropy of the hyperfine interaction. The isotropic Mu_T curve follows Equation 3.4, bearing the 'tell-tale' feature of a polarisation at $B = 0\,\text{gauss}$ of 0.5. Another feature is the field at which the inflexion point occurs. This equals 0.577

(i.e. $\frac{1}{\sqrt{3}}$) times the hyperfine field, as can easily be derived by double differentiation of Equation 3.8 below. In marked contrast, is the curve for the anisotropic Mu_{BC} site. The repolarisation curve for Mu_{BC} is orientation dependent, and as a result, for crystalline materials the polarisation at $B=0$ can vary between 0 and $\frac{1}{2}$. As the angle is increased, moving further from the direction of axial symmetry, the low-field polarisation is reduced, as is shown in Figure 3.14. Considering the simple case of an anisotropic muonium site

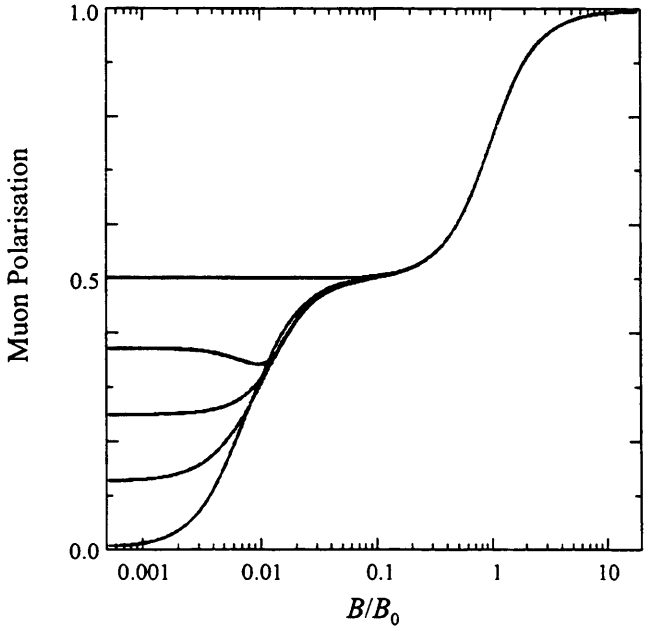

Figure 3.14: Repolarisation curves for axially symmetric anisotropic muonium, as a function of the angle of the field to the axis of symmetry. From top to bottom $\theta=0$, 30, 45, 60 and 90^0, where $H_0 = \frac{A}{\gamma_e+\gamma_\mu}$ (from [8]).

with axial symmetry, at an angle of $\theta = 0^0$ (i.e. along the direction of axial symmetry) the repolarisation curve is identical with the isotropic case, shown in Figure 3.13, with a low-field polarisation of $\frac{1}{2}$. The characteristic field where repolarisation begins, between 0.5 and 1.0, is determined by the isotropic component of the hyperfine coupling, and can be seen to be independent of orientation in Figure 3.14. An abrupt change in the slope of the polarisation can occur, sometimes generating a 'cusp', as seen in Figure 3.13, and also seen, to a lesser extent, as a dip at $\frac{B}{B_0} = 0.01$ in the small-angle orientation of Figure 3.14. This 'cusp' is a result of an avoided level crossing resonance (ALC) between muonium triplet states. Consider Figure 3.15, it appears that the energy levels

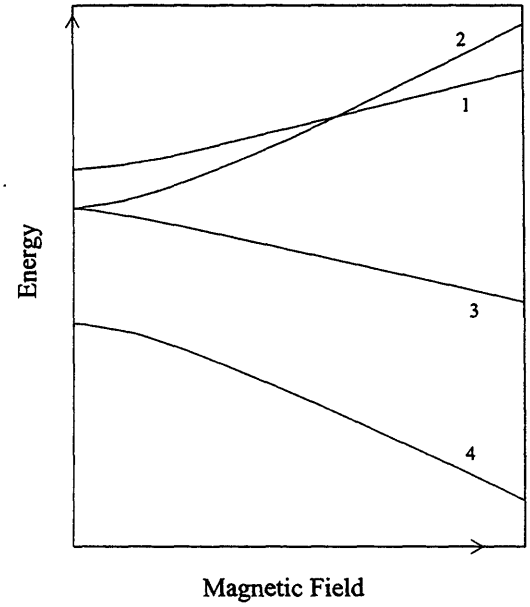

Figure 3.15: Energy levels for anisotropic Mu_{BC} where $\theta = \frac{\pi}{2}$ ([111] symmetry axis perpendicular to the applied field) (from [11]).

1 and **2** cross at high fields; this does not actually occur. These levels only approach *very* closely to each other, and a correct description is that of 'avoided level crossing'. Under such circumstances, with the energy levels 1 and 2 being exceedingly close, muon resonance can occur, similar to that which occurs when an RF-field is applied at the resonance magnetic field, see Section 3.2.2, whereby the muon begins to flip between the two energy levels, leading to a rapid loss of polarisation and an increase in the polarisation relaxation rate. As the external applied field is increased, the energy levels begin to move further apart until resonance no longer occurs, and the polarisation begins to return.

At this point it would be useful to introduce the parameters which are used to describe the axially symmetric hyperfine interactions; these are A_i and D_1. Although the muonium state is referred to as anisotropic, it is considered that there still exists an isotropic component of the hyperfine interaction. The hyperfine constant for the isotropic centre is 'A', and similarly, the isotropic component of the hyperfine constant for an anisotropic muonium centre is written as 'A_i'. The hyperfine tensor of Equation 2.20 can be expressed as the sum of the isotropic part and a traceless dipolar part D (where $D = 2B$),

referred to as D_1 for an axially symmetric centre, see Equation 2.25. To understand the effects of the D_1 component, a useful illustration would be to consider a football (analogous to the isotropic centre) and then deforming it into the shape of a rugby ball (analogous to the axially symmetric centre), thereby 100 % isotropy is lost with a degree being maintained along the axis of the ball.

In general, the experimental repolarisation curves are a composite of the curves of the differing site types, existing in varying relative fractions. As such the polarisation curve can be split into four different regimes :

1) The diamagnetic fraction

2) The isotropic paramagnetic fraction

3) The low-field anisotropic fraction

4) The high-field anisotropic fraction

It is the addition of each of these regimes which leads to the variation in the shape and details of the repolarisation curves. The repolarisation technique is especially useful in the identification of muonium states, and the estimation of hyperfine parameters. In situations where there is a distribution of hyperfine parameters, which leads to a broadening of the TF-μSR signals (e.g. Figure 2.12) beyond detection, such as in the disordered amorphous materials, an estimate of the hyperfine interactions can still be made.

As mentioned earlier in Section 3.2.1, in a longitudinal field, the diamagnetic fraction is constant. This constant is attained via normalisation of the $t = 0$ asymmetry. Therefore, when generating theoretical fits, the diamagnetic fraction is considered to be independent of the magnitude of the magnetic field, and remains a fixed parameter.

The simplest of the paramagnetic states occurs when the muonium 'sits' at the high symmetry interstitial site or is rapidly diffusing through the lattice network. By considering Equation 3.4, for the high transition frequencies of ω_{24} leading to the 2nd term being unresolvable, the Equation can thus be simplified to[7] :-

$$P = \frac{\frac{1}{2} + \left(\frac{B}{B_0}\right)^2}{1 + \left(\frac{B}{B_0}\right)^2} \tag{3.8}$$

where P is the muon polarisation. This increases from the low-field value of 0.5 to a

maximum of 1.0 with the inflexion point being given by $B_0 = \frac{A}{\gamma_e + \gamma_\mu}$. B is the longitudinally applied magnetic field, A is the hyperfine coupling, and γ_e and γ_μ are the electron and muon gyromagnetic ratios.

For the low-field region of the anisotropic muonium, the situation is complicated by the orienation dependence of the muonium site. As already mentioned for crystalline materials, the polarisation signal can vary signifcantly for the different angles, already seen in Figure 3.14. Consider, therefore, the situation when either a polycrystalline or disordered sample is used. Under such circumstances, the orientation becomes angle-averaged, and by taking an average of the polarisation of such curves as in Figure 3.14, repolarisation curves can be produced as in Figure 3.16 for different magnitudes of anisotropy. If a mathematical fit is made to these curves, a reasonable approximation is

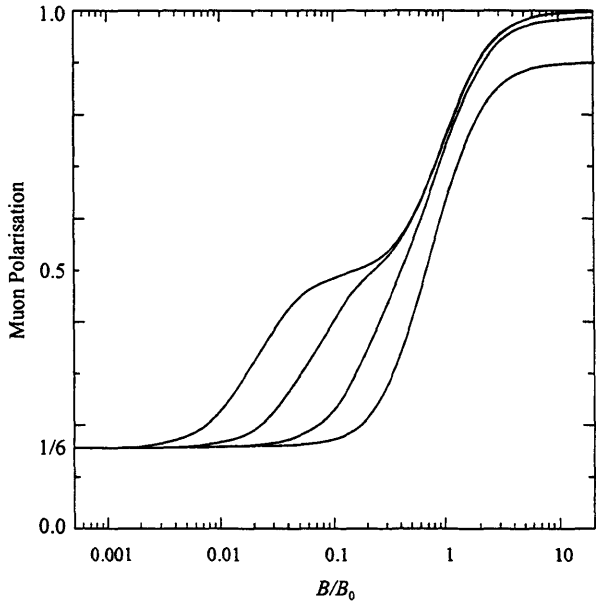

Figure 3.16: Calculated polycrystalline averaged repolarisation curves as functions of the muonium uniaxial symmetry. From left to right, $\frac{D_1}{A} = 2$, 6, 20 and 60 %. (From [8]).

found to be given by :

$$q = \frac{1}{2}\left(\frac{\frac{1}{3} + \left(\frac{B}{B_1}\right)^2}{1 + \left(\frac{B}{B_1}\right)^2}\right) \tag{3.9}$$

where $B_1 = \frac{D_1}{\gamma_e - \gamma_\mu}$, and B is the applied external field. It should be stressed that Equation 3.9 serves only as an approximation, but is accurate in the simple regime, generally

at low fields, where avoided level crossing resonance is far away. As the field is increased to approach the level crossing region, then the approximation serves as a poor fit, and a full numerical calculation is necessary (the deviation of the approximation from the computed full calculation is illustrated later in this section).

Considering the case where there is no longer any axial symmetry, a third new parameter can be introduced, that of D_2, which can be defined as the departure from axial symmetry. In terms of the football analogue used to describe D_1, this term D_2 is equivalent to squashing the rugby ball perpendicular to its axis of symmetry, thereby removing all isotropy. This case is known as the 'fully anisotropic' muonium centre. A consequence of a total loss of isotropy is that there are no orientations where zero-field polarisation is preserved. As a consequence, the polarisation at zero-field remains zero for all orientations, whether the sample is crystalline, polycrystalline or amorphous. An approximation to the numerically calculated repolarisation can be expressed as[8] :-

$$P = \frac{1}{2}\left(\frac{x^2}{1+x^2}\right) + \frac{1}{3}\left(\frac{y^2}{\frac{15}{16}+y^2}\right) + \frac{1}{6}\left(\frac{z^2}{\frac{5}{12}+z^2}\right) \tag{3.10}$$

where

$$x = \frac{B}{B_0} = \frac{(\gamma_e+\gamma_\mu)\,B}{A_i}, \qquad y = \frac{B}{B_1} = \frac{(\gamma_e-\gamma_\mu)\,B}{D_1}, \qquad z = \frac{B}{B_2} = \frac{(\gamma_e-\gamma_\mu)\,B}{D_2}$$

It is by fitting the experimental curves with Equation 3.10 that approximations of the three parameters A_i, D_1 and D_2 can be obtained; and it is from these parameters that the level of a site's anisotropy can be gained, and therefore an understanding of the site and its local environment furthered. As Equation 3.10 is only an approximation, deviations from the full numerical calculation do occur. As with the calculation from Equation 3.9, the deviation becomes predominant in the region of the level crossings. Such level crossings predominate at high fields, and therefore, the approximation of Equation 3.10 is suitable for the fitting of low-field experimental data. Hence, at high fields the deviation tends to be significantly large; at low-fields the deviation is small, as is shown in Figure 3.17.

The final scenario, for an anisotropic site at **high fields** requires a different fitting procedure. The theoretical expressions used to fit the experimental data are, again, ap-

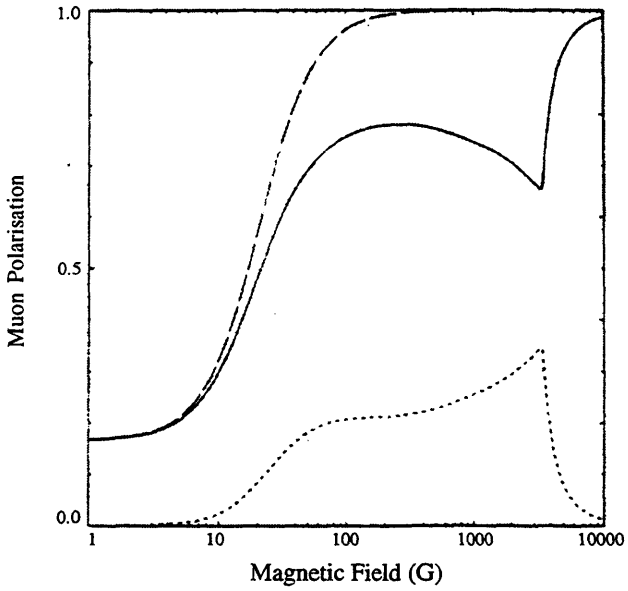

Figure 3.17: Repolarisation curves for the Mu_{BC} centre, calculated from the approximate expression (— — —) of Equation 3.10 ($A_i = 67.3$ MHz, D_1 -50.6 MHz and $D_2 = 0$ MHz) and the full numerical calculation for pcr-Si (——). The deviation of the approximation from the full calculation is shown as (- - - -) (from [8]).

proximations, and thus deviations with field can occur. For a high-field approximation, P.F. Meier derived an expression [9],[10] for anamalous muonium, and showed a satisfactory correlation with the calculated data for the full spin Hamiltonian. The full spin Hamiltonian for the anomalous muonium state can be written as Equation 3.11.

$$\mathcal{H} = \boldsymbol{I}.\boldsymbol{A}\boldsymbol{S} - g_\mu \mu_\mu \boldsymbol{B}.\boldsymbol{I} - g_e \mu_e \boldsymbol{B}.\boldsymbol{S} \tag{3.11}$$

where **I** and **S** denote the electron spins respectively, **B** is the applied field and **A** is the anisotropic coupling tensor. At high fields, the Zeeman term of the electron dominates, and some of the electron spins are decoupled from the muon, reducing their hyperfine interaction. The muon can then undergo Larmor precession in an effective field, B_{eff} where :

$$\mathcal{H}_\pm = -g_\mu \mu_\mu \boldsymbol{I}.\boldsymbol{B}_{eff,\pm} \tag{3.12}$$

and which can be split into components of :

$$\mathbf{B}^x_{eff,\pm} = \mp \frac{h\delta}{2\gamma_\mu} \sin\theta\cos\theta \qquad \text{and} \qquad \mathbf{B}^z_{eff,\pm} = B \mp \frac{h\nu}{2\gamma_\mu} \mp \frac{h\delta}{2\gamma_\mu} \cos^2\theta \tag{3.13}$$

Here, $\gamma_\mu = g_\mu \mu_\mu =$ 13.55 MHz/kG denotes the gyromagnetic ratio of the muon, and θ is the angle between the symmetry axis of the Mu_{BC} centre and the external field. So consider the magnetic fields :

$$B_\nu = \frac{h\nu}{2\gamma_\mu} \qquad \text{and} \qquad B_\delta = \frac{h\delta}{2\gamma_\mu} \tag{3.14}$$

where $\nu = A_\perp$ and $\delta = A_{||} - A_\perp$, and define the reduced fields as

$$\beta_+ = \frac{B_\nu + B}{B_\delta} \qquad \text{and} \qquad \beta_- = \frac{B_\nu - B}{B_\delta} \tag{3.15}$$

where B is the external field, and then

$$\gamma_+ = \frac{\beta_+^2}{1+2\beta_+} \qquad \text{and} \qquad \gamma_- = \frac{\beta_-^2}{1+2\beta_-} \tag{3.16}$$

The average longitudinal polarisation is then given by a time independent part

$$p(\theta) = p_+(\theta) + p_-(\theta) \;=\; \frac{1}{2}\left(\cos^2\alpha_+ + \cos^2\alpha_-\right) \tag{3.17}$$

and an oscillating part with an amplitude of

$$p^{osc}(\theta) = p_+^{osc}(\theta) + p_-^{osc}(\theta) \;=\; \frac{1}{2}\left(\sin^2\alpha_+ + \sin^2\alpha_-\right) \tag{3.18}$$

where $\tan\alpha_\pm = B^x_{eff,\pm}/B^z_{eff,\pm}$.

$$p_-(\theta) = \frac{1}{2} - \frac{1}{2}\left(\frac{\sin^2\theta\cos^2\theta}{\beta^2 + (1+2\beta)\cos^2\theta}\right) \tag{3.19}$$

For a polcrystalline sample, the average over all the angles leads to :

$$\langle p_\sigma \rangle = \frac{1}{2} - \frac{1}{2}\frac{1}{(1+2\beta_\sigma)}\left[\frac{2}{3} + \gamma_\sigma - \gamma_\sigma(1+\gamma_\sigma)\,A(\gamma_\sigma)\right] \tag{3.20}$$

where

$$\sigma \;=\; \pm 1$$

and

$$A(\gamma_\sigma) \;=\; \frac{1}{\sqrt{\gamma_\sigma}}\arctan\frac{1}{\sqrt{\gamma_\sigma}} \qquad \text{if} \quad \gamma_\sigma > 0 \tag{3.21}$$

$$\;=\; -\frac{1}{2\sqrt{-\gamma_\sigma}}\ln\left|\frac{1+\sqrt{-\gamma_\sigma}}{1-\sqrt{-\gamma_\sigma}}\right| \qquad \text{if} \quad \gamma_\sigma < 0 \tag{3.22}$$

Depending on the signs of B_ν and B_δ, either $\langle p_+ \rangle$ or $\langle p_- \rangle$ exhibits the cusp at the reduced field $\beta_\sigma = 0$. Due to the assumption of the Hamiltonian, of Equation 3.12, that the system is in a high field, like the approximations of Equations 3.9 and 3.10, there occurs a deviation away from the full numerical calculation, but this time in the low-field regime. This deviation is shown in Figure 3.18, and it can be seen that at high fields the

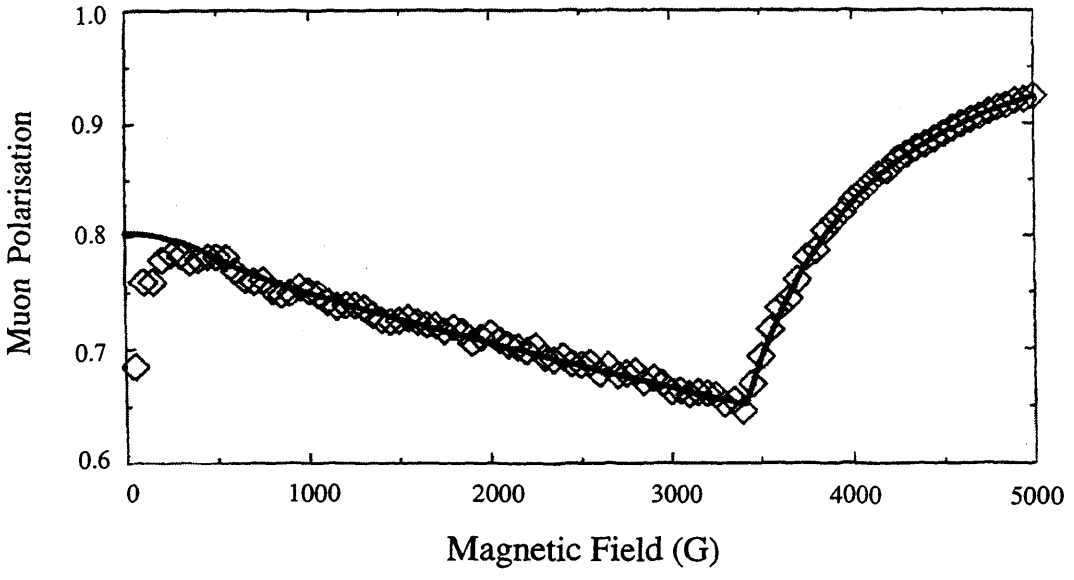

Figure 3.18: Longitudinal polarisation versus magnetic field for pcr-Si, calculated with the full spin Hamiltonian of Equation 3.11 ($\diamond$), and the approximated result of Equation 3.20 (solid line) (from [9]).

fit is generally excellent, but at low fields the approximation cannot be used. Since the approximation assumes an average over all angles, it is therefore particularly suitable for the high-field fitting of polycrystalline and disordered materials.

As a consequence of the field limitations of the approximate Equations 3.10 and 3.20, during the fitting procedure in the low-field regime Equation 3.10 has been used, and in the high-field regime Equation 3.20 has been used.

Bibliography

[1] '*Rutherford Appleton Laboratory Annual Report 1994 - 95*', Rutherford Appleton Laboratory Technical Report RAL-TR-95-050, (1995).

[2] '*Lecture Notes from the Training Course in Pulsed μSR Techniques*', S.H. Kilcoyne (editor), Rutherford Appleton Laboratory Technical Report RAL-TR-96-007, (1996).

[3] '*Condensed Matter Research Using the ISIS Pulsed Muon Source* - An introduction to the μSR technique at ISIS', introduction leaflet available from ISIS Pulsed Muon Facility (1998).

[4] A. Schenck. *Muon Spin Rotation Spectroscopy - Principles and Applications in Solid State Physics*, Adam Hilger Ltd., (1985) §7.1.2.

[5] C.A. Scott, B. Hitti and S.P. Cottrell, '*Radio-Frequency Techniques at the ISIS Pulsed Muon Source*', Rutherford Appleton Laboratory Report, RAL-94-101, (1994).

[6] S.R. Kreitzman, B. Hitti, R.L. Lichti, T.L. Estle and K.H. Chow, Phys. Rev. **B 51**, (1995), 13117.

[7] R.A. Ferrel and F. Chaos, Phys. Rev. **107**, (1957), 1322.

[8] F.L. Pratt, Phil. Mag. Lett **75**, (1997), 371.

[9] P.F. Meier, Hyp. Int. **86**, (1994), 723.

[10] D.W. Cooke, M. Leon, M.A. Paciotti, P.F. Meier, S.F.J. Cox, E.A. Davis, T.L. Estle, B. Hitti, R.L. Lichti, C. Boekema, J. Lam, A. Morrobelsosa and J. Oostens, Phys. Rev. **B 50**, (1994), 4391.

[11] B.D. Patterson, Rev. Mod. Phys. **60**, (1988), 69.

Chapter 4

Sample Preparation and Diagnosis

For the samples studied in this work, several different methods of preparation have been used. For the polycrystalline samples, specimens were obtained by crushing either single crystal wafers or polycrystalline lumps to powder form. The amorphous samples were prepared by evaporation, sputtering or glow-discharge deposition. The glassy samples were obtained by melt-quenching into ingots which were subsequently crushed. The preparation method for each sample, on which measurements have been made, is shown in Table 4.1.

Of the deposition techniques, only sputtering has been performed in-house by the present author. The glow-discharge samples were prepared at the Palo Alto Research Centre of the Xerox Corporation in California, by Dr R.A. Street. The electron beam evaporation was performed at the then Leicester Polytechnic by Dr Bevin. The melt-quenching preparation of the glasses was performed by Professor E. Mytilineou, in the research laboratories of the Department of Physics, University of Patra, Patras in Greece. The focus of this chapter will be primarily on the sputtering technique, but attention will also be made to the diagnosis of the materials, or more specifically measuring whether the materials which are thought to be amorphous, are actually that.

Sample	Preparation method	Substrate or melt temperature (°C)
pcr-Si	Crushed c-Si wafer	—
$p-$type pcr-Si ($x\,10^{17}cm^{-3}$)	Crushed p-type c-Si wafer	—
a-Si	Electron-beam evaporation	290
a-Si:H	Glow-discharge	290
p-type a-Si:H	Boron-doped glow-discharge	290
n-type a-Si:H	Phosphorus-doped glow-discharge	290
pcr-Ge	Crushed pcr-Ge lumps	—
a-Ge	Sputtered	290
a-Ge:H	Sputtered	290
pcr-GaAs	Crushed c-GaAs wafer	—
pcr-GaP	Crushed c-GaP wafer	—
a-Se	Scraped from Xerox a-Se plate	–
g-$Ge_{10}Se_{90}$	Melt-quenched & crushed	850
g-$Ge_{22}Se_{78}$	Melt-quenched & crushed	–
g-$Ge_{33}Se_{67}$ ($GeSe_2$)	Melt-quenched & crushed	–
g-$Si_{10}10Se_{90}$	Melt-quenched & crushed	–
g-$Si_{20}Se_{80}$	Melt-quenched & crushed	1100
g-$Si_{33}Se_{67}$ ($SiSe_2$)	Melt-quenched & crushed	1100

Table 4.1: Preparation methods and substrate or melt temperatures for all samples discussed in this thesis. pcr-: polycrystalline, a-: amorphous, g-:glassy.

4.1 Preparation of polycrystalline samples

As can be seen from Table 4.1, all of the polycrystalline samples used in the experiments were prepared by crushing crystalline wafers or polycrystalline lumps. Both wafers and lumps were obtained from various commercial companies, with the wafers most probably having been cut from ingots grown by the Czochralski method. The samples were packed into aluminium sample holders, suitable for use at the Rutherford Appleton Laboratories. The sample materials were packed into a recess in the holder, and covered with a retaining mylar film which was clamped in place with a retaining ring as, illustrated in Figure 4.1. The holder was then mounted on the cold-finger of a CCR

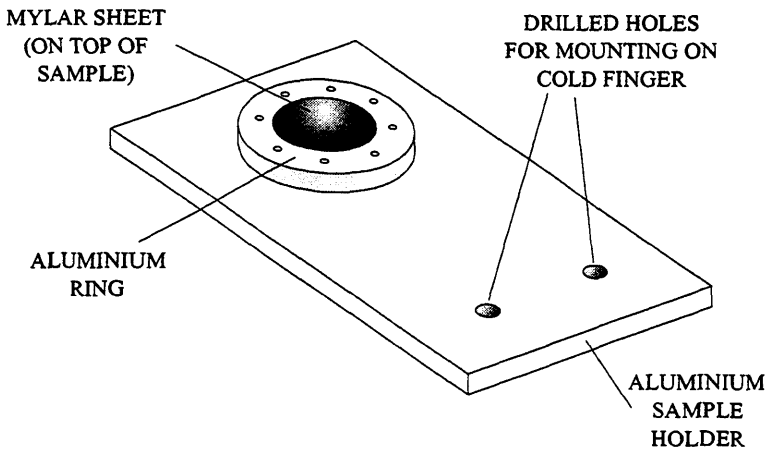

Figure 4.1: Schematic illustration of the sample holder used on the EMU beamline.

(closed cycle refrigerator) cryostat. It is imperative that the sample area exposed to this beam is maximised in order to take full advantage of the muon beam dimensions and to minimise background signals from the aluminium ring or back-plate. To avoid the latter problem and also to maximise the probability of the muons thermalising in the sample, two things are necessary; firstly the amount of material contained in the sample holder should be maximised and, secondly, the number of inter-grain pockets should be minimised. On the former point-of-note, without a large quantity of sample material, the μSR experiments would potentially produce error-burdoned results by including the muon signals of those muons which are not thermalised in the sample, but pass straight through, thermalising in the back-plate of aluminium sample holders. So as to reduce

the possibilty of such uncertainties, for samples of low quantity, titanium absorption and thermalising foils are attached in front of the holder, between the sample and the beam. These foils absorb low-energy muons, and reduce the energy of the higher energy muons, so that they will thermalise in the sample itself. To accomplish the minimisation of the inter-grain pockets, it is necessary to reduce the average grain size to a small value. This is done by crushing the preliminary sample, whether it be a wafer or lumps, with a mortar and pestle. Using such a technique, grain sizes in the range of $\approx 50\,\mu$m to $\approx 2\,$mm were obtained, with an average probably in the region of $750\,\mu$m.

One of the unfortunate consequences of the aforementioned method of sample preparation is the susceptibility of the sample material to oxidation. In their intrinsic forms, prior to crushing, such oxidation probelms would be negligible, especially since the μSR techniques are not generally used as surface probes. After crushing, the available surface-area for such oxidation processes is immense; and significantly, there is the possibility of effects from such reactions, since the muon is no longer guaranteed to have thermalised in the pure bulk material, but may thermalise on the oxidised surface within the bulk of the powder. Of interest though, is the comparison of a-Si and a-SiO, which can lead to the possible consequences of large-scale surface oxidation. Of primary concern to the experiments is the possible effect, if any, on the relative fractions of the muon states that such oxidation may have. In Chapter 5 of this thesis, the relative fractions and hyperfine parameters are shown for both c-Si and pcr-Si. Excellent fittings for pcr-Si are presented using the parameters of c-Si. As such, although oxidation should be a concern in sample preparation, it seems any contribution from SiO_2 or SiO_x is negligible. Even though many of the materials presented in this thesis may have suffered oxidation, the behaviour of the materials can be assumed to behave to akin to the pure unoxidised forms.

4.2 Electron beam evaporation of pcr-Si to produce a-Si

Many materials cannot be deposited by the simple technique of *thermal evaporation* (see Section 1.2.1), principally because their vaporisation temperatures are too high. To avoid this problem, electron beam evaporation can be used. A schematic illustration of the experimental set-up is shown in Figure 4.2. In an evacuated environment, a filament

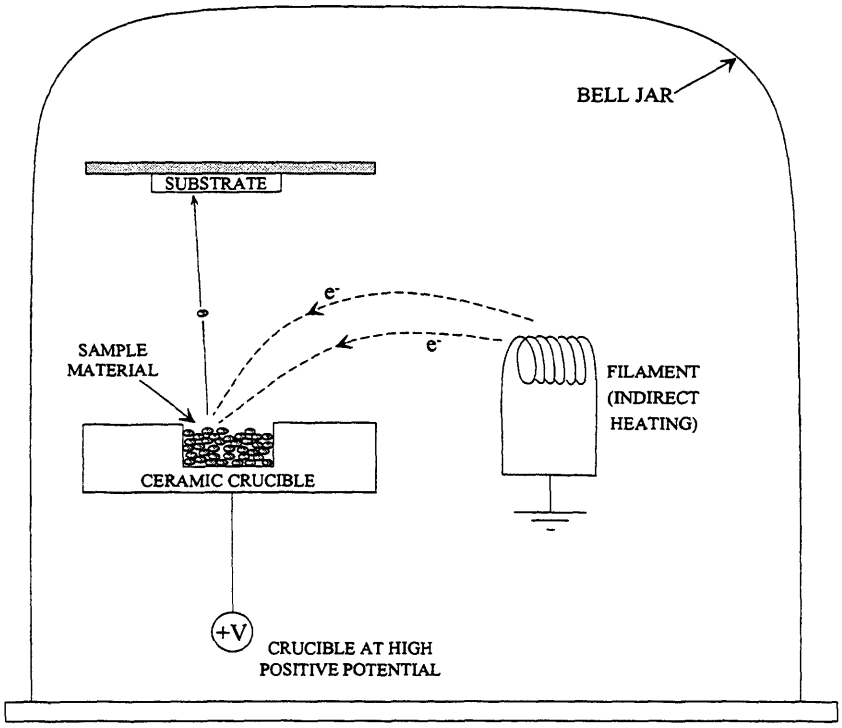

Figure 4.2: Schematic illustration of the electron beam evaporation set-up.

is heated to a high temperature, emitting electrons. These electrons are then accelerated by a very high positive potential. Travelling at great speed, the electrons are focused onto a small area of the sample material in the crucible. The electrons bombard the small area of the sample material, heating the local area to very high temperatures, allowing the sample to evaporate and condense on the substrate, as well as most of the chamber surfaces. The resulting films were scraped off the glass substrates, crushed to small flakes and then mounted in a sample holder as described in the previous section.

4.3 Sputtering techniques

As mentioned earlier in Section 1.2.1, the sputtering deposition technique is widely used for preparing amorphous materials is thin-film form. Sputtering is a physical deposition technique, relying on the collision of energetic ions with a source target to 'knock off' some of the target material, which can then collide with a substrate so as to form a deposit. A schematic illustration of a sputtering chamber plasma is illustrated in Figure 4.3. Depending on the conditions in the sputtering chamber, two differing types

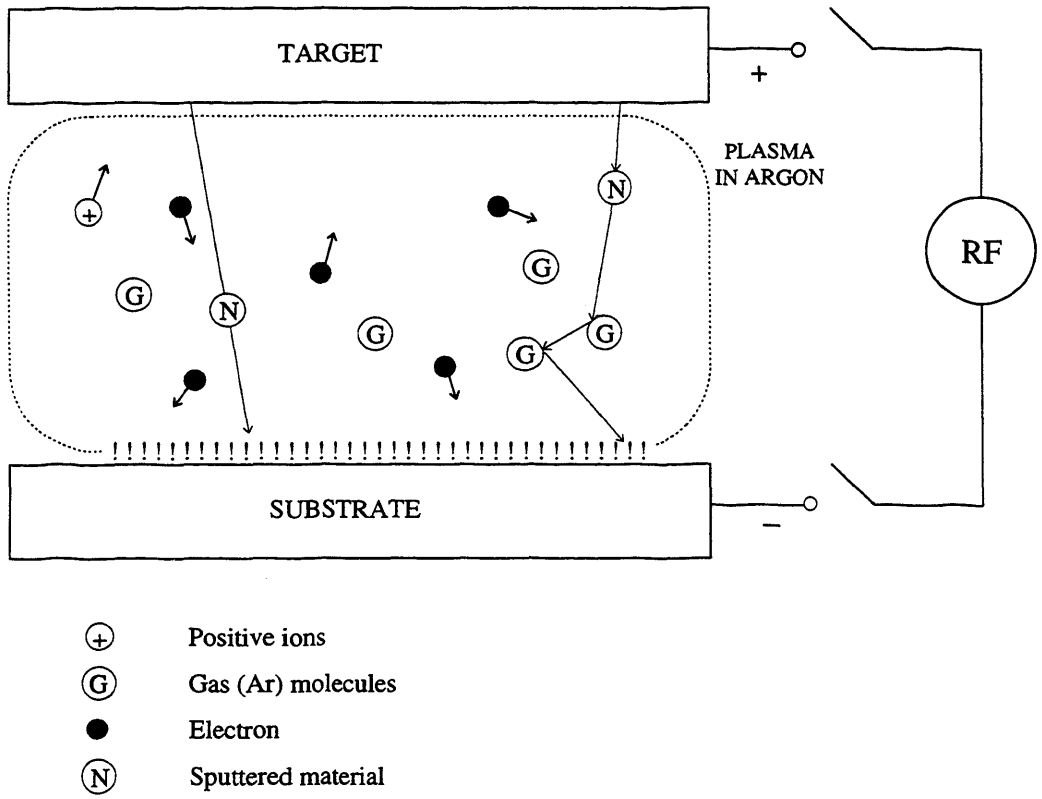

Figure 4.3: Schematic illustration of a d.c. plasma.

of technique can be applied, either *sputter etching* or *sputter deposition.* Both techniques involve the removal of material, but the difference is from which electrode the material is removed. As the name suggests, sputter etching involves the removal of material from the substrate, of primary use in the cleaning of a substrate before the deposition of any material. The substrate can be grounded or held at a finite potential; of these, the latter is generally used, since the films produced tend to be of higher quality.

There are several different techniques of sputtering: dc sputtering, self-bias dc sputtering and perhaps the most commonly used, rf sputtering. All work on the same principles, whereby a potential difference is applied between the target cathode and the substrate anode, and a plasma is struck. This produces energetic positive argon ions which collide with the negative target, ejecting target material towards the substrate. As is obvious from the names, the primary difference is the type of voltage applied between the electrodes, which subsequently has significant effects on the behaviour of the plasma, as well as the materials suitable to act as targets; e.g. insulators can only be sputtered with a rf voltage applied, but not a dc voltage.

4.3.1 D.C. sputtering

In the dc sputtering technique, there is the problem of charge build-up on the cathode, which in-turn can lead to a depletion of electrons within the plasma. To avoid this charge-loss, a 'blocking' capacitor can be introduced, which in effect stops the self-bais from 'draining' away into the rest of the circuit. Such an arrangement is shown in Figure 4.4. To understand the sputtering mechanisms, the behaviour of the electrodes

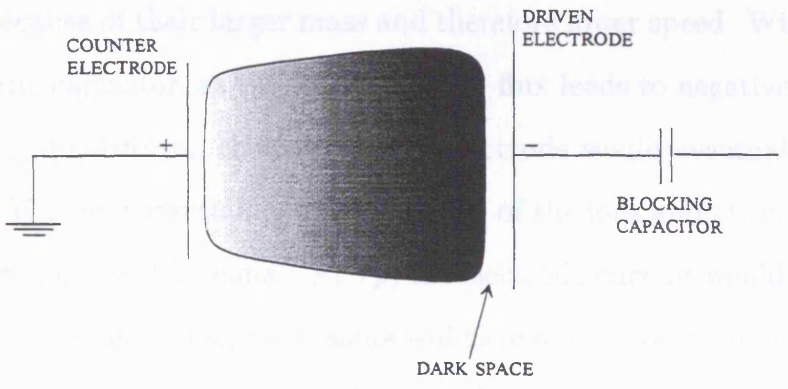

Figure 4.4: Schematic illustration blocking capacitor in the sputtering set-up.

must be understood, which can have an effect on the plasma behaviour. Since the 'anode' is grounded, and thereby always has a potential of zero, the 'cathode' connected to the blocking capacitor, can have a variable potential and is referred to as the 'driven electrode'. The expected behaviour is shown in Figure 4.5. If the driven electrode begins at a large negative potential, then electrons will be repelled from it and positive ions will

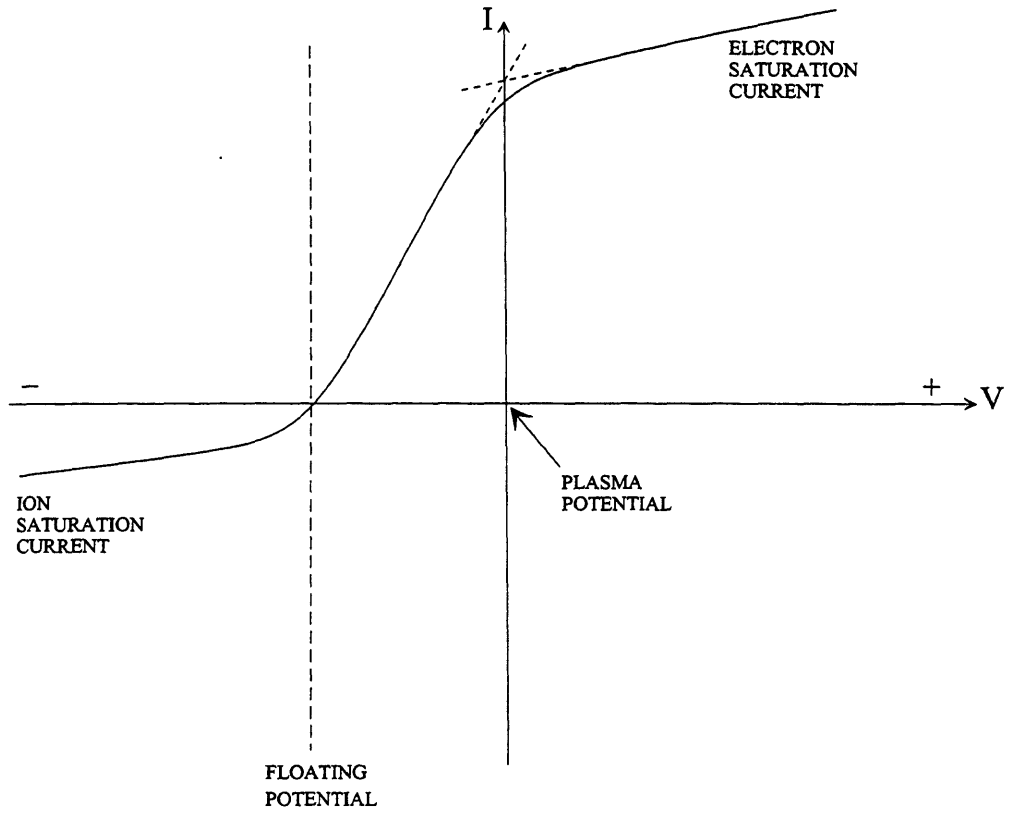

Figure 4.5: Current and potentials in d.c. sputtering.

be attracted, thereby producing a small ion current. The ion current remains small, even at saturation point, because of their larger mass and therefore lower speed. Without the inclusion of the blocking capacitor, as the larger electron flux leads to negative charging of the chamber walls and substrate, then the driven electrode would eventually rest at the *floating potential*, V_F, the potential at which the flux of the ions and of the depleted electrons, at the electrode, would be equal. At V_F, the electrode current would therefore average out to zero. At the same time, the plasma will have a net positive potential, due to the abundance of slow-moving positive ions, but the plasma current will be dominated by fast-moving electrons, inducing a larger electron current, and a potential between the floating and plasma potentials. In the outer regions of the plasma, the electron current will be less, due to fewer electrons being available. When the capacitor is introduced, the electrode can no longer 'rest' at the floating potential, but a self-bias of the electrode develops, whereby a large negative self-bias can occur. Thus, this technique is known as *self-bias dc. sputtering.* At the negative electrode, there is a larger negative potential

than the floating potential, the ions become dominant in the plasma and have a larger energy than the electrons. With this larger energy, the ions leave the plasma and collide faster with the target, thus becoming dominant in the sputtering dynamics.

4.3.2 RF Sputtering

So as to be able to sputter insulating targets, for which d.c. charging of their surface would lead to an extinguishing of the plasma, radio-frequency sputtering is used. The technique is similar to d.c. sputtering, except that the applied electric field oscillates at a radio-frequency. A capacitor must, again, be coupled in series with the target, for situations when the target (cathode) is a conductor. If the target material is an insulator, then it is first glued to the metal electrode surface, which is then connected to the rf power supply. The substrate (anode) is grounded, and therefore retains a potential of zero, but the plasma maintains a fluctuating positive plasma potential, as is shown in Figure 4.6. If an r.f. field is applied between the electrodes, electrons

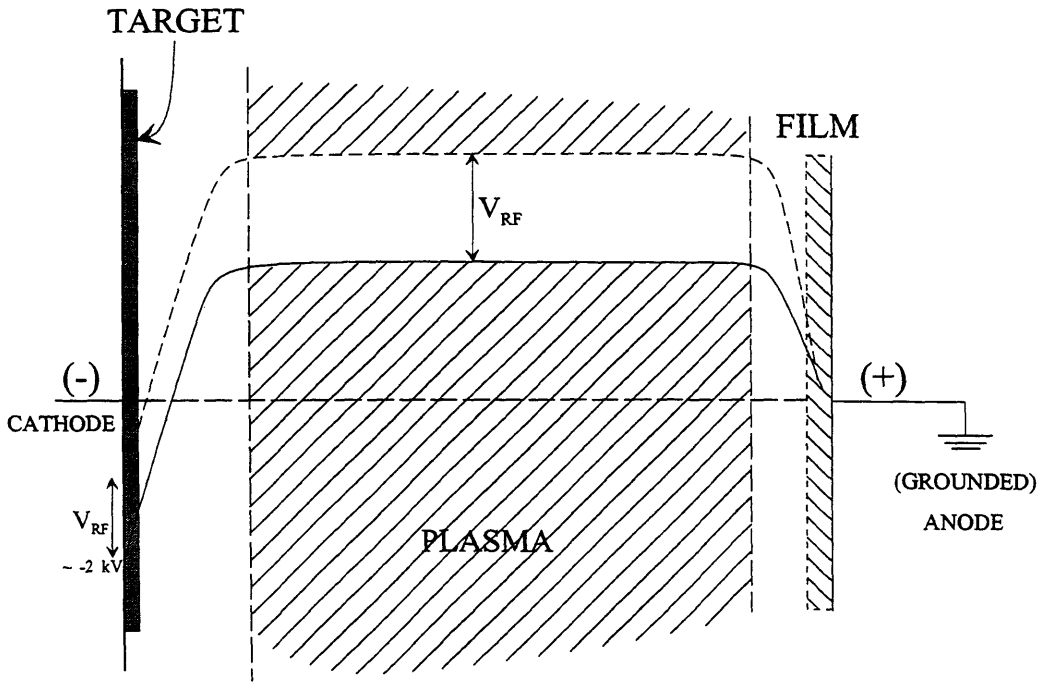

Figure 4.6: Schematic illustration of the potential distribution for RF-bias sputtering.

are accelerated towards the target during the first (positive) half-cycle, and during the second (negative) half-cycle, the ions will be accelerated towards the target. As already

discussed, the electrons are lighter and can therefore move faster, and as such, the target can develop and maintain a large negative bias, as shown in Figure 4.6. As the ions are accelerated to the target by the r.f. field, they experience a potential of about 2 kV near to the target (cathode), thereby accelerating further until they collide with the target itself. It is the heavy-ion bombardment of the target that again leads to sputtering, i.e. the knocking of atoms from the target which then travel to the substrate. Also, in the process, electrons are knocked from the target and travel to the plasma; it is this secondary electron emission which sustains the discharge. Unfortunately, even though there is a tendancy for the ions to be accelerated towards the cathode, excited ions can bombard the substrate (anode), resulting in re-emission of the target material. If the substrate is no longer grounded, and a positive bias potential is applied, the rate of target atom re-emission can be reduced, perhaps because of a lower impact energy of the ions.

Thus far, only self-bias sputtering has been discussed, but the method known as bias sputtering is also commonly used, in which a bias is applied to the substrate electode. The bias potential is intended to control the ion species types, and thereby the substrate etching rate, and also the deposition rates. In general, the intention of sputtering is 'sputter deposition', where the deposition rate is higher than the etching rate; for 'sputter etching' the case is reversed. The materials prepared in-house at Leicester were deposited using an applied r.f.-field, with an applied d.c. bias potential. The actual system will now be described.

4.4 Sputtering at Leicester

In the preparation of in-house samples, a *Nordiko NM-2000-T8-SE1* sputtering system was used. This system is composed of many separate units, controlling different tasks in the sputtering procedure, as illustrated in Figure 4.7.

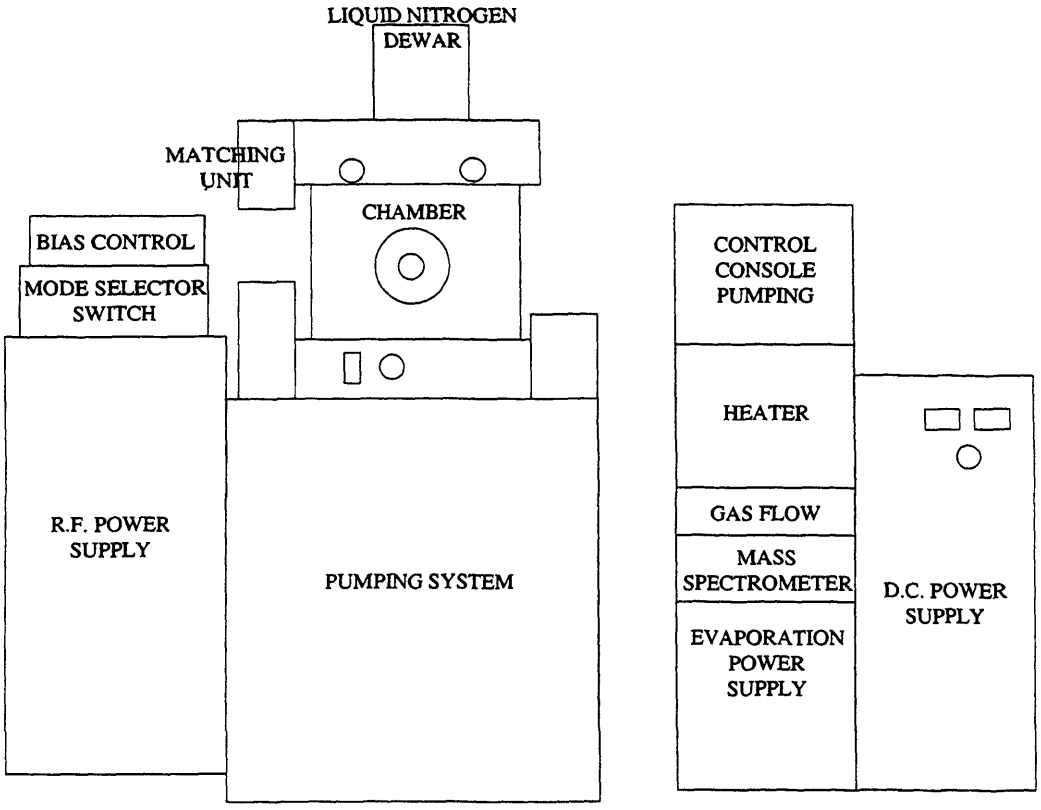

Figure 4.7: Schematic diagram of the Leicester sputtering system.

4.4.1 Sputtering Chamber

The chamber contains a substrate electrode and a rotatable multi-electrode turret, the latter consisting of a station for evaporation, an electrode for conventional sputtering, and an electrode for high-rate magnetron sputtering. A schematic of the chamber is shown in Figure 4.8. Each of these three stations is surrounded by a stainless steel earth shield, and insulated from this by 'PTFE' insulation. The electrode for conventional sputtering can accommodate 8" diameter source targets but as the targets used in this work were 4" in diameter, a stainless steel 'roof' containing a hole of this diameter was fitted over the target. The substrate electrode was 8" in diameter, with a target-substrate separation of 5 cm, although this value could be varied between 1 and 5 cm. Although the samples were deposited at room temperature, a heating element is fitted into the substrate electrode, so as to allow deposition at higher temperature. To ensure good themal contact, thin malleable copper gaskets were inserted between the substrate's copper platen, which locks into position on the electrode, and the heater. Temperatures

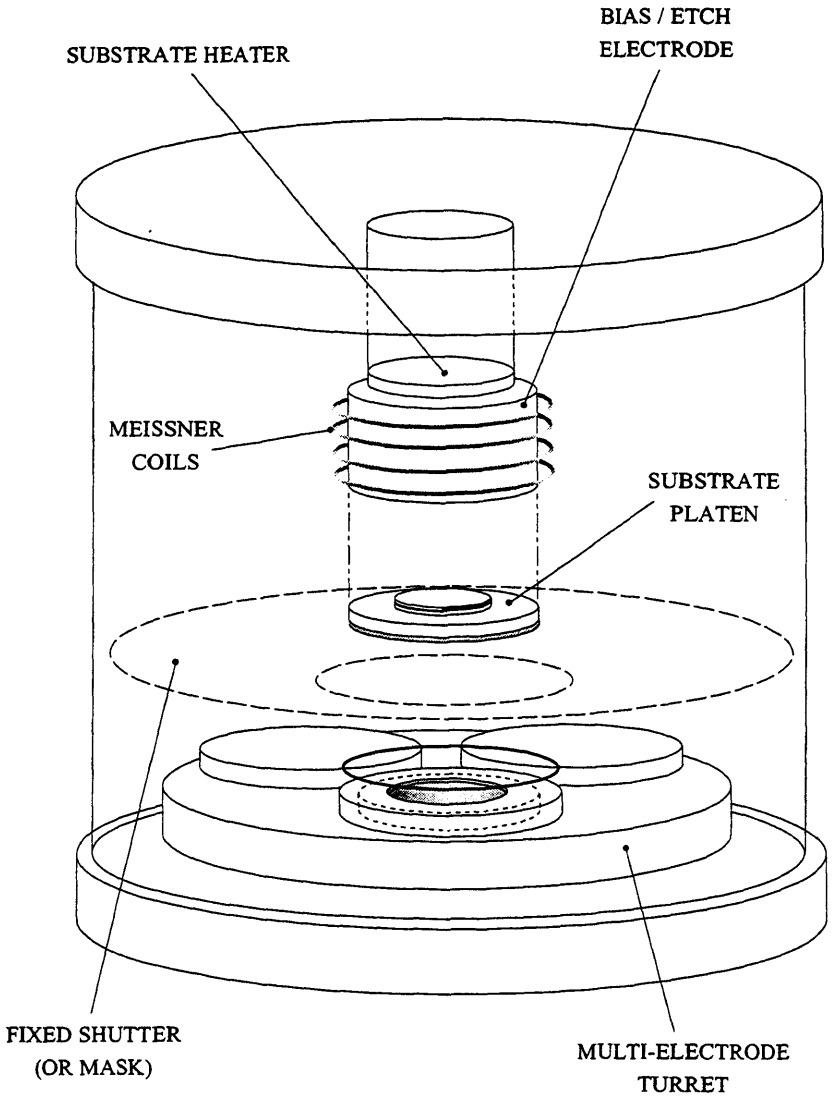

Figure 4.8: Schematic diagram of the chamber of the Leicester sputtering system.

up to 400°C are possible, controlled via a *Eurotherm* temperature controller connected to a chromel-alumel thermocouple. In order to improve the quality of films produced, a moveable shutter is fitted in front of the substrate (not shown in Figure 4.8 for reasons of clarity), so as to allow pre-sputter etching of the substrate and also pre-sputter bombardment of the target to remove surface dirt and any oxide layer. Hollow circular Meissner coils, which can be filled with liquid nitrogen, surround the space between the target and substrate, and help to improve the vacuum in the chamber.

4.4.2 Vacuum and gas-flow control systems

The pumping system consists of two main parts; a diffusion pump and a rotary pump. Chamber evacuation begins with the 'Leybold-Hereus D30A' rotary pump, used for preliminary evacuation, and to maintain the pressure at the outlet of the diffusion pump to a level below the critical value at which the diffusion pump can operate. The 'Varian VHS-250 mm' diffusion pump is a 6" oil diffusion pump, and has a liquid nitrogen trap, placed between the high-vacuum isolation valve and the diffusion pump. If the critical value of the backing pressure is breached, then oil vapour from the rotary pump can diffuse up towards the chamber. To reduce this risk, a foreline trap between the rotary pump and the diffusion pump is fitted. With both pumps working, and the Meissner coils filled, a chamber pressure of 2×10^{-7} Torr can be attained. During the sputtering process, with a continuous flow of argon and/or hydrogen gas controlled by gas flow controllers, a pressure of between 3 - 6 Torr is typical.

4.4.3 RF Power Supply

For sputtering at Leicester, r.f. sputtering is generally used in preference to d.c. sputtering. The r.f. is generated by a crystal-controlled generator, with a fixed frequency of 13.56 MHz and a maximum power of 1250 kW; its output impedance is 50 Ω, matched with the generator-electrode cable-feed. For bias sputtering (Section 4.3.2), power is supplied to both electrodes via a 'power divider'. A matching unit is available to tune the reflected and forward power. For the deposition of the samples described in this thesis, the substrate was grounded. Power was therefore only applied to the target electrode, i.e. bias-sputtering was not used.

4.4.4 Sample preparation

For the deposition of the a-Si, a-Ge and a-Ge:H films, the preparation techniques were the same. A standard 4" diameter crystalline Si or Ge target was used, glued with silver apoxy to the surface of a copper electrode plate. For the substrate, aluminium foil was wrapped around the substrate electrode. Extensive cleaning of both the aluminium foil

and the sputtering chamber was performed prior to pump down and sputtering. The foil was cleaned via the following procedure:

a) Washed with *tepol* degreasing solution.

b) Washed with acetone, and then rinsed with distilled water.

c) Washed with methanol, and again rinsed with distilled water.

The sputtering chamber was cleaned in a similar way to the substrate, with a tepol solution, rinsed, washed with methanol, rinsed with distilled water, and then allowed to dry. If deposits were present on the chamber walls and windows, these were removed with a coarse scouring pad prior to the above cleaning procedure.

The chamber was closed and pumped down overnight, with the liquid-nitrogen trap being filled every 8 hours. Shortly before deposition, on the next day, liquid nitrogen was added to the *Meissner coils*, to condense and trap water vapour still remaining in the chamber. This process reduces the chamber pressure from $\approx 6 \times 10^{-6}$ to 2×10^{-7} Torr. The r.f. power, 240 W, was supplied across the electrodes, and argon and hydrogen (for hydrogenated materials) gas admitted to the gas control units. When the desired gas flow rate was achieved, the plasma was 'struck' using an electric-power gun. If the plasma would not strike, the argon plasma gas flow rate was increased from ≈ 30 scc/min up to ≈ 100 scc/min for several seconds. To reduce the reflected power to close to zero, the matching unit was *tuned*. With the substrate shutter closed, pre-sputtering took place for about 30 minutes so as to remove impurities from the target and chamber surfaces. The shutter was then 'opened', so as to begin sputtering, and the system left to run for between 5 - 7 hours, depending on the required sample thickness. Film deposition conditions are shown in Table 4.2. After sputtering, the semiconductor deposits were still bonded to the aluminium base substrate. To remove the sample material from the aluminium foil, they were submerged in concentrated hydrochloric acid, and left for about one hour. The sample was then filtered-off from the HCl and washed thoroughly with distilled water, and then left to dry. To obtain sufficient material for μSR studies, it was necessary to repeat the whole process several times until the desire amount, normally at least 1 g, had been accumulated. Such a method of extracting the sample

Parameter	Values
RF-power	240 W
Reflected power	$\approx$ 0 W
DC-bias voltage	710 V
Substrate temperature	Room temperature
Gas flow rate	Ar $\approx$ 30 scc/min (unhydrogenated films)
	Ar $\approx$ 27 scc/min, $H_2 \approx$ 3 scc/min (hydrogenated films)
Chamber pressure	3 - 6 Torr

Table 4.2: Deposition parameters for the Leicester r.f. sputterer.

material from the substrate, presents the likelihood of introducing large quantities of surface OH molecules. Unfortunately, it is not known if such OH surface contamination will affect the relative fractions or hyperfine parameters of the a-Ge:H sample. With the development of the slow-muon facility on the DEVA beamline at the Rutherford Laboratories, the measurement of sputtered thin films a-Ge:H would be a worthwhile experiment, from which, due to the minimal oxidation of the material surface and the omission of the HCl/water extraction procedure, conclusions of any effects from possible contamination of the a-Ge:H material presented in this thesis can be made. There is the possibility of contamination taking place during the deposition procedure itself. With sufficient cleaning of the chamber and also a sputter-etching before sputter-deposition, the chamber environment should present few contaminants. Reliable and established techniques of assessing the contamination levels exist, such as chemical microanalysis e.g. mass spectrometry, and also EDAX (energy dispersive X-ray analysis), and further work could include the analysis of the materials discussed in this thesis, as well as any future deposited materials.

4.5 Diagnosis of the samples

An issue of principal importance is that a deposited material is known to either crystalline or amorphous. Both electron and X-ray diffraction offer reliable methods of assessing lattice structures. For the amorphous and glassy materials considered within this thesis, X-ray diffraction was performed, expecting to see a diffraction pattern consisting of rings (or halos), instead of sharply defined Bragg spots or rings (see Figure 1.4) characterising a crystalline lattice.

4.5.1 X-ray diffraction

The wavelength of X-rays (typically 1 Å) is comparable to the interatomic spacings in solids, and therefore a crystal behaves like a three-dimensional diffraction grating for the X-rays. Rather like measuring the separation between diffraction maxima to calculate the spacing between the lines on the grating, as is done for optical experiments, for X-ray diffraction, measuring the separation of the X-ray diffraction maxima from a crystal allows the calculation of the size of the unit cell, and by measuring the intensities of the diffracted beams we can obtain information about the arrangements of atoms within the unit cell. The diffraction of X-rays results from the interaction of X-ray photons of wavelength λ with the charge field of all the extranuclear electrons in a solid.

Consider Figure 4.9, which assumes that monocromatic X-rays are directed towards a

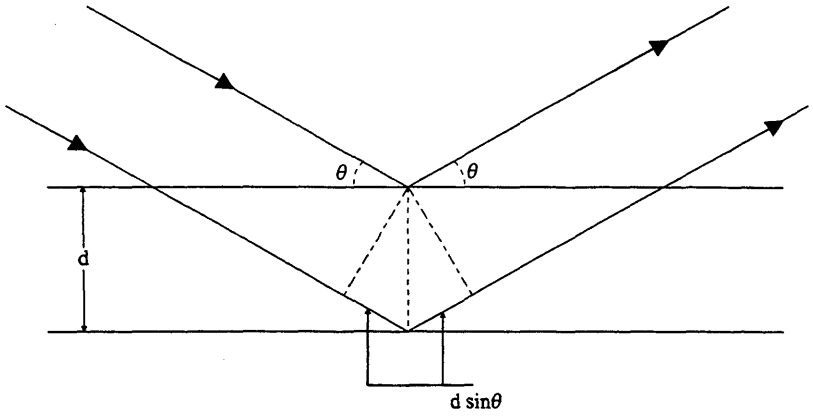

Figure 4.9: Schematic illustration of Bragg reflection. Scattering of X-rays off successive planes is in phase if the path difference $2d\sin\theta$ is an integral number of wavelengths $n\lambda$.

crystal in a parallel beam, incident to a series of parallel planes of atoms, at a glancing

angle of θ. A basic experimetal set-up is shown in Figure 4.10, where β corresponds to

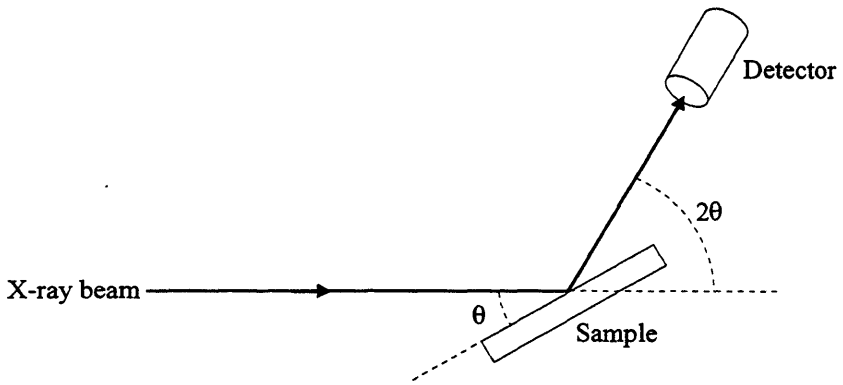

Figure 4.10: Schematic illustration experimental geometry used for X-ray diffraction experiments.

the incident angle between the sample and the X-ray beam, and is not necessarily equal to the θ of Figure 4.9. Coherent scattering from a single plane is insufficient to obtain diffraction maxima. For such maxima, successive planes must scatter in phase, which can occur only if the path difference for scattering off two adjacent planes is an integral number of wavelengths. From Figure 4.9, however, the additional path travelled can be seen to be $2d\sin\theta$, where d is the spacing of the planes. Therefore the condition for the occurrence of a maxima is :

$$2d\sin\theta = n\lambda \tag{4.1}$$

where n is an integer. This expression is known as Bragg's Law. The Bragg equation predicts only the position of the centre of the expected diffraction pattern for a given wavelength and family of Bragg planes, and does not address the intensity distribution in the diffraction pattern. For the purposes of this thesis, consideration will only be made of the diffraction pattern itself, that is to say, the position of the maxima. Since the crystalline or polycrystalline materials possess long-range order, and the parallel set of Bragg planes (of atoms) are repeated to an infinite extent, a regular well-defined diffraction pattern of spots (crystal) or fine, clear rings (polycrystalline) will result on photographic film. On the other hand, if the sample is amorphous or glassy, only short-range order persists, and therefore the Bragg planes (atoms) are not repeated throughout

the material, and therefore, no distinct precise spots or circles, only non-precise halos (wide bands of circles), will be seen on the photographic film.

4.5.2 Electron diffraction

A second method of structural analysis is electron diffraction. The diffraction of electrons from the atomic nuclei demonstrates both the periodic structure of solids and of wave-particle duality of the electron. As a charged particle, the electron interacts strongly with solids and can penetrate only a few hundred Ångstrom units into a crystal before it must suffer either an elastic or inelastic encounter. The electron is therefore suitable for the study of surface layers and thin films, but poor for the study of bulk structural arrangements. As a result of the bulk nature of the materials discussed in this thesis, electron diffraction was rejected as a method of structural diagnosis, favouring X-ray diffraction instead.

Chapter 5

Measurements and discussion - Elemental group IV semiconductors

In this, the first of three experimental data chapters, the results of repolarisation measurements on some group IV elemental semiconductors will be presented and discussed. With regard to the samples, various types of silicon and germanium have been analysed. For silicon, intrinsic, p-type, n-type and hydrogenated samples, with both polycrystalline and amorphous structures, have been studied. Investigations of germanium have been less rigorous; only three types of sample have been studied, pcr-Ge, a-Ge and a-Ge:H. Of primary interest will be the characterisation of the muonium states with reference to where the muon/muonium resides. As mentioned earlier in Chapter 3, this involves the extraction of certain parameters from both TF and LF experiments, mainly initial amplitudes and relaxation rates. Discussion of the results will include consideration of the possible dynamics occurring within the samples by the analyses of the amplitude and relaxation rate dependence on the external magnetic field, temperature and doping concentrations.

Few μSR studies have been made on disordered materials, whether 'amorphous' or glassy. As a preliminary to investigations of these, measurements are here reported on polycrystalline samples, which carry the benefit of behaving very similar to the well-studied crystalline samples but without features relating to sample orientation. While the amorphous samples also lack this orientation dependence, striking differences from

crystalline behaviour are evident. One problem with μSR experiments is that if the sample has a particularly large diamagnetic fraction, then there is only a very small paramagnetic fraction that can repolarise, and as such, little can be concluded about the material in terms of the muonium sites, and also about any possible dynamic effects such as state conversions. To avoid such problems, hydrogenated materials, in which many of the residual dangling bonds are passivated and the diamagnetic fractions thereby reduced, have been included in the investigations.

This chapter will present experimental data from TF-μSR and LF-μSR investigations, both repolarisation curves and relaxation rates, and where relevant some of the acquired RF-μSR data, also. Theoretical fittings will be presented for the LF-μSR data, yielding site fractions and hyperfine parameters. Finally, the relevance of the results will be discussed, including a comparison of the behaviour of silicon and germanium samples.

5.1 Sample preparation

For the preparation of Si and Ge samples, both sputtering and glow-discharge deposition techniques were used. An extract of Table 4.1, presenting samples relevant to this chapter, is given in Table 5.1. As mentioned in Chapter 4, it was essential to produce as much material as possible, in order to have a large area (normally $\approx$ cm^2) to expose to the muon beam and, of course, of thickness sufficient to stop the muons. Obtaining sufficient quantity of material was no problem in the case of the polycrystalline specimens, but for the amorphous samples, it was necessary to deposit for several hours or even days to produce the required amounts.

5.2 Silicon

As perhaps the most studied semiconductor, silicon seems to be a reliable starting point from which to study other materials. Crystalline silicon has been investigated by muon spectroscopy by several groups since the 1970s[1, 2, 3]. Our studies begin with pcr-Si, which does not have the orientation dependence of c-Si, but retains the rigid lattice of

Sample	Deposition type	Temperature (°C)
pcr-Si	Crushed c-Si wafer	—
p−type pcr-Si (x 10^{17}cm^{-3})	Crushed p-type c-Si wafer	—
a-Si	Electron-beam evaporation	290
a-Si:H	Glow-discharge	290
p-type a-Si:H	Boron-doped glow-discharge	290
n-type a-Si:H	Phosphorus-doped glow-discharge	290
pcr-Ge	Crushed pcr-Ge lumps	—
a-Ge	Sputtered	290
a-Ge:H	Sputtered	290

Table 5.1: Growth conditions for silicon and germanium samples.

bond lengths and angles, and also the periodicity of the interstitial tetrahedral 'cage' sites. We then move on to doped pcr-Si and finally the amorphous samples.

Two types of measurement are reported: TF-μSR to yield the diamagnetic fractions and LF-μSR to produce repolarisation curves. For both, the relaxation rates of the signals are also important measurements to make and these will be reported.

5.2.1 Experimental TF-μSR results

By measuring the temperature dependence of the muon polarisation with a magnetic field applied transverse to the beam polarisation, the diamagnetic fraction of the sample can be found, i.e. the proportion of muons which reside in diamagnetic sites. The procedure, which relies on comparison with silver for which the diamagnetic fraction is unity, has been described in Section 3.3.1.

Diamagnetic fraction

The temperature dependence of the diamagnetic fraction f_d for the various types of silicon studied are shown in Figure 5.1. It is instructive to compare these fractions and

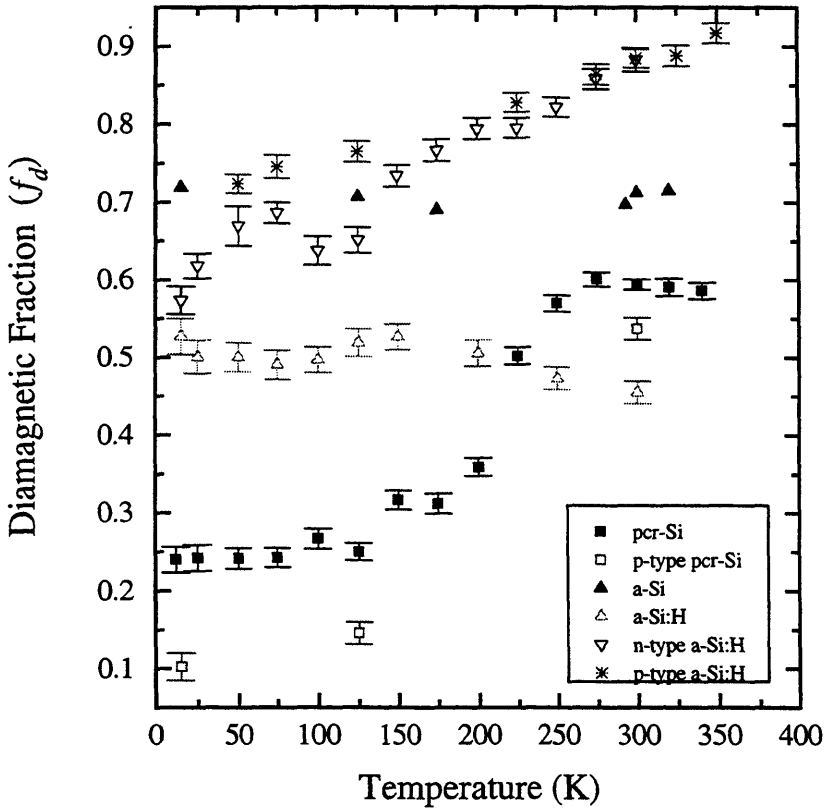

Figure 5.1: Diamagnetic fraction of all the silicon materials, measured in an evacuated sample environment.

their temperature dependence.

From Figure 5.1, it can be seen that at low temperatures the pcr-Si samples have the lowest diamagnetic fractions, with $p-$type pcr-Si starting, at low temperatures, at about 10 % and pcr-Si at about 24 %. The f_d of both materials is temperature dependent, increasing with temperature, with a rapid increase in f_d occurring above about 150 K, indicating the conversion of paramagnetic states to diamagnetic states. The Czochralski growth technique tends to produce high-quality low-defect wafers; as such few defects are expected in the pcr-Si and $p-$type pcr-Si samples, except those found along grain-boundaries or at surfaces, introduced by the crushing of the silicon wafers. In addition, defects might be expected as a result of doping, but since the $p-$type pcr-Si has a

diamagnetic fraction below that of pcr-Si, dopant-induced defects seem unlikely.

In contrast, the a-Si sample has a significantly larger f_d than either of the polycrystalline materials, being about 70 %. This is as expected since materials deposited using electron-beam evaporation tend to contain a large number of defects, especially dangling bonds, at which the muon can reside leading to an increase in f_d. For the a-Si:H sample, hydrogen has been incorporated into the lattice, thereby passivating a large number of dangling bonds; as such, there are fewer such sites for the muon to become attached to, and a reduction in f_d to about 50 % occurs. For both the a-Si and the hydrogenated a-Si:H samples, f_d is essentially independent of temperature. This is in marked contrast to the clear temperature dependence of f_d for the polycrystalline samples for $T > 150$ K.

Both of the highly doped a-Si:H samples, with doping levels of 10^{-2}, exhibit a value of f_d greater than for intrinsic a-Si:H, and at the lowest temperatures approximately equal to the f_d of a-Si; for $p-$type a-Si:H, $f_d \approx 70$ % and for $n-$type a-Si:H, $f_d \approx 60$ %. As for intrinsic a-Si:H, the incorporated hydrogen will have passivated many of the dangling bonds in the material, but by the addition of phosphorus ($n-$type a-Si:H) and boron ($p-$type a-Si:H) to the lattice network, dopant-induced defects can occur. This leads to an increase in the number of dangling bonds and an increase in the f_d over the intrinsic a-Si:H sample, thereby virtually negating any f_d reduction as a result of the passivation of any dangling bonds. In contrast to both intrinsic a-Si and a-Si:H samples, the diamagnetic fractions of the $n-$type and $p-$type doped a-Si:H samples exhibit a temperature dependence, and the curves for both $n-$type and $p-$type a-Si:H virtually overlap. From this point of view, the doped a-Si:H samples appear to behave more akin to the polycrystalline samples than to the unhydrogenated amorphous samples. Their diamagnetic fractions are approximately constant up to about 150 K, at which point f_d begins to increase, though not as rapidly as for the polycrystalline samples.

Relaxation rates

As well as measuring the initial asymmetry from the raw data curves, it is beneficial to measure and analyse the relaxation rates of the asymmetry, potentially yielding infor-

mation on the site dynamics. The relaxation rates of the TF-μSR polarisation known as $1/T_2$ or λ_2 curves, where $1/T_2 = \lambda_2$, as a function of temperature and reciprocal temperature, are shown in Figure 5.2.

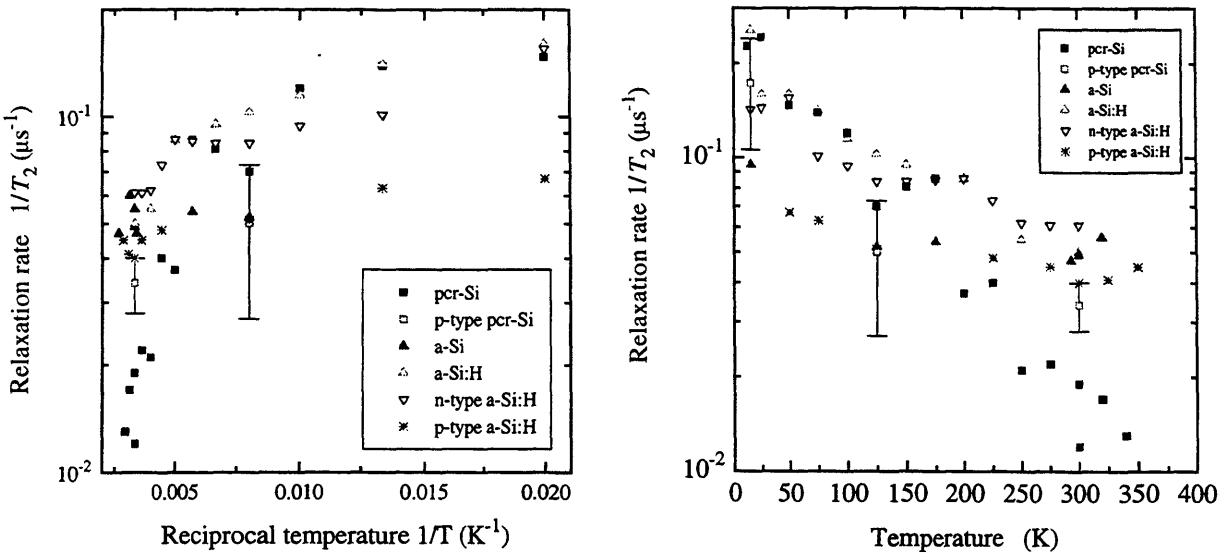

Figure 5.2: The dependence of $1/T_2$ on reciprocal temperature (*left*), and temperature (*right*), for all the silicon materials.

From Figure 5.2, it can be seen that at low temperatures pcr-Si has a relaxation rate of about $1/T_2 = 0.25\,\mu s^{-1}$, which is larger than all the other silicon samples except intrinsic a-Si:H. On the logarithmic scale of the $1/T_2$ axis, the relaxation rate approximates to a straight line as the temperature is increased, thereby indicating that $1/T_2$ decreases exponentially with temperature. On the other hand, for the $p-$type pcr-Si, which at low temperatures is $\approx 0.175\,\mu s^{-1}$, of a similar order to that of pcr-Si, the relaxation rate does not at first sight appear to decrease exponentially, although a significant temperature dependence does occur. However, if the uncertainty in the data is considered, then an exponentially decaying temperature dependence of the relaxation rate is certainly plausible. At this point it should be pointed out that the UDA fitting program, used at the Rutherford Laboratories for the analysis of the raw data, has problems in fitting relaxation rates below about $0.1\,\mu s^{-1}$, where rates of between 0 and $0.1\,\mu s^{-1}$ generate fits of comparable validity, i.e. equivalent χ^2 values.

The behaviour of the a-Si sample is once again different to that of the polycrystalline

samples. Its low-temperature relaxation rate is only $0.095\,\mu s^{-1}$, although, because of the large uncertainties incurred for $\lambda_2 < 0.1\,\mu s^{-1}$, this value is more likely to be comparable with the values for higher temperatures, where $\lambda_2 \approx 0.05\,\mu s^{-1}$. As such, it is possible that the $1/T_2$ behaviour is flat, and therefore, as for the diamagnetic fraction, there might be little temperature dependence of the relaxation rate. The a-Si:H relaxation rate behaves almost exactly the same of that of the pcr-Si sample. At low temperature, its relaxation rate is $\lambda_2 = 0.255\,\mu s^{-1}$, and this exponentially decreases with an increase in temperature. So, although the f_d of a-Si:H behaves similar to that of a-Si, its relaxation rate behaves much more like that of the polycrystalline silicon samples.

For the doped samples, the situation again differs from that of their diamagnetic fractions. The $n-$type a-Si:H has a low-temperature relaxation rate of about $\lambda_2 = 0.14\,\mu s^{-1}$ and subsequently experiences a slow exponential decay with increase in temperature. In contrast, the $p-$type a-Si:H exhibits quite different behaviour. As with the a-Si sample, even at low temperatures, the relaxation rate is negligible, $\lambda_2 \approx 0.07\,\mu s^{-1}$, and can be seen to be almost independent of temperature.

5.2.2 Experimental LF-μSR results

Repolarisation curves and theoretical fittings

As mentioned earlier in this thesis, crystalline silicon is perhaps the most widely studied of all the semiconductors. From this breadth of research, many of the various parameters of the muonium states, such as relative fractions and hyperfine parameters, are already known. As such, crystalline silicon is the ideal starting point for research into other materials.

LF-μSR experiments on the undoped pcr-Si, were performed at different temperatures and magnetic fields. The repolarisation curves obtained from such experiments are shown in Figure 5.3. Also in the figure are curves showing the theoretical fittings to the experimental data. The parameters used to generate these fits are given in Table 5.2.

So as to allow a comparison between the pcr-Si and the c-Si samples, the known parameters for the crystalline material are also presented. As can be seen, the majority of

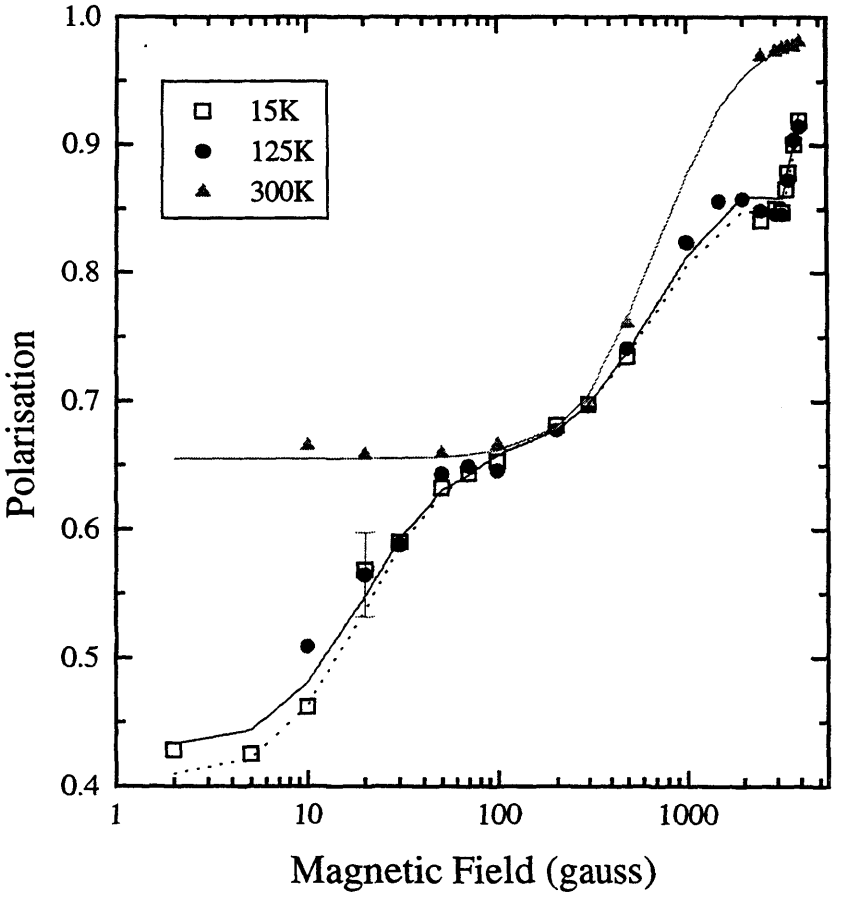

Figure 5.3: The field dependence of the polarisation for pcr-Si.

Sample	T (K)	Dia.	Isotropic		Anisotropic		
		f_d (%)	f_{Mu_T} (%)	A (MHz)	$f_{Mu_{BC}}$ (%)	A_{iso} (MHz)	D (MHz)
c-Si	0[a]	7.5	61	2006	36.8	67.33	50.5
pcr-Si	15	9	50	2000	41	67.33	50.5
pcr-Si	125	11	52	2000	37	67.33	50.5
pcr-Si	300	32	67	2000	0	—	—

Table 5.2: The relative fractions and hyperfine parameters for c-Si (from [4]), and the fitting parameters and fractions for the experimental data on pcr-Si.

[a]The hyperfine parameters refer to extrapolations to 0 K.

the fitting parameters for pcr-Si bear near agreement with those of c-Si. The anisotropic hyperfine parameters were chosen to agree exactly with those of c-Si, and the isotropic component, A, is reduced by an insignificant amount. Although the relative fractions vary with temperature, the hyperfine parameters appear to be independent of the temperature. At the two lower temperatures, there is very little difference in the relative fractions. At temperatures $> 150K$, as well as an increasing f_d, there is a total loss of bond-centre sites (Mu_{BC}), and an increase in the number of tetrahedral sites (Mu_T). The agreement between the theoretical and experimental curves is excellent, even to the extent of reproduction of the high-field cusp at 3400 gauss

The repolarisation curves for p-type pcr-Si are shown in Figure 5.4, along with the theoretical fittings. The fitting parameters used to generate these curves are shown in Table 5.3, from which the parameters of $p-$type pcr-Si are seen to bear a close relation to those of both c-Si and pcr-Si. There is no change in the value of hyperfine parameters from those for the pcr-Si sample and only a very small variation of the relative fractions between the two samples. At low temperature, the Mu_T and Mu_{BC} states exist in almost equal concentrations, but again, at high temperatures some of the paramagnetic states have converted to diamagnetic, and a predominance of the Mu_T state occurs once more, with a total loss of Mu_{BC} states. Even using the approximate fitting procedures, no dopant-induced increase in the diamagnetic fractions occurs, and thus it seems unlikely that any of the samples suffer from the presence of dopant-induced defects.

Moving away from the well studied crystalline matrix of the silicon samples, samples composed of the less understood amorphous network were investigated. The results of LF-μSR experiments on amorphous silicon, a-Si, are shown in Figure 5.5. As with the earlier samples, theoretically generated curves are imposed on the figure and the fitting parameters used to generate these curves are shown in Table 5.4. The parameters differ from those of the crystalline and polycrystalline silicon materials. There is a much larger diamagnetic fraction and, as a corollary, a smaller paramagnetic fraction. In addition, the behaviour with temperature varies significantly from that of the earlier mentioned materials. For the a-Si sample, at low temperatures, the anisotropic Mu_{BC}

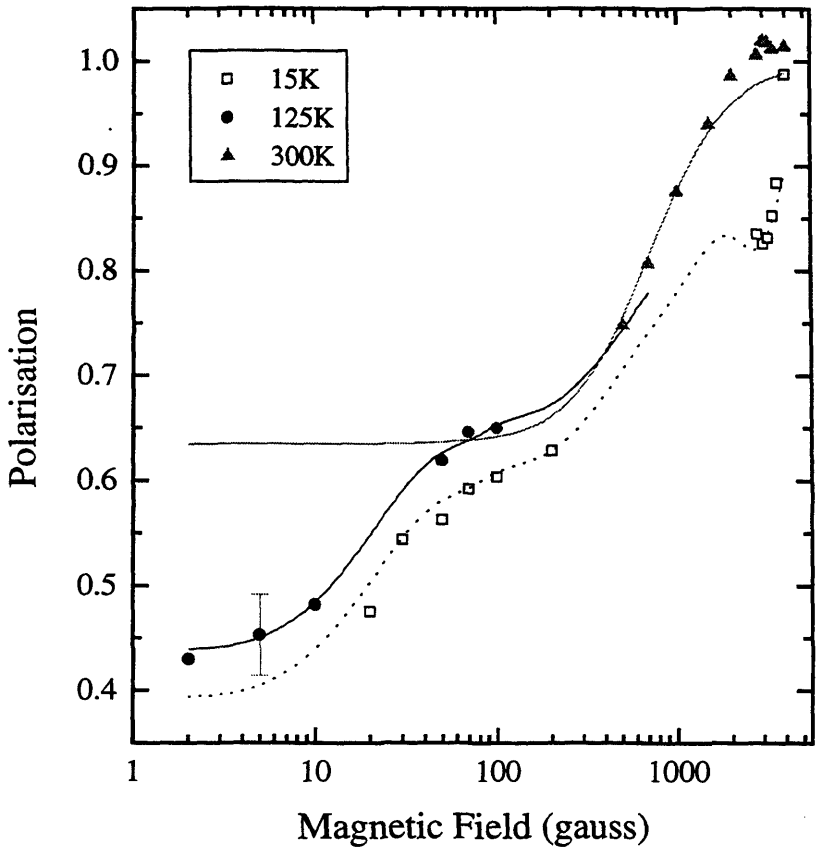

Figure 5.4: The field dependence of the polarisation for p−type pcr-Si. *(It should be noted that in the low-field region at 300 K, where there are no data points, the theoretical fitting is shown so that a comparison can be made with the fittings of the pcr-Si.)*

Sample	T (K)	Dia.	Isotropic		Anisotropic		
		f_d (%)	f_{Mu_T} (%)	A (MHz)	$f_{Mu_{BC}}$ (%)	A_{iso} (MHz)	D (MHz)
c-Si	0[a]	7.5	61	2006	36.8	67.33	50.5
p-type pcr-Si	15	5	57	2000	35	67.33	50.5
p-type pcr-Si	125	11	54	2000	35	67.33	50.5
p-type pcr-Si	300	27 (3)	73 (4)	2000 (200)	0 (4)	—	—

Table 5.3: The relative fractions and hyperfine parameters for c-Si (from [4]), and the fitting parameters and fractions for the experimental data on p-type pcr-Si. It should be noted that the numbers in brackets, for the 300 K data, represent the uncertainty in the fitting, arising as a consequence of the shortage of low-field data.

[a]The hyperfine parameters refer to extrapolations to 0 K.

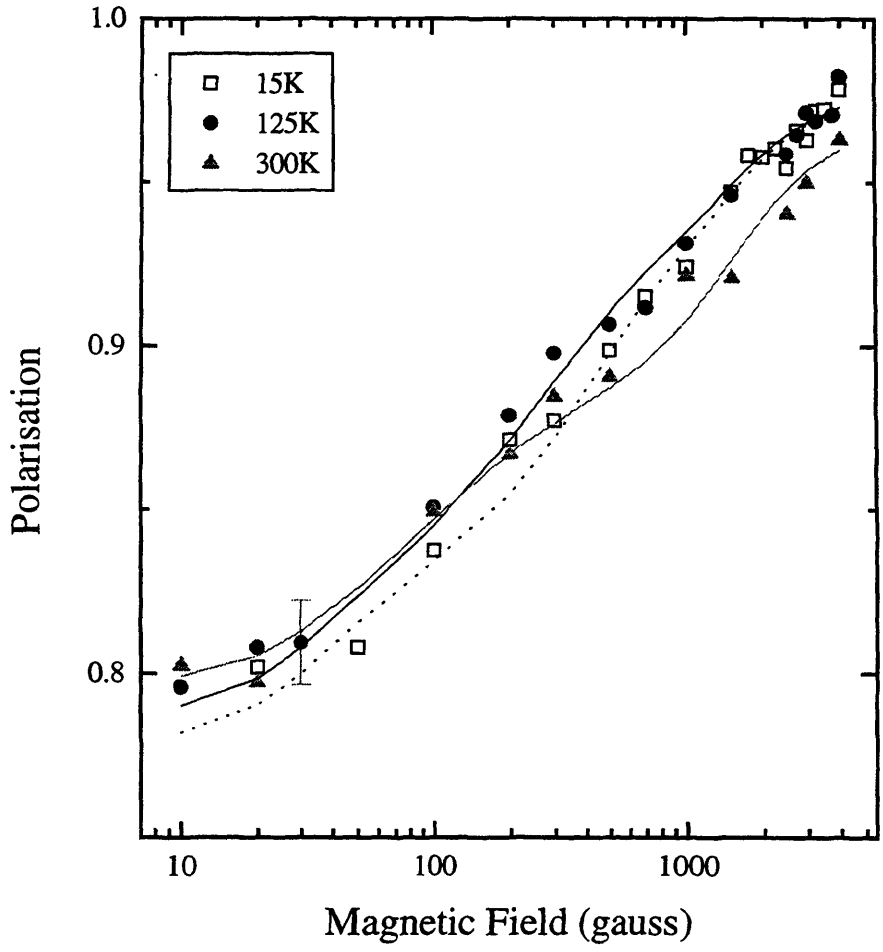

Figure 5.5: The field dependence of the polarisation for a-Si.

Sample	T (K)	Dia.	Isotropic		Anisotropic		
		f_d (%)	f_{Mu_T} (%)	A (MHz)	$f_{Mu_{BC}}$ (%)	A_{iso} (MHz)	D (MHz)
c-Si	0[a]	7.5	61	2006	36.8	67.33	50.5
a-Si	15	69	12	4000	17	1000	110
a-Si	125	70	12	4000	16	700	110
a-Si	300	68.5	19	4000	10	350	110

Table 5.4: The relative fractions and hyperfine parameters for c-Si (from [4]), and the fitting parameters and fractions for the experimental data on a-Si.

[a]The hyperfine parameters refer to extrapolations to 0 K.

centre dominates over the isotropic Mu_T centre; as room temperature is reached, this dominance is reversed with a larger Mu_T fraction. As expected from Figure 5.1, the diamagnetic fraction remains independent of temperature. The hyperfine parameter A of the Mu_T site is independent of temperature, remaining at 4000 MHz, very near to the vacuum-state value of 4463 MHz, and thereby indicating a very large electron density on the Mu_T site. The Mu_{BC} site, though, appears to possess a large amount of anisotropy, with a value of $D = 110$ MHz, and an extremely high value of A_{iso} (when compared to c-Si) of 1000 MHz. The A_{iso} value reduces with an increase in temperature, indicating that the electron density over the μs lifetime of the site decreases with increase in temperature. The degree of anisotropy of the Mu_{BC} site remains constant with temperature at $D =$ 110 MHz, a value twice as large as that for c-Si and pcr-Si.

The results for the a-Si:H sample vary from those of the a-Si, most noticeably in the relative fractions of the occupied sites. The repolarisation curves of a-Si:H are shown in Figure 5.6 and the parameters used to generate the theoretical curves are shown in Table 5.5.

From the fitting parameters, it can be seen that there exists a predominance of paramagnetic sites, with a fractionally larger percentage of Mu_{BC} sites (35%) to Mu_T sites (25%). The fractions of the different sites remain approximately constant with temperature, with the ratio of relative fractions remaining approximately equal. The hyperfine parameters resemble those of a-Si at low temperature, although they are independent of temperature. With a near-vacuum state A value of 4000 MHz, there is a large electron density on the muon site. For the anisotropic sites $A_{iso} = 1000$ MHz. There is a high degree of anistropy of the hyperfine interaction for the anisotropic centre as evidenced by the value of D which at 110 MHz is relatively large.

The first of the doped amorphous samples to be considered is the $n-$type a-Si:H. The repolarisation data and the theoretical curves are shown in Figure 5.7. For the theoretical curves in the figure, the fitting parameters are shown in Table 5.6. In contrast to a-Si:H, the $n-$type a-Si:H exhibits a greater temperature dependence of the relative fractions. At low temperature, there are approximately equal fractions of diamagnetic

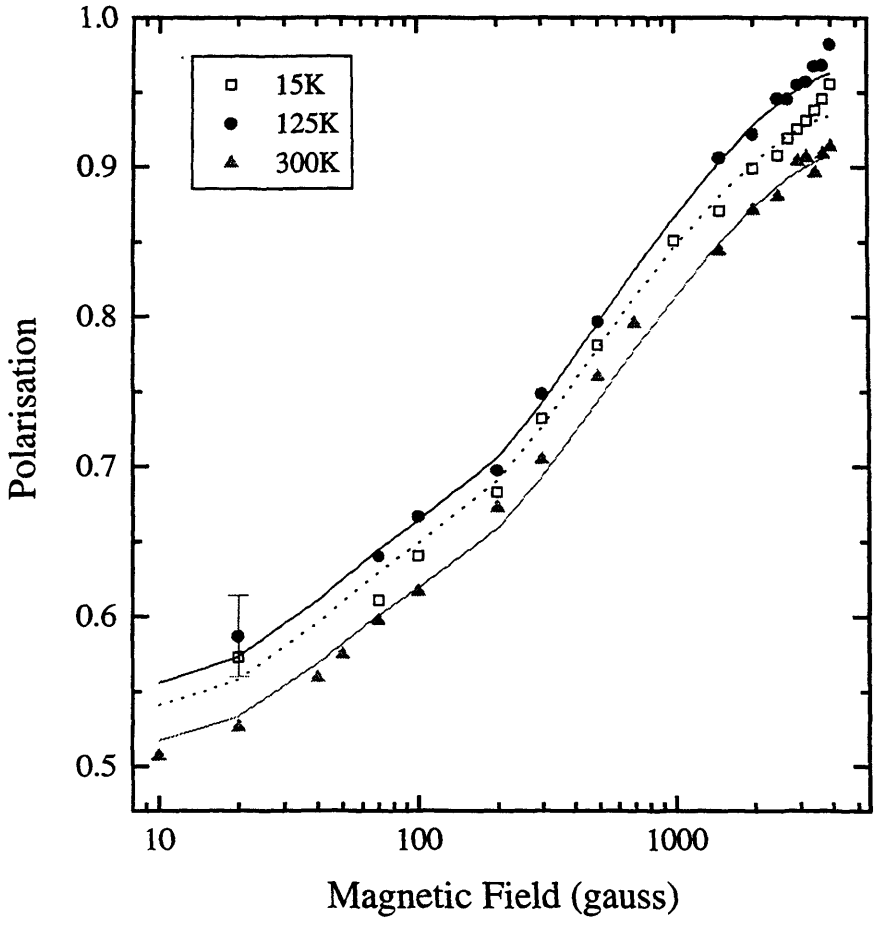

Figure 5.6: The field dependence of the polarisation for a-Si:H.

Sample	T (K)	Dia.	Isotropic		Anisotropic		
		f_d (%)	f_{Mu_T} (%)	A (MHz)	$f_{Mu_{BC}}$ (%)	A_{iso} (MHz)	D (MHz)
c-Si	0[a]	7.5	61	2006	36.8	67.33	50.5
a-Si:H	15	35	25	4000	35	1000	110
a-Si:H	125	35	28	4000	35	1000	110
a-Si:H	300	31.5	28	4000	33	1000	110

Table 5.5: The relative fractions and hyperfine parameters for c-Si (from [4]), and the fitting parameters and fractions for the experimental data on a-Si:H.

[a]The hyperfine parameters refer to extrapolations to 0 K.

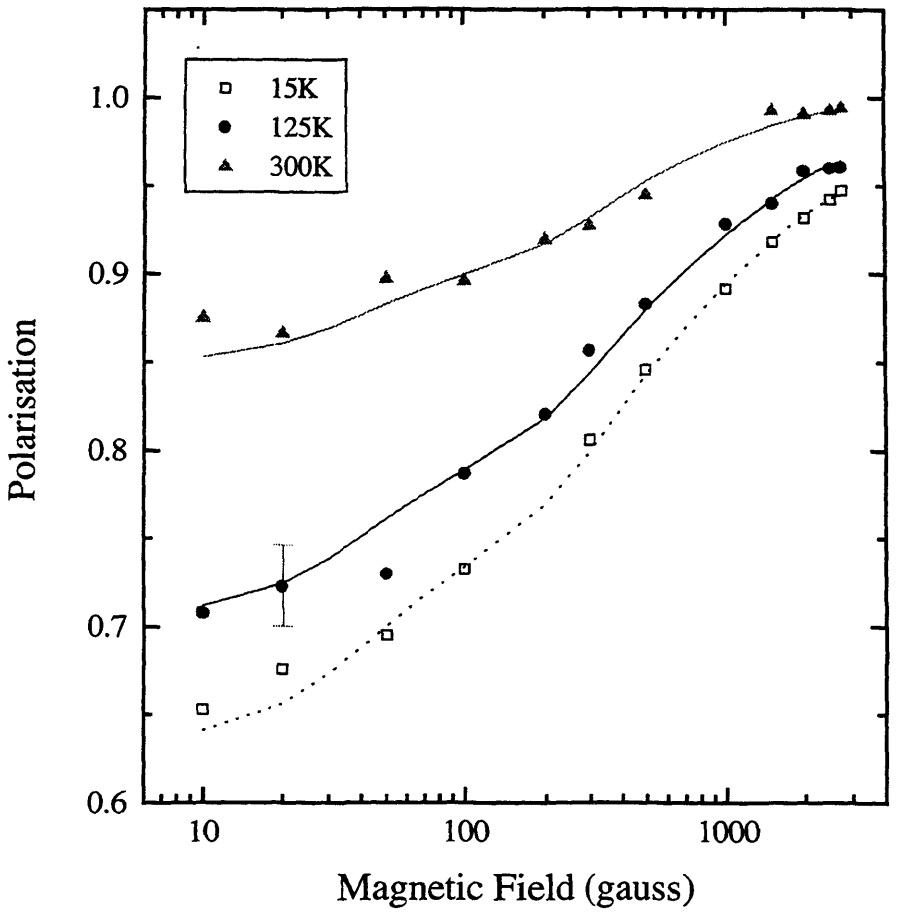

Figure 5.7: The field dependence of the polarisation for $n-$type a-Si:H.

Sample	T (K)	Dia.	Isotropic		Anisotropic		
		f_d (%)	f_{Mu_T} (%)	A (MHz)	$f_{Mu_{BC}}$ (%)	A_{iso} (MHz)	D (MHz)
c-Si	0[a]	7.5	61	2006	36.8	67.33	50.5
n-type a-Si:H	15	50.5	16	4000	30	1000	110
n-type a-Si:H	125	60	13	4000	25	1000	110
n-type a-Si:H	300	80	5	4000	15	1000	110

Table 5.6: The relative fractions and hyperfine parameters for c-Si (from [4]), and the fitting parameters and fractions for the experimental data on n-type a-Si:H.

[a]The hyperfine parameters refer to extrapolations to 0 K.

and paramagnetic sites. As the temperature is increased, the percentage of diamagnetic fraction increases, thereby reducing the paramagnetic fraction. At all temperatures there is a predominance of Mu_{BC} site over Mu_T sites. However, at room temperature, the fraction of Mu_T sites is negligibly small at 5%, whereas the fraction of Mu_{BC} sites remains significant at 15%. The hyperfine parameters mirror those of the a-Si:H sample, exactly. With a near-vacuum state A value of 4000 MHz and anisotropic parameters of $A_{iso} = 1000$ MHz and $D = 110$ MHz, the tetrahedral cage-centre site retains a very large electron density on the muon site, although for the bond-centre site the isotropic component of the hyperfine interaction is low, and there is a large degree of anisotropy.

Unfortunately, the p-type doped amorphous a-Si:H is severely compromised by a lack of data, as can be seen in Figure 5.8. Theoretical fittings have been made to the data, but few conclusions can safely be made. Nonetheless, the fitting parameters are shown in Table 5.7. Unlike the $n-$type a-Si:H, the diamagnetic fraction dominates at all temperatures. Unlike for a-Si:H, the paramagnetic fractions are dependent upon temperature. At low temperatures, the Mu_{BC} and Mu_T sites exist in equal fractions; but, as the temperature is increased, the Mu_{BC} site is the more predominant of the paramagnetic sites, until at room temperature, there are no longer any Mu_T sites, only Mu_{BC}. The hyperfine parameters remain equal to those of undoped a-Si:H, where there exists the near-vacuum state A value of 4000 MHz and parameters for the anisotropic centre of $A_{iso} = 1000$ MHz and $D = 110$ MHz.

Relaxation rates

Another tool for interpretation available from the μSR data is the variation of decay rates of the asymmetry data with field and temperature. For an LF-μSR experiment, the relaxation rate is often referred to as λ_1 or $1/T_1$; this is in contrast to the symbol for TF-μSR, λ_2 or $1/T_2$. The experimental relaxation rates of all the aforementioned silicon samples are shown as a function of field for different temperatures in Figures 5.9 (15 K), 5.10 (125 K), and 5.11 (300 K). From Figure 5.9, it can be seen that, at low fields, there is a large variation of magnitude and field dependence of the relaxation rates with the

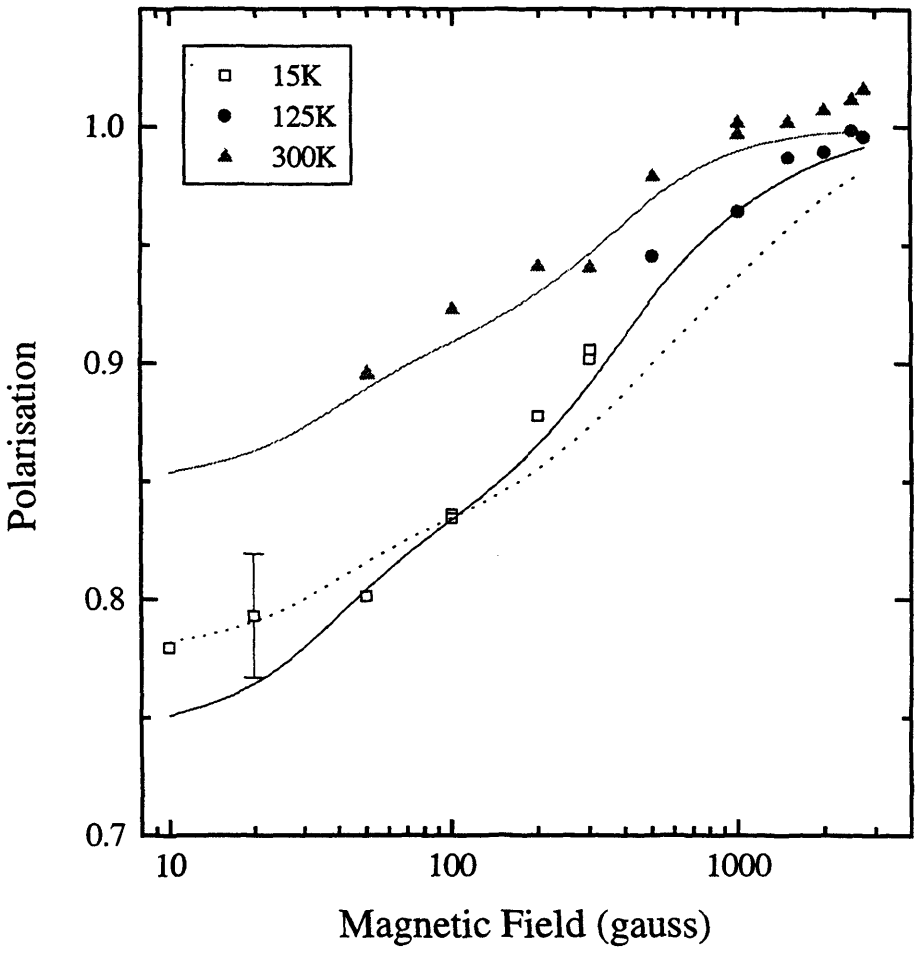

Figure 5.8: The field dependence of the polarisation for p—type a-Si:H.

Sample	T (K)	Dia.	Isotropic		Anisotropic		
		f_d (%)	f_{Mu_T} (%)	A (MHz)	$f_{Mu_{BC}}$ (%)	A_{iso} (MHz)	D (MHz)
c-Si	0[a]	7.5	61	2006	36.8	67.33	50.5
p-type a-Si:H	15	67	16	4000	17	1000	110
p-type a-Si:H	125	67	6	4000	27	1000	110
p-type a-Si:H	300	82	0	—	18	1000	110

Table 5.7: The relative fractions and hyperfine parameters for c-Si (from [4]), and the fitting parameters and fractions for the experimental data on p-type a-Si:H.

[a]The hyperfine parameters refer to extrapolations to 0 K.

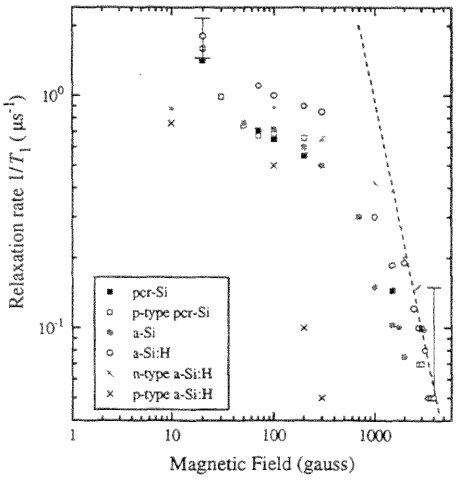

Figure 5.9: The field dependence of the $1/T_1$ for all silicon samples at 15K. The dashed line (- - -) represents a B^{-2} dependence.

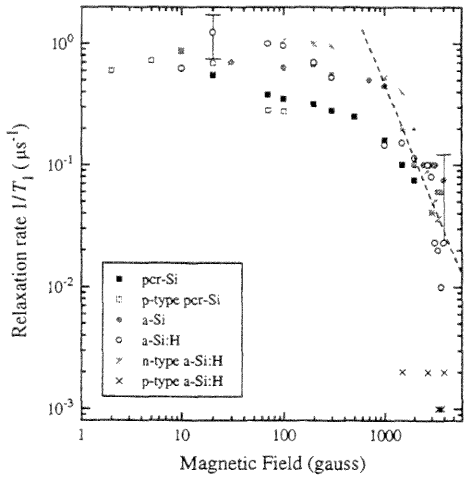

Figure 5.10: The field dependence of the $1/T_1$ for all silicon samples at 125K. The dashed line (- - -) represents a B^{-2} dependence.

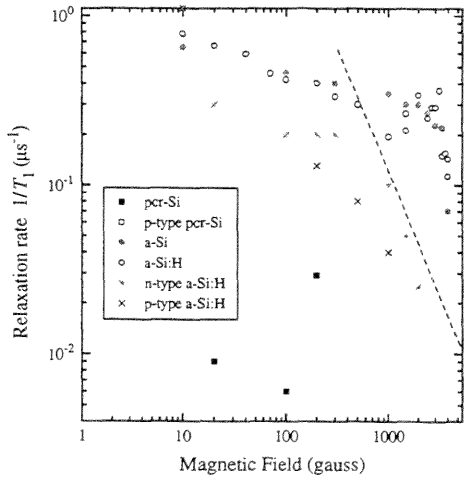

Figure 5.11: The field dependence of the $1/T_1$ for all silicon samples at 300K. The dashed line (- - -) represents a B^{-2} dependence.

sample type. At this low temperature of 15K, in the low-field regime the relaxation rates of the polycrystalline, a-Si:H and $n-$type a-Si:H samples are noticeably greater than for the other silicon samples. As the field is increased, these four samples suffer rapid losses in their relaxation rates such that, the two polycrystalline samples quickly begin to overlap with most of the other silicon samples, although a-Si:H maintains a $1/T_1$ larger than the others until very high fields, $B > 1\,\mathrm{kG}$, are attained. In contrast, the $p-$type a-Si:H loses any relaxation at a low field of $\approx 200\,\mathrm{gauss}$, in comparison to the other materials which lose relaxation at about 2000 gauss.

With a small increase in temperature to 125K, a change in the behaviour of the $1/T_1$ curves can be seen, as shown in Figure 5.10. At this higher temperature only the relaxation rate of the a-Si:H and $n-$type a-Si:H samples remains noticeably larger than the other samples. Both of the polycrystalline samples, again behave similar to each other, and not too disimilar to the other silicon samples. A rapid loss of low-field relaxation rate does not seem to occur for any sample. By 1000 gauss, the $1/T_1$ curve for each material begins to overlap; and in the high-field regime, the curves exhibit a B^{-2} dependence, although this occurs at the higher field of about 2000 gauss.

To understand such a B^{-2} dependence, it is important to first consider the charge exchange process that may occur in **some** materials. Upon forming in the sample, if the Mu_T^0 is ionised and becomes Mu^+, the ionised electron will 'carry off' some spin polarisation, the amount being dependent on the ionisation rate. The Mu^+ can then recapture an electron to form Mu_T^0 again. If the ionisation rate is small, and the lifetime of each Mu_T^0 is long, then time-averaged the muonium will appear to be paramagnetic rather than diamagnetic. Such an ionisation/recapture process will continue until the decay of the muon. When *slow* charge exchange occurs, the mean lifetime of the Mu_T^0 is much larger than the period of hyperfine oscillation ($\frac{2\pi}{\omega_{24}}$). The muon polarisation undergoes numerous oscillations before Mu_T^0 ionises. As such, the fractional loss in polarisation per charge exchange cycle is the amplitude of the oscillating component, i.e. $A_{24} = \frac{1}{2(1+x^2)}$ where $x = \frac{B}{B_0}$ (*cf.* Equation 3.4). It is therefore expected that the $1/T_1$ relaxation rate is proportional to the amplitude of this polarisation, and therefore

$\frac{1}{T_1} \propto \frac{1}{1+x^2}$. Therefore when slow charge exchange takes place, generally at high fields where ω_{24} is large and therefore the oscillation period small, $\frac{1}{T_1} \propto B^{-2}$.

From Figure 5.11, at room temperature and low-fields, the a-Si:H and a-Si maintain a larger relaxation rate than the other silicon samples, albeit reduced in their initial magnitudes. The high-field $1/T_1$ tail-off is less pronounced at 300K than for the lower temperatures, and it would be difficult to confirm any B^{-2} dependence since the tail-off regime, for those materials in which it can actually be seen, appears to occur at a higher field, $B > 3000\,\text{gauss}$. For the polycrystalline materials, $p-$type pcr-Si and pcr-Si, few data points are represented in the figure due their $1/T_1$ values being equal to zero, and therefore little or no relaxation of the polarisation occurs at any field. It therefore seems that, as the temperature is increased, the overall magnitude of the relaxation rates is reduced, as is the magnitude of the gradient of the $1/T_1$ curves. Furthermore, with an increase in T, the $1/T_1$ tail-off region, in which a B^{-2} dependence can occur, shifts to higher fields.

5.2.3 Discussion

As expected for polycrystalline material, low diamagnetic fractions were found in both intrinsic and p-type pcr-Si. The f_d was lower in the doped sample, the most likely cause being a difference in growth conditions; a difference in growth temperature (unknown for these materials) could easily account for variations in the concentration of mid-gap defect states. It is important to note that the f_d of the polycrystalline materials is still much larger than the 7.5% expected for crystalline silicon. As well as defects in grain-boundaries, other possible sources of defect/diamagnetic centres include vacancies and dislocations. All such defects can be introduced in the crushing procedure, to produce polycrystalline samples from the crystalline wafers. In c-Si at low temperatures, where f_d is very low, the paramagnetic Mu_T or Mu_{BC} states are energetically favoured[4]. The temperature dependence of f_d for polycrystalline materials is very similar to that of c-Si, with f_d remaining constant up to the 150 - 200 K region, where a rapid increase in f_d occurs by the ionisation of paramagnetic centres, believed to be Mu_{BC}. For tempera-

tures > 250 K (certainly in pcr-Si), a plateau is reached, suggesting that since $f_d < 1$, paramagnetic centres must still be present, although no longer being ionised. From the fitting parameters of Tables 5.2 and 5.3, it becomes apparent that above 250 K, all of the Mu_{BC} has either been ionised to a diamagnetic state, possibly Mu^+_{BC}, or converted to Mu_T.

In comparing the $1/T_1$ and $1/T_2$ relaxation rates of the pcr-Si samples, the value of $\lambda_1 \approx 2.0\,\mu s^{-1}$ is approximately an order of magnitude larger than the value of λ_2 ($\approx 0.20\,\mu s^{-1}$). As such, it seems that the dominant relaxing species is paramagnetic muonium, possibly in a Mu_T state. By examining the fitted isotropic parameter ($A = 2000$ MHz), it seems likely that for these polycrystalline silicon samples, muonium diffusion occurs via a neutral Mu_T state. With the agreement of the hyperfine parameter between c-Si and the polycrystalline samples, it can be concluded that the nature of the site in the polycrystalline material, particularly the structure of the cages through which the muonium will diffuse, remains unchanged from those of the crystalline sample. This is of little surprise since it would be difficult to see how the crushing of a crystalline sample would change its cages and periodicity. With the dominance of Mu_T at all temperatures, it can be concluded that it is the favoured site, in agreement with earlier studies on c-Si[5], even though Mu_{BC} is believed to be the site of lowest energy[3]. Since the hyperfine parameters of Mu_{BC} remain constant with temperature, and identical to the parameters of c-Si, it seems that the nature of this site also remains unchanged from that in c-Si. Thus bond lengths and angles appear to remain unchanged, certainly up to 125 K, which is not surprising in the inflexible network of a crystalline lattice. Even in the p-type pcr-Si, the interaction between the muon and electron remains unchanged from c-Si, and constant with temperature, and thus the unpaired electron, residing in an anti-bonding orbital, comes under no influence of the acceptor states of the silicon.

With the transition from the order and periodicity of a crystalline lattice, to the continuous random network of an amorphous system, many changes occurred (see Figure 5.1). The diamagnetic fraction of all the amorphous materials was significantly higher than the polycrystalline, primarily because of their differing growth conditions. Being a phys-

ical process, and thus involving collisions, electron-beam deposition produces the largest defect concentration, as seen by its large diamagnetic fraction, $f_d \approx 71\%$. The glow-discharge decomposition of silane to produce the hydrogenated a-Si materials, depends on the adjustment of significant parameters, particularly substrate temperature, plasma r.f. power and gas pressure. A balance has to be struck between defect concentration and deposition speed, as well as promoting the growth of a-Si:H films (as opposed to a-Si:H_x). For doped a-Si:H, the dopant atoms are incorporated into the amorphous structure substitutionally from phosphine (n-type) and diborane (p-type). As a consequence of their group-V and group-III structures, respectively, they introduce coordination defects, whereas in c-Si, the dopants are 'forced' into a coordination number of four, thus minimising the substitutional disorder. In the heavily doped p-type and n-type a-Si:H samples, large numbers of coordination defects are therefore expected, thus generating large concentrations of dangling bonds, which increase the f_d of the materials.

Noticeably, the a-Si sample has the largest f_d of all the materials, and thus it can be assumed that it also has the largest concentration of dangling bonds - not entirely surprising since there was no hydrogen incorporated into the network to passivate them. Since more than half the muonium fraction in a-Si, a-Si:H, p-type and n-type a-Si:H is diamagnetic, this supports the view that the Si–Mu complex is energetically the single most favoured centre at all temperatures up to room temperature. This is significantly different to the behaviour of the polycrystalline materials, where paramagnetic states dominated.

The f_d of both a-Si and a-Si:H are independent of temperature, suggesting that no ionisation processes take place, and thus that the paramagnetic states are more stable, particularly the Mu_{BC} state. This is supported by the parameters of Tables 5.4 and 5.5, in which it is seen that the relative fractions remain virtually temperature independent for a-Si:H. In the doped a-Si:H samples, the diamagnetic fractions begin to slowly increase with temperature at about 150 K, indicating the ionisation of paramagnetic states. By examining the parameters of Tables 5.6 and 5.7 it can be seen that, by room temperature, all the Mu_T has been lost for p-type a-Si:H, and very little remains for n-type a-Si:H.

Mu_{BC} remains the dominant paramagnetic site for both doped samples, and it is almost independent of temperature, similar to the Mu_{BC} site of undoped a-Si:H. It is known that for the bond-centre species to be stable, the Si-Si separation in this centre must exceed that in the normal crystalline silicon bond by as much as 40%[6]. Therefore, this stability and predominance of the Mu_{BC} centre is likely to be a consequence of the existence of a degree of strain within the random network of all the amorphous materials, generating pre-stretched Si–Si bonds[8], and thereby favouring the formation of the bond-centre states or catalysing the conversion of Mu_T to Mu_{BC}. The behaviour of the *p*-type a-Si:H, appears to indicate the possibility of Mu_T to Mu_{BC} conversion at lower temperatures, and near room temperature, the ionisation of Mu_{BC} centres to diamagnetic, since f_d remains constant up to 125 K, whilst a rapid loss of Mu_T sites occurs, and at 300 K, all the Mu_T sites have been lost, either ionised or converted to Mu_{BC}.

By examining the hyperfine parameters of the amorphous samples, the nature of the isotropic centre remains unchanged and independent of hydrogenation or dopants. The isotropic parameter A remains noticeably larger than that of c-Si, near to that of the vacuum-state muonium, and therefore it seems that the cages of the amorphous network may actually be larger than those of the crystalline structure. The parameters of the bond-centre remain constant for all hydrogenated a-Si:H samples, and thus it seems that dopants have little effect on the nature of the Si–Si bonds. Furthermore, the parameters are all independent of temperature, thus indicating an appreciable stability of the amorphous network. The anisotropic hyperfine parameter is noticeably larger than for c-Si in all the amorphous materials. An explanation for this difference could be that the muon lies along the bond but displaced from the bond-centre position[7]. This would be expected to lead to an enhanced contact interaction between the muon and its electron, as found.

For the a-Si sample, at low temperatures the hyperfine parameters all remain equal to those of the hydrogenated materials, and thereby the nature of both isotropic and anisotropic centres appears to be common to both sets of materials. With an increase

in temperature, there appears to be no change of the isotropic centre, but a reduction in the muon-electron hyperfine interaction of the anisotropic centre occurs. Hence, the electron of the anisotropic centre has a reduced spin-density on the muon site, which could almost be considered as the electron spending less time on the muon site. There is the possibility that the anisotropic muonium is constantly losing and gaining an electron, in which case, the fraction of time that any electron resides on the muon site would be reduced. What mechanism may explain such a behaviour? In a-Si, since there is no lattice hydrogen to passivate the dangling bonds and break weak Si–Si bonds, at higher temperatures the muonium may be diffusing through the lattice from bond-centre to bond-centre via dangling bonds. The bond-centre site could be considered as a deep-level muonium trap, and at the low temperature of 15 K, not enough escape energy would be available, and thus the site would behave more akin to that of a-Si:H. If hydrogen is incorporated into the lattice, then the hopping distance between each dangling bond would be greater, and thus diffusion via these dangling bonds less probable.

By considering the $1/T_1$ relaxation rates of a-Si and the hydrogenated a-Si samples, little variation of the temperature and field-dependence occurs between the different samples, the only exception being p-type a-Si:H. The p-type a-Si:H is interesting in that at higher temperatures it has very little or no Mu_T at all. At 15 K, all samples have noticeable $1/T_1$ rates, although the p-type a-Si:H $1/T_1$ rate falls away much faster than any other material, although it is uncertain why this occurs. At 125 K, again the magnitude of the $1/T_1$ rates are all comparable, but the p-type a-Si:H, which has a negligible Mu_T concentration at this temperature, has virtually no relaxation at any field. With the further increase of temperature to 300 K, no Mu_T exists for p-type a-Si:H, but the $1/T_1$ rate has noticeably increased, though not to the levels of the other materials. It thus seems that the the Mu_T centre is again the dominant relaxing species, large enough to mask any Mu_{BC} contribution. By 300 K for p-type a-Si:H, the $1/T_1$ character of Mu_{BC} can be seen. It is unseen at the lower temperature of 125 K probably as a consequence of too little energy, and thus further adding to the argument of Mu_{BC} diffusion at higher temperature, where diffusion can be very temperature sensitive.

It can generally be seen that in the amorphous structures there is a predominance and stability of the bond-centre site not seen in the crystalline silicon samples. The cage-centre site though, appears to be much less stable and not as favoured in the random networks of the amorphous materials. There appeared to be few effects of dopants on either the polycrystalline or amorphous materials. For example, it was expected[5] that by the addition of dopants the relative fractions of each site would vary in both sets of materials. In the p-type pcr-Si sample, even with the few data points available, since $f_d\,(15\,\mathrm{K}) \approx f_d\,(125\,\mathrm{K})$, there appears to be little indication of a step in the f_d at about 50 K. At this temperature, the ionisation of boron dopants is expected, generating an increased density of holes, which are then captured by Mu_{BC} centres, resulting in a diamagnetic Mu^{+}_{BC} centre. It would seem that hole capture by the Mu_{BC} is possibly being severely limited. A possibility is that the dopant energy levels are deeper in the gap than in c-Si (further from the valence band), thereby restricting the low-temperature promotion of holes to the valence band, with a higher ionisation temperature required, and thus reducing the overall number of holes available. This possibility would seem unlikely in the polycrystalline material where dopant energy levels vary little from the crystalline material. A second possibilty would be the premature recombination of electron-hole pairs, thus starving the bond-centre of a hole. Could the electron of the dangling bonds provide such a recombination centre? It should be stressed once again that, with only three data points, little certainty can be afforded on the matter. For the p-type a-Si:H sample, due to no sub-50 K points being measured, no discussion can be made with regard to such dopant ionisation.

For n-type c-Si, it was found[5] that f_d was initially higher than in the intrinsic sample, attributed to the ionisation of phosphorus dopants. The f_d of the n-type a-Si:H is only fractionally larger than that of the intrinsic a-Si:H sample, although a low-temperature step is clearly seen, which could indicate the possibility of dopant ionisation from the exchange of an electron yielding Mu^{-}_{T} centres. Unfortunately, from TF-μSR analysis, little discrimination can be made between the different diamagnetic species μ^{+}, Mu^{+}_{BC}, and Mu^{-}_{T}. Without further muon spectroscopy studies, little can be said about these

ionised diamagnetic states.

In Figure 5.12, with the addition of phosphorus dopant to c-Si, making the material

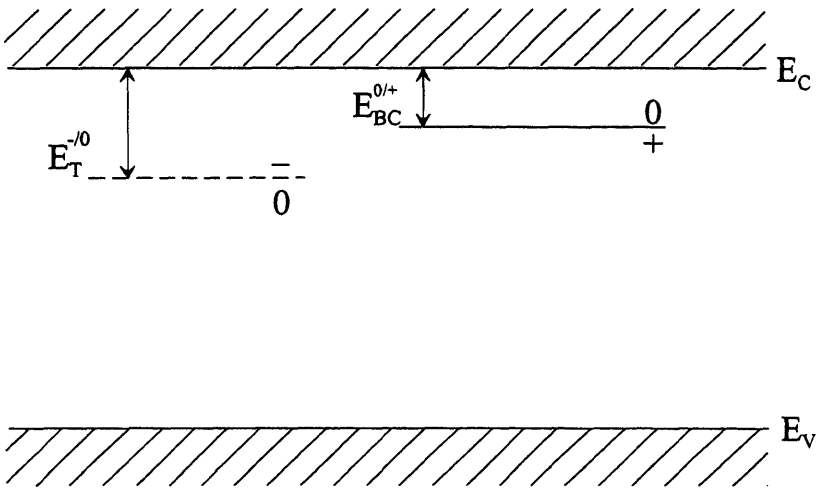

Figure 5.12: The energy levels within the gap for muonium in Si.

strongly n-type, at room temperature the Fermi level would lie above both muonium levels, leading to a predominance of Mu_T^- and Mu_{BC}^0 at the two sites. It would therefore be expected that for an n-type material, the favoured room temperature paramagnetic state would be the bond-centre site. This is seen in the n-type a-Si:H sample, although the bond-centre site could not be said to be clearly dominant. For an intrinsic or p-type material, the Fermi level would lie at or below the midgap, most probably below either muonium-related levels[5], thus the expected states would be Mu_T^0 and Mu_{BC}^+. As such, the dominant paramagnetic site expected for the intrinsic and p-type pcr-Si and a-Si:H samples would be the Mu_T centre. This is clearly seen in the polycrystalline samples, but for the intrinsic amorphous samples there appears to be no clearly dominant paramagnetic state, and for p-type a-Si:H, the complete opposite is seen, whereby the dominant state at room temperature is the Mu_{BC} centre. Once again though, it seems probable that the pre-stretched nature of the Si–Si bonds in the amorphous network favours the predominance of bond-centre sites over diamagnetic sites, and thus direct comparison with the results of c-Si can be dangerous since, afterall, the crystalline and amorphous silicon materials have quite different structures.

5.3 Germanium

In this section, a report is made of the measurements obtained from TF-μSR and LF-μSR studies on pcr-Ge, a-Ge and a-Ge:H. By the near-fraternal relationship in group IV, crystalline germanium has many properties similar to silicon. In pcr-Ge, tetrahedral cage sites and bond-centre sites, in which the muonium can tarry, have both been identified. As for amorphous Si, it is not obvious that analogous sites would be favoured in amorphous Ge since, for example, symmetrical atomic cages do not exist in random networks. The results for the germanium samples will now be presented, and comparisons made later with the results from silicon, presented earlier in this chapter.

5.3.1 Experimental TF-μSR results

Diamagnetic fraction

The temperature dependence of the diamagnetic fractions for the various germanium samples are shown in Figure 5.13. Considering the pcr-Ge, at low temperature, there

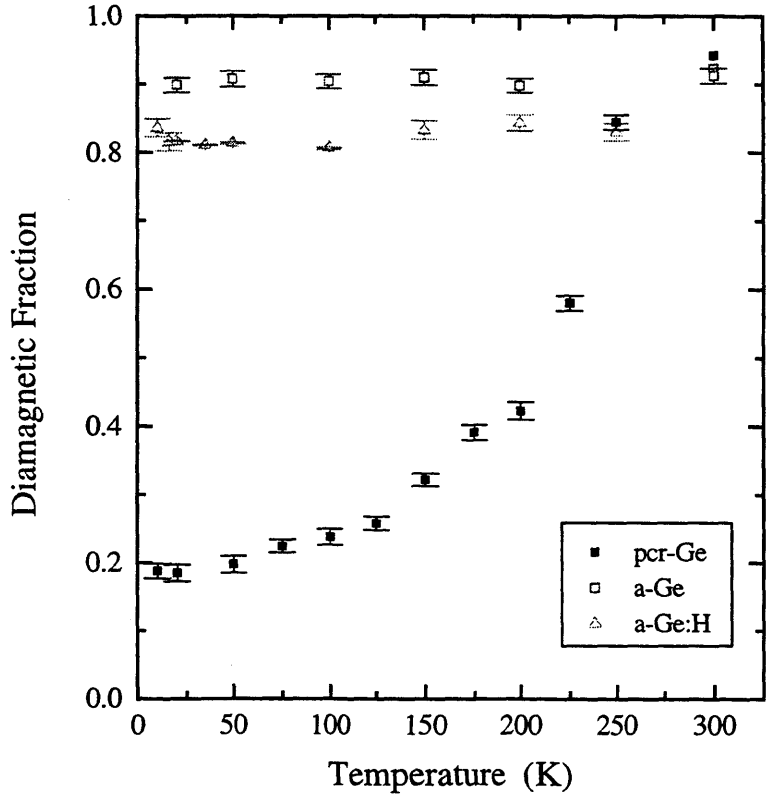

Figure 5.13: Diamagnetic fraction of all the germanium materials.

occurs a diamagnetic fraction of only $\approx 20\%$, the vast majority of the muonium residing in paramagnetic sites which we shall later infer are associated with muonium in the T and BC sites. The f_d is extremely temperature dependent; as the temperature is increased, f_d increases, indicating the ionisation of the neutral states. At 300 K, diamagnetic centres are by far the dominant state, with f_d reaching 94%. In contrast, the amorphous germanium samples, a-Ge and a-Ge:H, exhibit very large diamagnetic fractions of $\approx 80\%$ for a-Ge:H and $\approx 90\%$ for a-Ge at all temperatures. As with the a-Si and a-Si:H samples, the high diamagnetic fractions can be associated with muonium attached to dangling bonds with the lower f_d of the hydrogenated sample being a consequence of their passivation by the hydrogen. Unfortunately, since the f_d values of the amorphous samples are so high, there is a only a small concentration of paramagnetic sites capable of being repolarised in LF-μSR measurements.

Relaxation rates

The λ_2 curves, where $1/T_2 = \lambda_2$, for germanium are shown in Figure 5.14 at a transverse field of 20 gauss. It can be seen that the low-temperature λ_2 rates of pcr-Ge and a-Ge:H are comparable with those of the polycrystalline samples. All the Ge samples appear to

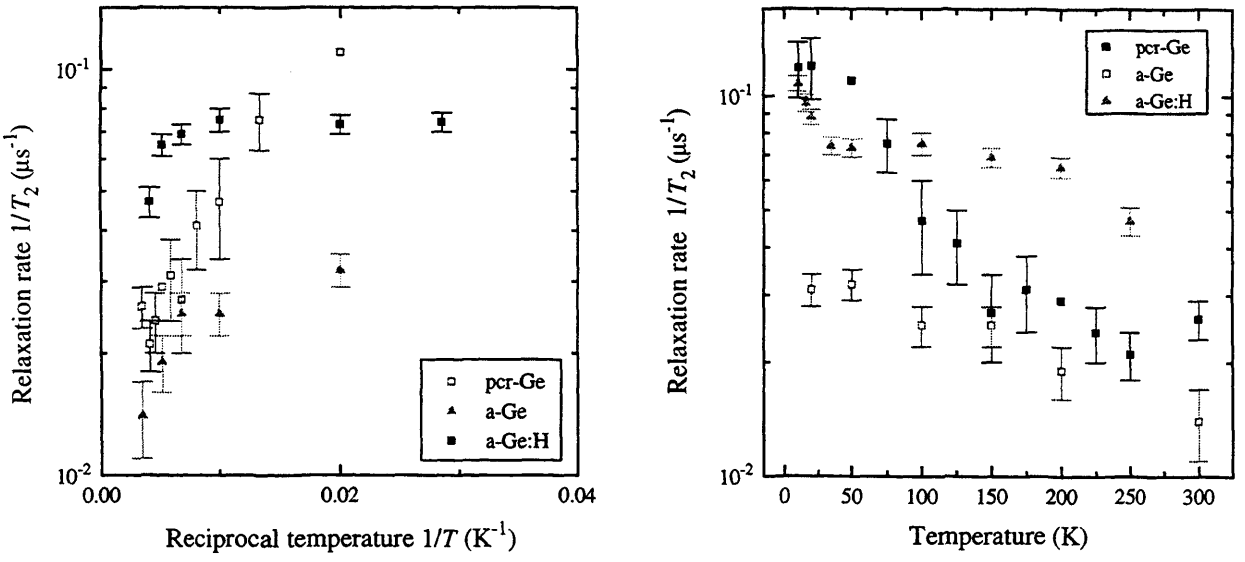

Figure 5.14: The dependence of $1/T_2$ on reciprocal temperature (*left*), and temperature (*right*), measured at 20 gauss, for all the germanium materials.

exhibit a temperature dependence, though the pattern of behaviour differs. The $1/T_2$

values for the pcr-Ge sample approximate to an exponential reduction with temperature. By inspection, the $1/T_2$ for the a-Ge would also appear to fall exponentially, although, due to the uncertainty of the reliability of such small relaxation rates, it is more likely to be non-relaxing, and therefore indepenent of temperature. In contrast, the $1/T_2$ temperature dependence of a-Ge:H does not fall exponentially, but suffers a rapid $1/T_2$ decay as the temperature is increased, and then levels-off at mid-range temperatures. For high temperatures, $> 200\,\mathrm{K}$, $1/T_2$ begins to slowly fall, although not reaching the negligibly small magnitude of pcr-Ge and a-Ge, which by 250 K had relaxation rates of about $0.02\,\mu s^{-1}$.

5.3.2 Experimental LF-μSR results

Repolarisation curves and theoretical fittings

As for silicon, LF-μSR experiments on the germanium samples were performed at various temperatures. The experimental repolarisation curves for pcr-Ge are shown in Figure 5.15, along with theoretical fittings to the data. The parameters used to generate these fittings are shown in Table 5.8. The parameters for c-Ge[4] are also presented, so as to allow comparison with those for the pcr-Ge sample. Unlike c-Si and pcr-Si, the fitting parameters are noticeably different for c-Ge and pcr-Ge. At low temperatures, c-Ge exhibits a small diamagnetic fraction (10%), but for pcr-Ge no diamagnetic fraction is required to fit the data of Figure 5.15, even though, in Figure 5.13, it was demonstrated experimentally from TF data that pcr-Ge has a low-temperature f_d of about 20%. It has to be said that the fitting parameters for the 50 and 100 K data appear to be physically nonsensical. Whereas hyperfine parameters very similar to those of c-Ge might be expected, those attained in the fittings yield an isotropic centre similar to that in c-Ge, and an anistropic centre more abundant than in c-Ge with hyperfine parameters of $A_{iso} \approx 2360\,\mathrm{MHz}$ and $D \approx 1000\,\mathrm{MHz}$. As a demonstration of the deviation of the polycrystalline data from the crystalline fitting, in Figure 5.15 the repolarisation curve for low-temperature c-Ge is shown (dashed curve). Two differences can easily be seen between the two sets of low-temperature data. Firstly, at low-fields the c-Ge polarisation

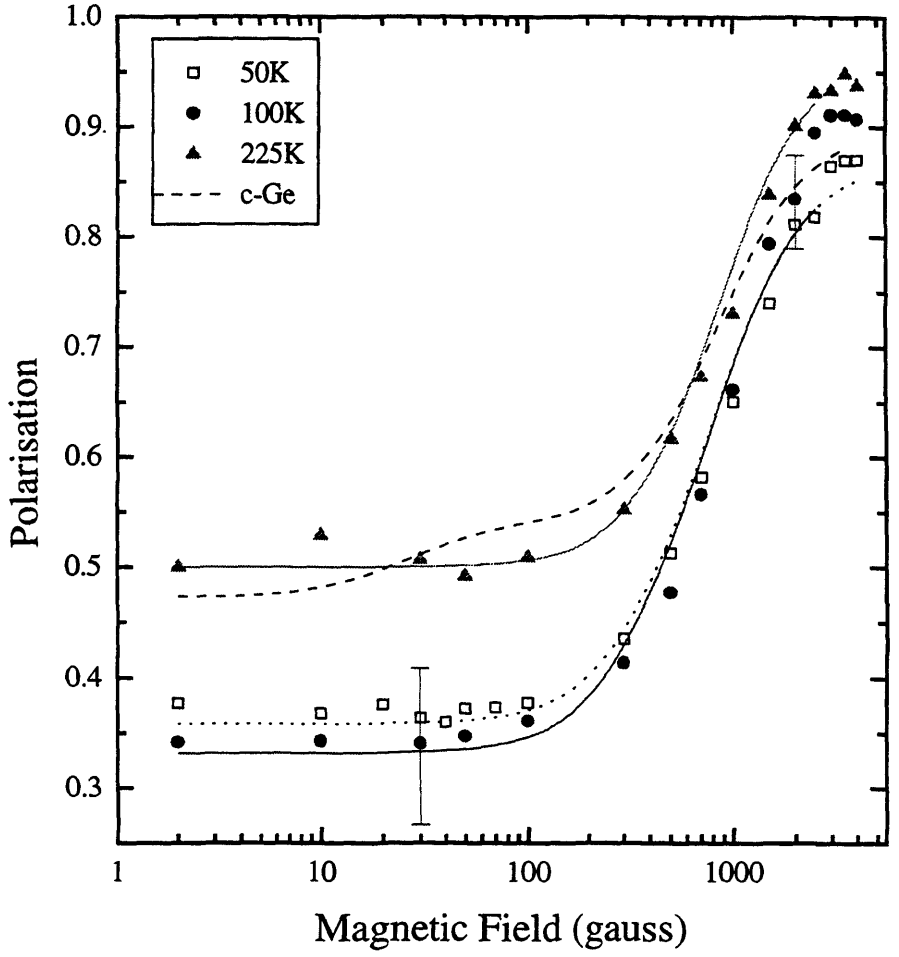

Figure 5.15: The field dependence of the polarisation for pcr-Ge. Also included is the repolarisation curve for c-Ge, using low-temperature hyperfine parameters (from [4]).

Sample	T (K)	Dia.	Isotropic		Anisotropic		
		f_d (%)	f_{Mu_T} (%)	A (MHz)	$f_{Mu_{BC}}$ (%)	A_{iso} (MHz)	D (MHz)
c-Ge	0[a]	10	72	2360	8	96.5	69.2
pcr-Ge	50	0	65	2360	20	2360	1000
pcr-Ge	100	0	56	2360	31	2360	1000
pcr-Ge	225	3	94	2360	0	—	—

Table 5.8: The relative fractions and hyperfine parameters for c-Ge (from [4]), and the fitting parameters and fractions for the experimental data on pcr-Ge.

[a]The hyperfine parameters refer to extrapolations to 0 K.

is more than 10% greater than of pcr-Ge, although in the high-field regime, the curves are beginning to converge. The second difference is that for pcr-Ge at all temperatures, no low-field step can be seen, but even with only 8% $f_{Mu_{BC}}$ a step can clearly be seen at about 100 gauss in the c-Ge curve.

The large anisotropic hyperfine parameters of pcr-Ge (A_{iso}) are usually indicative of a diffusing isotropic muonium centre, and such a centre having this very large distortion parameter (D) seems nonsensical. A wide-range of parameters were tested, but only those presented in Table 5.8 come near to fitting the experimental data. At present, it is not possible to say where the uncertainty, or even a solution, is to be found. It could be considered that the fitting procedure is flawed, which, since based on assumptions, is certainly possible; although this explanation appears unlikely. By eyeball inspection of the 50 and 100 K repolarisation curves it can be seen that the polarisation rises from about 35% at low-field, to around 90% at high fields; with a single step at a field of about 2000 - 3000 gauss. The dilemma represents itself as follows: if the muonium centres present were 100% Mu_T then the minimum value of the polarisation should be 50%, not 35%. As such, an anisotropic component must be added, which, for 100% Mu_{BC}, would have a low-field polarisation of $\frac{1}{6}$th. Therefore, there appears to be two paramagnetic centres present, but the presence of a single step usually indicates the presence of only one paramagnetic centre. Since this step occurs in the high-field region, it would be assumed to be an isotropic centre. To surmise, on the one hand, from the repolarisation step, only a single paramagnetic centre is expected, but so as to reduce the low-field polarisation then two paramagnetic centres are needed. The fitting parameters represent somewhat of a compromise: two paramagnetic centres, one bearing only isotropic characteristics, and the second bearing both isotropic and anisotropic characteristics. At the present time no explanation suggests itself.

Two further samples were prepared and analysed, a-Ge and a-Ge:H. Unfortunately, for the a-Ge sample, the diamagnetic fraction was so large, $f_d > 90\%$, that virtually no paramagnetic sites were available for repolarisation of the muon spin to take place. As a consequence, only repolarisation measurements for a-Ge:H will be presented. These are

shown in Figure 5.16. Included in the figure are the theoretical curves to the experimental data, for both 15 K and 200 K. The parameters used to generate the fittings are shown in Table 5.9. From TF data (Figure 5.13), the a-Ge:H sample possesses a large diamagnetic fraction of about 80% at all temperatures. A similar value is found from fitting the LF repolarisation data. The Mu_T and Mu_{BC} sites are roughly equally occupied (10% and 13% respectively) at 15 K. At 200 K, there is a small increase in the value of f_d and the Mu_T and Mu_{BC} continue to have approximately equal fractions of 8% and 9.7% respectively. As such it can be considered that, for temperatures less than 200 K, the relative fractions remain roughly independent of temperature. This is in contrast with the temperature dependence of the relative fractions for pcr-Ge, where at 225 K practically all the muonium resides in the tetrahedral cage-centre, with no bond-centre sites present.

A temperature dependence of the hyperfine parameters occurs for a-Ge:H. At 15 K, the hyperfine parameter of the isotropic centre is small at $A = 1100$ MHz. This centre varies noticeably from the corresponding centres of c-Ge and pcr-Ge, which both had an A value of 2360 MHz. The hyperfine parameters for the anisotropic centre are also very much smaller than the corresponding values for pcr-Ge, whose anisotropic hyperfine parameters appeared rather nonsensical. For a-Ge:H, at 15 K, the isotropic component, A_{iso}, is equal to 245 MHz, compared to 96.5 MHz for c-Ge, and the degree of anistropy, D, is equal to 56 MHz, not much smaller than the $D = 69.2$ MHz for c-Ge. With an increase in temperature to 200 K, the hyperfine parameters remain similar to those for the low temperature, with the only change being that A_{iso} reduces to 135 MHz, maintaining the bond-centre site as the most likely site-type.

Relaxation rates

For the LF-μSR experiments on the germanium samples, the relaxation rates, λ_1 or $1/T_1$, of the asymmetry curves are shown, for pcr-Ge and a-Ge:H, in Figure 5.17. From the figure, it can be seen that there occurs a marked difference in the field dependence of $1/T_1$ between the pcr-Ge and a-Ge:H samples. At low fields, the relaxation rates are all

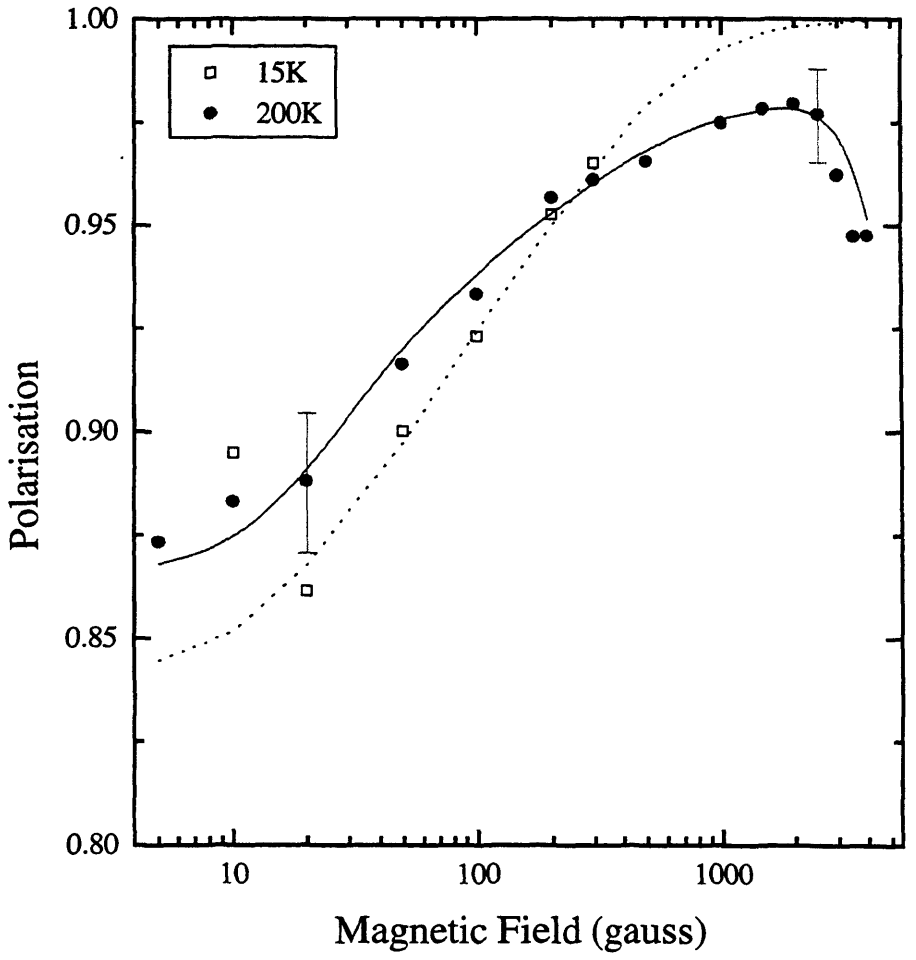

Figure 5.16: The field dependence of the polarisation for a-Ge:H, where the 15 K fitting has been derived exclusively from the Pratt expression and the 200 K fitting from a combination of the low-field Pratt formula and the high-field Meier expression.

Sample	T (K)	Dia.	Isotropic		Anisotropic		
		f_d (%)	f_{Mu_T} (%)	A (MHz)	$f_{Mu_{BC}}$ (%)	A_{iso} (MHz)	D (MHz)
c-Ge	0[a]	10	72	2360	8	96.5	69.2
a-Ge:H	15	77	10	1100	13	245	56
a-Ge:H	200	80.9	8	1100	9.7	135	56

Table 5.9: The relative fractions and hyperfine parameters for c-Ge (from [4]), and the fitting parameters and fractions for a-Ge:H.

[a]The hyperfine parameters refer to extrapolations to 0 K.

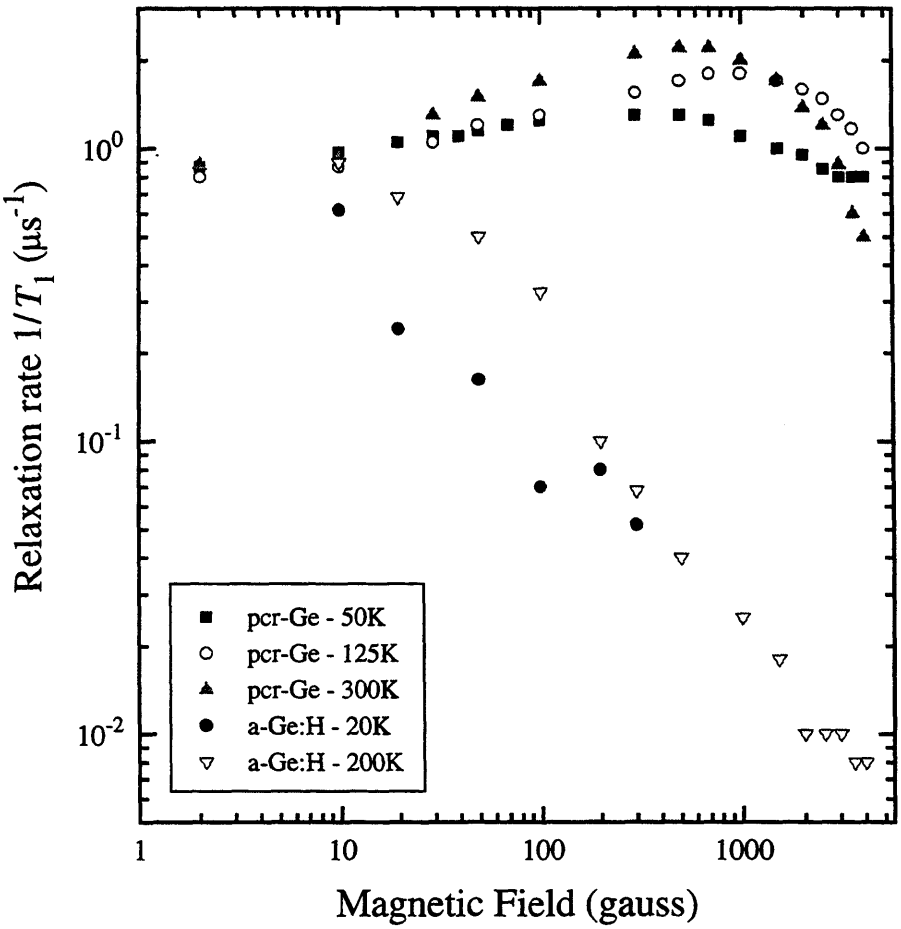

Figure 5.17: The field dependence of the $1/T_1$ for all germanium samples at all temperatures.

approximately equal, but as the field is increased the $1/T_1$ curves begin to diverge. For the pcr-Ge sample, with an increase in field $1/T_1$ increases up to a maximum. For each temperature, the $1/T_1$ maximum occurs in approximately the same field range of 500-1000 gauss. Subsequently, each $1/T_1$ curve suffers a fall-off, though at different rates. The high-field $1/T_1$ decay appears to be a maximum at 300 K and is lower with a reduction of temperature. The $1/T_1$ curves for a-Ge:H behave quite differently to those for pcr-Ge. Instead of a low-field rise of $1/T_1$, there occurs a rapid $1/T_1$ decay, such that even at low fields the relaxation rates, at both 20 and 200 K are more than an order of magnitude less than the corresponding values for pcr-Ge. Furthermore, no mid-field maximum occurs, and the decays are monotonic. In the high-field regime, $B > 1000$ gauss, the relaxation rates reach very small values, $1/T_1 \approx 0.03\,\mu s^{-1}$. The $1/T_1$ behaviour of a-Ge:H exhibits little change with temperature; the only difference being in the low-field region.

5.3.3 Experimental RF-μSR results

As well as the standard μSR techniques (i.e. TF-μSR and LF-μSR), studies using the RF-μSR technique have been performed. Owing to the development status of the RF-μSR facility at the ISIS facility, only two samples, pcr-Ge and a-Ge:H, have been studied. The results of these experiments, all performed with an RF-power of 160 W, are presented in this section of the thesis.

The time integral RF spectra for muonium in pcr-Ge at 25 K are shown in Figure 5.18. Presented in the figure are the spectra for both the paramagnetic and diamagnetic sites. The measurements were performed at different temperatures; in Figures 5.19 and 5.20 the RF spectra for pcr-Ge at 100 K and 175 K are displayed. The curves imposed on the experimental data are Lorentzian fittings to the data. The resonance field and maximum amplitude of the resonance peaks are presented for each temperature, in Table 5.10. In

Temperature (K)	Diamagnetic site		Paramagnetic site	
	Resonance field (G)	Amplitude	Resonance field (G)	Amplitude
25	1497	-0.074	13.08	-0.0098
100	1497	-0.100	14.36	-0.0074
175	1497	-0.111	—	—

Table 5.10: Resonace parameters for pcr-Ge, at 25K, 100K and 175K.

Figure 5.18, a distinct well-defined resonance peak can be seen for muonium residing in diamagnetic sites. From Table 5.10, the resonance peak is known to occur at 1497 G, and the amplitude of this peak is -0.074. The spectra representing the paramagnetic sites differ from the diamagnetic spectra. Two aspects quickly become apparent, the first being that the resonance peak for the paramagnetic centre spectrum although less broad, it has a much smaller amplitude. The second point-of-note is that the resonance field occurs at the much lower field of 13.08 G, with an asymmetry amplitude of -0.0098, almost an order of magnitude smaller than the signal for the diamagnetic centre. As discussed in Section 3.2.2, this difference of the resonance fields occurs as a consequence

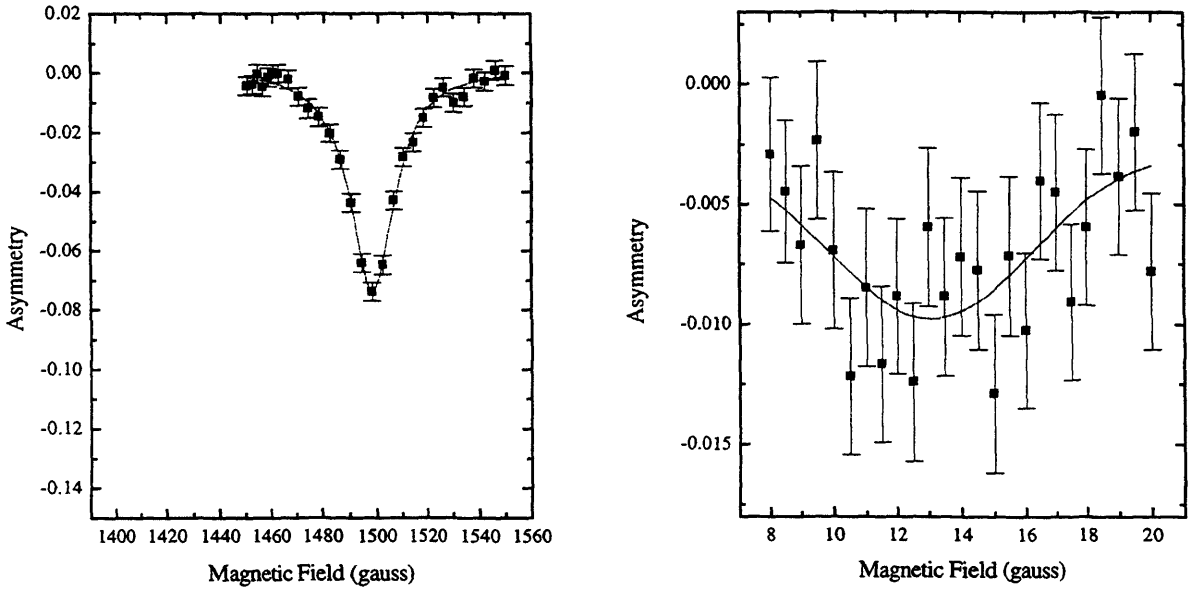

Figure 5.18: The field dependence of the RF-asymmetry for pcr-Ge at 25K, for both diamagnetic sites (*left*) and Mu_T sites (*right*).

of the gyromagnetic ratio γ of the diamagnetic muon being about 0.014 MHz/G, and the effective γ of muonium at low fields being $\approx$ 1.4 MHz/G. This 10^2 difference of the effective γ values results in a 10^2 difference of the field at resonance. As the temperature is increased to 100 K, see Figure 5.19, the diamagnetic resonance peak occurs at the same field, though with a slightly larger amplitude of -0.10, consistent with the TF-μSR results of Figure 5.13. For the paramagnetic spectra though, the curve is extremely shallow, and indeed, though a Lorentzian fit has been fitted to the experimental data, it is not certain whether a genuine peak can actually be seen. Assuming that the peak is genuine, the resonance occurs at virtually the same field, $\approx$ 14 gauss, and the resonance amplitude is reduced to -0.0074, in agreement with the trend of the fitting parameters presented in Table 5.8. With a further increase in temperature to 175 K, the RF spectrum changes once again, as shown in Figure 5.20. For the spectrum of the diamagnetic site, the resonance field again occurs at 1497 G, in agreement with the results of both 25 K and 100 K. However, the magnitude of the signal increases further to -0.111, again reproducing the trend seen in Figure 5.13. As can be seen from Figure 5.20, the resonance peak is no longer present, represented in Table 5.10 by an omission of any parameters.

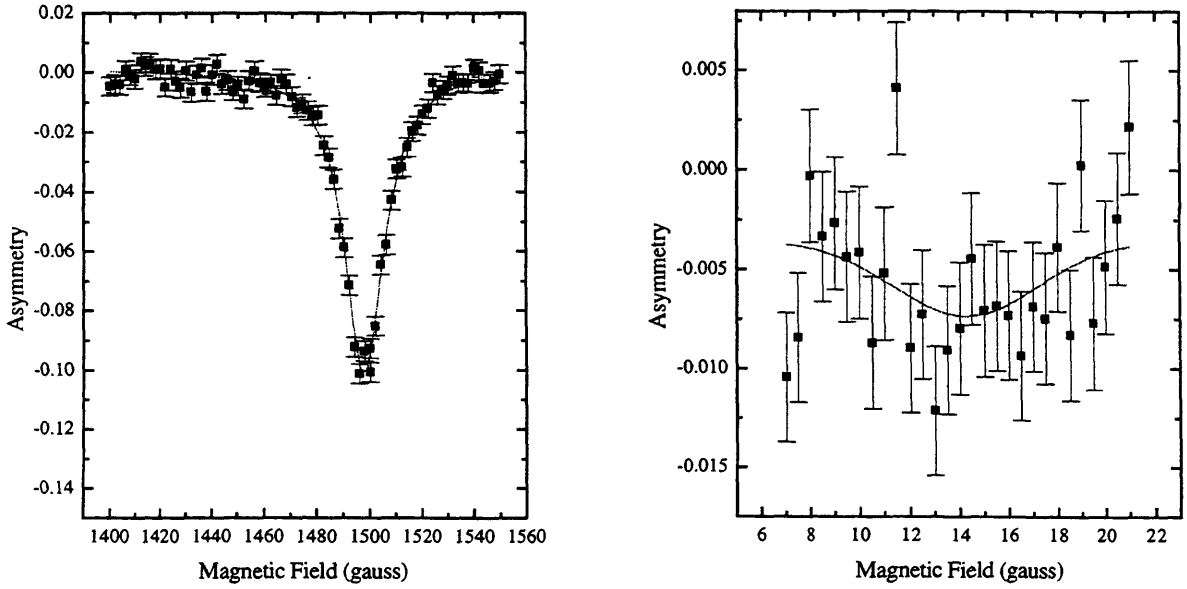

Figure 5.19: The field dependence of the RF-asymmetry for pcr-Ge at 100K, for both diamagnetic sites (*left*) and Mu_T sites (*right*).

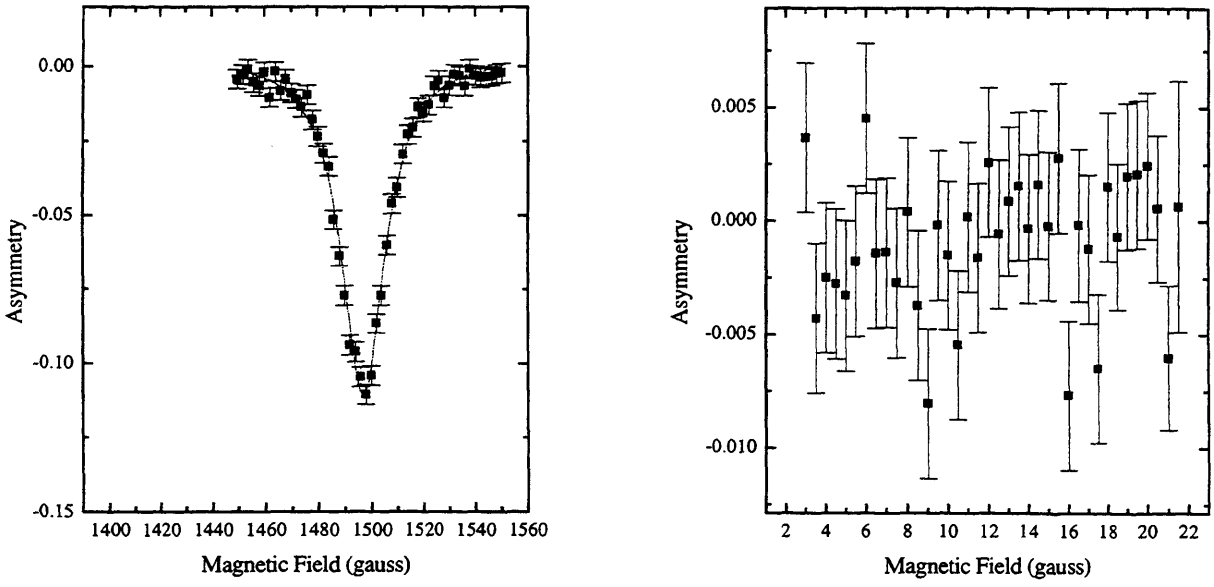

Figure 5.20: The field dependence of the RF-asymmetry for pcr-Ge at 175K, for both diamagnetic sites (*left*) and Mu_T sites (*right*).

It is not certain what is responsible for this loss of a peak. Either loss of Mu_T sites or magnetic broadening leading to excessive scatter are both possibilities.

In addition to the pcr-Ge, RF-μSR experiments were performed on a-Ge:H. The time integral RF spectra for muonium at 25 K and 100 K are shown in Figures 5.21 and 5.22, respectively. Presented within each figure is the behaviour for the diamagnetic and expected paramagnetic (tetrahedral) muonium sites. The curves imposed onto the diamagnetic spectrum is simply a Lorentzian fitting to the experimental data. For the low-field spectra, the right of the figures, no Lorentzian fit has been applied since, at both 25 K and 100 K no muonium signal can be seen in the data. The parameters of the resonance peaks of the spectra at 25 K and 100 K are shown in Table 5.11. The amplitude

Temperature (K)	Diamagnetic site		Paramagnetic site	
	Resonance field (G)	Amplitude	Resonance field (G)	Amplitude
25	1497	-0.115	—	—
100	1497	-0.121	—	—

Table 5.11: Resonance parameters for a-Ge:H at 25K and 100K.

of the diamagnetic signal was -0.115, larger than the comparable amplitude for pcr-Ge at 25K, which was -0.074. Once again, the resonance field was 1497 G, consistent with the field for pcr-Ge. As with the spectrum at 25 K, a sharp well-defined resonance peak is clearly seen in Figure 5.22 for the high-field diamagnetic site at 100 K, whose amplitude increases to -0.121, in agreement with the diamagnetic signal increase for pcr-Ge. At low fields though, no muonium resonance peak was detected.

5.3.4 Discussion

The TF behaviour of pcr-Ge is in some respects very much different from that anticipated. Although the temperature dependence of the diamagnetic fraction behaves as expected from the results for c-Ge[4], the parameters from the fittings of the LF-μSR repolarisation curves would appear to be rather nonsensical. The low-temperature f_d

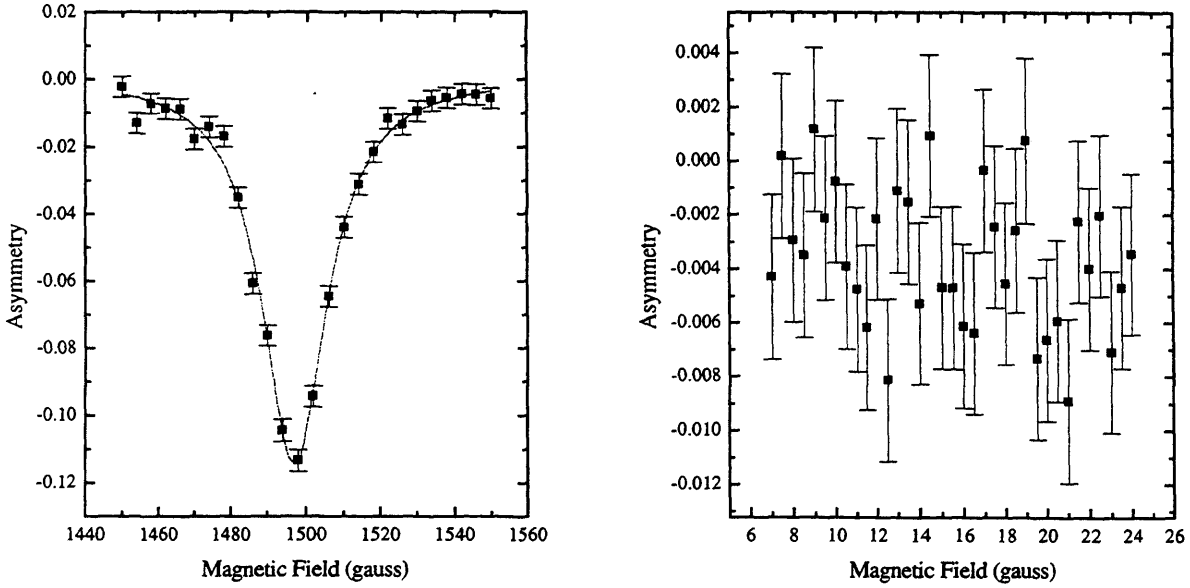

Figure 5.21: The field dependence of the RF-asymmetry for a-Ge:H at 25K, for both diamagnetic (*left*) and Mu_T sites (*right*).

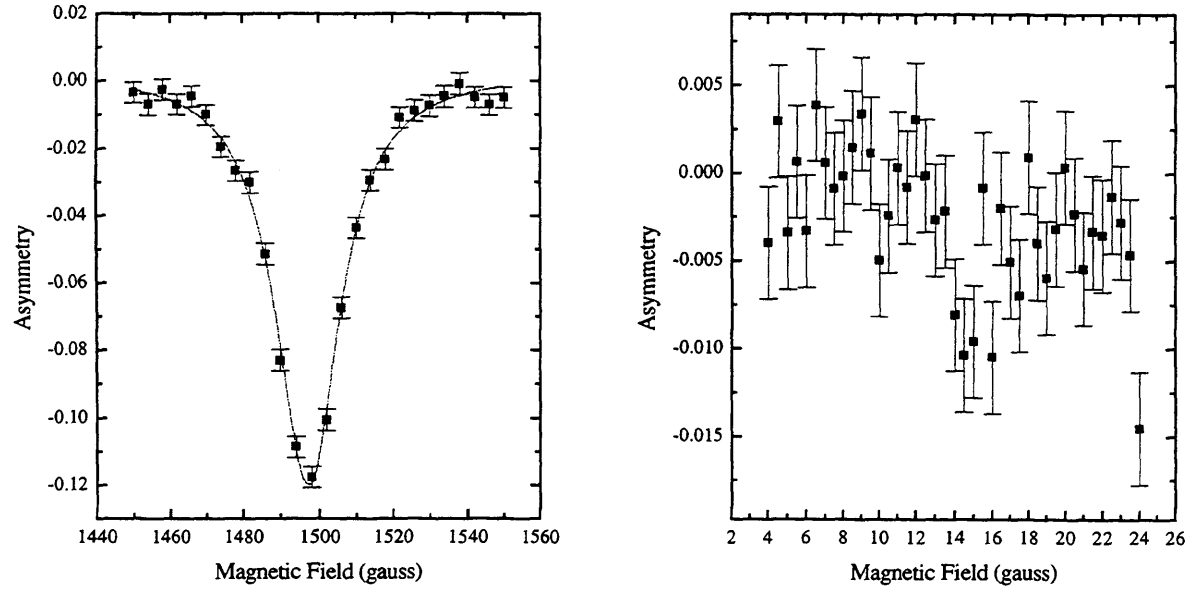

Figure 5.22: The field dependence of the RF-asymmetry for a-Ge:H at 100K, for both the diamagnetic centre (*left*) and in the region of Mu_T sites (*right*).

begins low, as expected from the crushed c-Ge wafer, indicating few dangling-bond defect centres, with the remaining paramagnetic fraction being associated with muonium in T and BC sites. This value is very similar to that of pcr-Si, which was prepared under almost identical conditions. Similar to pcr-Si, with an increase in temperature there occurs an increase in f_d, associated with the ionisation of neutral Mu_T^0 and Mu_{BC}^0 states. Such behaviour differs from that in c-Si, in which the bond-centre site ionises at a lower temperature than the T site. These neutral species have nearly equal energies, although Mu_T^0 is apparently theoretically favoured[9]. On the curve of Figure 5.13, there are no obvious steps, unlike those seen for the pcr-Si curve of Figure 5.1. Such steps tend to indicate ionisation of paramagnetic states, or electron capture/trapping. Since the f_d curve behaves differently to that for pcr-Si, certainly at high temperatures, the ionisation of paramagnetic centres is probably occurring differently to that for silicon. Since both centres are thought to have equal energies, with only a very shallow energy barrier between the two, it would seem that both states are being ionised simultaneously, as well as T $\leftrightarrow$ BC site conversions, with little restriction due to the shallow barrier. For temperatures above room temperature, the diamagnetic fraction is virtually 100%, and thus there is no longer any paramagnetic fraction.

By comparing the magnitude of the $1/T_2$ relaxation rate, which as with pcr-Si decreases exponentially with temperature, and the $1/T_1$ relaxation rates of Figure 5.17, it can be seen that the λ_1 is more than an order of magnitude larger than λ_2. Upon examining the fitting parameters of Table 5.8, $A = 2360\,\text{MHz}$ indicates a delocalisation of the electron, and therefore intimating that the Mu_T centre is a diffusing isotropic muonium. This value of the hyperfine parameter A is also equivalent to the known value associated with Mu_T in crystalline germanium. The hyperfine interaction of this Mu_T centre appears to be independent of temperature and since it is also the dominant paramagnetic state, it would therefore seem that it is also the energetically favoured and more stable of the two paramagnetic centres, in agreement with theory[9]. By considering this Mu_T dominance, and the magnitude of the λ_1 relaxation rate, it would seem likely that it is also the dominant relaxing species. Judging by the magnitude of the $1/T_1$ rate,

this postulate would appear likely. In considering the fitting parameters, the nonsensical values greatly compromise and complicate the issue of analysis. The most striking oddity is that at room temperature; TF-μSR measurements indicate an f_d of nearly 100%, whereas to allow any form of theoretical fitting, the f_d had to be set at near-zero. Such a phenomenon may arise as a consequence of the rapid site T $\leftrightarrow$ BC site conversions, but unfortunately, no obvious model would appear to easily explain such contradictions. At 225 K, f_d is approximately 60%, but the low-field polarisation of Figure 5.15 begins at 50%, less than the measured diamagnetic fraction. Since the f_d curve appears to be in agreement with those obtained by other groups for c-Ge[10], the complication would appear to arise in the LF-μSR measurements.

In moving to the amorphous structures of a-Ge and a-Ge:H, it can be seen that the diamagnetic fraction for both materials is greatly larger than for pcr-Ge, which we assume is associated with muons attached to dangling bonds. Such is the magnitude of the fractions, that there is little or no paramagnetic fraction for the a-Ge:H and a-Ge materials. The f_d of these materials bears a close similarity to the behaviour of the a-Si and a-Si:H materials, for which the f_d of the hydrogenated materials was less than the non-hydrogenated, and furthermore, for both Ge and Si, f_d is virtually independent of temperature. As such, there would appear to be no ionisation of neutral Mu^0_T and Mu^0_{BC} states, and potentially a greater stability of the paramagnetic sites. The $1/T_2$ relaxation rates of these amorphous materials again behave differently from those of the pcr-Ge. The TF-polarisation of a-Ge appears to be non-relaxing and independent of temperature. For the a-Ge:H, relaxation of the polarisation does occur, and thus is temperature dependent, akin to the $1/T_2$ of pcr-Ge and the silicon samples (both crystalline and amorphous).

By considering the results of the LF-μSR measurements, the repolarisation curves and $1/T_1$ relaxation rates behave very differently from the pcr-Ge. At high-fields, for the 200 K data, a fall off in the polarisation can be seen for a-Ge:H, suggesting the onset of a minimum, at a magnetic field larger than presently available on the EMU beam line. This minimum, or cusp, is a signature of an anisotropic bond-centre; for

Mu_{BC} in c-Ge, it should occur at 4835 gauss[11]. In considering the parameters from the approximations, for both 15 and 200 K, it can be seen that the Mu_{BC} centre is only slightly the more favoured of the paramagnetic states, and neither site exhibits any large degree of temperature dependence, similar to a-Si:H. The hyperfine parameter of the isotropic centre, where $A = 1100$ MHz is smaller than the corresponding value of 2360 MHz for c-Ge, and as such suggests that the diffusing muonium is perhaps encountering smaller more distorted cage centres, in which the electron of the Mu_T is spending less time on the muon site with an increased interaction with the local lattice. By considering the $1/T_1$ rates of a-Ge:H, since the curves for 15 and 200 K virtually overlap, it seems that the dynamic processes are common to both temperatures. The magnitude of λ_1 is larger than λ_2, indicating that a paramagnetic centre is again the dominant relaxing species. Since favourability of the Mu_T centre is only slightly lower than for the Mu_{BC} site, and the relaxtion rate of a Mu_T centre tends to be larger than for Mu_{BC}, is seems likely that a diffusing Mu_T centre is once again the dominant relaxing species. There does appear to be a major difference in the field dependence of $1/T_1$ for the pcr-Ge and a-Ge:H, although both materials for all temperatures, share a common low-field relaxation rate of about $1\,\mu s^{-1}$. What is most likely happening is that, for both material types, with an increase in field (B) there is a period of constant λ_1, followed by a critical field, varying with material and temperature, at which the λ_1 begins to fall off. The data of Figure 5.17 is probably misleading, as a consequence of the difficulties in determining relaxation rates from the UDA software of the ISIS Facility (see Section 3.3.1). Therefore, the principal difference between the λ_1 relaxation rates is this critical field; for pcr-Ge it is approximately 1000 - 2000 gauss, and for a-Ge:H it is about 10 - 20 gauss. The field dependence of $1/T_1$ for the silicon materials behaves very similar to that of pcr-Ge; indeed only the $1/T_1$ behaviour of p-type a-Si:H resembles that of a-Ge:H. As to the cause of this critical field, alas, that is still uncertain.

The anisotropic centre has hyperfine parameters very much different to those of the pcr-Ge, but more akin to those of c-Ge. The distortion of the electron spin-density appears to vary very little from that of c-Ge, and at these low temperatures is indepen-

dent of temperature. The anisotropic hyperfine parameter is noticeably larger than for c-Ge at $A_{iso} = 245\,\text{MHz}$ at low temperature, although it varies with temperature. An explanation accounting for this difference of A_{iso} between c-Ge and a-Ge:H is that in the amorphous phase, the Ge–Ge bonds have been elongated with respect to those in the crystalline material, as was likewise postulated for the amorphous silicon samples. Such weak bonds would form favourable sites for the insertion of a muon. Formation of the bond-centre site requires an elongation of the bond by as much as 40%, and such pre-stretched bonds, expected in an amorphous structure, should lead to a smaller formation energy and greater stability. The larger isotropic component of the hyperfine constant for these anisotropic sites in the a-Ge:H compared to that for the crystal, could possibly arise as a consequence of the muon lying along an elongated bond but displaced from the centre towards one of the neighbouring Ge atoms.

5.4 Aperçu

Although both group IV semiconductors are physically similar, μSR experiments expose marked differences in the nature of the sites adopted by muonium (hydrogen).

Silicon, the more understood of the two materials, exhibits site preferences in agreement with other research, demonstrating the bond-centre to be the site of lowest energy, while the isotropic centre is maintained as the most favoured of the paramagnetic sites. For germanium, on the other hand, since only nonsensical fittings could be made, it is difficult to make similar conclusions to those of Si. Such irregular results are perhaps evidence of the equal energy of both T and BC paramagnetic centres, which may in-turn induce unexpected dynamics, such as the simultaneous ionisation of each centre, and T $\leftrightarrow$ BC site interconversions.

The hyperfine parameters of pcr-Si show excellent agreement with those found by other research groups. By the introduction of an amorphous CRN, the nature of the paramagnetic sites changes, whereby the Mu_T becomes near vacuum-state, and the Mu_{BC} adopts a near-Mu_T isotropic hyperfine parameter while the anistropic hyperfine parameter (D) also undergoes a noticeable increase, indicating a possible displacement of the

muon from the bond-centre position. Again, the behaviour of pcr-Ge differs to that of pcr-Si, whereby the some hyperfine parameters do not agree with those of other research. Possibly as a consequence of potentially unexplained dynamics, the parameters for the anistropic centre are much greater than for other groups', whereby the isotropic and anisotropic hyperfine parameters exhibit nonsensical values, although the hyperfine parameter for Mu_T remains in agreement. With an amorphous network though, such discrepancies do not seem to arise; realistic hyperfine parameters, similar to those found for c-Si by other groups, are found, although a reduction in the muon-electron coupling of the Mu_T centre does occur. The major drawback to measurements on the amorphous germanium samples were the over-large diamagnetic fractions, probably arising as a consequence of poor deposition conditions, inducing large numbers of defects and possible contaminants.

A good candidate for future experiments would be amorphous germanium samples: intrinsic and hydrogenated, deposited and stored in conditions likely to reduce defects, e.g. above room-temperature deposition, oxidation and possible HCl contamination. Certainly, the prospect of slow-muon μSR experiments at the Rutherford Laboratories would allow the minimisation of contamination, since the sample material would not need to be broken-up, thereby reducing any oxidation effects, and also removed from the deposition substrate, reducing hydrogenation and other HCl contamination. Another topic of great potential for future consideration is the proposed T $\leftrightarrow$ BC site interconversions. The improved RF-μSR facilities at RAL may, once again, lend support to such investigations, particularly exploiting the techniques ability to discriminate between Mu_T and Mu_{BC} centres. In addition, the analysis of doped samples may add an extra source of information, perhaps removing the equal-energetics of the T and BC centres, or encouraging the formation of, say, a T centre, and amending the possible cycle of the T $\leftrightarrow$ BC site conversions.

Bibliography

[1] J.H. Brewer, K.M. Crewe, F.N. Gygax, R.F. Johnson, B.D. Patterson, K.W. Blazey, T.L. Estle and S.L. Rudaz, Phys. Rev. **B 32**, (1985), 530.

[2] R.F. Kiefl, M. Celio, T.L. Estle, S.R. Kreitzman, G.M. Luke, T.M. Riseman and E.J. Ansaldo, Phys. Rev. Lett. **60**, (1988), 224.

[3] S.F.J. Cox and M.C.R. Symons, Chem. Phys. Lett. **126**, (1986), 516.

[4] B.D. Patterson, Rev. Mod. Phys. **60**, (1988), 69.

[5] S.R. Kreitzman, B. Hitti, R.L. Lichti, T.L. Estle and K.H. Chow, Phys. Rev. **B 51**, (1995), 13117.

[6] T.A. Claxton, D.M. Maric and P.F. Meier, Chem. Phys. Lett. **192**, (1992), 29.

[7] R. Jones, Physica B **170**, (1991), 181.

[8] C.G. Van de Walle and N.H. Nickel, Phys. Rev. **B 51**, (1995), 2636.

[9] S.K. Estreicher and D.M. Maric, Phys. Rev. Lett. **70**, (1993), 3963.

[10] R.L. Lichti, S.F.J. Cox, K.H. Chow, E.A. Davis, T.L. Estle, B. Hitti and C. Schwab, (1999), *to be published.*

[11] P.F. Meier, Hyperfine Interact. **86**, (1994), 723.

Chapter 6

Measurements and discussion - III - V semiconductors

For this second of three experimental data chapters, the results of repolarisation measurements on the III-V semiconductors pcr-GaAs and pcr-GaP will be presented and discussed. Again, the primary interest will be the characterisation of the muonium sites and where the muon/muonium resides, via the extraction of certain parameters from both TF and LF experiments, principally the initial amplitudes and relaxation rates. No amorphous samples have been studied.

For the elemental semiconductors silicon and germanium, the overall nuclear spin is zero, and therefore only affects of the muon-electron interactions are detected in μSR data. In the III-V semiconductors, GaAs and GaP, a large percentage of nuclei possess nuclear moments, which complicates the situation, since, as well as the hyperfine muon-electron interaction, a nuclear-electron hyperfine interaction and also a superhyperfine nuclear-muon interaction occur. A further complication with these materials, is the existence of two inequivalent tetrahedral sites: from Figure 6.1, the zinc-blende structure of GaAs is shown. In the figure, the shaded atoms could represent the Ga atoms, and the unshaded atoms represent As; conversely, in a neighbouring cage, the atomic allocation would be reversed, leading to inequivalent cages in which Mu_T may tarry.

Over recent years extensive studies, both experimental and theoretical, have been carried out into the hyperfine structure of Mu_{BC} in GaAs and GaP, leading to calculated

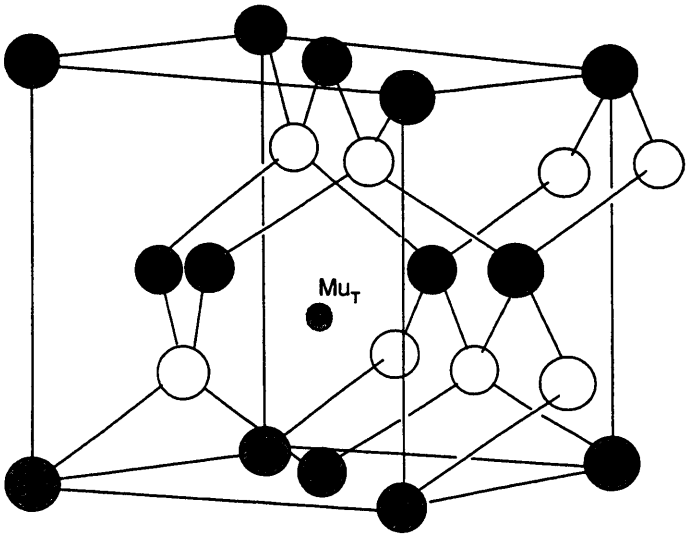

Figure 6.1: The zinc-blende structure of GaAs. In such a structure, the shaded atoms may represent gallium atoms, and the unshaded atoms arsenic. In the neighbouring cage, the allocation of atom types will be reversed.

values of the hyperfine parameters and relative fractions in c-GaAs and c-GaP. In c-GaAs, for anisotropic Mu_{BC}, $A_{iso} = 131.1\,\text{MHz}$ and $D = 86.71\,\text{MHz}$ ($A_{||} = 217.8\,\text{MHz}$ and $A_{\perp} = 87.74\,\text{MHz}$), whereas for isotropic Mu_T, $A = 2883.6\,\text{MHz}$[1]. The dependence of the hyperfine coupling on the local environment can be exploited in gaining a greater understanding of the muonium site, and therefore also of hydrogen in these materials, as demonstrated in Chapter 5 for Si and Ge. In general, a large hyperfine coupling indicates that the separation between the muon and the electron is small; and vice-versa that a small hypefine coupling indicates a large muon-electron separation.

It has been shown that the potential energy surface for neutral interstitial hydrogen has three minima: at the two inequivalent tetrahedral sites and near the BC site[2]. The presence of Mu_{BC} results in a trigonal distortion of the four bonds to each nearest-neighbour atom[3]. To accommodate the bond-centre hydrogen, the Ga–As bond actually relaxes by 35%. Furthermore, the H may form a stronger bond with the less electronegative Ga atom with an unpaired electron in a non-bonding orbital than it does with the more electronegative As atom. The reverse can also occur, with the hydrogen bonding with the As atom. Which configuration occurs is dependent upon two factors: the relative strengths of the Ga–H and As–H bonds, and the difference of stability of the lone elec-

tron when in the antibonding orbital of the As atom or the Ga atom. Even though the unpaired electron is more stable on the As, the As–H bond is stronger than the Ga–H bond, resulting in a competition between the two situations. Though shared by the Ga and As atoms, the spin density is higher on the As atom: 38% on Ga compared to 45% on As.

6.1 Sample preparation

For both pcr-GaAs and pcr-GaP samples, the crushing of the crystalline wafers was performed in-house. The crystalline wafers were purchased commercially. A summary of Table 4.1, presenting both samples relevant to this chapter is shown in Table 6.1. As mentioned in Chapter 4, it was essential that as much of the powdered sample be placed in the sample holder as possible, in order to increase the accuracy of the experimental data.

Sample	Deposition type	Temperature (°C)
pcr-GaAs	Crushed c-GaAs wafer	—
pcr-GaP	Crushed c-GaP wafer	—

Table 6.1: Growth conditions for pcr-GaAs and pcr-GaP samples.

This chapter presents the analysed experimental data for the TF-μSR and LF-μSR data, and their relaxation rates. Theoretical fittings have not been imposed on the data for GaAs, as will be explained later in this chapter.

6.2 Experimental TF-μSR results

By measuring the temperature dependence of the muon polarisation with a magnetic field applied transverse to the beam polarisation, the diamagnetic fraction of the sample can be found, i.e. the proportion of muons which reside in diamagnetic sites.

6.2.1 Diamagnetic fraction

The temperature dependence of the diamagnetic fraction for the pcr-GaAs and pcr-GaP samples is shown in Figure 6.2. It can be seen that for both materials, f_d is relatively

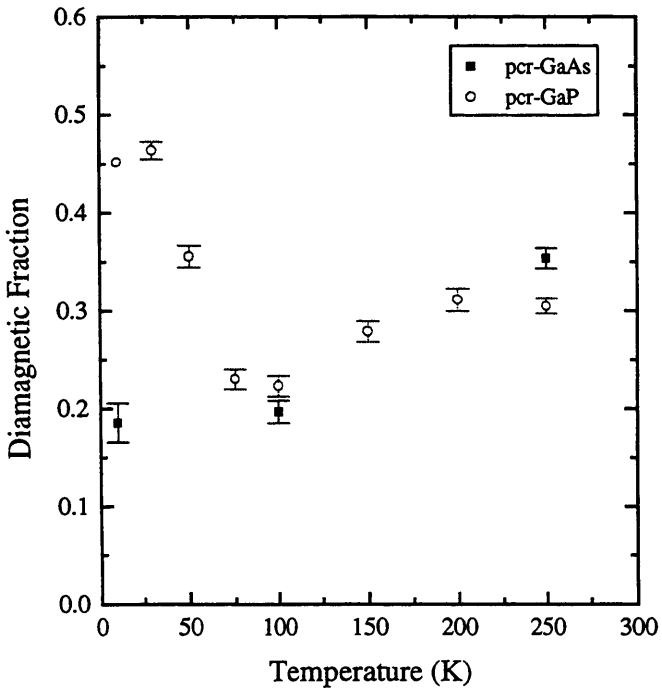

Figure 6.2: Diamagnetic fraction of the pcr-GaAs and pcr-GaP samples.

small, averaging at about 30% for most temperatures. The f_d of the pcr-GaAs appears to behave similar to that of the polycrystalline silicon samples, starting at about 20% at low temperatures, and rising with increase in temperature. Unfortunately, since there are only three data points, very little can be concluded about the mid-range of temperatures. With such low values of the diamagnetic fraction, it can be concluded that few defect centres occur within the material, probably because of a low defect density in the starting crystalline materials. The temperature dependence of f_d for pcr-GaP is different from that of pcr-GaAs. Starting at a higher value of 45%, f_d begins to rapidly fall with an increase in temperature, reaching a minimum of 20% at 100 K. For $T > 100$ K, f_d begins to slowly increase with increase in temperature. This difference in the temperature dependence of the two materials is somewhat surprising. It might be expected that for such similar systems, with near-identical preparation histories, the behaviours would be closer than observed.

6.2.2 Relaxation rates

The $1/T_2$ relaxation rates of pcr-GaAs and pcr-GaP are shown in Figure 6.3. Here there is clear similarity between the behaviour of the two materials. At low temperatures, the

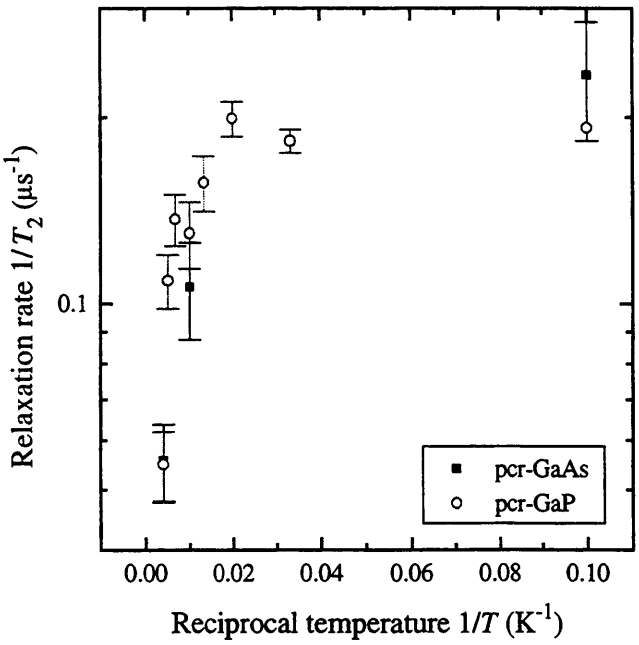

Figure 6.3: The temperature dependence of $1/T_2$, measured at 20 gauss, for pcr-GaAs and pcr-GaP.

relaxation rates are relatively high, and as the temperature is increased, a fall occurs, such that by 250 K the rates are negligibly small with $1/T_2 \approx 0.06\,\mu s^{-1}$. Interestingly, both of the $1/T_2$ curves resemble the curve for pcr-Si shown in Figure 5.2. On the logarithmic scale of the $1/T_2$ axis, the decay of the relaxation rate for pcr-GaP approximates to a straight line with increase in temperature, thus indicating an approximately exponential decay of $1/T_2$ with temperature. Of course, with so few data points for pcr-GaAs, an exponential decay is by no means certain.

6.3 Experimental LF-μSR results

6.3.1 Repolarisation curves and theoretical fittings

pcr-GaAs

The repolarisation curve of the LF-μSR data for pcr-GaAs is shown in Figure 6.4. Unfortunately, a full data set, from low to high magnetic fields, was obtained for this sample only at 100 K; at low and high temperatures, only high-field measurements were made.

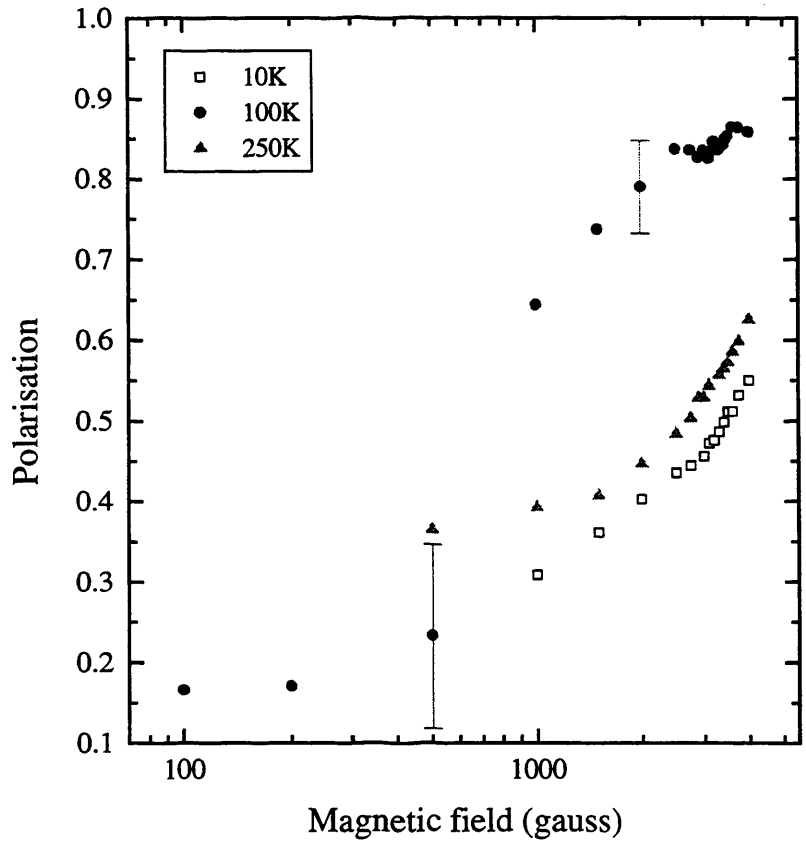

Figure 6.4: The field dependence of the polarisation for pcr-GaAs.

This lack of experimental data presents the first problem when trying to make theoretical fittings. Another difficulty is the existence of a large 'missing' fraction. As seen in Figure 6.4, for temperatures of 10 K and 250 K, even at high fields ($B > 1000$ gauss) the polarisation is still small, reaching only about 60%. A large 'missing' fraction can occur when the relaxation rate of the raw asymmetry curve is very large, and therefore much of the relaxation, and therefore the decay of asymmetry, occurs before the ISIS equipment can detect it. If a missing fraction is genuinely responsible for the region of

data where there appears to be an unusually low value of polarisation, there would be a large relaxation rate; and where the polarisation does not appear to be unusually low, there would be a small relaxation rate. This will be further discussed in Section 6.3.2.

An attempt was made to generate theoretical fits. These fits are not presented here because of a lack of their physical plausibility. When fitting the 100 K data, a value of $A \approx 6000$ MHz was obtained, which, being 50% larger than the hyperfine constant of vacuum muonium would seem to be highly implausible. Likewise for the fittings of the 10 K and 250 K data, an unreasonable value of A was found and furthermore a diamagnetic fraction of zero was needed, which represents a significant digression from the experimental TF value. With these findings, it was concluded that the fittings would be of little value.

pcr-GaP

The repolarisation curve of the LF-μSR data for pcr-GaP is shown in Figure 6.5. Unlike the pcr-GaAs sample, a reasonable amount of data were collected. As such, it was possible to produce theoretical fittings to the experimental data, shown as the lines in the figure. The parameters used to generate these fittings are shown in Table 6.2. It should be noted that no sensible fittings were possible for the data collected at 200 K, probably due to a low-field missing fraction occurring as a result of fast relaxation rates. The parameters for the wider-studied c-GaP are also presented in the Table.

It can be seen that the fitting parameters for pcr-GaP are significantly different to those of c-GaP and also the experimentally measured diamagnetic fraction presented in Figure 6.2. For both the low-temperature low-field data sets, the polarisation is very different from the corresponding regimes of the pcr-GaAs data. Strangely, for both 10 K and 50 K, the fitting parameters yield no diamagnetic fraction, even though the TF measurements suggest $f_d \approx 40\%$. Again, such a discrepancy intimates the possibility of a significant low-field missing fraction. From the fitting parameters, there are no anisotropic Mu_{BC} sites present; indeed it would appear that all the muonium resides in the isotropic Mu_T sites. Although the relative fractions of pcr-GaP differ from

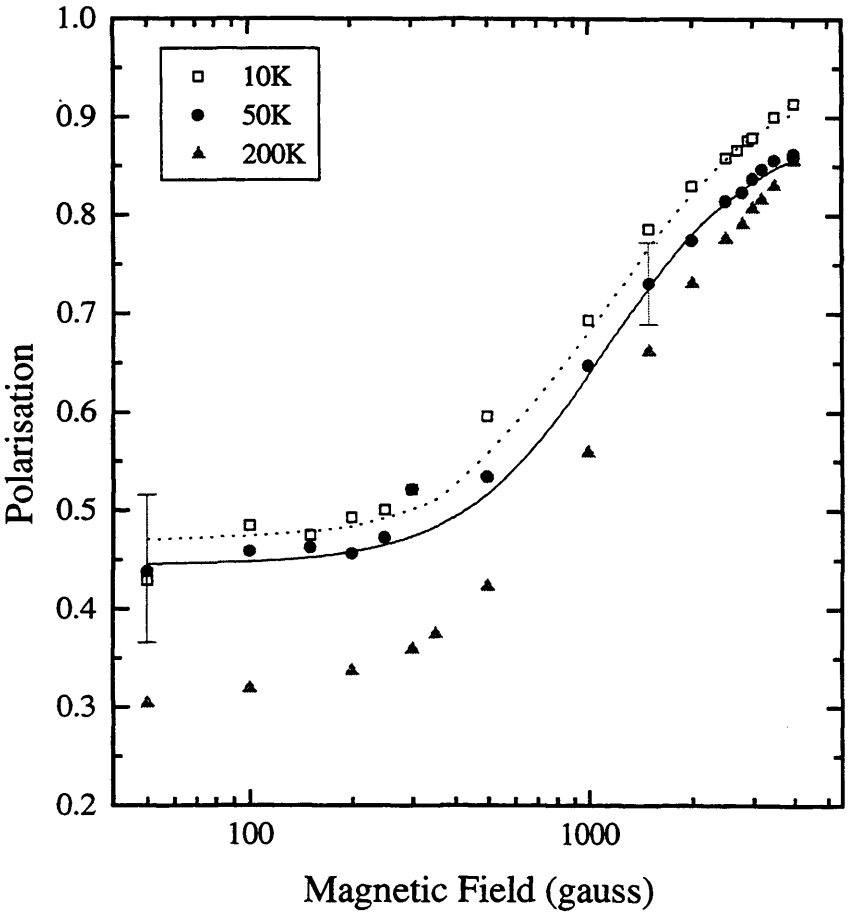

Figure 6.5: The field dependence of the polarisation for pcr-GaP.

Sample	T (K)	Dia.	Isotropic		Anisotropic		
		f_d (%)	f_{Mu_T} (%)	A (MHz)	$f_{Mu_{BC}}$ (%)	A_{iso} (MHz)	D (MHz)
c-GaP	10	11	72	2914	18	126	93
pcr-GaP	10	0	94	3200	0	–	–
pcr-GaP	50	0	89	3200	0	–	–
pcr-GaP	200	–	–	–	–	–	—

Table 6.2: The expected relative fractions and hyperfine parameters for c-GaP (from [4]), and the fitting parameters and fractions for the pcr-GaP.

those of c-GaP, the hyperfine parameter A remains similar; for c-GaP, $A = 2914\,\text{MHz}$, and for pcr-GaP, $A \approx 3200\,\text{MHz}$. As a consequence, there would appear to be little difference between the tetrahedral cage-centre sites of the crystalline and polycrystalline GaP samples.

Significantly, as the temperature is increased from 10 K to 50 K, still within a low-temperature regime, the missing fraction, $f_{missing}$, virtually doubles from 6% to 11%. As such, it could be expected that with a further temperature increase to 200 K, there would be an additional significant increase in $f_{missing}$. This will be further discussed later in Section 6.3.2, when considering the $1/T_1$ relaxation rates. As with the pcr-GaAs, it is postulated that an increase in $f_{missing}$ will coincide with an increase in $1/T_1$.

6.3.2 Relaxation rates

pcr-GaAs

The field dependence of the $1/T_1$ relaxation rates for pcr-GaAs are shown in Figure 6.6. Again, because of a lack of low-field data at both 10 and 250 K, conclusions will be difficult to make. At 10 K, the relaxation rate is relatively high with $1/T_1 = \lambda_1$ reaching a maximum of $9.0\,\mu\text{s}^{-1}$ at 2000 gauss. Subsequently, as the field is increased further, λ_1 slowly decreases. Such a field dependence of the relaxation rate does not directly agree with the proposal that the distinctly-low LF polarisation is attributed to the missing fraction, occurring as a result of very large relaxation rates undetectable to the ISIS instrumentation. However, if λ_1 is particularly large, then the ISIS instrumentation may still not detect any large initial rapid asymmetry decay, thus recording a lower λ_1 than is actually occurring. As can be seen from figure, at high fields, there is an approximately B_0^{-2} dependence of λ_1. Such a dependence can be a signature that a neutral centre has an isotropic hyperfine parameter.

When the temperature is increased to 100 K, a similar field dependence of λ_1 is seen. A maximum occurs at 1000 gauss, but at a smaller value of λ_1 than the maximum at 10 K. At high fields, λ_1 rapidly decreases such that at $B = 4000$ gauss, $\lambda_1 = 0.2\,\mu s^{-1}$, significantly less than the corresponding value for 10 K. Again, by considering the sig-

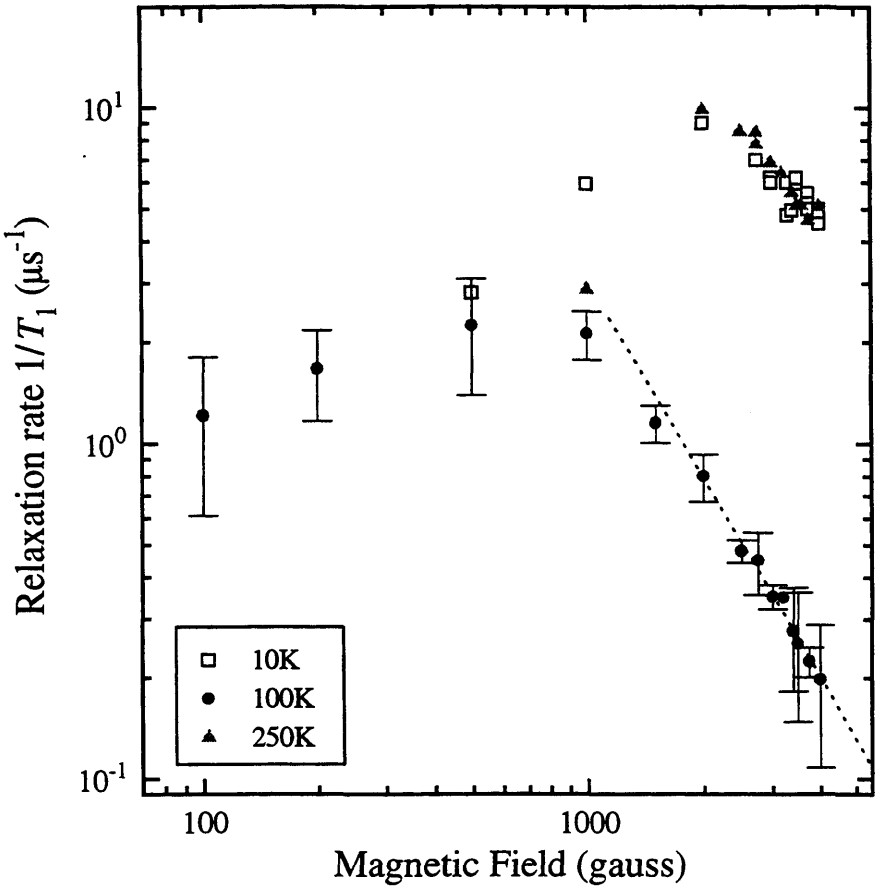

Figure 6.6: The field dependence of $1/T_1$ for pcr-GaAs. The dotted line represents a B_0^{-2} dependence.

nificant $f_{missing}$ at 100 K (see Figure 6.4), there seems to be an element of suspicion as to whether the λ_1 curve is genuine. With such low relaxation rates, no missing fraction would be expected; conversely, it is possible that, as with the 10 K data, very large relaxation rates may just be occurring, undetectable to ISIS instumentation, which then records a lower-than-actual value for λ_1. As can be seen from the Figure 6.6, at high fields, there is a clear B_0^{-2} dependence of λ_1, thereby again leading to the conclusion that the neutral centre possesses an isotropic hyperfine parameter.

Unfortunately, the number of data points for the 250 K measurements is even more limited than that for data at 10 K. Measurements only exist for fields greater than 1000 gauss. At high fields there is a clear overlap of data points with those of 10 K; the 1000 gauss point appears to be abnormally low, and does not agree with eye-ball inspection of the raw-data asymmetry curves. Again, such large relaxation rates correspond

to a significant missing fraction seen in Figure 6.4, though with so few data points, no firm conclusion can be made. As with the 10 and 100 K data, there is a high-field B_0^{-2} dependence of λ_1.

pcr-GaP

The field dependence of the $1/T_1$ relaxation rates for pcr-GaP is shown in Figure 6.7. With regard to the repolarisation curves for pcr-GaP (Figure 6.5) suffering large missing

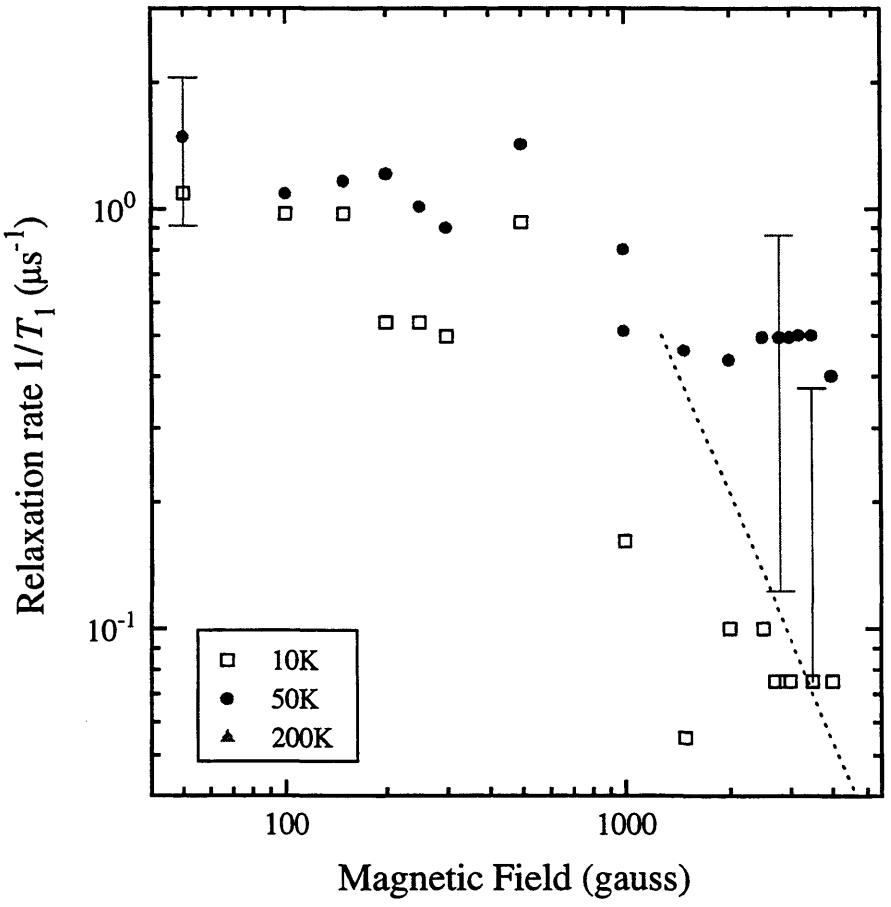

Figure 6.7: The field dependence of $1/T_1$ for pcr-GaP. The dotted line represents a B_0^{-2} dependence. *(It should be noted that due to log scale of the $1/T_1$, the zero values of the 200 K data cannot be seen on this figure.)*

fractions, it would appear that here there is a definite correlation between high relaxation rates leading to large missing fractions. When comparing the repolarisation curves and the $1/T_1$ curves of pcr-GaP, at both 10 and 50 K, the missing fractions are small, whilst $1/T_1$ remains small, although a minor increase in $f_{missing}$ coincides with the minor

increase in $1/T_1$ for the 50 K data. With further increase in temperature to 200 K, there was no measurable relaxation rate even though there is a significantly large $f_{missing}$. It is therefore assumed that, as an increase in $1/T_1$ occurred with an increase in temperature from 10 to 50 K, then likewise, an increase in $1/T_1$ between 50 and 200 K may also occur. If, at 200 K, the relaxation rate is simply too fast for the ISIS instrumentation to detect, which can occur when $1/T_1 > 10\,\mu s^{-1}$, then the raw data would yield a flat asymmetry curve, and a relaxation rate of $1/T_1 = 0\,\mu s^{-1}$. Such behaviour could lead to the large $f_{missing}$, inferred from Figure 6.5.

The dotted line in Figure 6.7 is a B_0^{-2} dependence. As can be seen, no clear B_0^{-2} dependence of λ_1 appears to occur exponentially, at any temperature, although the scatter in the points does not permit a firm conclusion.

6.3.3 Discussion

The diamagnetic fraction of pcr-GaAs behaves in a similar manner at low temperature to that of pcr-Si. At 15 K, f_d is about 20%, relatively low, although still larger than would be expected for c-GaAs. In the crushing process defects, such as dislocations and vacancies, could have been introduced. Certainly up to 100 K, f_d remains constant, indicating that no conversion of paramagnetic to diamagnetic states has occurred, although inter-paramagnetic conversion cannot at this stage be ruled out. By 250 K, only a small increase to about 36% has occurred, differing greatly to the significant increases seen in pcr-Si and pcr-Ge. As such it can be assumed that only a small concentration of paramagnetic states has been ionised to diamagnetic centres. By room temperature, the dominant diamagnetic centre is known to be Mu_T^-, located near a T_{Ga} site[5]. At these low temperatures, with $f_d < 40\%$ the paramagnetic state(s) are dominant. Alas, because of the low-field abnormality in the LF-polarisation data, no theoretical fittings were possible, and thus the dominant paramagnetic centre remains unknown. From the correlation of the field-regions of poor LF-μSR data with those fields at which large $1/T_1$ relaxation rates were found, it certainly seems likely that large values of $1/T_1$ relax the LF-asymmetry too fast for the ISIS equipment to permit determination of

an accurate value of a_0 (initial asymmetry), leading to a generous missing fraction. In Figure 6.8, is shown an illustration of how large relaxation rates can lead to a loss of the initial assymetry. Under conditions where a low $1/T_1$ relaxation rate occurs, the

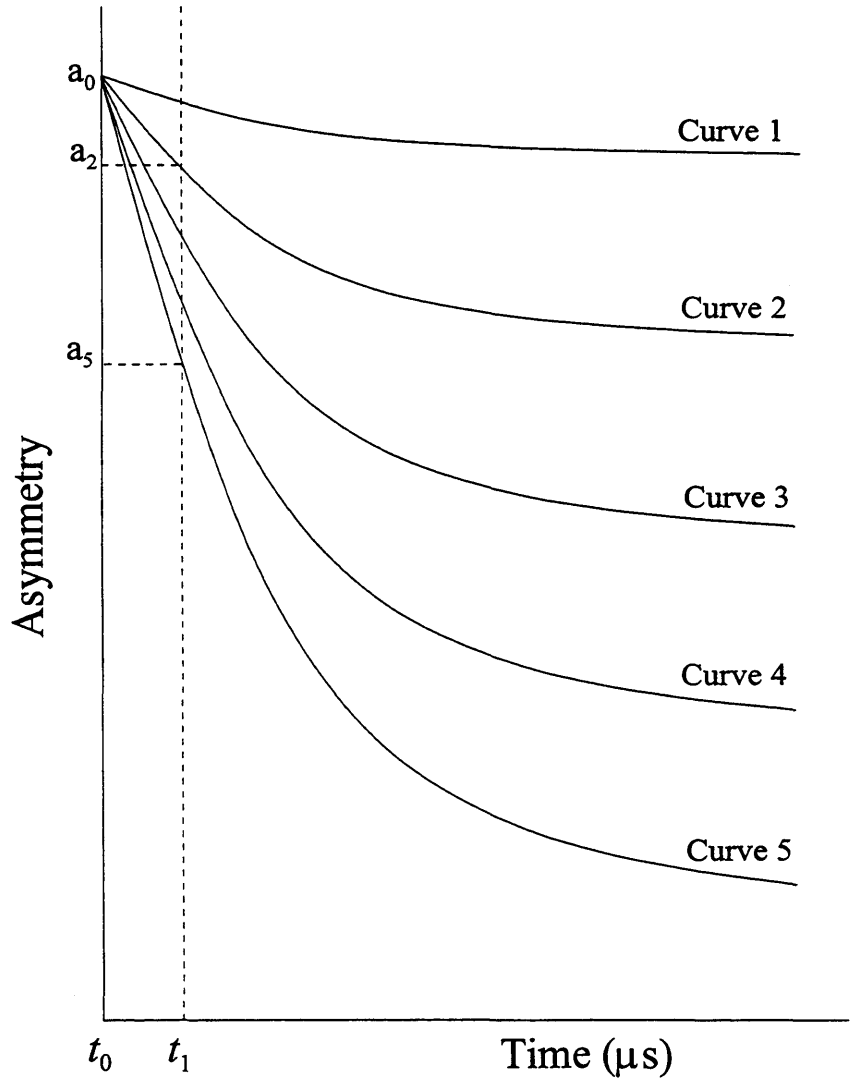

Figure 6.8: A schematic for the variation of the missing fraction with relaxation rate; where Curve 1 represents an asymmetry curve of low $1/T_1$, and with increasing curve number, so also $1/T_1$ increases. The 'true' initial asymmetry is shown as a_0, and a_2 and a_5 represent the measured asymmetry for 'conditions' 2 and 5, respectively.

initial asymmetry is approximately a_0. For a change of conditions, e.g. an amendment to the applied magnetic field, an increase in $1/T_1$ may occur; if $1/T_1$ is sufficiently large, it is thought that a sizeable missing asymmetry, $a_{missing}$, may occur. In Figure 6.8, for the 'conditions' of Curve 2, the $a_{missing}$ is equal to $a_0 - a_2$. For a further change of conditions, and a further increase in $1/T_1$, the missing asymmetry can increase, for

example, in Curve 5, which has a very large $1/T_1$, the $a_{missing} = a_0 - a_5$. It is postulated that the behaviour of pcr-GaAs corresponds to Curve 5 of the figure, whereby, a very large $1/T_1$ relaxation rate can lead to a significantly large missing fraction, and thus an abnormally low measured asymmetry.

By examining the low-field $1/T_1$, for all temperatures λ_1 *appears* to be very low with a distinct mid-field discontinuity. As such, there appears to be a 'missing fraction' of the relaxation rates, as well as the polarisation, and the discontinuity could mark a cut-off point below which the time resolution of the ISIS equipment has been exceeded. Interestingly, from Figure 6.4, it can be seen that for the high-field region, where a suitable quantity of data points are present, the 100 K polarisation is significantly higher than for 10 and 250 K. Such a larger polarisation coincides with the minima of the Mu_T hop rate[6], shown in Figure 6.9, and the $1/T_1$ relaxation rate, which occurs at 80-

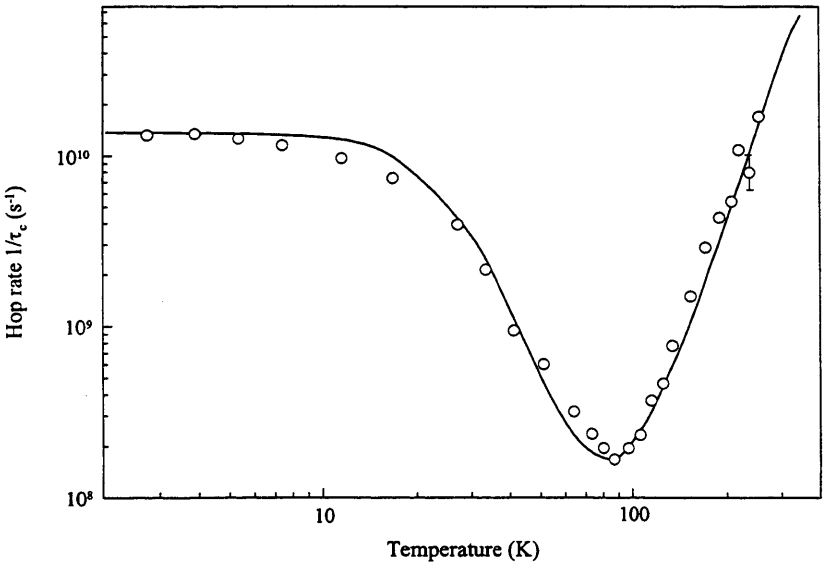

Figure 6.9: The temperature dependence of the Mu_T hop rate for c-GaAs.

100 K, and is almost two orders of magnitude smaller than at $T \leq 20$ K and $T \geq 200$ K. Furthermore, Kadono *et al*[6] found that for c-GaAs, at 100 K, the $1/T_1$ relaxation rate was increased five fold when reducing the magnetic field from 4000 gauss to 2000 gauss. Such an increase in the relaxation rate was not seen for pcr-GaAs, and thus it would seem likely that in the low-field region, the polarisation is again relaxing far too fast.

Since in Figure 6.6 it can be seen that the relaxation rates, at high-fields, are very

much smaller than for the 20 and 250 K, and thereby in agreement with Kadono *et al*, that there is a distinct correlation between high $1/T_1$ relaxation rates and Mu_T hopping rates, and a low polarisation most likely via a large missing fraction.

Although theoretical fittings, and hence estimates of the parameters for the centres, have not been possible, it might be expected that the relative fractions in pcr-GaAs would *approximately* agree with those for c-GaAs. It is known that the relative fractions for c-GaAs at low temperatures are $f_d = 9\%$, $f_{Mu_T} = 63\%$ and $f_{Mu_{BC}} = 35\%$, and therefore the Mu_T centre is by far the most dominant of all the site types. Similarly, the accepted value of the hyperfine parameter of the isotropic centre, A, is known to be 2884 MHz at low temperatures[4], thus indicating a pseudo-vacuum state muonium.

Considering that the pcr-GaP sample had been prepared from a crystalline wafer, in a technique identical to that of pcr-GaAs and pcr-Si, the low-temperature diamagnetic fraction at about 45% is much higher than might have been anticipated. In such a quasi-crystalline intrinsic sample, the concentration of dangling bonds would be expected to be very low, leading to a small f_d. With an increase in temperature, f_d begins to fall, reaching a minimum at about 100 K, after which a slow increase in f_d occurs up to room temperature. Such behaviour, very much different to that witnessed in the group-IV materials of Chapter 5, indicates the conversion of diamagnetic states to paramagnetic Mu^0 states. The f_d should therefore be considered in wider terms than just the dangling bond state; for example, states other than the μ^+ could typically be Mu^-, where the muonium Mu has gained an additional electron, $(\mu^+e^-e^-)$ or Mu^+, where the muonium has lost its electron. Without having examined doped pcr-GaP samples, it is difficult to understand what is leading to this low-field loss of f_d. A possible explanation could be that upon entering the sample, the muon adopts not just a single electron, but two electrons to become Mu^-. With an increase in temperature, the second electron is lost and the muonium converts to a paramagnetic Mu centre. In the intrinsic pcr-GaP though, the ability to capture two electrons would appear unlikely, and therefore an additional explantion would appear to be necessary. Further confusion is added when the GaP behaviour is compared with that of GaAs. Upon examination of the $1/T_2$ relaxation

rates, there is a near-overlap of the curves for pcr-GaP and pcr-GaAs, and furthermore, other research groups have found the behaviour of GaP to bear close correlation with that of GaAs.

Unlike the fast-relaxing pcr-GaAs sample, theoretical fittings were made for the LF-polarisation of the pcr-GaP. The results were strikingly similar to the polarisation curves of pcr-Ge, fitting to which suggested no diamagnetic fraction was present, even though from the TF-μSR results it is inferred that the low-temperature f_d was about 45%. A surprise is that no bond-centred muonium appears to be present; in other words, the muonium entirely favours isotropic paramagnetic sites. This is in disagreement with the accepted parameters for c-GaP, seen in Table 6.2, where, although Mu_T is the dominant site, sizeable Mu_{BC} and f_d fractions exist, and no missing fraction is present. As such, there is a likelihood that the large experimental missing fractions are a result of high relaxation rates. There is a great deal of scatter in the relaxation rates at low temperatures. This indicates that the UDA analysis software is having difficulties in fitting the data, which usually indicates either very large or very small, almost negligible, relaxation rates. By 200 K though, it would appear that the polarisation is non-relaxing, which is most likely a consequence of very large relaxation rates being undetectable, much in the same way as for pcr-GaAs. It seems probable that, even though a smooth polarisation curve results (Figure 6.5), low-field relaxation rates are leading to a measured polarisation lower than is actually the case, and that this smaller polarisation forces a lower f_d, which in turn alters all the relative fractions.

What is clear from the results for pcr-GaP, as well as for pcr-GaAs, is that the dominant site is certainly the Mu_T centre, though with such large relaxation rates, its seems unlikely that the muonium is actually in a 'free' pseudo-vacuum state, since this would require the electron to have a large spin-density on the muon site, impeding relaxing interactions with the lattice. Of course, in both GaAs and GaP materials, a large percentage of nuclei possess nuclear moments leading to additional nuclear-muon and nuclear-electron interactions. With large numbers of nuclear moments, it seems likely that these nuclear interactions could present significant relaxation processes.

6.4 Aperçu

Like silicon and germanium, discussed in the previous chapter, GaAs and GaP have been widely studied using μSR techniques. Yet, surprisingly, much in a way similar to that of pcr-Ge, the results of both pcr-GaAs and pcr-GaP have proved very difficult to reasonably fit. It is thought that an abnormally large missing fraction is the culprit for such problems. As such, for future research into these two materials, a research facility, such as TRIUMF in Canada, where large relaxation rates can be measured, should be used. In addition, an improvement of the fitting procedures, which are still in their infancy, will be needed, taking into account large relaxation rates, large missing fractions and dynamic processes. The exploitation of RF-μSR techniques could present another arm of support in understanding these difficult III-V materials, as would the analysis of doped GaAs and GaP. In agreement with the early designs on the outset of the research documented within this thesis, the deposition and analysis of amorphous forms of GaAs and GaP would present worthy materials for future research and investigation, using the increasing varities of μSR techniques available within Britain and also further afield.

Bibliography

[1] R. Kiefl, J.W. Schneider, H. Keller, W. Kündig, W. Odermatt, B.D. Patterson, K.W. Blazey, T.L. Estle and S.L. Rudaz, Phys. Rev. **B 32**, (1985), 530.

[2] D.M. Maric, S. Vogel, P.F. Meier and S.K. Estreicher, Phys. Rev. **B 40**, (1989), 8545.

[3] J.W. Schneider, K.H. Chow, R. Kiefl, S.R. Kreitzman, A. MacFarlane, R.C. DuVarney, T.L. Estle, R.L. Lichti and C. Schwab, Phys. Rev. **B 47**, (1993), 10193.

[4] B.D. Patterson, Rev. Mod. Phys. **60**, (1988), 69.

[5] K.H. Chow *et al*, Phys. Rev. **B 51**, (1995), 14762.

[6] R. Kadono, R.F. Kiefl, J.H. Brewer, G.M. Luke, T. Pfiz, T.M. Riseman and B.J. Sternlieb, Hyp. Int. **64**, (1990), 635-640.

Chapter 7

Measurements and discussion - Chalcogenides

In this, the third of three experimental data chapters, the results of repolarisation measurements on chalcogenide semiconductors, namely amorphous Se, and Ge_xSe_{1-x} and Si_xSe_{1-x} glasses with $x \leq 0.33$, will be presented and discussed. Of principal interest will be any correlation between the characterisation of the muonium sites and the atomic structure, which is known to change on the addition of the cross-linking elements Ge and Si from the predominantly chain-like structure of a-Se to effectively two- and three-dimensional structures with possible atomic cages in the Ge_xSe_{1-x} and Si_xSe_{1-x} glasses.

Although it is known that small percentages of hydrogen incorporated into the chalcogenide alloys affect their optoelectronic properties[1, 2], no detailed studies have been made. It is through μSR techniques that further detection and identification of potential bonding sites for isolated hydrogen will hopefully be made.

As with the elemental semiconductors silicon and germanium, the nuclear spin of selenium is negligible, reducing any complications arising from nuclear-electron hyperfine as well as superhyperfine nuclear-muon interactions. Also, as for the polycrystalline and amorphous materials of Chapter 5, the glassy chalcogenides carry the advantage of a lack of orientation dependence, and thus no attention needs to be made with regard to the angle of the samples with respect to the muon beam and detectors.

This chapter will present the analysed experimental data for the TF-μSR and the LF-μSR experiments. Repolarisation curves, diamagnetic fractions, and $1/T_1$ and $1/T_2$ relaxation rates will be shown. Fittings from theoretical approximations will be presented for the LF-μSR data, yielding the relevant site fractions and hyperfine parameters. The relevance of the results will then be discussed.

7.1 Sample preparation

With the exception of the a-Se sample, all of the chalcogenide alloys were prepared by Professor E. Mytilineou, of the University of Patra, to whom sincere thanks is owed. A summary of Table 4.1, presenting samples relevant to this chapter, is shown in Table 7.1. Each melt-quenched material was ground, tightly packed into an aluminium holder,

Sample	Deposition type	Temperature (°C)
a-Se	Scraped from Xerox a-Se plate	–
g-$Ge_{10}Se_{90}$	Melt-quenched & crushed	850
g-$Ge_{22}Se_{78}$	Melt-quenched & crushed	–
g-$Ge_{33}Se_{67}$ ($GeSe_2$)	Melt-quenched & crushed	–
g-$Si_{10}10Se_{90}$	Melt-quenched & crushed	–
g-$Si_{20}Se_{80}$	Melt-quenched & crushed	1100
g-$Si_{33}Se_{67}$ ($SiSe_2$)	Melt-quenched & crushed	1100

Table 7.1: Growth conditions for amorphous and glassy chalcogenide samples.

covered by a mylar film, and then placed in the cryostat of the EMU beamline. As perhaps the simplest of the chalcogenides, a-Se would seem to be a reasonable starting point from which to study the more complex alloy chalcogenides.

7.2 Experimental TF-μSR results

Once again, by the measurement of the muon polarisation with a magnetic field of 20 gauss applied transverse to the beam polarisation, the sample's diamagnetic fraction, f_d, can be found as a function of temperature, and which can later be used in the theoretical fittings of the LF-μSR data.

7.2.1 Diamagnetic fraction

The temperature dependences of the diamagnetic fractions for the various chalcogenides are shown in Figure 7.1. As well as gaining information on the fraction of diamagnetic

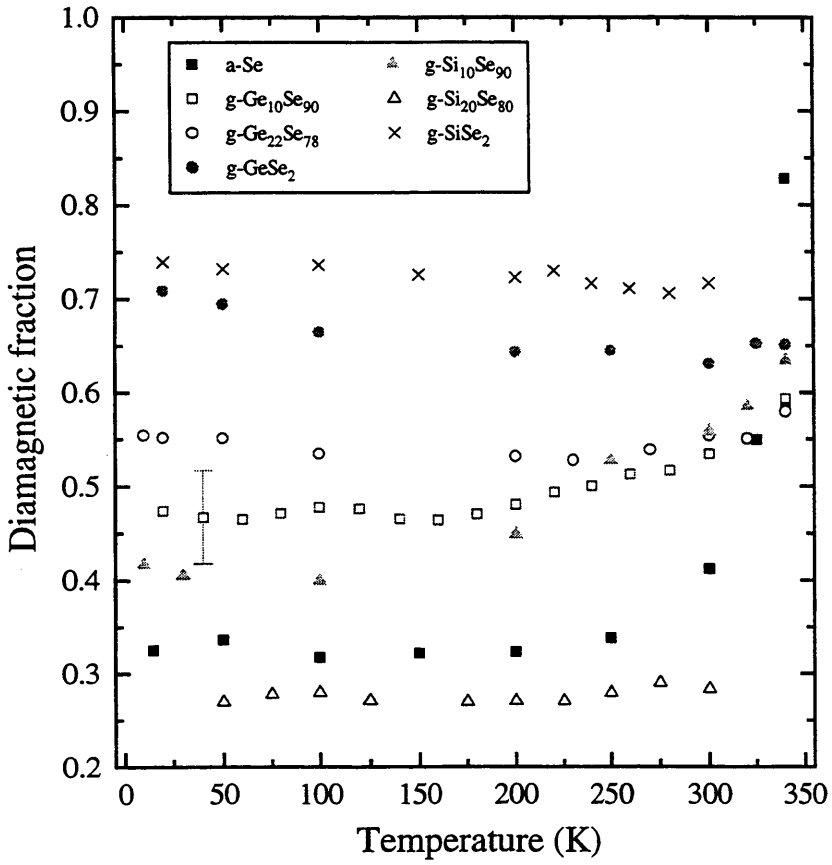

Figure 7.1: Diamagnetic fraction of the chalcogenides as a funtion of temperature.

sites, it is instructive to compare the fractions, and their temperature dependences, of all the samples, particularly with regard to the effects of increasing the germanium or silicon content in the selenium-based alloys.

From Figure 7.1 it can be seen that, with the addition of germanium or silicon to

selenium, the diamagnetic fraction changes considerably, both in terms of magnitude and temperature dependence. Beginning with the intrinsic a-Se sample, there appears to be little temperature dependence of f_d at low temperatures, the value remaining at approximately 32%. Approaching 300 K however, f_d begins to increase rapidly such that at 340 K f_d is equal to 82%, leaving very few muons residing in paramagnetic sites. The increase appears to coincide with the onset of the glass transition.

With the addition of germanium or silicon, there is, in general, an increase in f_d, with the g-$Si_{20}Se_{80}$ sample being an exception. On the whole though, f_d scales approximately inversely with Se content, shown in Figure 7.2. For all of the alloys, except for above

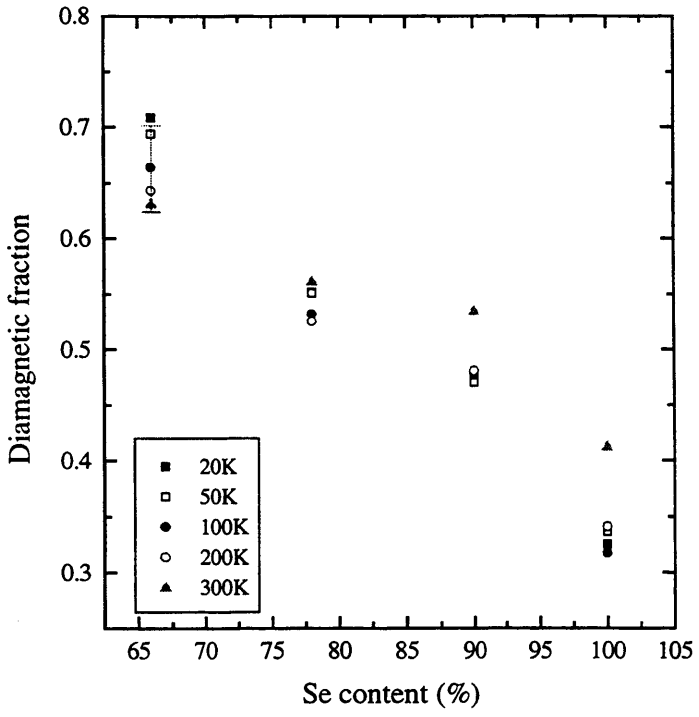

Figure 7.2: The variation of diamagnetic fraction with selenium content for the Ge-Se glasses.

300 K, virtually no temperature dependence is observed (seen clearly in Figure 7.2). Interestingly, the alloys can be separated into two groups: those exhibiting a small, sometimes very small, increase of f_d with temperature, and those that exhibit a small reduction of f_d with temperature. Only the g-$GeSe_2$ and g-$SiSe_2$ samples fall into the latter category, the remaining alloys falling into the former. Indeed, in Figure 7.1, these two 33% alloy materials are grouped closely and have significantly larger diamagnetic

fractions than the other alloys. On a cautionary note though, if the error bars ($\approx 10\%$) had not been removed from the figure for reason of preservation of clarity, then any increase or decrease of f_d with temperature could be seen to lie within experimental uncertainty. The significantly small f_d of g-$Si_{20}Se_{80}$ seems at odds with the other materials, especially since the preparation conditions were common to all, with a-Se being the obvious exception. With such a disparity, it will prove useful to consider later, in Section 7.2.2, as to whether the $1/T_2$ relaxation rate of g-$Si_{20}Se_{80}$ also differs significantly from that of the other alloys.

7.2.2 Relaxation rates

Noticeable relaxation effects were observed in the TF asymmetry curves. The $1/T_2$ curves for a-Se, g-$Ge_{10}Se_{90}$, g-$Ge_{22}Se_{78}$, g-$GeSe_2$, g-$Si_{10}Se_{90}$, g-$Si_{20}Se_{80}$ and g-$SiSe_2$ are shown in Figure 7.3. Unlike the diamagnetic fractions, the relaxation rates are significantly

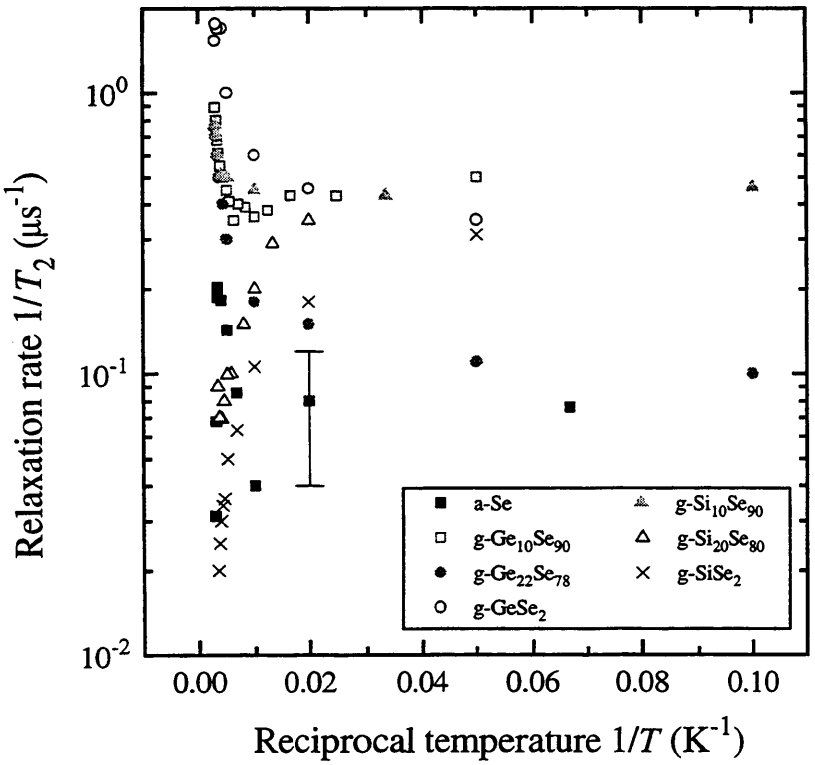

Figure 7.3: The temperature dependence of $1/T_2$, measured at 20 gauss, for the chalcogenides.

dependent on temperature. Again, groupings can be made, in which to express the

temperature dependence of the $1/T_2$ rates. The first of the three groups contains a-Se, which has its own unique $1/T_2$ behaviour. With an increase in temperature, $1/T_2$ is flat, then increases to a maximum of about $0.2\,\mu s^{-1}$ at 300 K and subsequently rapidly decreases to a value $\approx 0.03\,\mu s^{-1}$ at 340 K.

The second group of materials contains g-$Ge_{10}Se_{90}$, g-$Ge_{22}Se_{78}$, g-$GeSe_2$ and g-$Si_{10}Se_{90}$, whose relaxation rates increase with an increase in temperature. At low temperatures, the $1/T_2$ of g-$Ge_{22}Se_{78}$ and g-$GeSe_2$ increase approximately exponentially with temperature, in contrast to that of g-$Ge_{10}Se_{90}$ and g-$Si_{10}Se_{90}$, which remains approximately temperature independent, until about 250 K when $1/T_2$ begins to increase. The magnitude of $1/T_2$ varies significantly, such that $1/T_2$ of g-$GeSe_2$ is about 5 times larger than that of g-$Ge_{22}Se_{78}$. The $1/T_2$ curves of g-$Ge_{10}Se_{90}$ and g-$Si_{10}Se_{90}$ materials are very similar and almost overlap.

The third group of matarials contains g-$Si_{20}Se_{80}$ and g-$SiSe_2$, whose relaxation rates decrease with temperature, though no exponential relationship appears to occur. At low temperatures, their relaxation rates are comparable with those of g-$Ge_{10}Se_{90}$, g-$GeSe_2$ and g-$Si_{10}Se_{90}$ at about $0.35\,\mu s^{-1}$ but, following a subsequent rapid decrease with temperature, the values of $1/T_2$ fall to between 0.02 and $0.07\,\mu s^{-1}$ at 300 K, negligible in comparison to the corresponding values for g-$Ge_{10}Se_{90}$, g-$Ge_{22}Se_{78}$, g-$GeSe_2$ and g-$Si_{10}Se_{90}$.

7.3 Experimental LF-μSR results

7.3.1 Repolarisation curves and theoretical fittings

With the magnetic field aligned parallel to the beam polarisation, LF repolarisation curves were generated at 20, 100 and 300 K, with fields in the range 0 to 4000 gauss.

a-Se

The repolarisation curves derived from the LF-μSR data for a-Se are shown in Figure 7.4. Also shown in the figure are the theoretical approximations to the experimental data.

The parameters used to generate these fittings are shown in Table 7.2. Unlike silicon, germanium, gallium arsenide and gallium phosphide, no 'accepted' hyperfine parameters exist for selenium, and thus no comparisons can, as yet, be made. In the figure, perhaps the most obvious characteristic of the curves is, for measurements at 20 and 100 K, what appears to be a high-field 'Meier' cusp. Such a cusp represents a characteristic signal of muonium residing in anisotropic bond-centre or radical states. The depth of the cusp represents about 10% of the polarisation, larger than the uncertainty in the data, which is about 5%. Furthermore, at 100 K, the abundance of experimental data produces a relatively smooth curve, with very little scatter of the data points. It would seem that the cusp is a genuine feature.

Upon examination of the parameters in Table 7.2, it is seen that at low temperatures (< 100 K) the anisotropic paramagnetic state is the dominant site-type. At 20 K, diamagnetic sites and isotropic paramagnetic sites are equally favoured, although by 100 K, the two paramagnetic states are approximately of equal favour, with the diamagnetic fraction almost half that of the anisotropic fraction. By 300 K, all tetrahedral sites have been lost, but a discrepency arises between the TF-μSR experimentally measured f_d of Figure 7.1 and the fitting parameters of Table 7.2. Whereas the TF-μSR data shows an increase to about 40% for f_d at 300 K, the fitting parameters show a reduction to 10%. This anomaly will be discussed in greater detail later in Section 7.3.3. It thus seems that the fitting parameters for 300 K are nonsensical and should be treated with a great deal of caution. At 20 K, the tetrahedral site has a low hyperfine constant, $A = 1400$ MHz; for the anisotropic site, the hyperfine interaction is also low at $A_{iso} = 147$ MHz, close to the expected A_{iso} of a molecular radical state (200 - 400 MHz), with a large D of 61 MHz, indicating a large distortion of the electron spin-density on the muon. With an increase in temperature to 100 K, the isotropic hyperfine parameter has further decreased to $A = 1000$ MHz. The anisotropic hyperfine parameter remains approximately unchanged, though with an increase in D to 100 MHz, there is further distortion of the electron spin-density. With further increase of temperature to 300 K, there has apparently been a total loss of isotropic sites. For on the anisotropic site, the

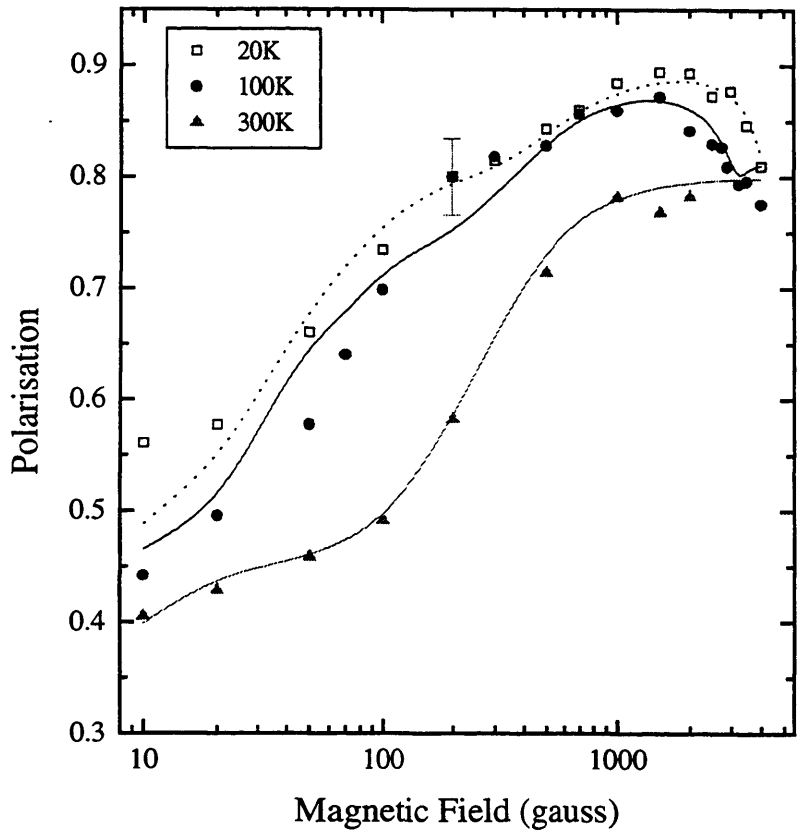

Figure 7.4: The field dependence of the polarisation for a-Se.

Sample	T (K)	Dia.	Isotropic		Anisotropic		
		f_d (%)	f_{Mu_T} (%)	A (MHz)	$f_{Mu_{BC}}$ (%)	A_{iso} (MHz)	D (MHz)
a-Se	20	26	25	1400	41	147	61
a-Se	100	20	36	1000	38	135	100
a-Se	300	10	0	—	70	700	15

Table 7.2: The fitted hyperfine parameters and relative fractions for a-Se. Note that the symbols Mu_T and Mu_{BC} are not really appropriate for chalcogenides, in which there are no sites with tetrahedral symmetry and for which there is no independent evidence for bond-centre sites. The terminology has been retained from the known sites in Group IV materials, but in this chapter should be interpreted as muonium in isotropic and anisotropic sites respectively.

fitted hyperfine parameter, A_{iso}, has increased to 700 MHz and D has drastically fallen to 15 MHz. Again, an element of caution should be maintained for these 300 K fittings, and furthermore the 700 MHz value of A_{iso} would appear to be physically too large for an anistropic centre, and thus very unlikely.

g-$Ge_{10}Se_{90}$

The repolarisation curves derived from the LF-μSR data for g-$Ge_{10}Se_{90}$ are shown in Figure 7.5. Also shown in the figure are the theoretical approximations to the experimental data, with the parameters used to generate these fittings being shown in Table 7.3. Unfortunately, for this g-$Ge_{10}Se_{90}$ sample, not even a hint of a high-field 'cusp' can be seen. A dominant diamagnetic fraction possibly accounts for its absence. With an increase in temperature, as expected from Figure 7.1, f_d remains constant, but almost all of the isotropic paramagnetic sites are lost, whilst, as with the a-Se material, there is an increase in the fraction of anisotropic paramagnetic states. At about 200 - 250 K though, the TF-μSR measurements record an increase in f_d, indicating the conversion of paramagnetic to diamagnetic states; the apparent loss of f_{Mu_T} and increase in $f_{Mu_{BC}}$ may be consequences of the fitting procedure trying to account for a missing fraction and therefore a low fitted value of f_d. The f_d is only slightly lower than the experimentally measured value though (common for the fitting procedures of most of the materials contained within this thesis), and the fitted parameters do not accurately reflect the mild increase of f_d above 200 K. Again, significant missing fractions occur at all temperatures, reminiscent of the results of a-Se, although on the whole, unlike for a-Se, the relative fractions do not appear to be physically unreasonable.

Considering the hyperfine parameters, at 20 K the isotropic muonium state with $A = 4000$ MHz, is virtually that corresponding to a near-vacuum state free muonium. Again, as for the a-Se sample, the anisotropic state, with an $A_{iso} = 250$ MHz and $D = 25$ MHz, would appear to be a molecular radical, rather than a bond-centre muonium state. With an increase in temperature to 100 K, the nature of neither paramagnetic state varies to any extent, apart from a noticeable reduction in the distortion of

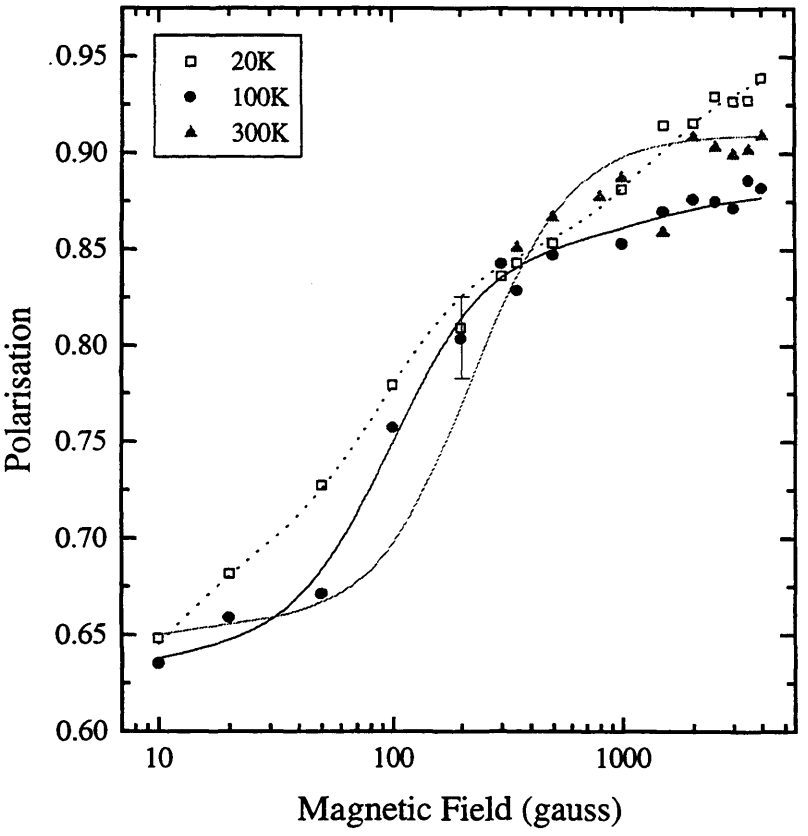

Figure 7.5: The field dependence of the polarisation for g-$Ge_{10}Se_{90}$.

Sample	T (K)	Dia.	Isotropic		Anisotropic		
		f_d (%)	f_{Mu_T} (%)	A (MHz)	$f_{Mu_{BC}}$ (%)	A_{iso} (MHz)	D (MHz)
g-$Ge_{10}Se_{90}$	20	43	20	4000	32	250	25
g-$Ge_{10}Se_{90}$	100	40	5	4000	43	275	5
g-$Ge_{10}Se_{90}$	300	40	0	—	51	625	5

Table 7.3: The fitted hyperfine parameters and relative fractions for g-$Ge_{10}Se_{90}$. See caption for Table 7.2 for the meaning of Mu_T and Mu_{BC}.

the electron spin-density for the radical muonium state, indicated by $D = 5\,\text{MHz}$. Continuing in the g-$Ge_{10}Se_{90}$ samples' behavioural similarities with a-Se, at 300 K, there is the total loss of an isotropic centre and the fitted hyperfine parameter of the anisotropic paramagnetic state has increased to $A_{iso} = 625\,\text{MHz}$, and the anisotropic parameter has fallen to $D = 5\,\text{MHz}$. Judging by the behavioural similarities of g-$Ge_{10}Se_{90}$ to a-Se, and the physically unreasonable value of $A_{iso} = 625\,\text{MHz}$, it would seem likely that a similar high-temperature dynamic mechanism is occurring, and thus these high-temperature parameters should be treated with an element of caution, since the mathematical approximations used do not take into account any such dynamics.

g-$Ge_{22}Se_{78}$

The repolarisation curve of the LF-μSR data for g-$Ge_{22}Se_{78}$ is shown in Figure 7.6 along with the theoretical approximations to the experimental data. The parameters used to generate these fittings are shown in Table 7.4. From the figure, a two-step repolarisation curve can be seen, indicating the presence of two differing paramagnetic sites, one isotropic and the other anisotropic. As expected, f_d remains approximately constant at all temperatures between 20 – 300 K, at about 46%; in addition, the fraction of isotropic paramagnetic sites remains nearly constant, at about 25%. On the other hand, the fraction of anistropic paramagnetic sites is reduced, though only to a small extent, with an increase in temperature, such that at 20 K, $f_{Mu_{BC}} = 29.2\%$, and at 100 and 300 K, $f_{Mu_{BC}} \approx 22\%$.

This temperature independence is seen also in the hyperfine parameters, both isotropic and anisotropic. At all temperatures measured (20, 100 and 300 K), A is equal to 4000 MHz, indicating that the isotropic state remains unchanged. For the anisotropic state, since at 20 K, $A_{iso} = 200\,\text{MHz}$ and $D = 15\,\text{MHz}$, it would seem that, as for the previous sample, the state is actually a molecular radical, as opposed to a bond-centre state. With an increase in temperature, the anisotropic parameter D remains constant, but a small decrease of A_{iso} occurs, to 130 MHz at 100 K and 110 MHz at 300 K, less indicative that with an increase in temperature, the muonium radical is the favoured

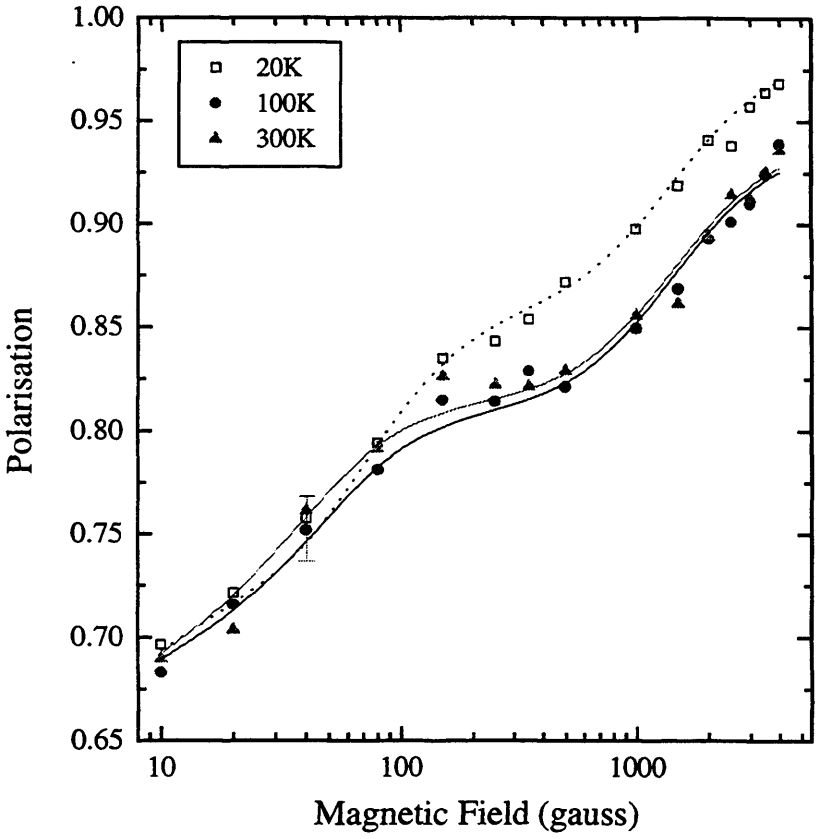

Figure 7.6: The field dependence of the polarisation for g-$Ge_{22}Se_{78}$.

Sample	T (K)	Dia.	Isotropic		Anisotropic		
		f_d (%)	f_{Mu_T} (%)	A (MHz)	$f_{Mu_{BC}}$ (%)	A_{iso} (MHz)	D (MHz)
g-$Ge_{22}Se_{78}$	20	44	25.2	4000	29.2	200	15
g-$Ge_{22}Se_{78}$	100	46	26	4000	22	130	15
g-$Ge_{22}Se_{78}$	300	46	25.5	4000	22.7	110	15

Table 7.4: The fitted hyperfine parameters and relative fractions for g-$Ge_{22}Se_{78}$. See caption for Table 7.2 for the meaning of Mu_T and Mu_{BC}.

anisotropic site type. Such all-round temperature independence leads to the possibility that with an increase in Ge content from 10 to 20% in the samples, there occurs an increase in the overall stability of the material.

g-$GeSe_2$

The repolarisation curves of the LF-μSR data for g-$GeSe_2$ are shown in Figure 7.7. Theoretical approximations are presented, overlayed on to the experimental data, and the parameters used to generate these fittings are shown in Table 7.5. Unlike with the earlier considered chalcogenide alloys, the f_d of g-$GeSe_2$ is reduced with an increase in temperature, from 54.5% at 20 K to 40% at 300 K. At low temperatures, $f_p = 46\%$, with the isotropic site being the favoured of the paramagnetic states. As the temperature is increased, the two paramagnetic states are now equally favoured, with $f_{Mu_T} = f_{Mu_{BC}} = 25\%$, although with the overall increase in f_p, the diamagnetic states and paramagnetic states are equally favoured by the muon. At 300 K though, with the reduction in f_d, the diamagnetic sites no longer dominate, since $f_d = 40\%$ and $f_p = 60\%$. As with the 100 K data, both paramagnetic site-types are again equally favoured.

The hyperfine parameters vary very little from the earlier alloys, retaining values very similar to $Ge_{22}Se_{78}$. At low temperatures, the hyperfine parameter of the isotropic centre is $A = 2750$ MHz. The anisotropic parameters are indicative, once again, of a radical, since $A_{iso} = 200$ MHz and $D = 22$ MHz. With an increase in temperature to 100 K, the isotropic centre appears to be unchanged, but the anisotropic centre has a small increase in A_{iso} to 260 MHz, and a noticeable increase in D to 50 MHz. It is suggested that the anisotropic centre is still a radical, but with an increased distortion of the electron spin density. With further increase of temperature to 300 K, although the hyperfine parameter of the isotropic centre has increased to 4000 MHz, few physical changes appear to have occurred, with a near-vacuum isotropic muonioum state and anisotropic radical state still present, since the anisotropic parameters remain unchanged.

g-$Si_{10}Se_{90}$

Repolarisation curves for g-$Si_{10}Se_{90}$ are shown in Figure 7.8. As for the g-$Ge_{10}Se_{90}$

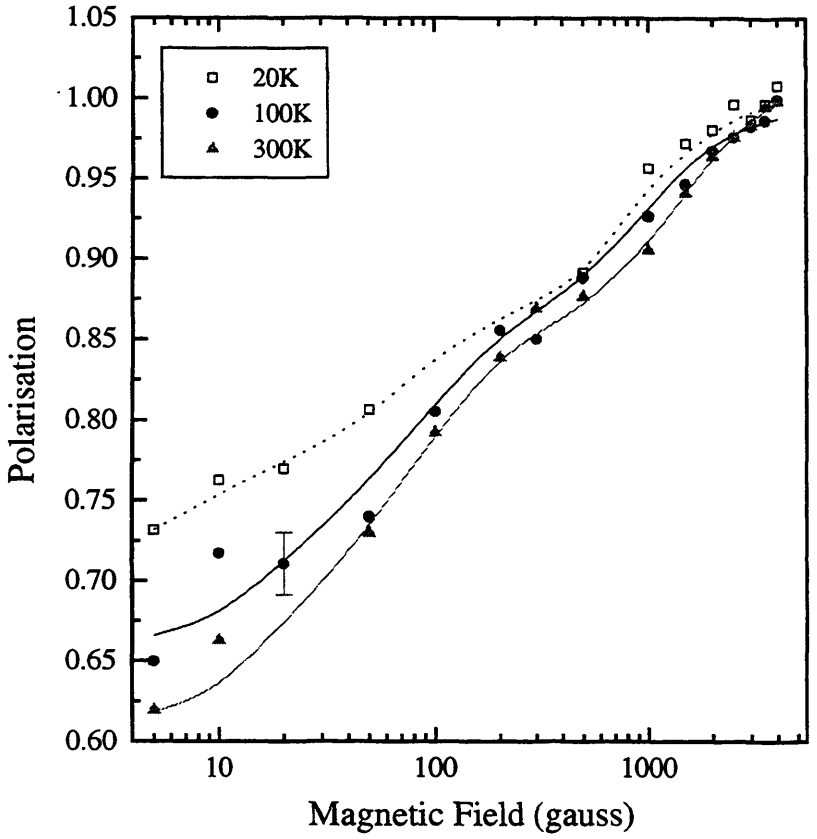

Figure 7.7: The field dependence of the polarisation for g-$GeSe_2$.

Sample	T (K)	Dia.	Isotropic		Anisotropic		
		f_d (%)	f_{Mu_T} (%)	A (MHz)	$f_{Mu_{BC}}$ (%)	A_{iso} (MHz)	D (MHz)
g-$GeSe_2$	20	54.5	27.5	2750	18.5	200	22
g-$GeSe_2$	100	49	25.5	2750	25	260	50
g-$GeSe_2$	300	40	30	4000	30	260	50

Table 7.5: The fitted hyperfine parameters and relative fractions for g-$GeSe_2$. See caption for Table 7.2 for the meaning of Mu_T and Mu_{BC}.

sample, though dissimilar to the earlier germanium-selenium alloys, the repolarisation curves of the g-$Si_{10}Se_{90}$ sample present little immediate evidence for two paramagnetic states. From the fitting parameters, presented in Table 7.6, it can be seen that at low temperatures, although two paramagnetic sites are present, there is a much larger fraction of anisotropic centres, such that $f_{Mu_T} = 13\%$ and $f_{Mu_{BC}} = 35\%$. With an increase in temperature to 100 K, the isotropic muonium states are completely lost, and the fraction of anisotropic sites increases to 44%, thus indicating the possibility of T $\rightarrow$ BC conversion. With a further increase in temperature to 300 K, the fraction of anisotropic sites is reduced to about 32%. For the diamagnetic fraction, at low temperatures f_d remains constant at about 43%, and therefore is approximately equally favoured by the muon. With an increase to 300 K, f_d increases to 57.5%, almost twice the fraction of the paramagnetic site, thereby indicating the conversion of paramagnetic to diamagnetic states. Although the relative fractions do differ between the g-$Si_{10}Se_{90}$ and g-$Ge_{10}Se_{90}$, the virtual loss of the tetrahedral site at 100 K, and the dominance and nature of the anisotropic centres, is common to both materials. This can be compared to the stability of the relative fractions for both g-$Ge_{22}Se_{78}$ and g-$GeSe_2$, and their radical-like anisotropic centres at high as well low temperatures. Significantly, g-$Si_{10}Se_{90}$ does not encounter the discrepancy of the differences between the experimentally measured f_d and the value obtained from fitting to the LF-μSR data.

At low temperature, the hyperfine parameters differ little from those of g-$GeSe_2$. The isotropic hyperfine parameter A is approximately 2000 MHz. The anisotropic centre hyperfine parameter, A_{iso}, at 300 MHz, once again indicates a molecular radical, with a noticeable degree of distortion of the spin density since $D = 40$ MHz. As the temperature is increased, the nature of the anisotropic centre remains unchanged, although the isotropic paramagnetic centre has been lost. With a further increase in temperature to 300 K, the anisotropic hyperfine parameter increases to 550 MHz, larger than the expected range of the radical, 200 - 400 MHz.

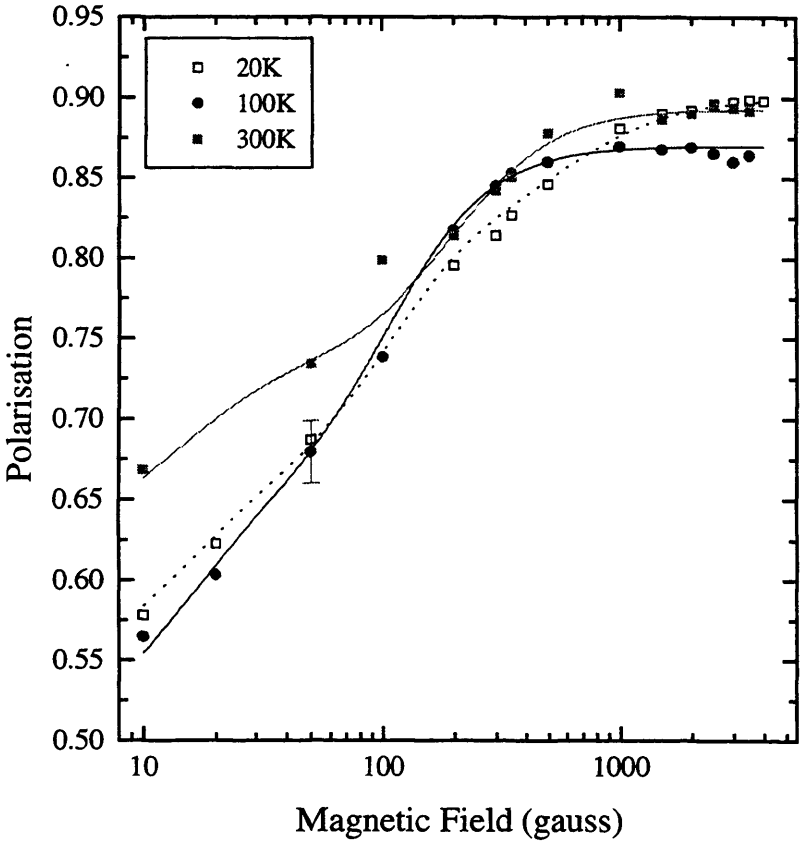

Figure 7.8: The field dependence of the polarisation for g-$Si_{10}Se_{90}$.

Sample	T (K)	Dia.	Isotropic		Anisotropic		
		f_d (%)	f_{Mu_T} (%)	A (MHz)	$f_{Mu_{BC}}$ (%)	A_{iso} (MHz)	D (MHz)
g-$Si_{10}Se_{90}$	20	42	13	2000	35	300	40
g-$Si_{10}Se_{90}$	100	43	0	—	44	300	40
g-$Si_{10}Se_{90}$	300	57.5	0	—	31.8	550	40

Table 7.6: The fitted hyperfine parameters and relative fractions for g-$Si_{10}Se_{90}$. See caption for Table 7.2 for the meaning of Mu_T and Mu_{BC}.

g-$Si_{20}Se_{80}$

The repolarisation curves for g-$Si_{20}Se_{80}$ are shown in Figure 7.9. Upon inspection of the figure, it is clear that the relative fractions of the diamagnetic and paramagnetic sites differ from those of g-$Si_{10}Se_{90}$. The parameters used to generate these fittings, shown in Table 7.7, bear testimony to the difference of relative fractions with an increase in the silicon content of the alloy. From the table it is shown that, at low temperatures, there is very little diamagnetic fraction. As with many of the previous samples, f_d is smaller than the experimentally determined value of Figure 7.1. By analysis of both the results of Figure 7.1 and the fittings of Table 7.7, it is clear that the majority of the muons reside in paramagnetic centres. From the fittings, it would appear that the isotropic site is twice as likely to be the site of muonium residence than the anisotropic site. Unfortunately, with a discrepancy of 20% between the experimentally measured f_d and the value obtained from the LF-repolarisation curve, the relative fractions at 20 K are unlikely to be accurate, since to compensate for a low LF diamagnetic fraction, the relative fractions of the paramagnetic centres will be increased. There is no missing fraction present for this 20 K data and, as such, the reason for such a low LF diamagnetic fraction is unknown. With an increase in temperature to 100 K, the lack of any diamagnetic states remains, whilst the missing fraction increases to a significant 26.5%. From the parameters, it would seem that the isotropic site continues to dominate. At 300 K, there appears to be a total loss of anisotropic centres, and a significant increase in the fraction of diamagnetic centres. Again, the isotropic site would seem to remain dominant, but the missing fraction has substantially increased to 53%, possibly attributed to a large relaxation rate, as seen for the results of pcr-GaAs in the previous chapter, although to produce such a large $f_{missing}$ a dynamic process of site conversions is more likely.

From the hyperfine parameters, at 20 K the isotropic centre, with a hyperfine parameter of $A = 1500$ MHz, would appear to have a low electron-density on the muon site. Such a low A value does seem to be abnormally low, especially in comparison to the corresponding value for the other chalcogenide materials, and a value in the region of 2000 MHz, is more likely. It would seem to be more likely that an A of 2000 MHz

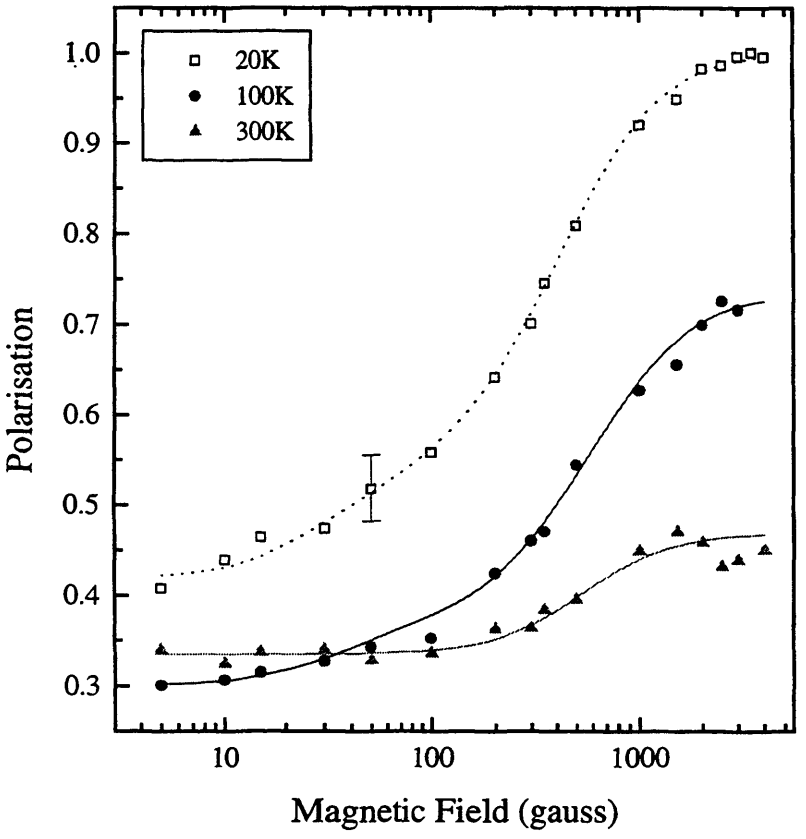

Figure 7.9: The field dependence of the polarisation for g-$Si_{20}Se_{80}$.

Sample	T (K)	Dia.	Isotropic		Anisotropic		
		f_d (%)	f_{Mu_T} (%)	A (MHz)	$f_{Mu_{BC}}$ (%)	A_{iso} (MHz)	D (MHz)
g-$Si_{20}Se_{80}$	20	5	63	1500	32	550	80
g-$Si_{20}Se_{80}$	100	0	53.5	2000	20	750	100
g-$Si_{20}Se_{80}$	300	20	27	1500	0	—	—

Table 7.7: The fitted hyperfine parameters and relative fractions for g-$Si_{20}Se_{80}$. See caption for Table 7.2 for the meaning of Mu_T and Mu_{BC}.

is common to all temperatures, and thus little change will occur in the nature of the isotropic centre with an increase in temperature, or at least, certainly up to 300 K. For the anisotropic paramagnetic centre, the high value of A_{iso}, equal to 550 MHz, should be treated with extreme caution bearing in mind the effects of the abnormally low LF diamagnetic fractions, which introduce the need to compensate via the relative paramagnetic fractions and also the hyperfine parameters of these paramagnetic centres. At 100 K, the nature of the paramagnetic states has changed very little, with only minor increases in the hyperfine parameters and the anisotropic parameter of either centre, but once again an A_{iso} value of 750 MHz would appear to be physically too large for an anisotropic centre, and it can again be considered to be dubious. With a further increase in temperature to 300 K, although the anisotropic paramagnetic centre has been lost, the nature of the isotropic centre remains unchanged, with $A = 1500$ MHz.

The behaviour of the g-$Si_{20}Se_{80}$ differs greatly from its nearest germanium analogue, g-$Ge_{22}Se_{78}$, where the isotropic muonium centre was near-vacuum state free muonium, and the anisotropic centre appeared to be a molecular radical, characterised by the much lower value of A_{iso}. Similarly, the relative fractions of g-$Si_{20}Se_{80}$ behaved very much different to those of the g-$Ge_{22}Se_{78}$, whose relative fractions remained almost constant at all temperatures.

g-$SiSe_2$

The repolarisation curves of g-$SiSe_2$ is shown in Figure 7.10. The parameters used to generate the fittings included on the figure are shown in Table 7.8. From these fitting parameters, it can be seen that there is a distinct difference in the behaviour of the relative fractions of the g-$SiSe_2$ and g-$GeSe_2$. For the g-$SiSe_2$, with an increase in temperature there occurs an increase in f_d from 68% at 20 K, to 80% at 300 K, opposite to the behaviour seen for g-$GeSe_2$. Similarly, the isotropic paramagnetic site of g-$SiSe_2$, is clearly temperature dependent, as at 20 K it accounts for a fraction of 20% of the muon sites, whereas at the higher temperature of 300 K, all isotropic sites have been lost; this can be compared with the stability of the site in g-$GeSe_2$, where the fraction

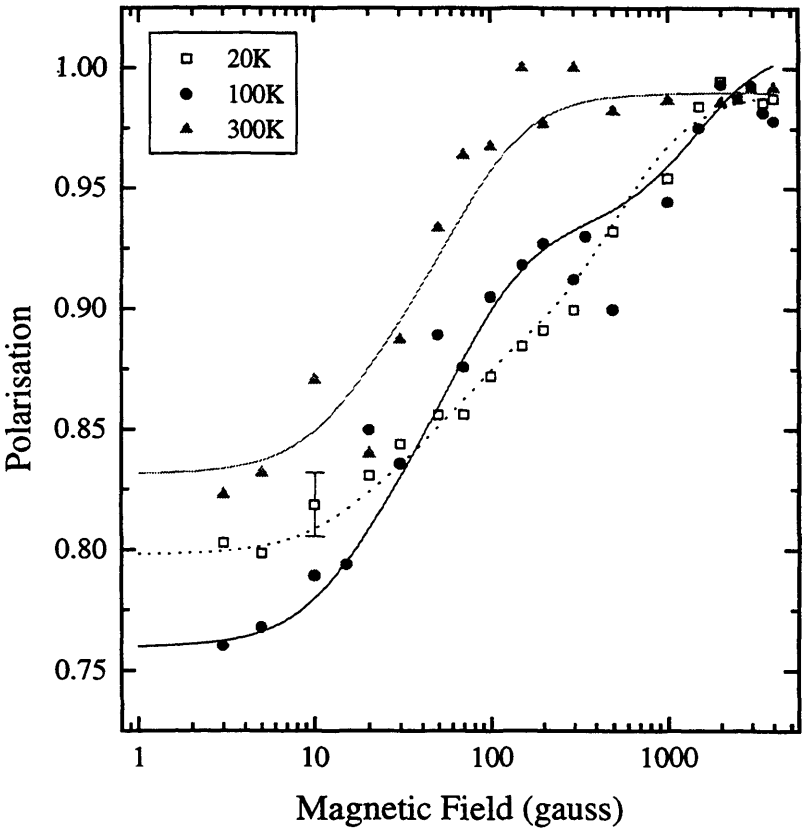

Figure 7.10: The field dependence of the polarisation for g-$SiSe_2$.

Sample	T (K)	Dia.	Isotropic		Anisotropic		
		f_d (%)	f_{Mu_T} (%)	A (MHz)	$f_{Mu_{BC}}$ (%)	A_{iso} (MHz)	D (MHz)
g-$SiSe_2$	20	68	20	1500	11	200	50
g-$SiSe_2$	100	65	15	4000	21	200	50
g-$SiSe_2$	300	80	0	—	19	200	50

Table 7.8: The fitted hyperfine parameters and relative fractions for g-$SiSe_2$. See caption for Table 7.2 for the meaning of Mu_T and Mu_{BC}.

remains consistently near to 28%. At low temperature, the anisotropic paramagnetic site accounts for the least number of sites in which the muon resides, where the anisotropic fraction is only 11%. With an increase in temperature, the site becomes stable, with an average fraction of 20%; so much so that at 300 K the anisotropic centre has become the only paramagnetic centre in which muons reside. Again, this can be compared to the g-$GeSe_2$ material, where, at 300 K, both paramagnetic centres are equally favoured.

The hyperfine parameters differ noticeably from those of 'near-neighbour' materials g-$GeSe_2$ and g-$Si_{20}Se_{80}$. At 20 K, the hyperfine parameter A of the isotropic centre is about 1500 MHz, in agreement with the isotropic centre of g-$Si_{20}Se_{80}$, though in disagreement with the free muonium of the isotropic centre for g-$GeSe_2$. With an increase in temperature to 100 K, the centre had an increased hyperfine parameter of $A = 4000$ MHz, indicating a conversion to a free vacuum-state muonium. Such a large increase in the hyperfine parameter for only a very small increase in temperature would, from experience with other materials, appear to be very unlikely, the necessary large-scale change of the material's structure to allow for a vacuum-state muonium, does not appear to be realistic. By 300 K, the isotropic centre has been lost. The anisotropic centre, with an isotropic parameter of $A_{iso} = 200$ MHz and an anisotropic parameter of $D = 50$ MHz, proves to be far more stable than the isotropic centre, since its parameters remain constant with an increase in temperature. Such parameters are similar to those of the g-$GeSe_2$ sample, and thus indicate that the state is a radical with a rather large degree of anisotropy.

7.3.2 Relaxation rates

a-Se

The $1/T_1$ relaxation rate curves of LF-μSR data for a-Se are shown in Figure 7.11. Unfortunately, the data points are very scattered which hinders understanding of the material, especially when comparing its $1/T_1$ behaviour with that of the Ge–Se and Si–Se materials. Two trends are immediately obvious from the figure. The first is that, with an increase in magnetic field, the relaxation rate is slightly reduced for all

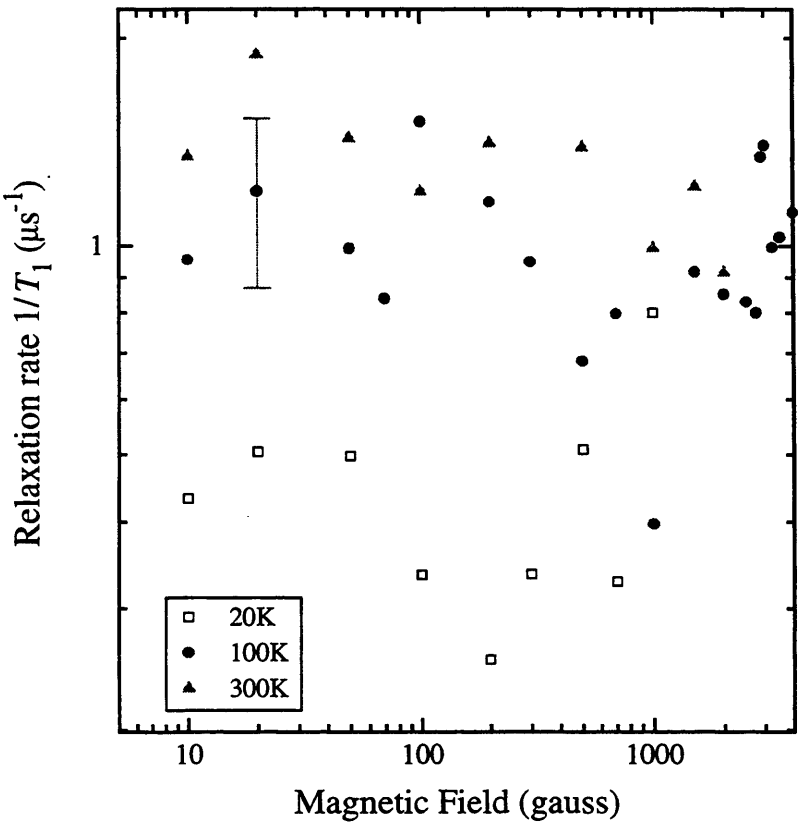

Figure 7.11: The field dependence of $1/T_1$ in a-Se.

temperatures. The decrease in $1/T_1$ is only gradual, especially when compared with the dramatic reductions of some of the silicon materials. The second trend is that $1/T_1$ at 20 K is almost 5 times smaller than the rates at 100 and 300 K, the curves for which virtually overlap. Because of such small reductions in $1/T_1$ with field, even at the high fields of > 3000 gauss, $1/T_1$ is still relatively large, at about $0.9\,\mu s^{-1}$ at 100 K but only about $0.3\,\mu s^{-1}$ at 20 K.

g-$Ge_{10}Se_{90}$

The $1/T_1$ relaxation rate curves of LF-μSR data for g-$Ge_{10}Se_{90}$ are shown in Figure 7.12. The $1/T_1$ behaviour is similar to that of a-Se, although again the data points are very scattered. One can, however, detect a mild field dependence, with $1/T_1$ falling with increase in field. Few data have been collected for low fields at 300 K, and consequently any field-dependence of $1/T_1$ at 300 K is uncertain. Nonetheless, there appears to be a greater degree of overlap between the results for 20 and 100 K with the 300 K data

being higher. The overall average of $1/T_1$ appears to be slightly less than that of a-Se, although at high fields the values are in near agreement.

g-$Ge_{22}Se_{78}$

The $1/T_1$ relaxation rate curves of LF-μSR data for g-$Ge_{22}Se_{78}$ are shown in Figure 7.13. The field-dependence of the $1/T_1$ appears to be similar to that of the a-Se and g-$Ge_{10}Se_{90}$ in the low-field regime and overlap of the data at all temperatures in the low-field regime. In the high-field regime though, at the low temperature of 20 K, a rapid fall of $1/T_1$ occurs; this reduction is so rapid that $1/T_1$ is negligible above about 3000 gauss. By comparison, at the higher temperatures of 100 and 300 K, a milder field dependence is seen, and the 100 K data points fall below those at 300 K.

g-$GeSe_2$

The $1/T_1$ relaxation rate curves of LF-μSR data for g-$GeSe_2$ are shown in Figure 7.14. From the figure, it can be seen that the field dependence differs somewhat from those of the previous materials. Rather than a gradual fall with field, at 100 and 300 K, there is a slight increase in $1/T_1$, rising to a maximum in the region of $B = 200$ gauss, followed by a fall to $\approx 0.4\,\mu s^{-1}$ at 4000 gauss. There again occurs a clear overlap of data, over much of the field range, at 100 and 300 K; whereas the relaxation rates at 20 K at high fields are almost an order of magnitude smaller than the corresponding values for the higher temperatures. Even though there is a lack of data in the mid-field region, for 20 K, a maximum in this region seems unlikely. At low fields, there appears to be little field dependence. The fall-off of $1/T_1$ occurs at a lower field than for g-$Ge_{22}Se_{78}$, beginning at about 500 gauss.

g-$Si_{10}Se_{90}$

The $1/T_1$ relaxation rate curves of LF-μSR data for g-$Si_{10}Se_{90}$ shown in Figure 7.15. At 20 K, the behaviour of $1/T_1$ is very similar to that at the same temperature for g-$GeSe_2$, where in the low-field region there is very little field dependence, with a fall-off in the mid-field regime only a little faster than for g-$GeSe_2$. As such, the $1/T_1$ behaviour is very

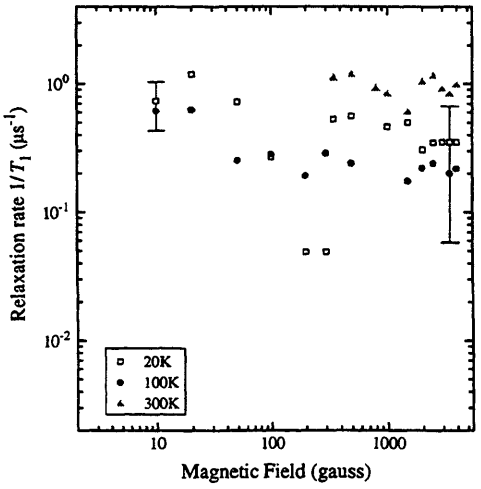

Figure 7.12: The field dependence of $1/T_1$ in g-$Ge_{10}Se_{90}$.

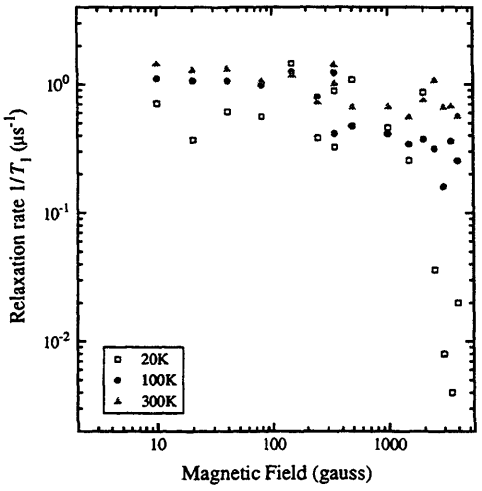

Figure 7.13: The field dependence of $1/T_1$ in g-$Ge_{22}Se_{78}$.

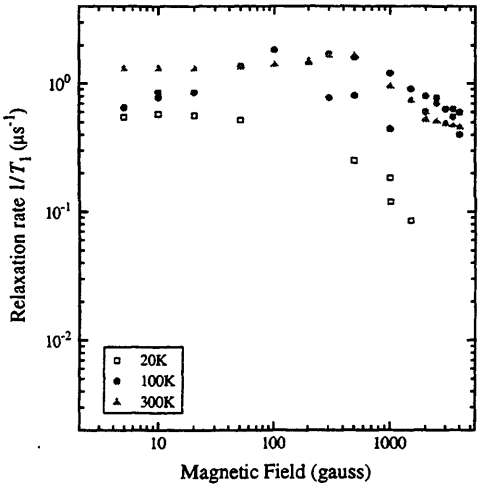

Figure 7.14: The field dependence of $1/T_1$ in g-$GeSe_2$.

different from that of the germanium analogue (g-$Ge_{10}Se_{90}$), which exhibited only a mild field dependence, although at very low fields the values of $1/T_1$ are very similar. For the 100 and 300 K data, which overlap, there is little similarity with the corresponding data for g-$GeSe_2$, but the data does resemble that of g-$Ge_{10}Se_{90}$, and moreso the g-$Ge_{22}Se_{78}$, in its magnitude and overlapping of data, although there does appear to be a greater field dependence.

g-$Si_{20}Se_{80}$

The $1/T_1$ relaxation rate curves of LF-μSR data for g-$Si_{20}Se_{80}$ are shown in Figure 7.16. Owing to the scatter on the data for all temperatures, it is difficult to make any definitive comments on the field dependence. As with the data from higher temperatures of the earlier materials, there appears to be a great deal of overlap of the results, and furthermore at all temperatures, $1/T_1$ appears to be almost independent of field, remaining at about $0.7-1.0\,\mu s^{-1}$, a magnitude comparable to the low-field rates for the earlier materials. As with the g-$Si_{10}Se_{90}$ sample, the g-$Si_{20}Se_{80}$ sample exhibits few similarities with its germanium analogue, g-$Ge_{22}Se_{78}$; aside from the similarities in the magnitudes of $1/T_1$, the field and temperature dependence are both absent.

g-$SiSe_2$

The $1/T_1$ relaxation rate curves of LF-μSR data for g-$SiSe_2$ are shown in Figure 7.17. The field dependence of the relaxation rate is very similar to that of g-$GeSe_2$, especially at the higher temperatures of 100 and 300 K. At 20 K, $1/T_1$ is field-independent up to about 1000 gauss, at which point it rapidly drops so as to be nearly negligible by 4000 gauss. As with the early materials, there is a great deal of overlap of the 100 and 300 K relaxation rates. Starting low at $1/T_1 \approx 0.3\,\mu s^{-1}$, with an increase in field the relaxation rates increase, and pass through maxima at a field of about $200-300$ gauss, similar to that of g-$GeSe_2$. After the maxima, there occurs a decrease of the relaxation rates at both temperatures.

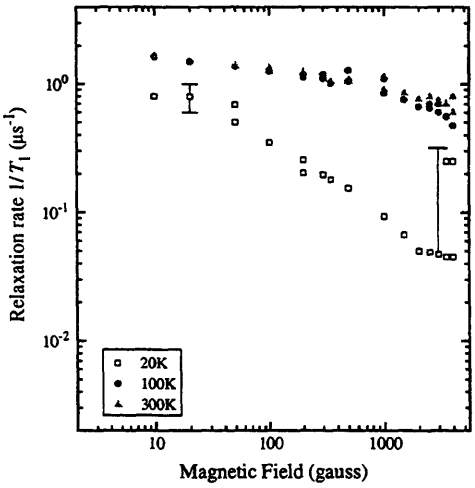

Figure 7.15: The field dependence of $1/T_1$ in g-$Si_{10}Se_{90}$.

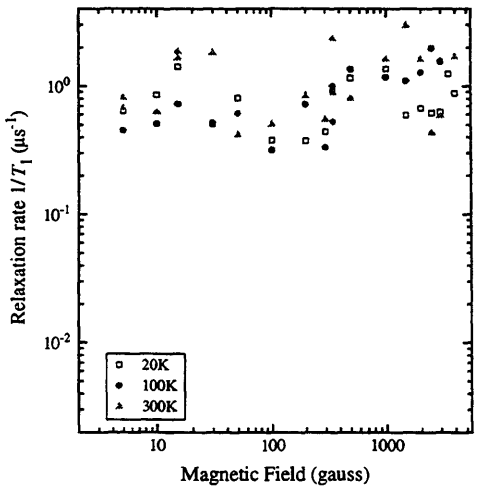

Figure 7.16: The field dependence of $1/T_1$ in g-$Si_{20}Se_{80}$.

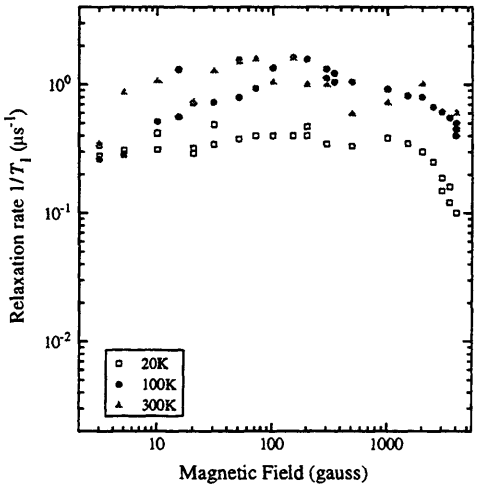

Figure 7.17: The field dependence of $1/T_1$ in g-$SiSe_2$.

7.3.3 Discussion

At low temperatures, the chalcogenide materials studied can be separated into two groups; those with a dominant paramagnetic fraction and those with a dominant diamagnetic fraction. At room temperature, the diamagnetic fraction dominates in all materials, except g-$Si_{20}Se_{80}$. There would appear to be a general trend of f_d scaling approximately inversely with Se content, although g-$Si_{20}Se_{80}$ is once again a notable exception, especially since it has the smallest f_d of all the chalcogenides studied. The effect of Si or Ge addition to Se appears to be quite significant in terms of the behaviour of implanted muons. Such effects are the behaviour of f_d with temperature, the magnitude of f_d and the competition between Mu_T and Mu_{BC} centres.

Selenium has a relatively straightforward chain-like structure, illustrated in Figure 7.18(a). As in the group IV semiconductors, selenium can also possess dangling-bonds, considered to be singly-occupied neutral defect states D^0. At low temperatures, the majority of muonium resides in paramagnetic sites, where the anisotropic bond-centres or the more probable radical states dominate over isotropic sites. The trapped-atom state appears to be absent, i.e. only the molecular radical state is formed. The contact interaction of this anisotropic site in Se, and in many of the other alloys, was found to be in the region of about 200 - 400 MHz, typical of the hyperfine parameter for molecular radicals[3].

Unfortunately, the chemical nature of the radical cannot be determined from the present results. A likely candidate is the attachment of muonium to selenium via a 'three-electron' bond[4]; if this is the case there must be a delocalisation of the unpaired electron along the otherwise intact a-Se chain, as in Equation 7.1:

$$Mu^0 + :Se\diagup\diagdown \longrightarrow Mu{-}\dot{S}e\diagup\diagdown \qquad (7.1)$$

At low temperatures, the concentration of diamagnetic and paramagnetic sites remains roughly constant. The prominent increase of f_d at about 250 - 300 K can be attributed to the conversion of $Mu_T \rightarrow Mu_{BC}$ sites (in this case referring to the radical centre). By room temperature, all the Mu_T centres have been lost, and Mu_{BC} is very much the dominant site-type. Judging by the increase in f_d above 300 K, it can be assumed that Mu_{BC} centres are ionised to diamagnetic states, such that by about 325 K, the

diamagnetic centres are the dominant muonium sites.

Inspecting the polarisation curve independently of any fitting mechanism, it can be seen that at low field the polarisation is about 40%, equal to the experimental value of f_d. Since for an anisotropic centre, the polarisation should begin at about 16% ($\frac{1}{6}$) and for an isotropic centre at 50%, the only way in which the LF-polarisation could have the low-field value of 40% would be if muonium formed diamagnetic centres only, i.e. no paramagnetic centres existed, which is clearly not true judging by the shape of the repolarisation curve. Coupled with a significantly large missing fraction, $f_{missing}$, of about 20%, it would appear that a system of complex dynamics is occurring. At present little is known of such mechanisms, but it is likely that they are revealed in the LF-μSR rather than the TF-μSR measurements. As with pcr-GaAs and GaP, missing fractions typically occur as a consequence of a rapid depolarisation of the paramagnetic centre, too fast for the equipment of ISIS to detect. Other possibilities could be the slow-formation of muonium, although this only tends to occur in electron-rich materials, such as heavily-doped n-type semiconductors.

Introducing germanium or silicon into the selenium structure appears to have a significant effect on the nature and predominance of the muonium centres. In any interpretation of the fittings, because of the difficulties of missing fractions in the repolarisation data, there is a noticeable degree of uncertainty. However, conclusions can be made from the general trends of the data. The anisotropic radical centre appears to be present in all samples, although in different percentages. By its presence in virtually all the materials at both low and high temperatures, it can be assumed to be relatively stable. With the exception of g-$Si_{20}Se_{80}$, for which significant differences between the TF measured f_d and the LF fitted f_d cast doubt on the suitability of the theoretical fittings. In addition, the relative abundance of isotropic centres appears to bear little relation to the percentage of the added element. The nature of the isotropic centres does change, both with the added element and the percentage of alloy material.

In a-Se and the selenium alloys of g-$Ge_{10}Se_{90}$ and g-$Si_{10}Se_{90}$, the anisotropic muonium centre, the radical, dominates. With further addition of Ge, in g-$Ge_{22}Se_{78}$ and g-$GeSe_2$,

the isotropic and anisotropic centres become almost equally probable. With the further addition of Si, in g-$Si_{20}Se_{80}$ and g-$SiSe_2$, at low temperatures the isotropic centre dominates, but at high temperature the parameters are much more uncertain. It therefore seems that with the addition of an added element, whether it be Ge or Si, there is an increase in the cross-linking of selenium 'chains', illustrated in Figure 7.18(b), allowing the possibility of cage-like interstitial centres. The hyperfine constants of the isotropic centres, and thereby the nature of the Mu_T sites, were found to depend on the type of the added element. With the addition of Ge, the Mu_T centre was found to be pseudo-vacuum like, having hyperfine constants of up to 4000 MHz. With the addition of Si however, the hyperfine constants were as low as 1500 MHz. In contrast, the anisotropic centres appeared to have little dependence on the added element-type, and showed little variation with temperature, again indicating a stable radical-type of centre.

7.4 Aperçu

As with the results for pcr-GaAs and pcr-GaP, the understanding and interpretation of the μSR results is very limited. Understanding the chalcogenides' behaviour is especially difficult since unexplored territory has been ventured into, and thus comparisons cannot be made against other's findings. Nevertheless, interesting observations have been made, which should, hopefully, lay a worthy foundation for future experiments. A proposal has been made for the nature of the dominant paramagnetic state, a molecular radical. The 'three-electron' bond has been suggested as the model for the radical in the chain-like selenium alloys.

Several issues must be addressed in future research into the chalcogenide materials. The nature of the radical and the variation of the chalcogenide lattice with reduced Se content should be understood. For this to occur, two other problems must be considered. Firstly, a reduction of the sizeable missing fraction, and also, enhancement of the fitting procedures to include dynamic processes that may be inducing these missing fractions. Secondly, consideration could be made of why the addition of Ge produces an isotropic centre of differing characteristics from when Si is added, whereby the isotropic centre

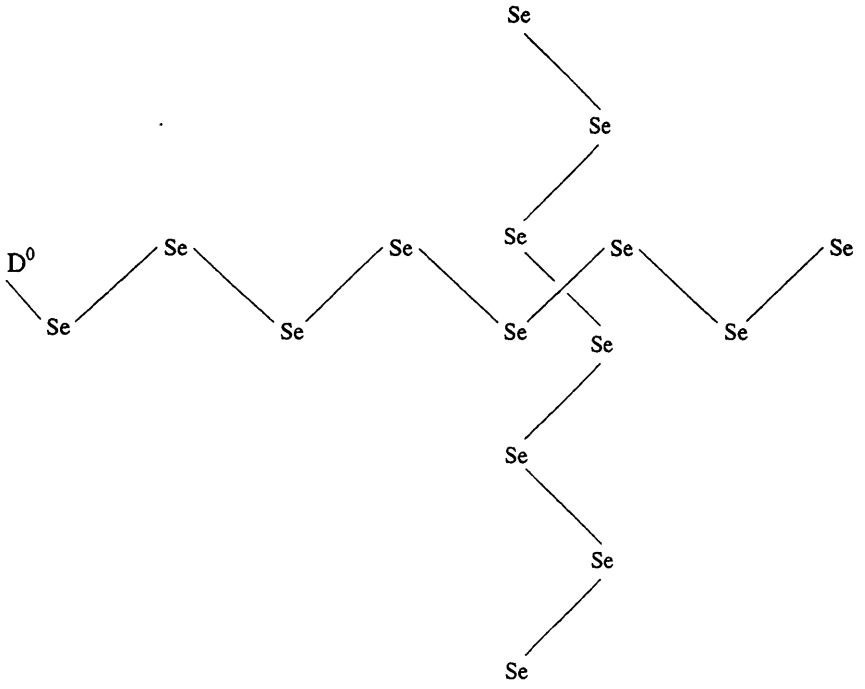

(a)

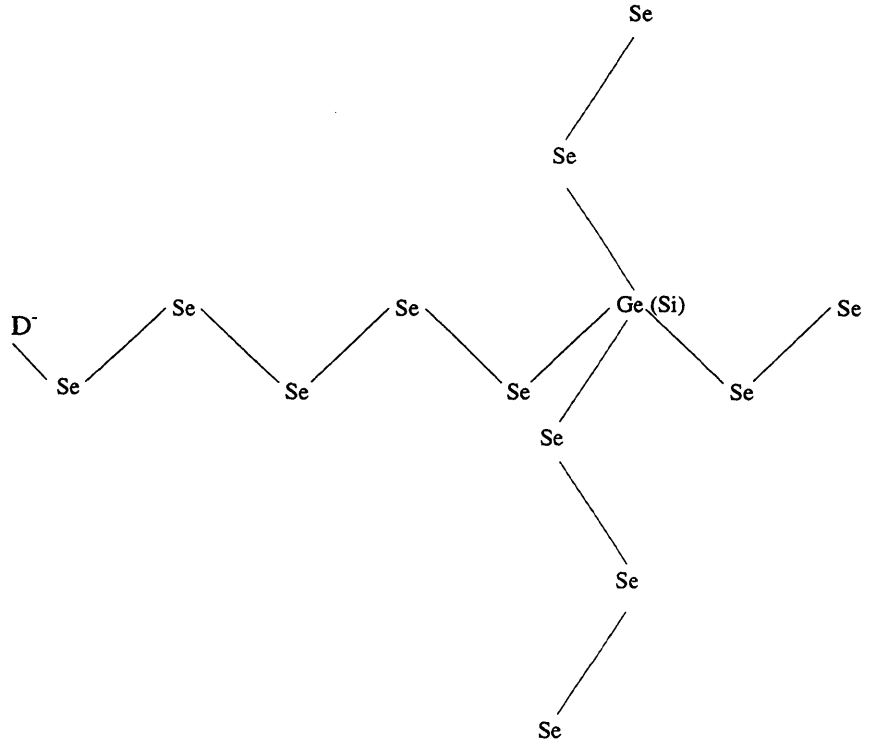

(b)

Figure 7.18: Schematic illustration of (a) chain-like selenium structure, where D^0 is a singly-occupied dangling bond and (b) cross-linked network of selenium, with either Ge or Si adopting four-fold coordination.

is nearly pseudo-vacuum like with added Ge, but with an addition of Si, a very low hyperfine coupling of 1500 MHz arises. What is therefore apparent, is that, there remains great potential future research into hydrogen in chalcogenide glasses, with several different areas of interest to study.

Bibliography

[1] H. Fritzche, V. Smid, H. Ugar and P.J. Gaczi, J. Phys. **42**, (1981), C4-699.

[2] E. Sleeckx, P. Nagels, R. Callaerts and M. Van Roy, J. Non-Cryst. Solids **164**, (1993), 1195.

[3] W. Hayes, in E.A. Davis, S.F.J. Cox (Eds.), Protons and Muons in Materials Science, Taylor and Francis, (1996), p. 87.

[4] M.C.R. Symons, in E.A. Davis, S.F.J. Cox (Eds.), Protons and Muons in Materials Science, Taylor and Francis, (1996), p. 265.

Chapter 8

Summary and Concluding remarks

Decades of research has resulted in an abundance of information on a variety of crystalline elemental and compound semiconductors, principally Si, Ge, GaAs and GaP. However, detailed understanding of the behaviour of hydrogen in these materials is sparse, even though trace amounts of this element are known to play an important role in determining their electronic properties. It was from a consideration of such a lack of true understanding of hydrogen processes, not only in crystalline but also in amorphous semiconductors and chalcogenide glasses, that this research was undertaken. The principal objectives have been :

- to simulate hydrogen in a variety of semiconductors (both crystalline, amorphous and glassy) by means of muon implantation
- to identify sites occupied by the muons and thereby to infer possible atomic locations for hydrogen and its role in the materials investigated
- to identify whether the μSR technique can discern between different structure-types, and can be used to indicate possible structures or structural changes
- to evaluate the potential of the longitudinal-field repolarisation technique for identifying sites occupied by muonium.

With regard to the last of these objectives, it should be stressed that the work described in this thesis represents the first attempt to fit theoretical expressions to repolarisation curves with a view to determining estimates of relative fractions and hyperfine parame-

ters of the centres involved. At the beginning of the research, expressions applicable to data obtained on polycrystalline or amorphous materials did not exist; two theoretical treatments, one an approximation to the low-field behaviour[1] and the other applicable at high fields[2], became available only during the course of the work. As such, the method is not a well-established technique and the results in this thesis should be considered in this light.

Even for materials where the relative fractions and hyperfine parameters of muonium are known from previous measurements, theoretical fitting of the repolarisation curves have revealed subtleties which, rather than casting doubt on the experimental data or the theory, have provided new information on the centres involved. In other cases, limitations of the existing theory (including omission of dynamic effects and nuclear hyperfine interactions) have been exposed.

An example showing excellent agreement between theory and experiment is that of pcr-Si (see Figure 5.3). The repolarisation curve in this case is fully accounted for by theory, using known values of the relative fractions and hyperfine parameters of the two paramagnetic centres, Mu_T and Mu_{BC}, and the diamagnetic fraction measured by TF-μSR. Even the cusp at 3400 gauss, associated with repolarisation of the Mu_{BC} centre, and occurring as a consequence of spin-flip transitions leading to the rapid depolarisation of the muon, is faithfully reproduced. For pcr-Ge, however, even with knowledge of similar information on the nature of the sites, theory and experiment disagree. It would appear that in this case interconversion of Mu_T and Mu_{BC} sites, coupled with similar ionisation energies for the two centres, are responsible for the discrepancies. Further work on this material should reveal more of this interesting dynamic behaviour.

For the *amorphous* forms of the above two Group IV semiconductors, new effects were expected and indeed found. It was postulated that in a-Si, at higher temperatures the muonium may be diffusing through the lattice from bond-centre to bond-centre via dangling bonds, a mechanism that is less likely to occur in a-Si:H as a consequence of the greater distance between dangling bonds. In particular, an enhanced stability of the bond-centre site, probably arising from the existence of pre-stretched bonds in

the disordered lattices, has been found. This result is of importance in connection with interpreting the role of H in a-Si:H, in particular the Staebler-Wronski effect which limits the performance of commercial solar cells made from this material.

Work on III-V compounds, namely GaAs and GaP, has been confined to polycrystalline forms of these two semiconductors. A complication with these materials is the existence of nuclear spins, the effects of which have not been incorporated into the theory used. Nevertheless, for pcr-GaP, it has been possible to determine the relative fractions and parameters of the muon states involved. Clearly a-GaAs and a-GaP would be good candidates for future studies, as well as samples with varying degrees of n- and p-type doping.

With regard to the chalcogenide glasses, unexplored territory has been ventured into. None of the selenium-based compounds studied has been previously investigated by any form of muonium spectroscopy. Our data clearly indicate the presence of more than one type of centre and the results have been analysed on the assumption of three site-types - one that is diamagnetic, and two that are paramagnetic, either isotropic or anisotropic. Although the latter two have been labelled Mu_T and Mu_{BC} for convenience, tetrahedral cage and bond-centre sites analogous to those in the Group IV or III-V structures are not expected. In some cases we have found that the isotropic site has a hyperfine parameter characteristic of vacuum-state muonium and in others, a radical-like anisotropic state is inferred.

Our 'broad-brush' survey of muonium in such a large and diverse variety of materials has demonstrated the value of the techniques adopted, while at the same time revealing new and important effects. For future progress, it will be necessary to concentrate on each of the three classes of materials investigated in more detail, with a view to elucidating the limitations of existing theory and providing indicators as to useful directions in which it can be developed in order to account for experimental data. In addition, other allied analysis techniques, such as RF-μSR should be exploited to provide a greater breadth of data from which interpretation can be made. Such a technique, not available for much of the course covered in this thesis, has only recently become available at the

Rutherford Laboratories, and it is hoped that the new facility on the DEVA beamline, now operating to an internationally high standard, will lend an extra arm-of-support to the scientists of both Britain and continental Europe, in providing further data, in particular for the interpretation of site-types and their dependence on temperature and the material's structure.

Bibliography

[1] F.L. Pratt, Phil. Mag. Lett **75**, (1997), 371.

[2] P.F. Meier, Hyp. Int. **86**, (1994), 723.